Fatigue crack growth assessment and fatigue resistance enhancement of aluminium alloys

Ma Mohin

A thesis submitted in partial fulfilment of the requirements of the University of Hertfordshire for the degree of Doctor of Philosophy

The programme of research was carried out in the School of Engineering and Technology, University of Hertfordshire

April 2018

Abstract

Fatigue damage of aluminium alloys is one of the key concerns in transport industries, particularly in the aerospace industry. The purpose of the project is to develop new knowledge and techniques against fatigue failure for these industries through a systematic investigation of fatigue resistance and crack growth behaviours of aluminium alloys.

Fatigue and fracture mechanics have been investigated analytically, numerically and experimentally in this project. Overload transient effect on fatigue crack growth has been examined by considering various parameters including crack closure, overload ratio (OLR), load ratio (R ratio), baseline stress intensity factor range, $(\Delta K)_{BL}$ and geometry. It was found that crack closure can be correlated qualitatively and quantitatively to all other parameters associated with overload transient behaviour. It is proposed that the effect of crack tip plasticity on the non-linearity of the compliance curve can be separated to obtain reliable crack closure measurement. In this project, different methods are used to better understand the transient retardation process so that the damage tolerance design (DTD) of the components made of aluminium alloys can be enhanced.

Another important parameter for fatigue and damage tolerance design (DTD) of engineering components is the threshold stress intensity factor range for fatigue crack growth, ΔK_{th}. A small variation in identification of ΔK_{th} can lead to a big change in overall estimation of fatigue life. In this project, an analytical model has been developed for aluminium alloys by fitting an analytical curve with raw crack growth data in order to identify the ΔK_{th}. This model has the capacity to identify ΔK_{th} for different aluminium alloys at various R ratios.

There is a great demand for enhanced fatigue life of aluminium alloys in the transport industry. This project has carried out a detailed investigation of electromagnetic treatment (ET) in the form of electropulsing treatment to develop an efficient technique for fatigue resistance enhancement. ET parameters including the treatment intensity, treatment time and the number of applications have been optimised. It is suggested that the duration of ET treatment can be used as the main parameter among all these to control the fatigue resistance of the aluminium alloy. The improvement in fatigue

resistance has been explained by the change in microhardness and conductivity of aluminium alloy due to ET. Additionally, the fracture morphology was analysed using scanning electron microscopy (SEM). The precipitates and dislocation characteristics were also studied using transmission electron microscopy (TEM). The outcomes of this investigation will help improve structural integrity by enhancing fatigue resistance of aluminium alloys.

Nomenclature

A	Area
AFGROW	Air force growth
ASTM	American Society for Testing and Materials
a	Half crack length
a_P	Crack length plus the overload plastic zone
a_t	Tolerable crack length
a_{crit}	Critical crack length
a_D	Delay distance due to crack growth retardation
a_{det}	Detectable crack size
α	Constraint factor
B	Magnetic field strength
b	Minor axis
BL	Baseline
β	Geometry factor
CA	Constant amplitude
CAA	Civil Aviation Authority
CCT	Centre-cracked tension
CPL	Crack propagation life
CPCA	Compression pre-cracking constant amplitude
CPLR	Compression pre-cracking load reduction
CTOD	Crack tip opening displacement
CST	Constant strain triangular
C	Material constant
C_f	Crack closure factor
DEF STAN	Defence Standard
DTD	Damage tolerance design
d	Diameter

$\frac{da}{dN}$	Crack growth rate
ΔK	Stress intensity factor range
$(\Delta K)_{BL}$	Baseline stress intensity factor range
ΔK_{eff}	Effective stress intensity factor range
ΔK_{th}	Threshold fatigue crack growth stress intensity factor range
$\Delta\sigma$	Stress range
Δa	Crack increment
$\frac{\Delta D}{D_i}$	Damage repairing parameter
EPFM	Elastoplastic fracture mechanics
E	Young's modulus
F	Force
ET	Electromagnetic treatment
ε	Strain
ε_{ys}	Yield strain
FAA	Federal Aviation Authority
FCG	Fatigue crack growth
FE	Finite Element
FEM	Finite element method
f	Frequency
GP	Guinier-Preston
HCF	High cycle fatigue
H_e	Element height
I	Current
J	Current density
ISO	International Organization for Standardization
K	Stress intensity factor
K_{max}	Maximum stress intensity factor
K_{min}	Minimum stress intensity factor

K_{OL}	Maximum stress intensity factor at overload
K_{op}	Crack opening stress intensity factor
K_{cl}	Crack closing stress intensity factor
K_C	Fracture toughness
LEFM	Linear elastic fracture mechanics
LSF	Low cycle fatigue
L_e	Element length
MSD	Multiple site damage
m	Material constant
NDI	Non-destructive inspection
N	Number of cycles/ fatigue life
NASA	National Aeronautics and Space Administration
N_d	Delay distance due to crack growth retardation
v	Poisson's ratio
OLR	Overload ratio
OL	Overload
OICC	Oxide induced crack closure
P	Load or pressure
Potential drop	Potential drop
PICC	Plasticity induced crack closure
PSB	Persistent slip band
$\% OL$	Percentage of overload
Q4	Four-noded quadrilateral elements
R	Load ratio or stress ratio
RICC	Roughness induced crack closure
r	Radius
r_P	Plastic zone size
RICC	Roughness induced crack closure
S	Stress
SENB	Single edge notched bend
SIF	Stress intensity factor

S-N	Stress vs number of cycles
SOLR	Shutoff overload ratio
$\frac{S}{N}$	Signal to noise ratio
SENB	Single edge notch bend
SEM	Scanning electron microscopy
SSY	Small-scale yielding
σ	Normal stress
σ_{max}	Maximum stress
σ_{min}	Minimum stress
σ_a	Alternative stress/ stress amplitude
σ_m	Mean stress
σ_{ys}	Yield stress
σ_0	Flow stress
σ_{cl}	Crack closing stress
σ_e	Endurance limit
σ_{op}	Crack opening stress
σ_T	Thermal stress
σ_{op}	Crack opening stress
TEM	Transmission electron microscopy
t	Thickness
τ	Shear stress
θ	Crack angle
U	Stress intensity factor range ratio
u	Breakdown voltage
VA	Variable amplitude
w	Width
X-FEM	Extended finite element method
y	Shape factor
γ	Shear strain

Contents

List of Figures

List of Tables

Acknowledgements

I would like to express my gratitude to my supervision team; Dr Yigeng Xu, Dr Andrew Lewis and Professor Andreas Chrysanthou for their dedicated support in this project. Their encouragement, patience and step-by-step technical guidance have helped me to complete this project. I also would like to thank other University of Herefordshire staff, especially Dr Anatolii Babutskyi and Dr Marzio Grasso for their support during this project.

I would also like to thank the University of Hertfordshire for giving me the opportunity to study for this PhD research project and providing me all the necessary facilities. I am grateful to my friends and colleagues who have inspired me to complete my project.

I would like to acknowledge my family's contribution including the financial support for this project. Without this help, it was impossible for me to finish this project. Finally, I would like to thank the Almighty Allah for everything.

1 Introduction

This chapter consists of three sections. The first section provides a brief contextual description of the project and its industrial relevance. The aims and objectives of the project are provided in the second section. The outline of this thesis is highlighted in the final section.

1.1 Background

Aluminium alloys are widely used in engineering structures where light weight is a priority [1]. The 2000 and 7000 series aluminium alloys are recommended for aerospace applications while the 6000 series is recommended for marine and automotive industries. The average demand of aluminium alloys in aircraft in 2015 was 47 % by weight [2]. Although composite materials are replacing aluminium alloys in aircraft manufacturing, advanced aluminium alloys with excellent properties are fighting back and making aircraft manufacturers' choice more difficult. Boeing has predicted that 38050 new aircraft will be produced from 2015 to 2034 at a total value of over US$5.6 trillion [3]. Meanwhile, Airbus has predicted this similar demand as the production of 32600 aircraft which has been estimated at a value of around US$4.9 trillion [4]. Again, for lightweight vehicles, the aluminium content will approach 35 billion pounds (16 billion kilograms) in weight by 2025, making lightweight vehicles the main market for aluminium alloys [5]. As a result, the demand for aluminium alloys for the aircraft and automobile manufacturing industries will grow even though it will have competition from steel and composite materials. However, the problem with aluminium alloys is that they are prone to fatigue cracking [6]. Maintenance and repair of structures result in huge financial cost and extra carbon emissions. To deal with this problem, detailed investigation of fatigue crack growth assessment and fatigue resistance enhancement of aluminium alloys are necessary to improve the service life of the structures. Eventually, these industries will save millions of dollars and reduce the greenhouse effect.

Fatigue is the continuous degradation of material performance under cyclic loading. Most of the engineering failure is caused by fatigue. An aircraft experiences quite different stresses during take-off and landing compared to cruising which induces variable amplitude (VA) fatigue loading on the aircraft structure. Fatigue damage can lead to catastrophic failure. Aviation accidents associated with the Comet, Aloha Airlines Flight 243, United Airlines Flight 232 and El Al Flight 1862 are some of the examples of such failures which have historical significance. By controlling the fatigue damage, such events could be made far less likely.

The constant amplitude (CA) loading effect gives general insights for fatigue design [7]. However, the structure usually experiences variable amplitude (VA) loading in a real application. Moreover, the behaviour of fatigue crack growth under VA loading is different from CA loading. In order to achieve more accurate damage tolerance design (DTD), fatigue crack growth analysis under VA loading needs to be implemented [8]. An overload along with CA loading is a simple form of VA loading. It is well known that overload leads to retardation of fatigue crack growth. The mechanism of this is yet to be fully understood. This phenomenon needs to be investigated quantitatively and qualitatively further based on linear elastic fracture mechanics (LEFM) before it can be adopted in a DTD approach.

The fatigue crack closure mechanism has been widely used to rationalise crack growth behaviour both under CA and VA loading [7, 8]. However, there is still a long-term debate about the existence and effectiveness of crack closure inside the fatigue research community. Some argue crack closure alone cannot explain overload transient fatigue crack growth behaviour [9, 10]. The separation of intrinsic (e.g. deformation heterogeneity) and extrinsic factors (e.g. crack closure) on fatigue crack growth is believed to be the key in successfully applying the crack closure concept. In this project, both compliance and replica techniques have been utilised to investigate fatigue crack growth behaviour under overload effect. The crack growth retardation due to the overload effect has been explained by the crack closure concept. Load ratio (R ratio), overload ratio (OLR), baseline stress intensity factor range, $(\Delta K)_{BL}$ and geometry effect in fatigue crack growth have also been analysed. An investigation has also been conducted to study the effect of crack tip plasticity on non-linearity of the compliance curve in order to improve the crack closure assessment. Furthermore, strip

yield model and finite element (FE) model of cracked aluminium sample have been generated in order to investigate the crack closure effect.

The fatigue crack growth threshold, ΔK_{th} can be taken as an important parameter for DTD. Any discrepancy identifying this parameter can lead to the false prediction of fatigue life [11, 12]. The real identification and application of this parameter will help develop more reliable DTD. Analytical modelling of this parameter will also be both cost and time effective. In this project, an analytical model has been developed to identify ΔK_{th} for different aluminium alloys based on significant parameters which are determined by the least squares method.

In addition, this project has considered a novel mechanism for the fatigue life enhancement of aluminium alloys. Electromagnetic treatment (ET) has been identified as a potential way to improve fatigue life of metal alloys [13-16]. In order to optimise the material properties which include higher fatigue resistance, the treatment parameters need to be controlled. Also, a detailed investigation of the effects of different parameters of ET on fatigue resistance is necessary. This will potentially help save millions of dollars in aerospace and automotive industry by improving the fatigue resistance of metals in the near future. In this project, the effects of ET treatment of aluminium alloys in the form of electropulsing treatment has been conducted in order to enhance the fatigue resistance. The change of microhardness and conductivity of the aluminium alloy due to ET have also been correlated to the improved fatigue resistance. Additionally, SEM fractographic analyses and TEM studies have been conducted to evaluate the effect of ET on the aluminium alloy.

1.2 Aims and objectives

The three aims of the project are:

- To have a further understanding of fatigue crack growth behaviour under variable amplitude (VA) loading.
- To understand and identify fatigue crack closure and fatigue crack growth threshold for the damage tolerance design (DTD).

- To understand the effect of electromagnetic treatment (ET) on fatigue resistance.

To achieve above aims, experimental, numerical and analytical analyses of fatigue behaviour of aluminium alloys have been conducted to attain the following objectives:

- To carry out a comprehensive literature review on the fundamental theories and research associated with the fatigue crack growth problem and ET effect on fatigue resistance.
- To conduct experimental research to understand crack growth behaviour under VA loading.
- To carry out detailed analytical and numerical simulation of the fatigue crack closure and fatigue crack propagation on engineering aluminium alloys.
- To evaluate and analyse numerical and experimental results and to investigate the elements affecting crack growth under VA loading.
- To study the crack tip plasticity effect in order to improve the crack closure measurement.
- To identify the fatigue crack growth threshold using the analytical technique to increase the reliability of the fatigue crack growth life prediction.
- To conduct the experimental research to understand the effects of different ET parameters on material characterisations which improve the fatigue life of aluminium alloy which include fatigue test, microhardness test, conductivity test, SEM and TEM.

1.3 Outline of the thesis

This thesis presents the research work carried out between October 2012 to March 2017 for the PhD project titled “Fatigue crack growth assessment and fatigue resistance enhancement of aluminium alloys”. It contains ten chapters. Chapter 1 gives a brief introduction of the background, aims and objectives of the project along with this outline of the thesis. Chapter 2 is a detailed literature review of theories, methods used and key findings associated with this project. Chapter 3 describes the research strategy adopted for this project. Chapter 4 and 5 present experimental and analytical analyses of fatigue crack growth under variable amplitude (VA) loading.

Effect of plasticity on compliance curve based crack closure measurement using experimental, finite element (FE) and analytical (e.g. strip yield model) analyses is explained in Chapter 6. An analytical model of identification of threshold stress intensity factor range for fatigue crack growth, ΔK_{th} is described in Chapter 7. The experimental analysis of electromagnetic treatment (ET) effect on fatigue resistance is presented in Chapter 8 and Chapter 9. Finally, conclusions of the project & further recommendations are highlighted in Chapter 10.

2 Literature review

This chapter reviews existing research studies, theories, engineering concepts and application related to the work carried out during this project. The understanding of these will yield more damage tolerant aluminium alloys for industries (including aircraft and automotive industries). Damage philosophies against fatigue failure, fracture mechanics and fatigue concepts are summarised first. Fatigue crack growth under both constant amplitude (CA) and variable amplitude (VA) loading has then been discussed. A detailed description of plasticity induced crack closure (PICC) follows. The concept of identification of threshold stress intensity factor for fatigue crack growth, ΔK_{eff} has been presented. Finally, a relatively new approach for improving fatigue resistance using electromagnetic treatment (ET) has been thoroughly reviewed.

2.1 Design approaches for structures against fatigue failures

DTD is one of the key tasks for ensuring aircraft airworthiness. Damage tolerance is the ability of the structure to resist fracture from pre-existent damage for a given period. Fatigue crack growth is one of the critical structural failure modes. To control this failure mode, the damage tolerance design (DTD) approach is widely used in industry. With time, structural design concepts have evolved to the current industrial standard DTD approach, starting from safe-life design and passing through fail-safe design.

2.1.1 Safe-life design

In safe-life design, the structure needs to be free of cracks during its design life. As soon as the crack initiates in the structure, it is considered to be out of order. To measure the fatigue life of the structure, extensive fatigue tests are performed on prototypes due to considerable scattering found in the results of fatigue life. Using the obtained mean stress and ultimate load capacity of the material, the maximum life is

predicted for the corresponding mean stress. The safety factor used here is usually 3-5 [17] because uncertainty in the loading spectrum requires larger safety factor. According to the Defence Standard (DEF STAN) 00-970 [18], safe life exceeds the service life by a factor of at least 2.0 for compact aircraft for safe-life design. The safe-life design is formed based on Miner's rule and S-N (Stress vs number of cycles) curve [19]. Under this design philosophy, fatigue crack growth life, which is sometimes greater than the fatigue crack initiation period, is not considered. So, the fatigue life of the structure remains short in this case. There are many limitations in S-N curves and Miner's rule assumptions and results, which make this design approach more vulnerable to use. Fatigue crack initiation which is a very random process and the presence of unanticipated structural damage, which caused a historical disaster, e.g. Comet disaster (Figure 2.1.1), lead to the downfall of this methodology [20]. As a result, the design of aircraft fuselage now follows a more advanced design approach. In spite of this, the safe-life design approach is still in use for aircraft landing gears, missiles and many helicopter components [19] where other design philosophies are not suitable.

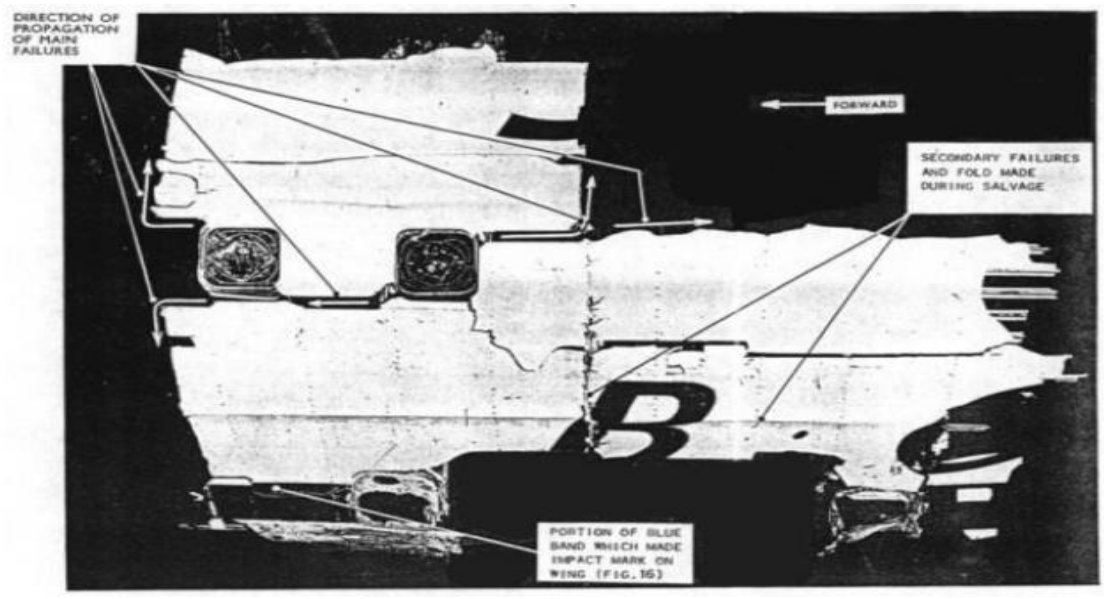

Figure 2.1.1 The wreckage of the first Comet G-LYP, showing the lack of crack arrest features and crack growth from window corner [21, 22].

2.1.2 Fail-safe design

The fail-safe design was introduced in late 1950's in order to address the issues related to the safe-life design approach [19]**.** In fail-safe design, the structure may possess cracks. However, multiple load paths and/or crack arrest features are employed so that single component failure does not lead to immediate loss of the whole structure [23]. Periodic inspection and structural repair are necessary to maintain the fail-safe condition under this methodology. This design approach does not consider the crack growth rate in defining the structural life. The major disadvantage of this design approach is that it requires the redundant structure to cope with the damage. This may lead to a severe weight penalty and fatigue life reduction [19, 24]. Also, redundancy [25] only increases the reliability of the structure, however, it does not always guarantee full safety such as in the case of structures subjected to multiple site damage (MSD), e.g. the accident with the Aloha Airlines Boeing 737 (Figure 2.1.2). However, the continued use of the ageing aircraft in the civil aviation beyond typical design life leads to growing concern relating to the airworthiness of the structures designed under the fail-safe methodology [19].

Figure 2.1.2 (a) B-737 aircraft operated by Aloha Airlines, after landing in Maui, (b) Multiple site damage (MSD) at a B-737 fuselage lap joint [18].

2.1.3 Damage tolerance design

The current damage tolerance design philosophy in the aerospace industry was introduced in the 1970s in response to the perceived limitations on weight saving and safety of the safe-life and fail-safe design approaches [24]. Also, the 45th amendment of the Federal Aviation Administration (FAA), Advisory Circular (AC) 25.571 [26] and the Civil Aviation Authority (CAA) Notice 89 [27] proposed the periodic inspection for aircraft. These regulation changes led to the realisation that the safe-life and fail-safe approaches have to be combined with damage tolerance design in the development of a new aeronautical structure [19]. Under this design approach, a crack may remain in the structure. However, the crack growth rate is monitored based on fracture mechanics. The inspection periods are also set up in a way so that the crack does not go beyond the critical limit starting from a detectable initial crack length. The planning of the period of the inspection and its implementation are the most important criteria under this methodology. Extensive emphasis is necessary on the non-destructive inspection (NDI) to maintain the reliability of the damage detection in this design methodology. An example of DTD methodology is explained in the details below (Figure 2.1.3).

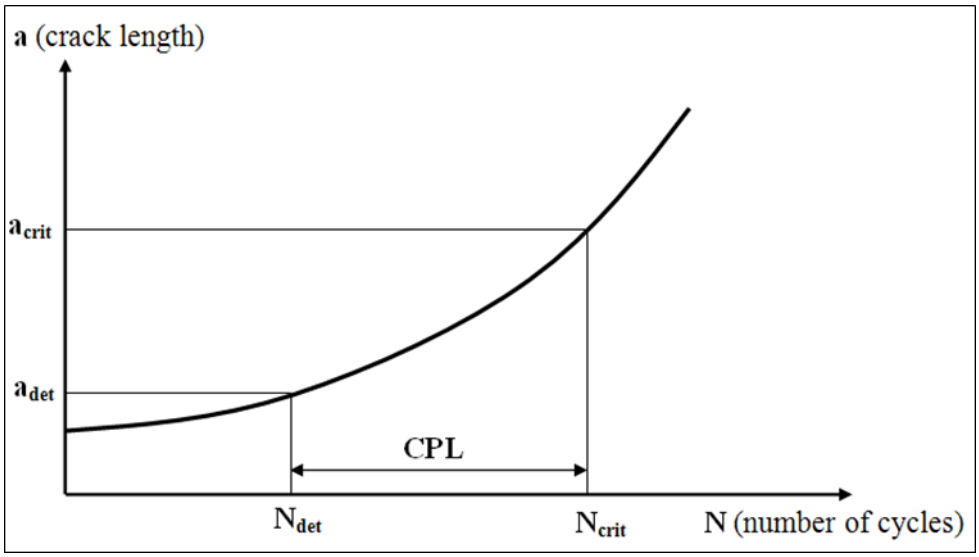

Figure 2.1.3 Illustration of damage tolerance design philosophy.

This Figure 2.1.3. shows the principle of DTD in which an understanding of the fatigue crack growth behaviour is required to predict the crack propagation life (CPL) from a detectable crack size (a_{det}) to the final critical crack length (a_{crit}) in the structure, with an inspection programme being set up to ensure that fatigue cracks are detected before the critical length is reached. The inspection interval is determined by dividing the CPL by a safety factor. This safety factor is usually 2-3 for detectable flow growth [17] and accounts for the uncertainties in the design for material properties, assumptions in the stress calculation, and loading estimations, etc.

Under the DTD approach, aircraft component cracks should grow in a controlled and predictable way. Therefore, the success of the DTD approach depends mostly on the accuracy of the fatigue crack growth life prediction under CA and VA loading.

2.2 Fracture mechanics theories in fatigue crack growth

In the nineteenth century, with the industrial revolution, there was a certain increase in the use of metals in different structures. Unfortunately, several devastating accidents took place in boilers, railways, ships, etc. and caused great loss of life and property. Design flaws and poor material selection were found to be the main reason behind these accidents. Scientists and engineers have endeavoured to find solutions to these problems and developed fracture mechanics theories. Fracture mechanics considers the effect of inherent flaws in the performance and durability of structures.

2.2.1 Structural discontinuity effect

Due to structural discontinuity, the stresses near the discontinuity such as a circular hole, elliptical hole (Figure 2.2.1) and crack, etc. become higher compared to the applied stress [28]. Kirsch [29] first calculated the stress level near a circular hole in 1898. The maximum stress, σ_{max} near the hole was three times bigger than the far field applied stress, σ. Inglis [30] measured the maximum stress, σ_{max} near the elliptical hole of a tension strip in 1913 and found that it can be calculated by the

expression, $\sigma\left(1+\frac{2a}{b}\right)$, where, σ is far field stress and a and b are major and minor axis of the elliptical hole, respectively (Figure 2.2.1). Griffith [31] developed an energy theory for crack propagation for brittle material in 1920 in which crack will grow provided that the total energy of the system is lowered by its growth.

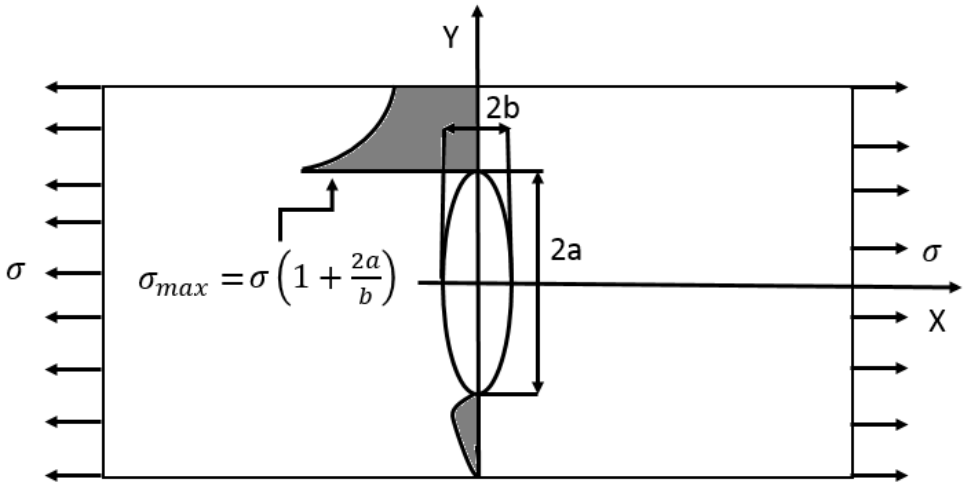

Figure 2.2.1 Stress distribution near the elliptical hole.

2.2.2 Linear-elastic fracture mechanics (LEFM)

The development and application of LEFM derived from Irwin's work [32] in the 1950s have proved to be powerful in understanding fatigue crack growth. In LEFM approach, the material is considered to be an elastic continuum. Moreover, the intensity of the stress field around the tip of a crack is characterised by a parameter called stress intensity factor, K, which is a function of the applied stress, crack length, and a geometrical factor [33]. LEFM theory is valid for elastic-plastic material provided that the crack tip plastic zone size is much smaller than the crack length itself, a condition called small-scale yielding (SSY) condition. High strength steel, precipitation hardened aluminium, polymers below glass transition temperature, ceramics, etc. are the materials (at room temperature), where LEFM is applicable when the SSY condition holds. Fatigue problems, which consider the stress of less than 30 % of yield stress are suitably analysed by it [28]. The effect of significant plastic deformation near the

crack tip beyond SSY can be accounted for by elastic-plastic fracture mechanics (EPFM) (Figure 2.2.2). Then, plastic collapse [34] occurs when the plastic deformation becomes excessive [35] and displacement becomes unbounded.

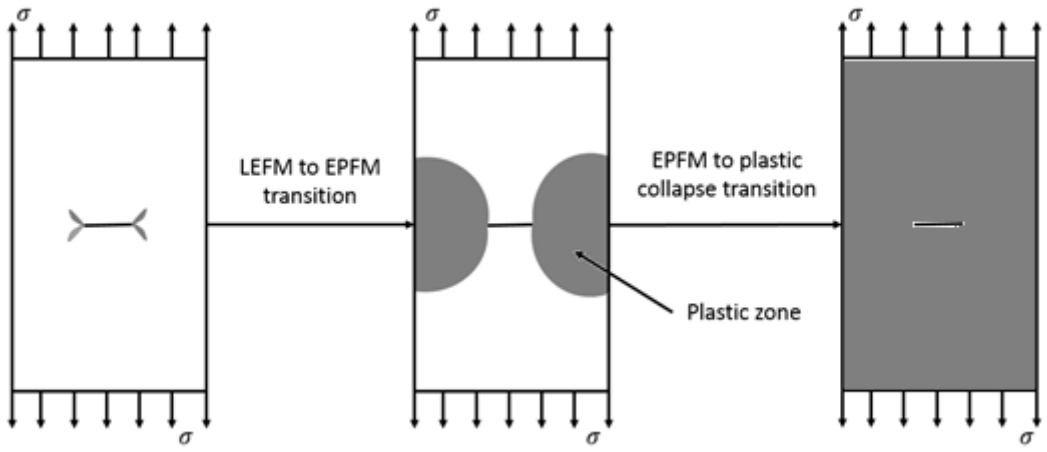

Figure 2.2.2 The transition of LEFM to plastic collapse through EPFM.

2.2.2.1Modes of fracture and plane stress/strain condition

Crack faces in a specimen, move with respect to each other due to loading. It is described using three independent modes or a mixture of two different modes (mixed mode) or a combination of all three modes (combined mode). The three independent modes are mode- I or opening mode, mode II or sliding mode, and mode III or tearing mode (Figure 2.2.3). Based on these modes, stress intensities are written as K_I , K_{II} and K_{III} , and the corresponding fracture toughness values are written as K_{IC} , K_{IIC} and K_{IIIC}.

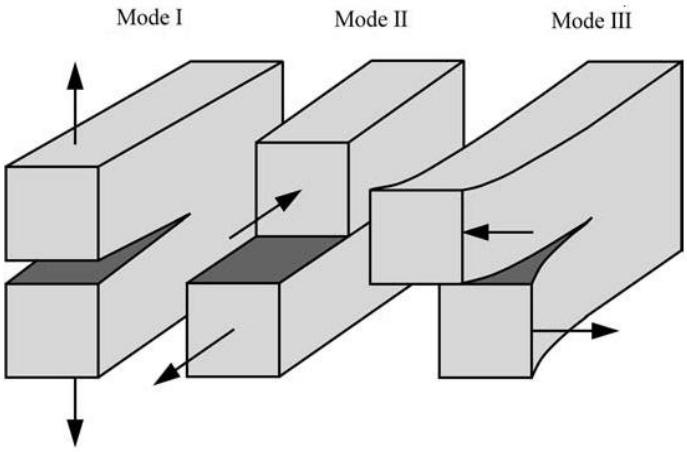

Figure 2.2.3 Modes of loading [7].

In Figure 2.2.4, normal stress and shear stress are denoted as σ and τ, respectively. Here, corresponding normal strain and shear strain are denoted as ε and γ, respectively.

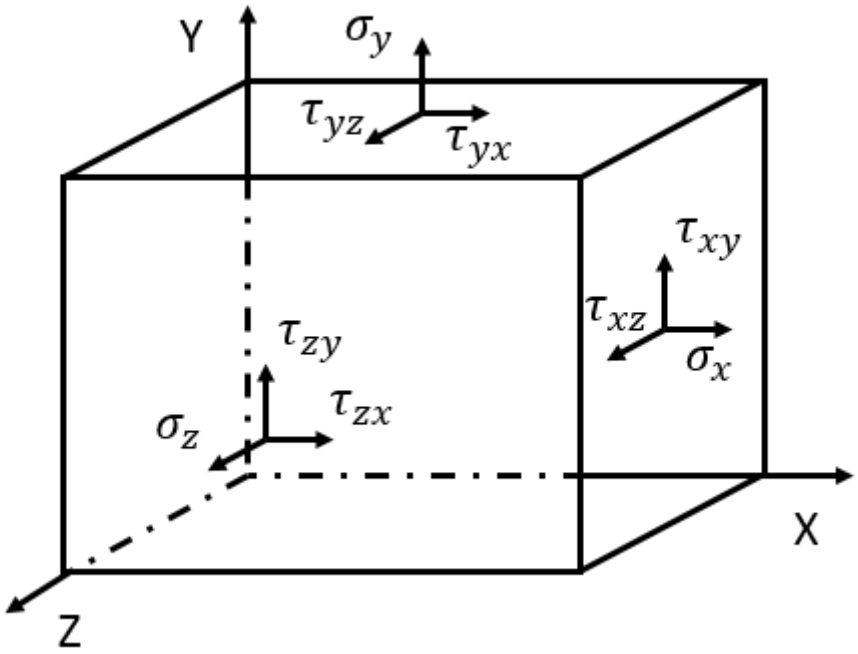

Figure 2.2.4 Stress components in a 3D coordinate system.

In plane stress, normal stress, σ_z and shear stresses, τ_{zy} and τ_{zx} are zero.

The stress tensor is then :

$$[\tau] = \begin{bmatrix} \sigma_x & \tau_{xy} \\ \tau_{yx} & \sigma_y \end{bmatrix} \quad (2.2.1)$$

and strain tensor,

$$[\gamma] = \begin{bmatrix} \varepsilon_x & \gamma_{xy} & 0 \\ \gamma_{yx} & \varepsilon_y & 0 \\ 0 & 0 & \varepsilon_z \end{bmatrix} \quad (2.2.2)$$

In plane strain, normal strain, ε_z and shear strains, γ_{zy} and γ_{zx} are zero.

The stress tensor is then:

$$[\tau] = \begin{bmatrix} \sigma_x & \tau_{xy} & 0 \\ \tau_{yx} & \sigma_y & 0 \\ 0 & 0 & \sigma_z \end{bmatrix} \quad (2.2.3)$$

and strain tensor,

$$[\gamma] = \begin{bmatrix} \varepsilon_x & \gamma_{xy} \\ \gamma_{yx} & \varepsilon_y \end{bmatrix} \quad (2.2.4)$$

2.2.2.2Stress, displacement field and stress intensity factor (SIF) ahead of the crack tip

The stress intensity factor (SIF) is used to describe the intensity of the stress field near the crack tip due to far-field loading. It depends on the specimen geometry, applied stress and the crack length.

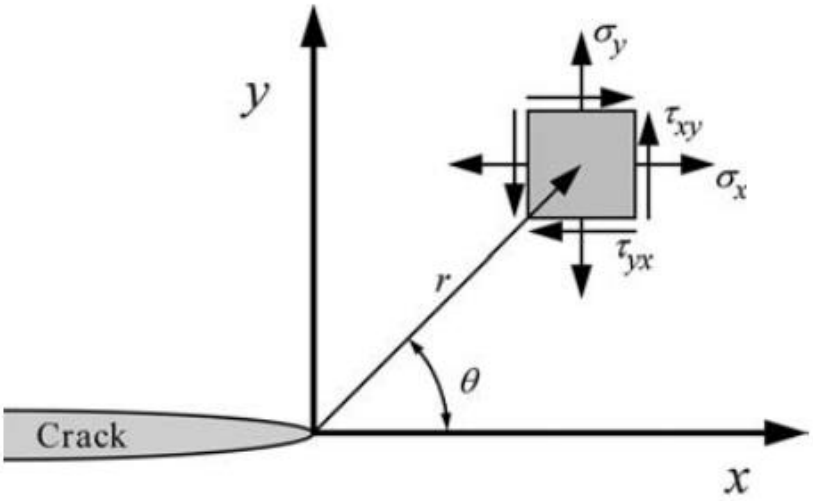

Figure 2.2.5 2D stress components ahead of the crack tip [7].

Irwin coined the term SIF [32]. If $Z(r)$ is a stress component with respect to the crack tip (Figure 2.2.5), then the SIF is defined as,

$$K = \lim_{r \to 0} \sqrt{2\pi r}\ \mathrm{Z}(r) \tag{2.2.5}$$

where, r is considered to be the distance of the stress component from the crack tip.

For different modes, SIFs in terms of stress components, distance, r and angular distance, θ are,

$$K_I = \lim_{r \to 0} \left(\sigma_y \sqrt{2\pi r}|_{\theta=0} \right) \tag{2.2.6}$$

$$K_{II} = \lim_{r \to 0} \left(\tau_{xy} \sqrt{2\pi r} |_{\theta=0} \right) \tag{2.2.7}$$

$$K_{III} = \lim_{r \to 0} \left(\tau_{yz} \sqrt{2\pi r} |_{\theta=0} \right) \tag{2.2.8}$$

If K reaches a critical value, fracture occurs. This critical SIF is called fracture toughness, K_c.

Based on the Westergaard approach [36] the stress components, very near to the crack tip, become

$$\begin{pmatrix} \sigma_x \\ \sigma_y \\ \tau_{yz} \end{pmatrix} = \frac{K_I}{\sqrt{2\pi r}} \cos\frac{\theta}{2} \begin{pmatrix} 1 - \sin\frac{\theta}{2}\sin\frac{3\theta}{2} \\ 1 + \sin\frac{\theta}{2}\sin\frac{3\theta}{2} \\ \sin\frac{\theta}{2}\sin\frac{3\theta}{2} \end{pmatrix} \tag{2.2.9}$$

When, r→0, the stress field near the crack tip has a singularity of $1/\sqrt{r}$. It should be noted that Equation 2.2.9 is only valid for the stress of the part of the material very close to the crack tip. For the part of the material away from the crack tip, Irwin [37] added an experimental stress term, $-\sigma_{0x}$ [7] to σ_x. So, the modified Westergaard equations become

$$\begin{pmatrix} \sigma_x \\ \sigma_y \\ \tau_{yz} \end{pmatrix} = \frac{K_I}{\sqrt{2\pi r}} \cos\frac{\theta}{2} \begin{pmatrix} 1 - \sin\frac{\theta}{2}\sin\frac{3\theta}{2} \\ 1 + \sin\frac{\theta}{2}\sin\frac{3\theta}{2} \\ \sin\frac{\theta}{2}\sin\frac{3\theta}{2} \end{pmatrix} + \begin{pmatrix} -\sigma_{0x} \\ 0 \\ 0 \end{pmatrix} \tag{2.2.10}$$

For evenly spaced collinear cracks in an infinite strip subjected to tensile load, SIF [7] (Figure 2.2.6) is

$$K_I = \sigma\sqrt{\pi a}\left(\frac{w}{\pi a}\tan\frac{\pi a}{w}\right)^{\frac{1}{2}} \quad (2.2.11)$$

where, a is the half crack length, and w is the width of the strip.

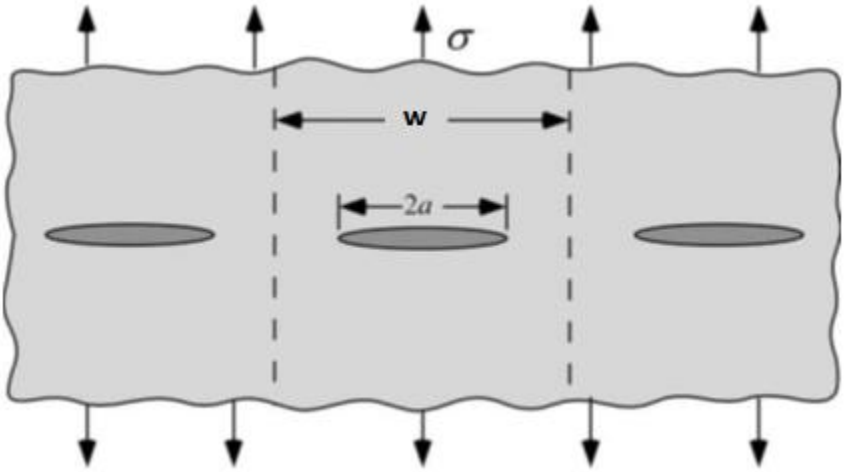

Figure 2.2.6 Collinear cracks in an infinite strip subjected to remote tension [7].

If there is a crack in a plate of finite strip, then SIF [38],

$$K_I = \sigma\sqrt{\pi a}F_I(\alpha) \quad (2.2.\ 12)$$

where,

$$\alpha = \frac{2a}{w} \quad (2.2.13)$$

According to secant formula SIF,

$$K_I = \sigma\sqrt{\pi a}\left[\sec\left(\frac{\pi a}{w}\right)\right]^{\frac{1}{2}} \quad (2.2.14)$$

Accuracy: ±0.3 % for α < 0.7 and 1 % for α = 0.8

A more accurate solution is the Tada solution,

$$F_I(\alpha) = (1 - 0.025\alpha^2 + 0.06\alpha^4)\left[\sec\left(\frac{\pi a}{w}\right)\right]^{\frac{1}{2}} \quad (2.2.15)$$

which has an accuracy of less than 0.2 % for all α values.

2.2.2.3Evaluation of plastic zone near the crack tip for mode I loading

It is not easy to describe the shape and size of the plastic zone near the crack tip. The material is assumed to be elastic-perfectly plastic for simple models (Figure 2.2.7).

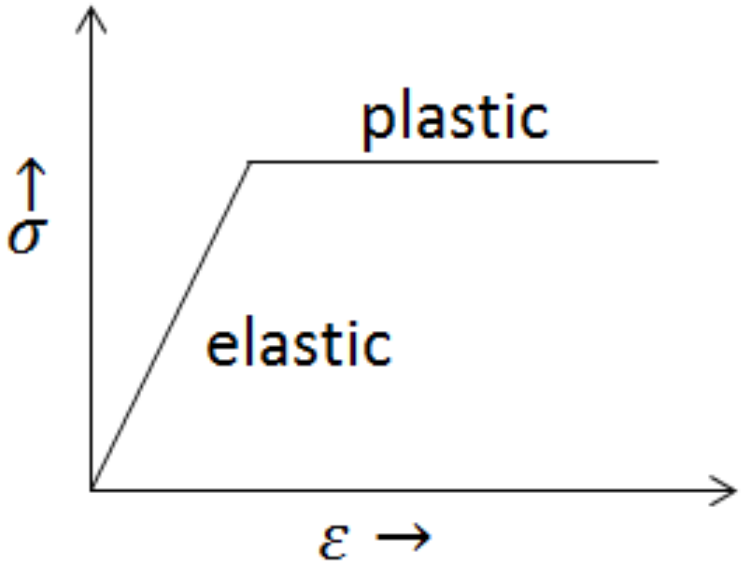

Figure 2.2.7 Stress vs strain curve of elastic-perfectly plastic material.

Figure 2.2.7 shows an elastic-perfectly plastic material model assuming no strain hardening or softening. The size of the plastic zone can be determined by locating a point along the crack axis, which satisfies the yield criteria to describe the range of plastic zone (Table 2.2.1) [28].

Table 2.2.1 Summary of the plastic zone size for different models.

	Plastic zone size (r_P)	
	Plane stress	**Plane strain ($\alpha = \frac{1}{3}$)**
Simplistic model	$\frac{1}{2\pi}\left(\frac{K_I}{\sigma_{ys}}\right)^2$	$\frac{1}{18\pi}\left(\frac{K_I}{\sigma_{ys}}\right)^2$
Irwin model (the crack tip is in the middle of the plastic zone. Therefore, the correction factor= $\frac{1}{2}$)	$\frac{1}{\pi}\left(\frac{K_I}{\sigma_{ys}}\right)^2$	$\frac{1}{3\pi}\left(\frac{K_I}{\sigma_{ys}}\right)^2$
Dugdale's model	$\frac{\pi}{8}\left(\frac{K_I}{\sigma_{ys}}\right)^2$	-

2.3 Fatigue

Fatigue of materials refers to the changes in properties resulting from the application of cyclic loads [39] and this change occurs in the form of degradation of material due to progressive and localised damage. Due to fatigue, failure of the structure occurs before the ultimate strength is reached. Fatigue failure often occurs suddenly without any noticeable warning, which explains why most of the mechanical failure is fatigue related. Mechanisms of fatigue failure need to be understood properly to improve the structural integrity of engineering components.

2.3.1 What is fatigue resistance?

The change in loading produces fluctuating stresses in the components, which leads to dislocations (i.e. dislocations are areas where the atoms are out of position in the crystal structure) [40] within the material. Dislocations pile-up created by this fluctuating loading produce persistent slip band (PSB) [41] as shown in Figure 2.3.1. This leaves tiny steps in the surface that serve as areas of high-stress concentration where fatigue cracks can initiate. If left untreated, these cracks within the microstructure of the material will propagate until fracture. Fatigue is considered to be a problem which can

affect any part or component that experiences variable or cyclical stresses [6]. As such, fatigue resistance is defined as a material's ability to endure cyclic stresses associated with fatigue.

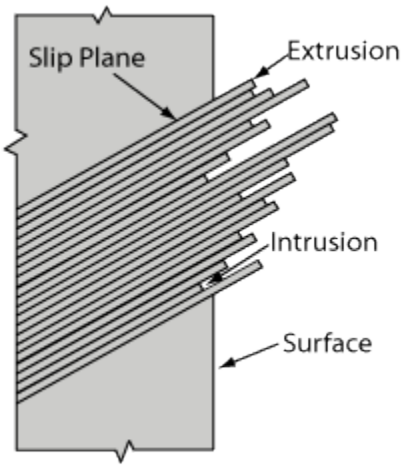

Figure 2.3.1 Slip band [41].

Fatigue can be classified into two main categories; low cycle (<100,000 cycles) and high cycle (>100,000 cycles) [42]. Low cycle fatigue occurs when materials undergo a high-level of stress which causes plastic deformation within the material [43]. The high stress causes dislocation movement [44] which prevent the material from returning to its original shape/form through the accumulation of dislocation density. On the other hand, high cycle fatigue is low-stress fatigue situation where the material deforms primarily elastically [43]. In this, fatigue is caused by elastic strains under a high number of load cycles before failure occurs [45]. The number of stress cycles until failure is used for measuring the fatigue life which is usually expressed using a stress vs number of cycles (S-N) semi-logarithmic graph as shown below (Figure 2.3.2).

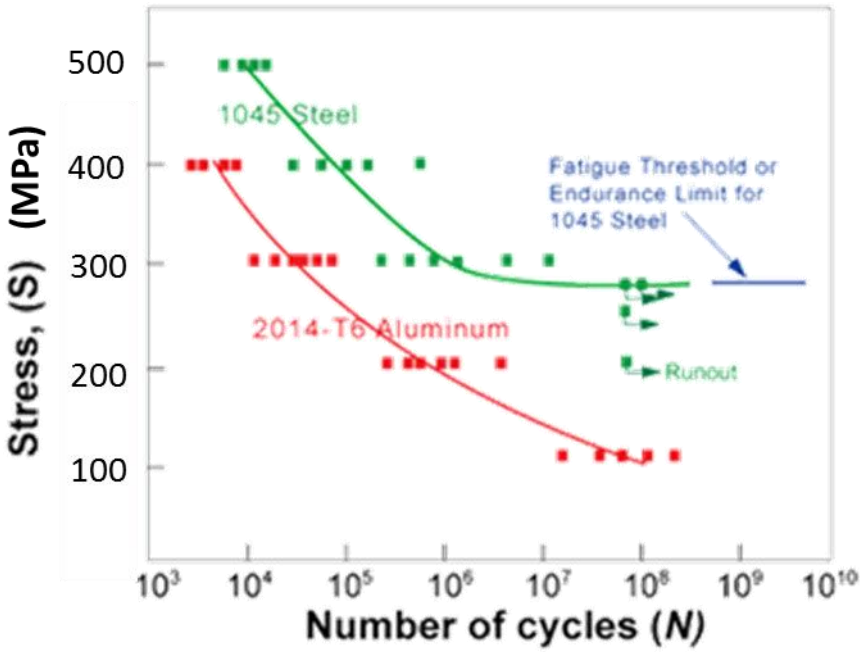

Figure 2.3.2 Stress vs number of cycles graph (semi-log scale) [46].

It is desirable to prolong the life of the material, which can be accomplished by reducing the effect of fatigue. This can involve reducing the magnitude of cyclic stress that the material experiences or using materials with enhanced fatigue resistance. The larger the number of fatigue cycles to failure, the larger the fatigue resistance of the material. A single stress application of the ultimate tensile stress (UTS) allows for one stress cycle before the material fails. As the stress decreases, the number of cycles to failure increases until a point where an infinite amount of repeated stresses will not cause the material to fail. This point is known as the fatigue limit or endurance limit (Figure 2.3.2). The fatigue limit is an important parameter during product design as it is assumed that a material will not fail due to fatigue when subjected to stresses below this limit. However, aluminium alloys have no such limit while steel has a fatigue limit (Figure 2.3.2).

In order to increase the service life of the components, it is essential to improve the fatigue resistance of the material. Fatigue resistance can be related to multiple factors. In Boardman's review [47], it is emphasised that the variation of microstructure, macro-structure, chemical composition, mechanical properties and their effect on fatigue life, should be taken into account when choosing the correct material for the application. Some scholars believe that there is a linear relationship between the fatigue strength

of metals and the hardness or tensile strength. However, this generalisation is not entirely true. Some other factors such as fabrication, surface treatments, finishing, service environment and heat treatment can also affect the fatigue resistance of material. In general, the fatigue crack initiation period is the most significant one, however, using the advanced technique of detecting a crack, it is found that a crack often develops at the early stage of the fatigue life (i.e. after as little as 10 % of the total lifetime) [47]. Eventually, the crack will continually propagate until fracture takes place. Fatigue resistance includes both the crack initiation and crack growth. The fatigue crack growth can be modelled as a sigmoidal curve which will be discussed in details in the later section.

2.3.2 Mechanical parameters of the fatigue loading

Repeated loading is normally idealised as cyclic loading in fatigue analysis as shown in Figure 2.3.3. Different stress parameters are used to describe the fatigue cycle. These are maximum stress, σ_{max}, minimum stress, σ_{min}, alternating stress or stress amplitude, σ_a, mean stress, σ_m, stress range, $\Delta\sigma$ and stress ratio, R.

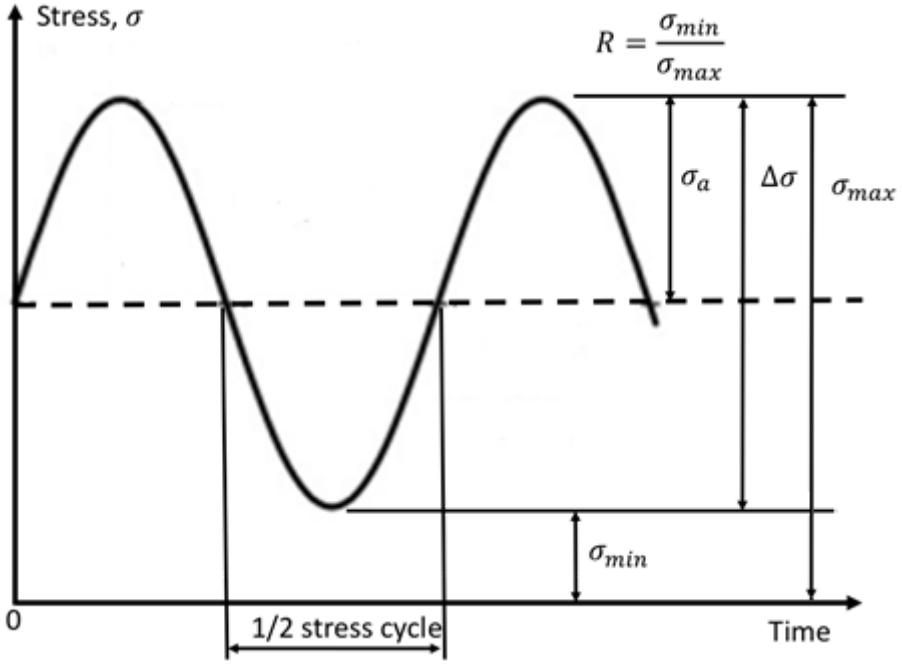

Figure 2.3.3 Cyclic loading.

where,

$$\Delta\sigma = \sigma_{max} - \sigma_{min} \quad (2.3.1)$$

$$\sigma_m = \frac{\sigma_{max} + \sigma_{min}}{2} \quad (2.3.2)$$

$$\sigma_a = \frac{\Delta\sigma}{2} \quad (2.3.3)$$

$$R = \frac{\sigma_{min}}{\sigma_{max}} \quad (2.3.4)$$

The minimum stress, σ_{min} increases with the increase of R at constant maximum stress, σ_{max}. When σ_{max}=-σ_{min}, the cyclic loading is termed as fully reversed loading cycle.

2.4 Fatigue crack growth behaviour

Fatigue crack starts from cyclic slip (Figure 2.4.1). Then, it grows to a certain limit before the final fracture occurs. Stress concentration factor (SCF), stress intensity factor (SIF) and fracture toughness, K_C are relevant parameters in these three stages, respectively.

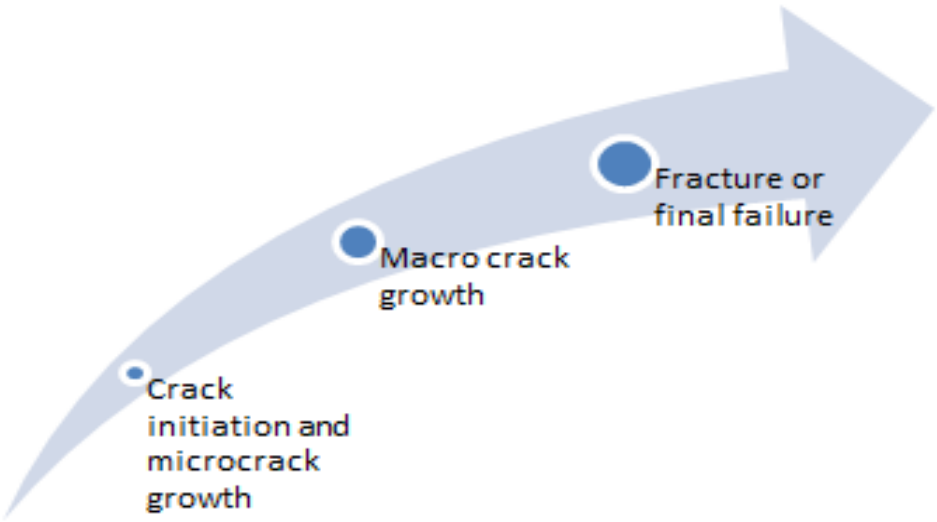

Figure 2.4.1 Crack growth process.

2.4.1 Fatigue crack propagation process

During fatigue loading, the surface of the component starts to become rough. Persistent slip bands (PSBs) are created including intrusion and extrusion profiles [28]. These initiate the fatigue crack. The radius of the curvature of the crack tip also influences the crack growth. In cyclic loading, during loading, the high plastic deformation near the crack tip due to the high-stress concentration advances the crack tip. Plastic deformation also makes the crack tip blunt. On the other hand, the crack tip sharpens during unloading. This process of blunting and re-sharpening continues while the crack advances. From the fractographic observation, striations or closely spaced ridges are usually found on the fracture surface caused by fatigue failure. When the fatigue load is interrupted, there is a formation of beachmarks, which are microscopically visible. In between the beach marks, there are several thousands of striations available (Figure 2.4.2.).

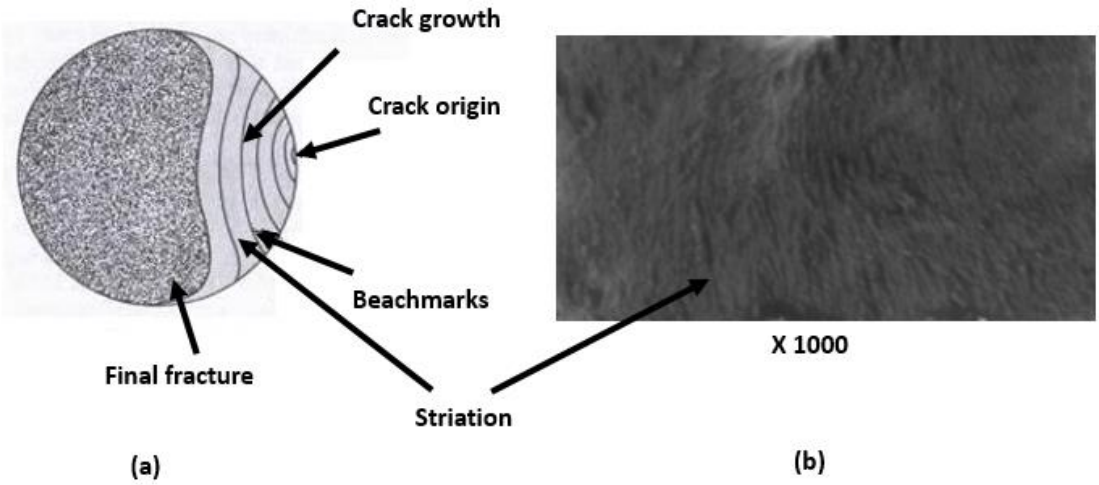

Figure 2.4.2 (a) Fracture surface due to fatigue [48] and (b) striation in aluminium alloy 2014-T6.

In mode I loading, the crack grows perpendicular to loading from the crack tip in a self-similar manner [8]. In mode II loading, the crack grows at a certain angle with the crack axis. According to Erdogan and Sih [49], this angle is approximately 70° from the plane of the crack which is very nearly the direction perpendicular to the maximum tangential stress at the crack tip (70.5°). Unlike for Modes I and II, there is no plausible micromechanistic model explaining a pure Mode III crack growth in ductile metals [50]. In the mixed mode (mode I and mode II) loading, the crack grows in the maximum normal stress (MTS) direction $\sigma_{\theta\theta}$ [49] or in the direction of minimum strain-energy-density factor [51]. Non-destructive testing (NDT) is used to monitor the fatigue crack growth. The fatigue loading is not fully reversed if the minimum load is kept zero during the fatigue crack growth test. For various loads, the test is repeated and crack length vs number of cycles (a vs N) graph is obtained (Figure 2.4.3).

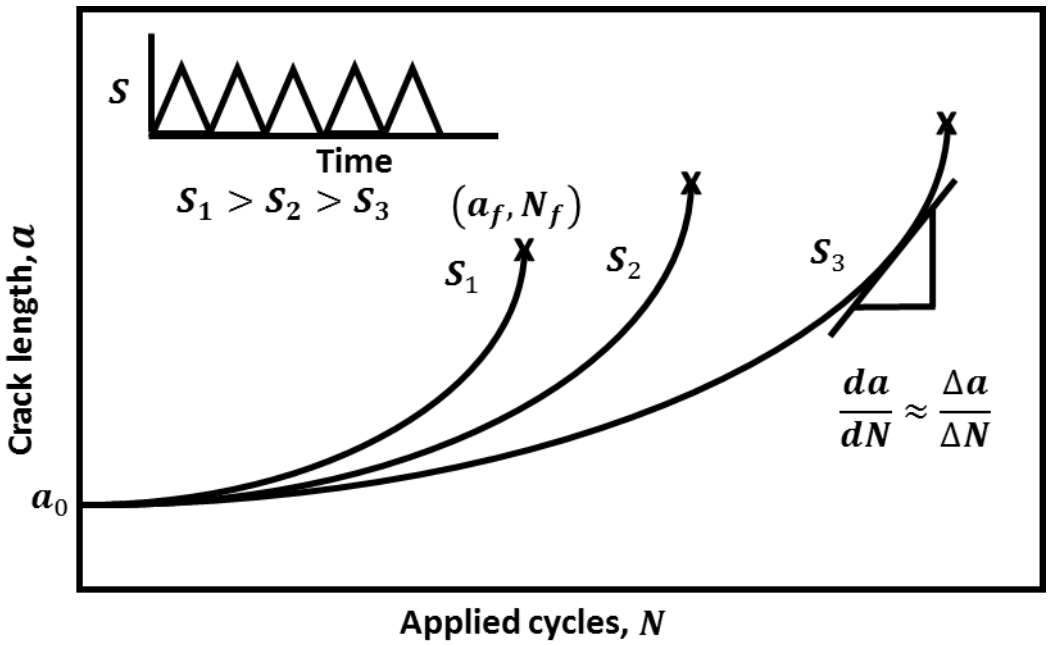

Figure 2.4.3 Crack length, a vs number of cycles, N curves for different loading, S on a single material.

After the crack growth period, ultimate fracture comes in effect. Fracture occurs in brittle/ cleavage fashion or ductile/rupture fashion depending on the material. The velocities of these two types of fracture are around 1060 m/s and 500 m/s, respectively [28].

2.4.2 Paris law and sigmoidal curve approach

In 1961, Paris [52] first introduced the role of K on fatigue crack growth of a physically large crack. To represent all the different curves of the a-N graph in a single curve, he came up with a new idea and introduced a graph of log-log plot of $\frac{da}{dN}$ vs ΔK (SIF range) (Figure 2.4.4). This is considered the kernel of all fatigue crack growth models. In 1963, based on empirical observation Paris and Erdogan [53] established a fatigue crack growth model for different load conditions using the power law. This model takes the consideration of stress intensity factor range, ΔK, and is commonly known as Paris law (Equation 2.4.1).

$$\frac{da}{dN} = C(\Delta k)^m \tag{2.4.1}$$

$$\Delta k = K_{max} - K_{min} \tag{2.4.2}$$

where, C and m are experimentally determined material constants and $\frac{da}{dN}$ is the crack growth increment per cycle (a being the crack length and N the number of load cycles), ΔK is stress intensity factor range, K_{max} is the maximum stress intensity factor and K_{min} is the minimum stress intensity factor.

The Paris law [53] is only applicable in the intermediate linear segment of region II. (Figure 2.4.4). This model is purely empirical. The crack growth rate was properly modelled by a single parameter, ΔK taking the effect of applied stress and crack length. The environmental effect (e.g. heat, humidity, etc.) is not considered here. The stress ratio, R which is ignored in this law, has an impact on the curve as C changes with the stress ratio, R. Only region II of the sigmoidal curve can be described by it [28]. For a wider range of ΔK, Equation 2.4.1 cannot be used to correlate experimental data effectively.

The plot of $\log \frac{da}{dN}$ vs $\log \Delta K$ for metal fatigue crack growth is a sigmoidal curve with three distinct regions which is shown below (Figure 2.4.4). It provides all the information of fatigue crack growth rate from the crack initiation to final fracture. The curve deviates from linearity both at high and low ΔK values. This curve moves left with the increase of R which indicates that the crack growth rate increases at high R.

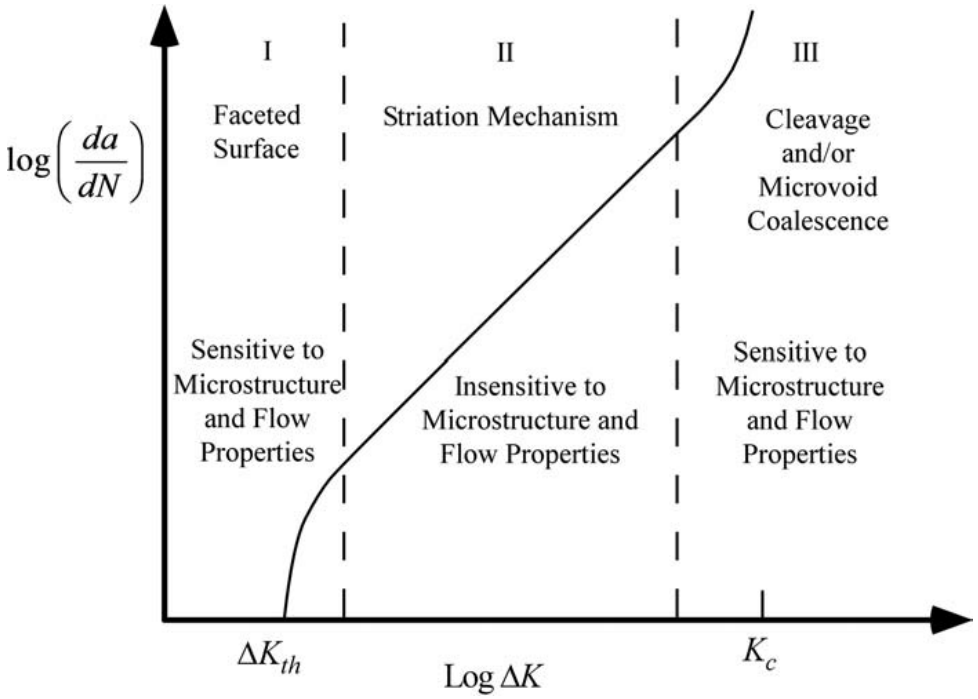

Figure 2.4.4 A Typical sigmoidal curve of representing fatigue crack growth rate [7].

Region I

This is the region of microcrack growth. The crack length becomes of the order of nanometers starting at the threshold SIF, ΔK_{th}. This region occupies most of the crack growth life compared to the other two regions. The crack growth rate is of the order of 10^{-6}-10^{-4} $\frac{mm}{cycles}$ typically [28]. Here, the crack growth approaches zero value asymptotically at the threshold value of ΔK_{th}. Microstructure, mean stress and environment have a large influence in this region. The load ratio, R is the most important factor controlling the magnitude of the threshold, ΔK_{th} [54, 55]. The threshold value, ΔK_{th} decreases with increase of R. This region follows the modified Paris law as proposed by Donahue et al. [56]. According to this,

$$\frac{da}{dN} = C(\Delta k - \Delta K_{th})^m \tag{2.4.3.}$$

$$\Delta K_{th} = C(1-R)^{\gamma}\Delta K_{th(0)} \tag{2.4.4}$$

$\Delta K_{th(0)}$ is the threshold value of ΔK at $R = 0$, C, m and γ are material constants.

Region II

The crack growth rate in this region is of the order of $10^{-4}\ \frac{mm}{cycles}$ to $10^{-2}\ \frac{mm}{cycles}$ [28]. Striations are only formed in this region of crack growth. The environment, mean stress and frequency have significant effects, while microstructure only has a small effect in this region. The curve follows a linear relationship between log $\frac{da}{dN}$ and log ΔK as Paris law is applicable in this region. When the change in R is considered, closely spaced parallel lines are created. The plastic zone ahead of the crack tip is bigger than the mean grain size, but smaller than the crack length [57, 58].

Region III

The crack growth rate in this region is of the order of $10^{-2}\ \frac{mm}{cycles}$ to $10^{-1}\ \frac{mm}{cycles}$ [28]. The environment has no significant effect in this region. At high ΔK values, the crack growth rate accelerates as the log $\frac{da}{dN}$ vs log ΔK curve becomes steep and asymptotic, while approaching fracture toughness, K_c. With the change of R, the curves get scattered and K_c can be reached early when R is increased. Microstructure, mean stress and thickness have a greater influence in this region. The component fails in this region. The curve in this region follows the Forman Law (1972) [57, 59] as follows,

$$\frac{da}{dN} = \frac{C(\Delta k)^m}{(1-R)K_C - \Delta k} \tag{2.4.5}$$

where, K_c is the fracture toughness, C and m are material constant. This law is also applicable in the stable intermediate growth of region II.

Many researchers [56, 60, 61] have attempted to generate models to explain all the parts or a specific portion of the sigmoidal curve. One of the mathematical representations of the complete sigmoidal curve by Hartman and Schijve [57, 61] in 1970 is;

$$\frac{da}{dN} = \frac{C_{HS}(\Delta k - \Delta K_{th})^{m_{HS}}}{(1-R)K_C - \Delta k} \tag{2.4.6}$$

where, the threshold, ΔK_{th} is included, C_{HS} and m_{HS} are material constant.

Because of the aggressive environment such as liquid environment, the sigmoid graph changes and the crack growth rate increases. For corrosion, the threshold ΔK_{th} can be increased because of the crack closure effect to be detailed later [28].

2.4.3 Overload effect on fatigue crack growth

Figure 2.4.5. shows three basic load sequences of overloads: a single overload, a block of overloads and periodic blocks of overloads.

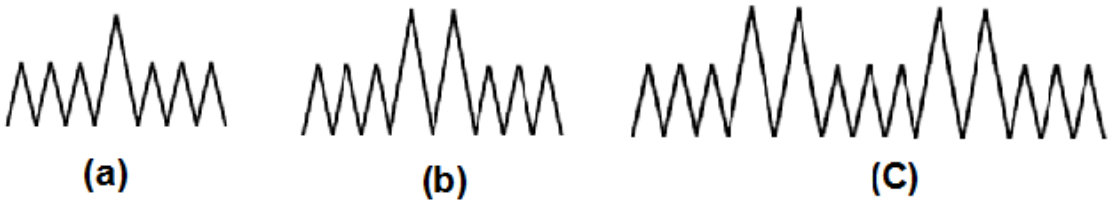

Figure 2.4.5 (a) A single overload, (b) a block of overloads and (c) periodic blocks of overloads.

When a single overload is applied to a structure with a crack, it initially accelerates the crack growth. Then, there will be a prolonged retardation of crack growth and eventually, crack growth rate will go back to the pre-overload condition. This effect is known as the post-overload transient effect [62-66].

Crack growth retardation was found more pronounced under a higher overload ratio (OLR) [9, 24, 62, 67].

$$OLR = \frac{\Delta K_{OL}}{\Delta K_{BL}} = \frac{K_{OL} - K_{min}}{K_{max} - K_{min}} \qquad (2.4.7)$$

where, K_{max}, K_{min}, and K_{OL} are the maximum, minimum and peak overload stress intensity factors. Therefore, ΔK_{OL} and ΔK_{BL} are the overload and the baseline stress intensity factor range. According to some studies [68, 69], it was found that there was no overload ratio (OLR) effect for OLR of 1.2-1.5, however, others [63, 70] found

decreased crack growth rate for OLR of 1.5 . Intermediate values of OLR cause the number of delay cycles to increase. For example, in the case of OLR of 2.0, there was immediate retardation at plane strain condition, and delayed retardation occurred after initial acceleration in plane stress condition [69]. High value of OLR (typically 2.5-3) caused crack arrest [69].

With the increase of R, the crack growth rate increased [71]. Reduced retardation with the increase of R was reported in some research works [24, 67]. The thickness of the specimen and the microstructure influenced the overload retardation effect [9]. The evidence found for the influence of the baseline stress intensity factor range, $(\Delta K)_{BL}$ was inconsistent [72]. On the one hand, intermediate $(\Delta K)_{BL}$ value or increase in $(\Delta K)_{BL}$ above a certain level diminised the retardation effect, while on the other hand, decreasing $(\Delta K)_{BL}$ led to the initial acceleration effect to be more pronounced. According to Borrego et al. [63], the crack growth retardation effect increases significantly with $(\Delta K)_{BL}$. More severe crack growth retardation was found when constant amplitude (CA) loading was incorporated with the block of overloads rather than a single overload [73]. Periodic single overload or block of overloads may enhance the retardation effect. However, there is an optimum distance between the two overloads or block of overloads [62]. Closely spaced overloads may lead to crack growth acceleration rather than retardation.

2.4.4 Evaluation of fatigue crack growth models under overload

In 1972, Wheeler [74] considered the overload effect and introduced a fatigue crack growth model [8, 57] as shown in Figure 2.4.6. The post-overload crack growth can be described as:

$$\frac{da}{dN} = \varphi_r f(\Delta K, R) \tag{2.4.8}$$

$$\varphi_r = \begin{cases} \left(\frac{R_y}{a_P - a}\right)^m ; (a + R_y) < a_P \\ 1 \qquad\quad ; (a + R_y) \geq a_P \end{cases} \tag{2.4.9}$$

where, $f(\Delta K, R)$ denotes the function of stress intensity factor range, ΔK and load ratio, R, φ_r =retardation parameter or, knock-down parameter, R_y=Normal plastic zone size, y=shape factor, a_P=crack length plus the overload plastic zone size and m=adjustable calibration factor, which is a material dependent exponent, which is used to account for the effect of load sequence on fatigue crack growth rate.

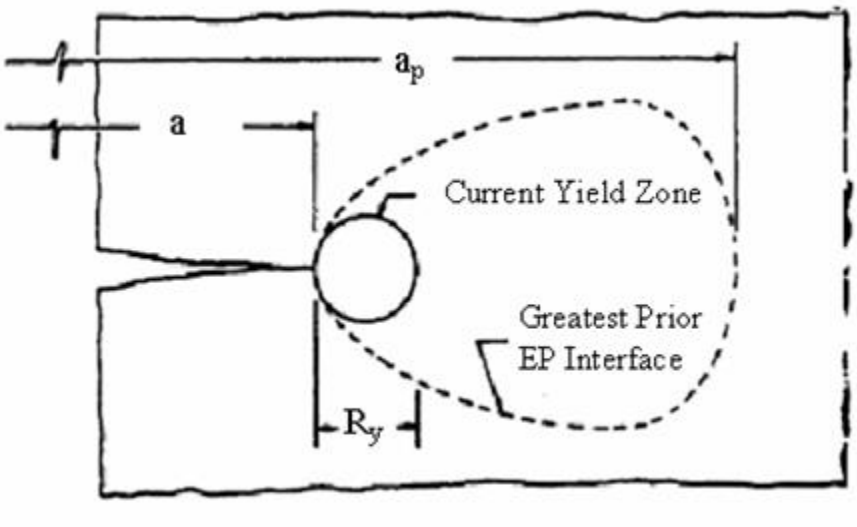

Figure 2.4.6 Crack tip yield zone [74].

According to beden et al. [57], the plastic zone size proposed by Wheeler is,

$$R_y = \frac{\pi}{4\sqrt{2}}\left(\frac{K_I}{\sigma_y}\right)^2 \tag{2.4.10}$$

In 1971, Willenborg [75] modified the stress intensity factor by taking the effect of the overload [8]. AFGROW [8] uses the generalised Willenborg model. According to this,

$$\Delta K_{eff} = K_{\max(eff)} - K_{\min(eff)} \tag{2.4.11}$$

$$R_{eff} = \frac{K_{\min(eff)}}{K_{\max(eff)}} \tag{2.4.12}$$

$$K_{\max(eff)} = K_{max} - K_{red} \tag{2.4.13}$$

$$K_{min\,(eff)} = K_{min} - K_{red} \tag{2.4.14}$$

K_{red} corresponds to the reduction of applied stress, $\sigma_{red} = \sigma_p - \sigma_{max}$, due to progress through the plastic zone [8, 75]. Here, the applied stress is the stress required to reach the distance, a_p (Figure 2.4.6). In this model,

$$R_y = \frac{1}{2\pi}\left(\frac{K_p}{\sigma_y}\right)^2 \tag{2.4.15}$$

$$K_{red} = \varphi\left(K_{max(ol)}\sqrt{1 - \frac{\left(x - x_{(ol)}\right)}{R_{y(ol)}}} - K_{max}\right) \tag{2.4.16}$$

$$\varphi = \left(\frac{1-\Delta K_{threshold}}{K_{max}}\right)/(SOLR - 1) \tag{2.4.17}$$

where, x=crack length, $x_{(ol)}$=crack length at overload, $\Delta K_{threshold}$=threshold value of ΔK at $R = 0$ and SOLR=Shutoff overload ratio [Ratio of the overload to the nominal load which is required to effectively stop further fatigue crack growth under nominal loading $\left(\frac{K_{\max(ol)}}{K_{\max}}\right)$]. For aluminium, titanium and steel, the SOLRs are 3.0, 2.7 and 2.0, respectively [8].

Based on this, the Forman equation [59] (Equation 2.4.5) becomes,

$$\frac{da}{dN} = \frac{C\left(\Delta K_{eff}\right)^m}{\left(1 - R_{eff}\right)K_C - \Delta K_{eff}} \tag{2.4.18}$$

In the main Willenborg model [75], φ was not included. However, in 1974 Gallagher and Hughes [76] proposed this generalised Willenborg model, where this term is

included [57] (Equation 2.4.17) . In their proposal, the effective stress intensity factor range and the apparent stress intensity factor range are the same. According to their model,

$$\frac{da}{dN} = \frac{C(\Delta K)^m}{(1 - R_{eff})K_C - \Delta K} \tag{2.4.19}$$

$$R_{y(ol)} = \left(\frac{K_{\max(ol)}}{\sigma_y}\right)^2 \left(\frac{1}{PSX\pi}\right) \tag{2.4.20}$$

where, PSX=stress state for given crack length (2- plane stress, 6- plane strain).

NASGRO (i.g. Fatigue crack growth prediction software developed by National Aeronautics and Space Administration(NASA)) [77] modified the generalised Willenborg model, where the acceleration effect due to the underload is being considered [57]. According to this model,

$$\varphi = 2.523\varphi_0/(1.0 + 3.5(2.5 - R_U)0.6, R_U < 0.25 \; or, 1.0, R_U \geq 0.25 \tag{2.4.21}$$

$$R_U = \frac{\sigma_{UL}}{\sigma_{max\,(OL)}} \tag{2.4.22}$$

φ_0=0.2 to 0.8 which is calculated experimentally. This model is used mainly in aircraft structures.

2.5 Effect of crack closure on fatigue crack growth

Fatigue crack closure is the phenomenon, which is widely considered to cause a reduction in fatigue crack growth driving force due to the contact of crack faces at the presence of positive load level during cyclic loading. In 1970, Elber [78] first observed this crack closure. He mentioned the striation peaks become flattened due to

deformation during the crack closure. According to this study, crack faces got closed at about half of the maximum load of a cyclic load as shown in Figure 2.5.1.

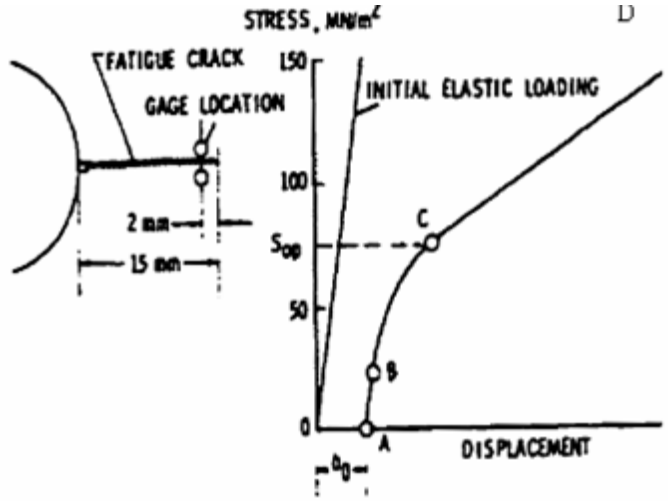

Figure 2.5.1 Crack closure results for fatigue crack growth [79].

2.5.1 Crack closure mechanism

During the fatigue loading, the crack does not actually open uniformly. There is a continuous transition from closed to open form. Therefore, it is very difficult to determine opening stress. Elber explained fatigue crack closure by the compliance curve observed in the thin sheets of cracked aluminium alloy 2024-T3 [78, 79]. At high loads fatigue crack compliance ($\mathrm{d}\Delta/\mathrm{dP}$, where Δ is crack flank displacement, and P is load) (Figure 2.5.2) showed the properties of cracked bodies, however, in low loads, it acted as the compliance of uncracked specimen. He explained the change in compliance in low loads is due to the contact of the cracked faces which is linked to the presence of residual strains left in the crack wake during fatigue crack growth. As a result, the reduction of fatigue crack growth occurs as the crack tip does not experience the full unloading considering the fact that crack advance only arises from cyclic plastic deformation at the crack tip when the crack face is open [10] (Figure 2.5.2). In other words, from $\sigma = o$ to $\sigma = \sigma_{op}$ crack remains closed, at $\sigma > \sigma_{op}$ crack opens.

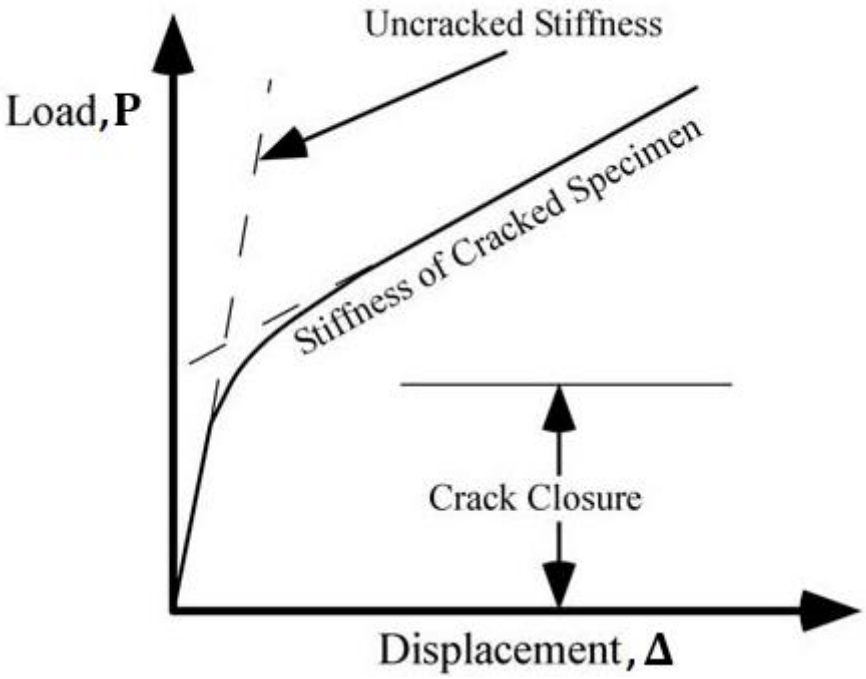

Figure 2.5.2 Change in compliance curve due to crack closure [7].

Elber [78, 79] first put forward the idea and modified the Paris law, substituting ΔK by effective stress intensity factor range, ΔK_{eff} which reduces with the occurrence of fatigue crack closure. The crack closure is illustrated below (Figure 2.5.3) which indicates that crack can only grow at higher portion of the loading when the crack is open.

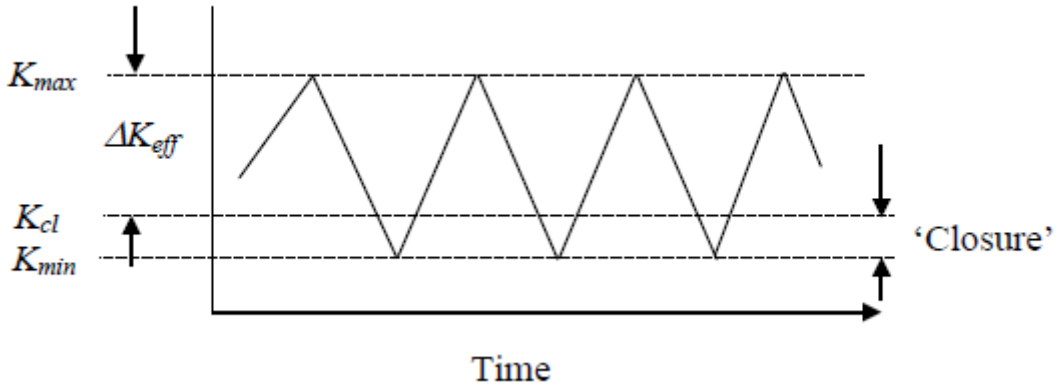

Figure 2.5.3 Definition of the effective stress intensity factor range (ΔK_{eff}) [10].

Elber defined the ΔK_{eff} as;

$$\Delta K_{eff} = K_{max} - K_{cl} \tag{2.5.1}$$

where, K_{max} is the maximum SIF of the cycle and K_{cl} is the SIF at which closure takes place during unloading. Effective SIF range, ΔK_{eff}, closure SIF range, ΔK_{cl} and SIF for fully open crack, K_{op} have been introduced based on this concept (Figure 2.5.3). K_{op} and K_{cl} are quite similar with some exception due to experimental condition. K_{op} differs in different alloys and loading conditions.

As such;

$$\Delta\sigma_{eff} = \sigma_{max} - \sigma_{cl} \tag{2.5.2}$$

$$\Delta K_{eff} = \beta \Delta\sigma_{eff}\sqrt{\pi a} \tag{2.5.3}$$

where, β = geometry factor.

For aluminium alloy 2024-T3, Elber [79] reported effective stress intensity range ratio as,

$$U = \frac{\Delta K_{eff}}{\Delta K} = \frac{K_{max} - K_{op}}{K_{max} - K_{min}} = 0.5 + 0.4R;\ 0 \leq R \leq 0.7 \tag{2.5.4}$$

According to Schijve [80], for the same material,

$$U = \frac{\Delta K_{eff}}{\Delta K} = 0.55 + 0.33R + 0.12R^2\ ;\ -1 \leq R \leq 0.54 \tag{2.5.5}$$

And the corresponding modified Paris law is;

$$\frac{da}{dN} = C\left(\Delta K_{eff}\right)^m = C(U\Delta K)^m \tag{2.5.6}$$

where, C and m are material constants that are determined experimentally.

2.5.2 Different types of crack closure effect

If a specimen with a crack is subjected to a fatigue loading, during loading the plastic zone forms at the crack tip. This plastic zone remains surrounded by the material. At unloading, the plastic zone is compressed by the elastic zone. In this process, residual stress including tension and compression is formed ahead of the crack tip. The compressive part of the residual stress retards the growth of the crack. After several number of cycles, the crack goes through the plastic zone and behind the crack tip, a plastic wake is formed. Elber [79] mentioned the crack closure happens due to the residual strain formed in this plastic wake (Figure 2.5.4). The plastic wakes, which are the permanent elongation of the crack lips/faces due to the plastic deformation, get closed before the minimum load is reached. This type of the crack closure is known as plasticity induced crack closure (PICC) [28, 81].

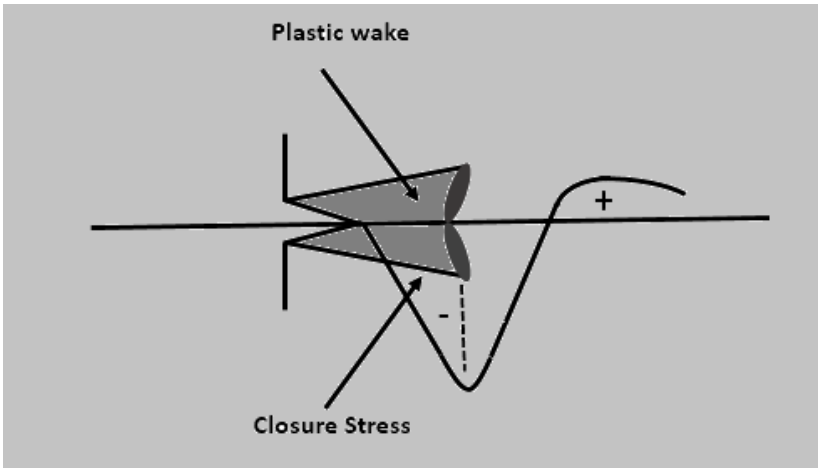

Figure 2.5.4 Plasticity induced crack closure (PICC) [28].

Phase transformed crack closure is quite similar to PICC. Here, residual strain is developed due to phase transformation, which is formed by the applied stress [7, 28, 81]. In the case of wedge induced (oxide/roughness) crack closure, the specimen with a fatigue crack is exposed to aggressive weather, corrosion products are formed in between the crack faces and these act as wedges. As a result, oxide induced crack closure (OICC) [7, 28, 43] is formed. On the other hand, the microscopic roughness due to fatigue fracture which becomes wedge between the crack surfaces is known as roughness induced crack closure (RICC). Microstructural heterogeneity can exist at a microscopic level. It raises the mixed mode condition at that particular point. The effect of Mode II of the mixed mode condition may create a mismatch between the two faces of the crack which also causes RICC [7, 28, 43, 81].

2.5.3 Applications of crack closure model

In crack closure approach, the crack tip becomes shielded when the first contact behind the crack tip occurs during unloading. This crack closure effect is capable of reducing the number of sigmoidal curves under different stress ratios to one sigmoidal curve. Numerous experimental (e.g. [9]) and modelling (e.g. [10, 24]) research works been published on the incidence of crack closure with a variety of fatigue phenomena related to its occurrence (i.e. micromechanical influences on fatigue and the behaviour of small fatigue crack). It has become very important with time to measure, characterise and predict crack closure to evaluate its effect on the crack growth rates. It is, however, very challenging to experimentally evaluate the crack closure as it is not easily measurable. At the same time, it is hard to analyse the displacement histories at the mid-section of a thick specimen. More appropriate numerical models are necessary to examine the effect of crack closure on fatigue crack growth. The study of T-stress is also becoming important in this case, which is being investigated by using the finite element method (FEM) [82]. The retardation effect due to overload is more influenced by the deformed plastic material behind the crack tip than the plastic zone ahead of the crack tip [57]. Moreover, the calculation of σ_{op} requires a large computational programme and long running time [57].

Air force growth (AFGROW) software uses closure factor, C_f in the crack closure model [8]. According to this,

$$C_f = \frac{\sigma_{op}}{\sigma_{max}} = 1.0 - \left[\left(1 - C_{f0}\right)(1 - 0.6R)(1 - R)\right] \quad (2.5.7)$$

$$C_f = R;\ R > R_{hi} \quad (2.5.8)$$

$$R = R_{lo};\ R < R_{lo} \quad (2.5.9)$$

where, C_{f0} is C_f for R=0 which is taken as the material property and it ranges from 0.3 to 0.5. R_{hi} is defined as the R-value above which the crack is always open and R_{lo} is defined as the R-value below which C_f is constant. Here, for $R > R_{hi}$ and $R < R_{lo}$, R shifting [8] or crack growth rate shifting as a function of R (Figure 2.5.5) is not possible.

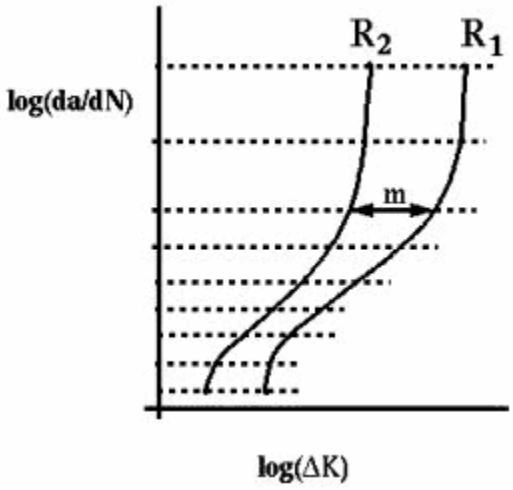

Figure 2.5.5 Crack growth rate shifting as a function of R [8].

Once the K_{op} is calculated, ΔK_{eff} can be calculated by the following equations.

$$\Delta K_{eff} = K_{max} - K_{op};\ K_{op} \geq K_{min} \quad (2.5.10)$$

$$\Delta K_{eff} = K_{max} - K_{min};\ K_{op} < K_{min} \tag{2.5.11}$$

Figure 2.5.6(a) is showing C_f vs R curve. Below R=-1/3, C_f becomes minimum and opening level cannot decrease below this value. When C_f reaches $C_f = R$, C_f increases with R values and the crack is considered fully open. During overload, the σ_{op} increases upto one fourth of the overload plastic zone (Fig. 2.5.6(b)). Underload effect is ignored in this model.

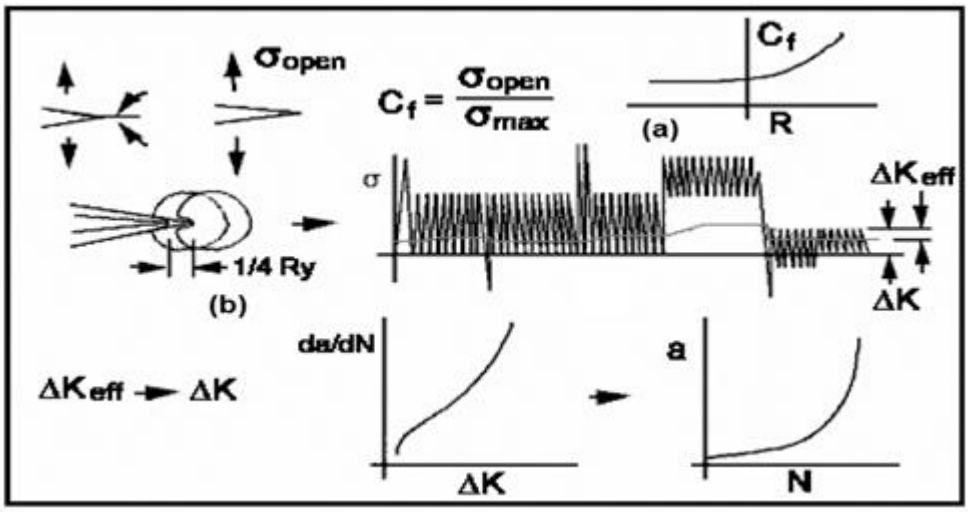

Figure 2.5.6 The schematically shown crack closure mechanism in AFGWROW model [8].

Newman models [83, 84] which were given between 1981 to 1982 is based on crack closure concept [57]. In these models, the detailed finite element method (FEM) was used to calculate cycle-cycle crack closure measurement by utilising an iterative solution procedure. According to the model which was given in 1981,

$$\frac{da}{dN} = C_1 \left[\frac{\Delta K_{eff}}{1-\left(\frac{K_{max}}{C_3}\right)^2} \right]^{C_2} \tag{2.5.12}$$

$$\Delta K_{eff} = \left(\sigma_{max} - \sigma_{op}\right) Y\sqrt{\pi a} \tag{2.5.13}$$

where, $C_1, C_2\ and\ C_3$ were calculated using least square regression at constant amplitude (CA) loading.

He modified the equation to

$$\frac{da}{dN} = C_1 \Delta K_{eff}^{C_2} \left[\frac{1-\left(\frac{\Delta K_O}{\Delta K_{eff}}\right)^2}{1-\left(\frac{K_{max}}{C_5}\right)^2}\right] \tag{2.5.14}$$

$$\Delta K_O = C_3\left(1 - C_4\frac{\sigma_O}{\sigma_{max}}\right) \tag{2.5.15}$$

$$K_{max} = \sigma_{max} Y\sqrt{\pi a} \tag{2.5.16}$$

where, Y is geometry factor, C denotes material constant, and a is the half crack length.

It was seen that the retardation and acceleration cancel each other for most of the load spectra. In 1997, Newman [85] came up with much more realistic finite element (FE) model to predict the fatigue crack growth rate. It uses Dugdale's strip yield model [86]. Strip yield type plastic zone is considered on the plastic wake which is left as residually stretched material. Beden et al. [57] considered this model as one of the best models to predict fatigue crack growth rate.

2.6 Plasticity induced crack closure under constant amplitude and variable amplitude loading

A short overview concerning plasticity induced crack closure (PICC) under CA and VA loading for the application of damage tolerance design (DTD) approach is presented

in this part of the thesis. The topics covers state of the art of PICC in metal fatigue research. Reviews of mechanics of PICC in plane stress and plane strain conditions, effects of specimen geometry and effects of VA loading on PICC in engineering materials (e.g. Aluminium Alloy 2024) are highlighted based on experimental and numerical studies available in the literature. Issues related to PICC are also presented here.

2.6.1 Background to the plasticity induced crack closure

The Linear elastic fracture mechanics (LEFM) approach was proved to be a revolution in the understanding of fatigue crack growth in the 1950's. In 1960's, the introduction of Paris law and the subsequent sigmoidal curve has simplified the analysis of fatigue crack growth. However, it is widely believed that any direct relation between ΔK and crack growth rates must take into account not only those phenomena occurring at a particular crack tip due to applied load but also micromechanical phenomena occurring behind and around the crack tip: in particular the incidence of crack flank contact during the load cycle or 'crack closure' [10]. This is taken as PICC which occurs due to residual plastic strain left in the crack wake [9, 87].

2.6.2 Mechanics of plasticity induced crack closure

During fatigue loading in ductile structures, materials near the crack tip undergo plastic deformation which does not fully reverse during unloading. When the crack advances to a certain distance, it leaves behind a reasonable amount of plastic stretch in the wake of the crack face. However, the surrounding elastic material which constrains the plastic stretch attempts to return to the original position as the load is removed. The resulting plastic stretch leads to premature contact of crack faces or plasticity induced crack closure (PICC) [79, 88]. Figure 2.6.1 shows schematically the developed plastic zone envelope for a fatigue crack which propagates under a constant ΔK magnitude.

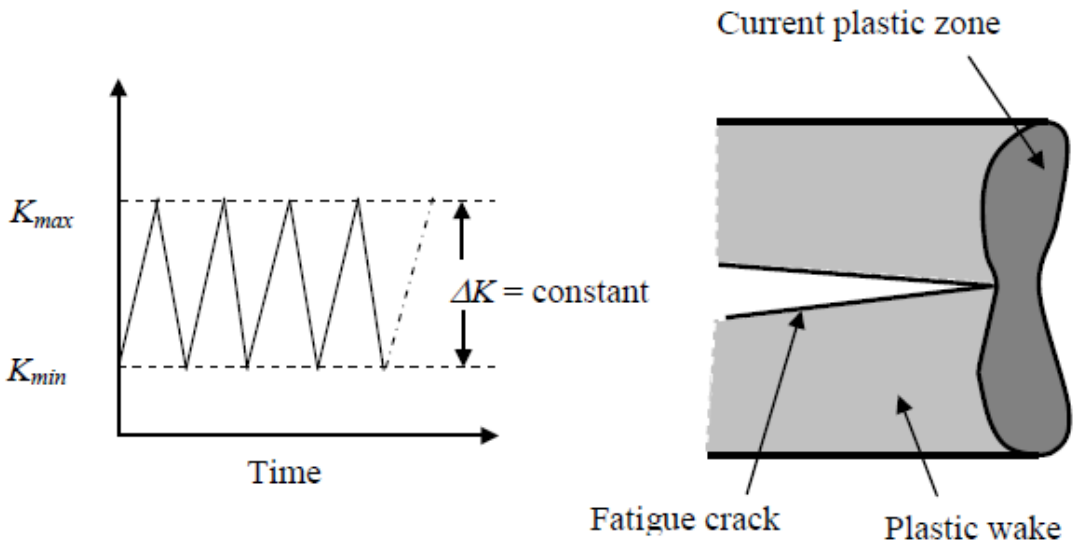

Figure 2.6.1 Schematic illustration of the development of plastic zone envelops for a propagating fatigue crack [7].

2.6.3 Plasticity induced crack closure in plane stress and plane strain conditions

Under a plane stress condition, plasticity induced crack closure (PICC) takes place due to the transfer of plastic material in the thickness direction from the axial direction (i.e. from the original surface to subsurface region). In this case, the volume conservation of material during plastic deformation has been maintained. This causes the material at the crack tip and the crack wake to become thinner and longer during crack growth. Moreover, each crack growth increment produces a part of this 'extra' material which eventually extends over the entire crack length [24, 89]. Models by [10, 90] are able to describe this situation. It is generally agreed that 'extra' material behind the crack tip can resist reversed deformation during unloading causing a reduction in the crack growth rate. Elber [79] noted that for his thin sheet specimens, the surfaces contacted only at discrete points or asperities on the fracture surfaces which was expressed as 'microcompatibility' [33]. From a rough calculation of crack surface area,

which is required to transmit the compressive crack closure load, he concluded that the surface compatibility should be of the order of 33 %.

Both the thin plate and the surface of a thick specimen usually act in a ‘‘*generalised plane stress state’’* by definition [91, 92]. If the plastic zone size is small compared to the length of the crack then it is called ‘small-scale yielding (SSY)*’.* At SSY fatigue crack growth when the crack is small, the stress state near the crack tip can behave as in a plane strain situation. The plastic zone at the crack tip is constrained against contraction along the crack front by the elastic material surrounding it. From a metal fracture and fatigue point of view, this can create a plane strain situation near the crack tip area even though the elastic part of the material may remain in plane stress situation. As a result, the ratio of the crack tip plastic zone size to plate thickness has been used as the main parameter in differentiating plane stress and plane strain conditions [10, 93].

Out-of-plane deformation under plane strain conditions is not allowed (e.g. middle plane of the thick specimen). There is no volume change of the material under plastic deformation by definition. Hence, various researchers (e.g. [94, 95]) are of the view that PICC cannot occur under these conditions [10, 96]. However, both experimental [9, 97, 98] and numerical [99, 100] studies have been reported to suggest that PICC can occur under plane strain condition. Thus, the issue of the occurrence of plain strain PICC is still controversial [100].

As the crack grows bigger, the plastic zone becomes higher, and the corresponding increase in plastic zone size results in a transition from plane strain to plane stress. This change of stress state has a significant influence on PICC via its effects on crack tip plastic zone sizes and crack opening displacement. Several researchers [9, 10, 101] studied the comparison of PICC in plane stress and plane strain condition and found higher PICC in the plane stress condition. Figure 2.6.2. shows one of these comparisons by Solanki et al. [101] which indicates that for the same centre cracked tension specimen at constant amplitude (CA) loading with R=0 , plane strain closure (0.15) is much more lower than plane stress closure (0.55).

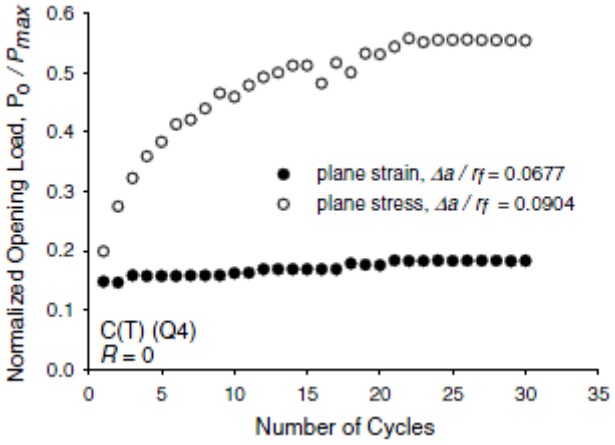

Figure 2.6.2 Comparison of PICC level in plane stress and plane strain condition [101].

The three dimensional investigation reported by Chemahini et al. [102] has revealed that a crack front may first close on a free surface (exterior) plane on the specimen, and closes last on the interior plane, showing that fully three dimensional closure behaviour corresponds to a continuous variation between two dimensional behaviour for plane stress on the specimen surface, and plane strain in the mid-plane [10].

2.6.4 Effects of specimen geometry on plasticity induced crack closure

The influence of fatigue specimen geometry upon closure response was studied by Fleck et al. [103, 104] and also reported by Solanki et al. [105]. The plane strain analysis was conducted for centre cracked tension (CCT), and single edge notched bend (SENB) specimens. At a load ratio of 0, PICC was observed for centre-cracked panels but not for bend specimens. PICC was not observed for CCT specimens for $R \geq 0.3$ under plane strain condition. For a transient period of crack growth, as the crack evolved from the state of a stationary crack to the steady state of a growing fatigue crack, PICC was enhanced for the CCT specimen format. The influence of crack specimen geometry upon closure was explained in terms of the T-stress (Figure 2.6.3). It is the second non-singular term of Williams's series expansion [106] for linear crack-tip stress field which acts parallel to the crack surface. A decrease in PICC has

been particularly observed for increasing T -stress ($\frac{T_{max}}{\sigma_0}$ where, T_{max} is the maximum value of T -stress and σ_0 is the flow stress) (Figure 2.6.3).

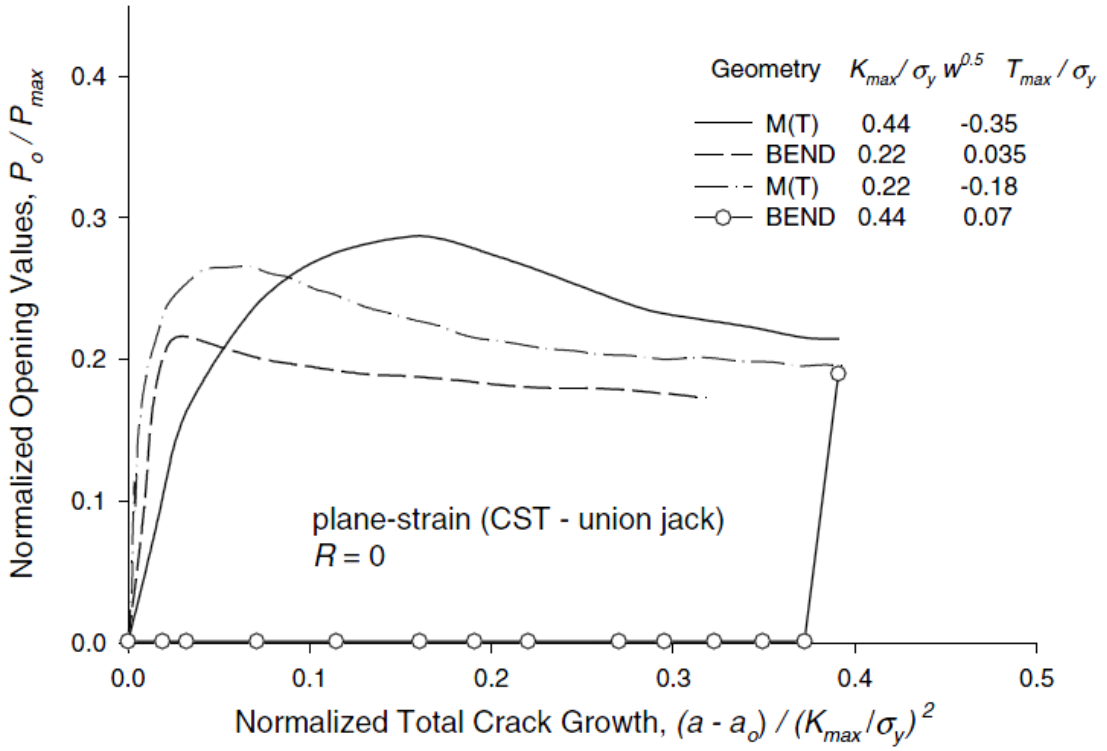

Figure 2.6.3 Geometry effects on PICC stabilisation in terms of normalised crack opening value [103, 105].

According to Roychowdhury et al. [82], the magnitude of the T-*stress* influences the closure process through two factors—the stationary crack opening displacement and the residual plastic deformation left (which is actually PICC by definition) in the SSY condition. It explained geometric effect on PICC using T-stress concept at $\overline{K} = 1$ and 2 ($\overline{K} = K_o/\sigma_0\sqrt{B}$, where $\overline{K}$ is a non-dimensional scaling measure for fatigue loading [107], K_{max} is maximum stress intensity factor and σ_0 is flow stress and B is thickness of the specimen) and found: (i) In the absence of T-stress, plastic contraction in the thickness direction compensated primarily for permanent stretching in the direction normal to the crack plane required for PICC (Figure 2.6.4(a)), (ii) negative T -stress ($\frac{T_{max}}{\sigma_0} < 0$) facilitated plastic contraction in the in-plane transverse direction which contributed to the larger share of material flow into the normal direction (Figure

2.6.4(b)), and (iii) for positive T-stress ($\frac{T_{max}}{\sigma_0} > 0$), both in-plane directions experience permanent stretching and the thickness direction alone undergoes plastic contraction (Figure 2.6.4(c)). Due to these processes, the crack opening level in the centre plane of the specimen increased for both positive and negative T-stress, however, it did not increased for absence of T-stress (Figure 2.6.5).

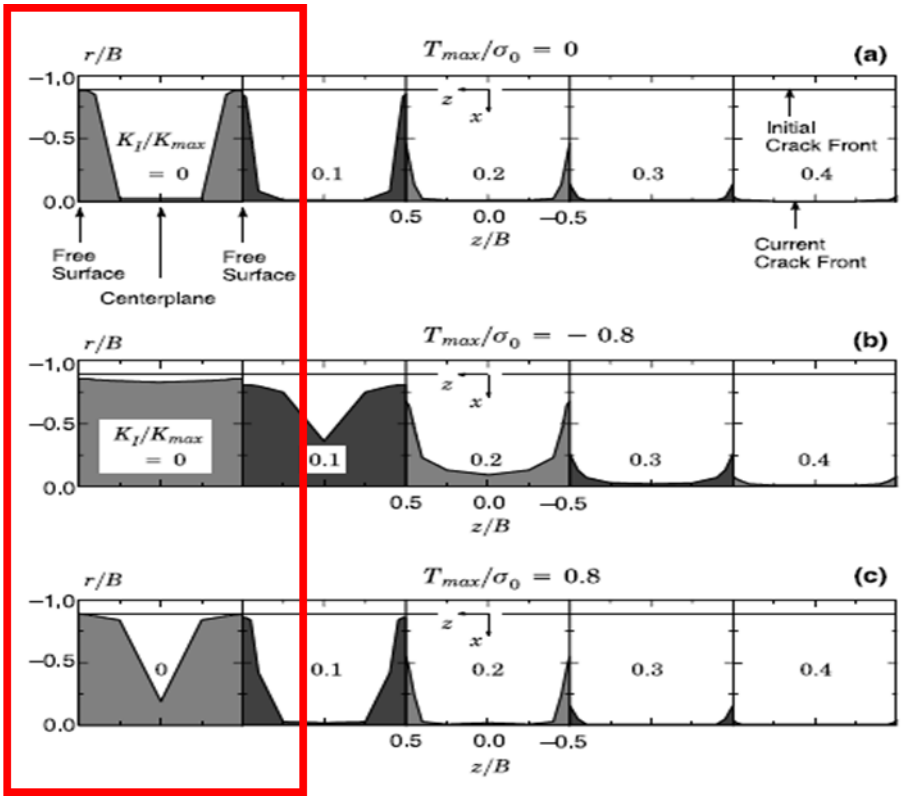

Figure 2.6.4 Effect of T-stress on evolution of crack face contraction over the symmetry plane during loading for $\overline{K}$=1 [82].

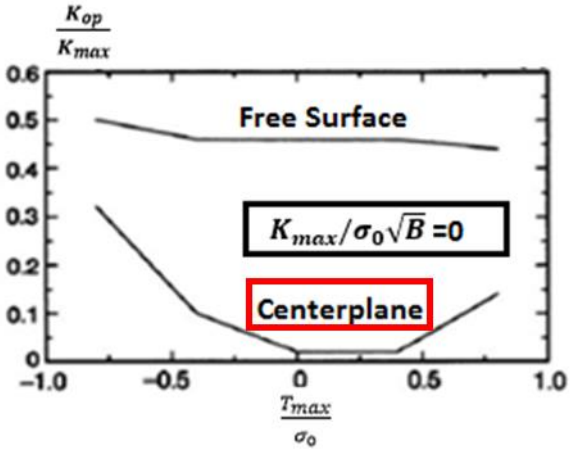

Figure 2.6.5 Effect of T-stress on steady-state values of normalised opening load for $\overline{K}$=1 [82].

2.6.5 Plasticity induced crack closure to rationalise the variable amplitude loading

VA loading gives more insights of the fundamentals of fatigue crack growth of structures than the constant amplitude CA loading as the VA loading is more relevant to the practical situation. Therefore, the PICC effect due to VA loading is more significant in residual life assessment. The CA loading spectrum along with overloads is considered as a simple form of VA loading. Various researchers have made contributions to understanding the fatigue crack growth behaviour under VA loading using PICC (e.g. [9, 108, 109]). Load interaction/sequence effects due to periodic overloads have also been explained by PICC in several studies (e.g. [10, 110]).

In mode I or 'opening mode' (see Figure 2.2.3) loading of the ductile material, when tensile overload is applied during the constant amplitude (CA) loading, this tensile overload usually leads to immediate but brief acceleration of crack growth, followed by prolonged retardation or crack arrest and then crack growth tends to reach pre-overload period crack growth level [9, 24] (Figure 2.6.7). However, there are also reports which suggest the absence of an initial acceleration in crack growth rates [111].

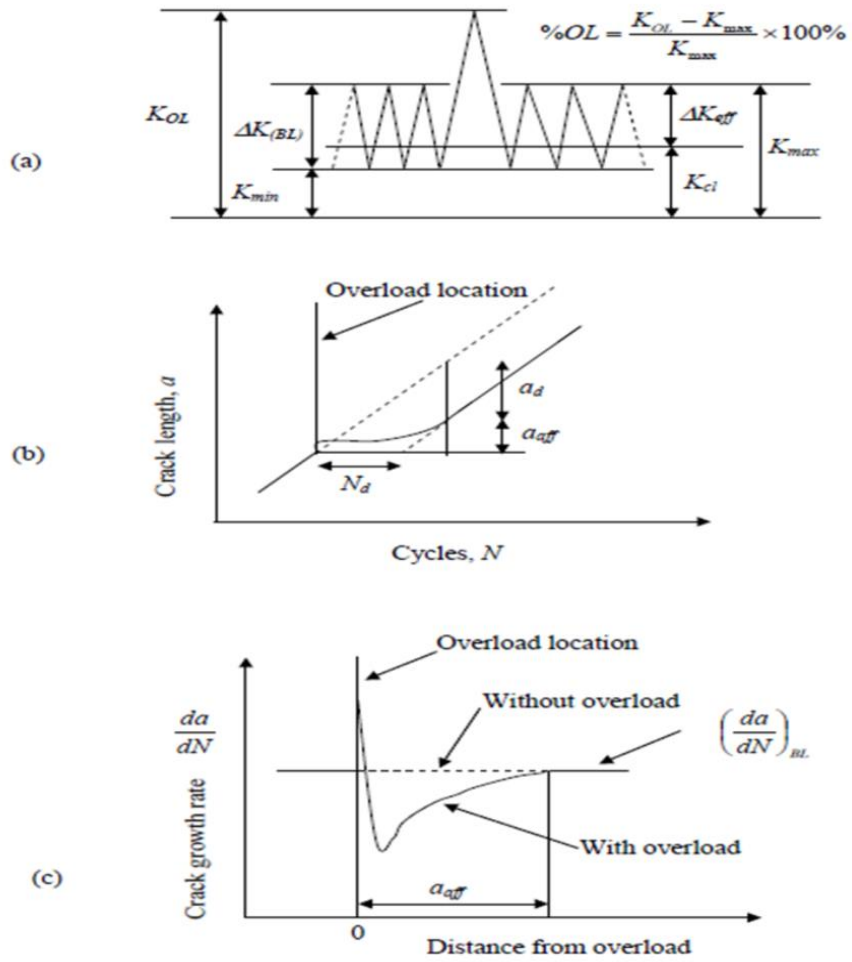

Figure 2.6.6 Schematic illustration of the effect of a spike (single) tensile overload, showing (a) loading nomenclature, (b) crack length vs number of cycles behaviour, and (c) crack growth rate vs crack length behaviour [10].

According to the study of Shin and Hsu [67], for higher R (e.g. 0.5, 0.7), the post overload crack growth rate shows: i) no brief acceleration, ii) a relatively short retardation period and iii) higher crack growth rate compared to the baseline crack growth rate after retardation. The retardation of crack growth is quantified by the delay distance, $a_{d,}$ or affected distance, $a_{aff,}$ or the number of delay cycles, N_d (Figure 2.6.7). The delay behaviour is typically a function of the baseline stress intensity range, $\Delta K_{(BL)}$, load /stress ratio, R, overload, $\%\ OL$ (Equation 2.6.1), sequence of loading and specimen thickness for a given material, microstructure and environment.

Overload is defined as,

$$\%\ OL\ = \frac{K_{OL} - K_{max}}{K_{max}} \times 100\% \tag{2.6.1}$$

where, K_{OL} is the maximum value of K during the overload cycle and K_{max} is maximum value of K during the CA loading.

The occurrence of a minimum in the crack growth rate at some distance after the application of a tensile overload is generally termed as 'delayed retardation'. Von Euw et al. [112] reported the distance between the application of the overload point and the delayed retardation is of one eighth to one quarter of the overload plastic zone size. The surface of the thick plate contains greater retardation distance than the middle plane which can be explained by the different level of PICC formed in plane stress and plane strain condition (see Figure 2.6.2). It has also been observed that the minimum crack growth in the middle of a thick plane occurs immediately after the application of the overload [113]. Several researchers [9, 10, 24] explained the post-overload retardation behaviour using PICC and reported that the post-overload retardation increased with the increase of the level of PICC.

In the literature, various mechanisms have been proposed to account for the post-overload phenomena, however, the precise mechanical origins remain open to discussion [114]. Some of the experimental observations suggest PICC alone cannot explain the retardation effect after the overload [115]. However, according to Fleck et al. [116], some of these controversies are due to i) the use of the insensitive closure measuring equipment and ii) different response between the bulk of a thick specimen and the surface during the post overload condition. Based on Dugdale's original work [86], using the concept of PICC, a modified 'strip yield' model was developed by Newman [85] which was used for fatigue life predictions during VA loading. The predicted fatigue crack growth life of this model under VA loading was compared with the experimental one for notched aluminium alloy 2024-T3 sheet. The predicted lives agreed well with the test data via the use of a fitting constraint factor to account for the influence of the finite thickness of the sample.

2.6.6 Issues related to plasticity induced crack closure in fatigue crack growth resistance

PICC has a great impact in reducing the crack growth driving force under VA loading. However, it cannot explain the influence of various mechanical, structural and environmental effects alone. For ductile engineering alloys, along with PICC, factors thought to influence the fatigue crack growth driving force include crack tip blunting, residual stresses ahead of the crack tip, static tearing, crack deflection and associated RICC processes, variations in crack front profile, and strain hardening, mean stress relaxation, the activation of near-threshold crack growth mechanisms [9, 81]. Therefore, the separation of the PICC from other factors is a challenge.

From the experimental study of Shin and Hsu [67], PICC was identified to be the primary cause of crack growth retardation during the overload effect. This study also reported that the crack-tip blunting and residual compressive stress became significant only when the PICC was inhibited from occurring at high R values (e.g. 0.65 and above). By using high R values (e.g. 0.8), Land et al. [117] observed crack growth retardation even though there was no PICC behind the crack tip. It was explained that the post-overload behaviour can be governed by residual compressive stresses in front of the crack tip. However, Mcevily et al. [118] reported that the relaxation of residual compressive stresses as the crack moves into the overload plastic zone actually gives rise to the enhanced PICC level, leading to the crack growth retardation. As a result, both of these processes are closely linked or 'equivalent'. It is to be worth noting here that the crack also needs to grow a certain distance before the PICC becomes enhanced and starts to retard fatigue crack growth [10, 24].

Issues related to the presence of PICC mainly in the plane strain condition and crack tip opening level measurement in defining PICC are also open for debate [9]. The different types of measurement techniques such as compliance, electrical potential, optical, acoustic, etc. along with intrinsic limitations have produced scattered results in crack opening/closing point measurement which eventually contribute to issues in PICC research [9, 119, 120]. The quality of raw load-displacement data has often been questioned in this case. According to McClung [88], during crack growth, σ_{OP} refers to the stress at which the crack is fully open and σ_{CL} refers to the stress at which any part

of the crack faces come into contact with each other. However, Donald [121] observed significant crack tip strain occurring below the conventionally defined σ_{op}. This kind of approach raises two questions [24] :

I. Will the crack grow when it is fully open?
II. Will the crack stop growing when its surfaces first come into contact?

As such, Wu and Ellyin [122] modified the conventional approach and proposed that the crack is fully open when the compressive stress at the crack tip becomes tensile and the crack closes when the crack tip stress becomes compressive from tensile.

2.7 Experimental procedure of measuring Plasticity induced crack closure

There are many experimental techniques available which are used so far to measure plasticity induced crack closure (PICC). Some of these are described briefly below.

2.7.1 Compliance techniques

The Compliance technique [98, 123-125] is the most widely used technique to measure the PICC. Here, the closure load is associated with the initial deviation from the compliance curve during unloading. An illustration of the compliance measurement using different types of gauges is shown in figure 2.7.1

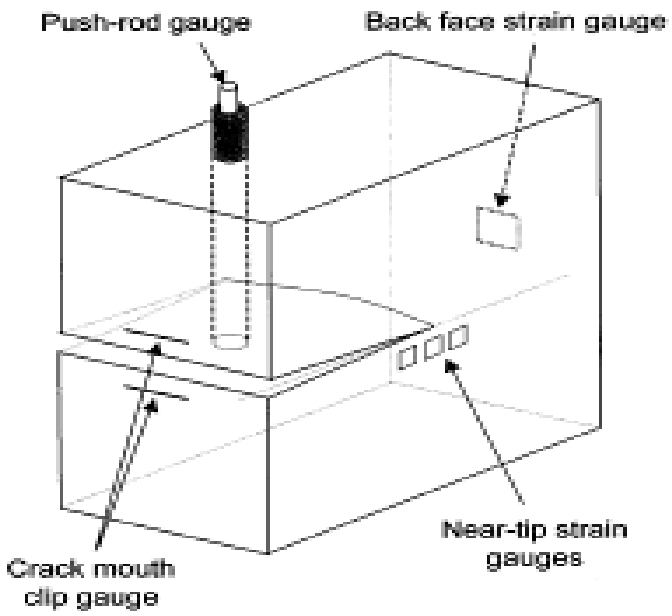

Figure 2.7.1 Mechanical compliance measurement with different types of gauges [98].

According to Lugo et al. [124], there are two main ways to determine the crack opening load using the compliance technique. These are load-displacement curve based and load-differential displacement curve based. The PICC has also been measured based on the slope variation of the upper and lower part of the compliance curve and curve fitting of the linear and second-order polynomial part of the compliance curve [9]. Different strain gauges may vary in measuring the closure point [121]. Considering this issue, the PICC has also been measured by a compliance ratio method near the crack tip and an adjustable compliance ratio method, which are taken as the location-independent methods where compliance does not depend on the position of the strain gauge [121, 126].

2.7.2 Direct measurement techniques

In-situ Scanning electron microscopy (SEM) was used to measure the PICC directly by measuring the variation of crack tip opening displacement (CTOD) and comparing it with the stress level used [127, 128]. High-resolution SEM improves the direct

observation of the PICC. However, this technique is limited to surface observation of the specimen only. The Moiré interferometry PICC measurement provides sub-micron accuracy and a full-field displacement map [129, 130]. The drawbacks of using this technique are as follows: it is limited to zero stress ratio, prone to unwanted loading during movement of the specimen and it is time-consuming. Moreover, like the in-situ SEM technique, Moiré interferometry can only be used to observe the surface behaviour of the PICC. The photoelastic technique is used mainly on transparent materials like polycarbonate [131]. The advantage of using the photoelastic technique is that this can investigate both the two-dimensional and three-dimensional effect of PICC. The optical method of caustics is used to measure the PICC by remotely measuring the stress intensity factor from the stress field near the crack tip [132]. An out of plane displacement field is determined by means of a virtual caustic onto a screen in front of the specimen. In the replica observation technique, replica material (i.e. Acetate) is used to attach to the surface of the specimen in the vicinity of the crack tip after spraying of acetone so that the image of the crack is reproduced on the replica to measure PICC [133]. Thermoelasticity has been used to quantify the crack closure mechanism is some materials [134, 135]. This technique measures the ΔK_{eff} around the crack tip region rather than inferring a value from the applied load. X-ray tomography has also been used to investigate the PICC mechanism [136, 137]. The sub-micron resolution of this technique provides insight into the internal behaviour of the crack closure while most of the other techniques are limited to the surface behaviour of the crack closure.

2.7.3 Indirect measurement techniques

The electrical potential drop (PD) technique has been used to measure plasticity induced crack closure (PICC) [137, 138]. A constant current is passed through the test specimen during the fatigue load cycle, and electrical potential over the crack surface is measured. The potential drop (PD) technique is capable of measuring PICC in high-temperature conditions [138]. This technique is only useful for an electro-conductive specimen like a metal. There are some drawbacks in this technique. For instance, mechanical contact between the crack faces due to oxidisation may lead to electrical

isolation. Also, the electrical isolation of the mounting of the test rig, which is necessary for this process, is quite difficult to achieve. The eddy current technique is based on electromagnetic induction [139, 140]. Like the potential drop (PD) technique, this technique is limited to electro-conductive materials. The acoustic emission (AE) technique is becoming popular in measuring the PICC [141, 142]. It is a phenomenon, where sound and ultrasonic wave radiation in the material are used. Noise from other sources such as the noise from the mounting of the test rig during the fatigue test may lead to a discrepancy in crack closure measurement.

2.8 Finite element study of plasticity induced crack closure

Finite element analysis is one of the most commonly used methods of analysing plasticity induced crack closure (PICC). Several key aspects related to finite element modelling are highlighted including element type, mesh refinement, stabilisation of crack closure, crack closure monitoring, crack advance scheme, etc. which are mainly considered during the analysis to achieve more reliable plasticity induced crack closure (PICC) results.

2.8.1 Element type configuration

Higher order elements perform better in computing the stress-strain field near the crack tip, but they demand more computational cost. There is always a compromise required in using the element during PICC simulation. In a two-dimensional model, constant strain triangular (CST) elements or 4-noded quadrilateral elements or higher order quadrilateral elements are generally used to simulate PICC [105, 143]. During plane-strain analysis, the incompressibility requirement associated with plastic strains may not be met by these elements. This can lead to plane-strain locking [144] where the finite element method (FEM) result shows stiffness far greater than would be expected, rendering the results useless. When locking occurs, the stresses oscillate from one element to the next. Using a “Union-jack” arrangement in CST and reduced integration scheme for both CST and quadrilateral element may avoid this plane-strain

locking [105, 143]. In the three-dimensional analysis, 8-noded or 6-noded element are usually used. The reduced integration scheme may also reduce the plane-strain locking in this case. It should be noted that the $\bar{B}$ element formulation can replace the volumetric strain at Gauss integration points with the average volumetric strain of the element [105, 145]. It may also solve this plane-strain locking.

2.8.2 Mesh refinement

During crack growth, the plastic zone forms just ahead of the crack tip due to the change of stress. The plastic zone due to plastic deformation at maximum loading is considered as a forward-plastic zone whereas the one, which is found at minimum loading due to compressive yielding, is considered as a reversed plastic zone. To model plasticity induced crack closure (PICC), a mesh convergence study based on element size, L_e, and plastic zone size, R_p (R_p=2r_p) is necessary. Additionally, proper discretisation of the plastic zone size enables the measurement of the crack increment, Δa, which is of the order of small fraction of the plastic zone [10]. This Δa is also equal to the element size, L_e, near the crack tip. This type of convergence study differs from the typical mesh convergence study where the finite element results at one point are compared [105].

Newman [146] used higher stress in a mesh convergence study based on forward and reversed plastic zone to simulate PICC. Discretisation of the plastic zone may have been performed with an insufficient number of elements here. Solanki et al. [101] recommended that convergence is a consequence of the number of elements existing in the reversed plastic zone during lower stress applied. For that, 3-4 elements are necessary within the reversed plastic zone. It was observed that the reversed plastic zone is one thenth of the forward plastic zone. This differs from the result of typical stationary crack, where the reversed plastic zone is one fourth of the forward plastic zone [147]. However, this can be due to the plastic wake formed behind the crack tip during the crack growth. McClung [148] suggested that mesh refinement should be based on a number of elements present in the forward plastic zone, and that adequate refinement to capture the reversed plastic zone is also important. Dougherty [149] proposed that the aspect ratio (ratio of the length and width of the element) of 2 should

be used in mesh refinement ahead of the crack tip. Several studies [24, 105, 143] advised that mesh density of $\frac{L_e}{r_p} \leq 0.1$ criteria should be satisfied ahead of the crack tip to simulate PICC. Park and Song [150] recommended using the mesh refinement which is based on the crack opening value comparable to the experimental value.

2.8.3 Stabilisation of plasticity induced crack closure

During the fatigue loading, a crack has to propagate a certain distance away from the stress field of the initial crack length to obtain the stabilised level of PICC. McClung [148] showed that this distance should be equal to the forward plastic zone size of the first loading cycle. Fleck and Newman [104] contradicted to this concept and found unstable crack closure even after the crack has propagated the distance of the forward plastic zone of the first loading cycle. According to Ward-Close and Ritchie [151], PICC stabilised when the crack has grown to 3-4 forward plastic zone sizes from the application of overload. However, McClung [148] found initial stabilisation of PICC followed by the subsequent decrease in PICC due to loss of elastic constraints results from extensive yielding around the crack tip. A Similar observation was observed in the study of Daniewicz and Bloom [152] due to less ligament size left ahead of the crack tip during crack growth.

2.8.4 Crack closure monitoring

As the crack grows, the boundary condition near the crack tip needs to be updated to simulate crack extension and the contact surfaces of the crack need to be free of penetration. Several mechanisms are employed to prevent the crack surface penetration and to simulate crack surface contact. Spring elements, truss elements, contact elements and cohesive elements have been used between the crack faces to prevent the penetration [105, 143]. The stiffness of the element is made high to prevent the crack from penetration, and it is made zero when the crack is open. The contact element is considered the more elegant approach, however, it has some issues

including convergence problems and long execution time [105]. The large stiffness of the spring element may lead to a source of numerical difficulty [105]. To overcome this, Solanki [153] used a more direct approach. Under this approach, nodal displacement is monitored during unloading. When it becomes positive to negative, a nodal fixity is applied to prevent the penetration, and nodal displacement is set to zero. The nodal displacement is then removed while loading when it becomes positive. In this study, an increment equal to 1 % of the maximum stress increment was used to monitor crack closure, as it provides a negligible variation of the contact forces along the closed surface. McClung [154] used a truss element together with two contact elements. The 'element death' option was used so that an element can be released anytime during loading irrespective of the magnitude of the deformation caused by the release of the node. As a result, fewer convergence problems were found in this case. The location of the crack opening assessment point in the model varies in different studies. The node at the crack tip, node behind the crack tip or 2nd node behind the crack tip are used to predict the crack the opening value [105, 143]. Dill amd Saff [155] used a contact stress method to calculate opening of the crack, which is independent of any single assessment location. This includes the entire crack surface nodal force distribution under the minimum loading. This method provided a slightly higher opening value than the value obtained from the node just behind the crack tip. On the other hand, the 2nd node behind the crack tip gives a comparatively lower opening value. Considering this issue, the use of this node is discouraged by [105].

2.8.5 Constitutive model used

The bilinear hardening stress-strain relationship was employed to model PICC due to its simplicity [96, 104]. A more complex model referred to as the Ramberg-Osgood power law was also as shown in Equation 2.8.1 used to generate PICC in order to investigate more detailed near-tip crack behaviour.

$$\varepsilon = \frac{\sigma}{E} + K\left(\frac{\sigma}{E}\right)^{n} \tag{2.8.1}$$

where, ε is strain, σ is stress, E is Young's modulus, and K and n are constants that depend on the material being considered.

Both these constitutive models gave a satisfactory result when compared with the experimentally measured PICC [143]. The PICC that was observed using bilinear material agreed well with the experimental results [78, 79] when low-stress level was implemented. On the other hand, the PICC generated using the power law was consistent with the experimental results of Lankford et al. [156] when high stress was used. Moreover, a multilinear hardening stress-strain curve was also used to generate PICC in the plane stress condition [149]. Here, the dependence of yield stress on increasing plastic strain was taken in consideration. In the study of Antunes et al. [157], both isotropic and kinematic hardening models were used to analyse PICC. The isometric model gave a higher level of PICC due to the extensive plastic deformation available in this model while the kinematic model gave a lower level of PICC. However, the PICC found from the kinematic model was more consistent with the experimental results.

2.8.6 Crack advance scheme

The most popular method used in fatigue crack growth simulation is the crack tip node release scheme [10, 24]. Here, to simulate the crack growth, the node at the crack tip is released every cycle so that the crack can propagate about one element size near the crack tip. The conventional node release scheme has nothing to do with the crack propagation life. Hence, it does not depend on the stress and strain condition near the crack tip. The node is usually released at any of the following situations: at maximum load level, at minimum load level, after the maximum load level, during the loading/unloading or during every 2nd load cycle, at the 98 % of the maximum load cycle, etc. [10, 105]. Solanki et al. [101] found no difference in crack opening value results when using either the maximum or minimum load node release scheme. However, McClung et al. [96] reported a significant difference in results. It was concluded that these differences were the consequence of using truss elements for

crack surface node fixity and that changing the boundary conditions on the crack surface nodes directly yields approximately the same results for any of the different crack advance scheme. Results presented by [101] showed good agreement between the minimum and maximum load node release schemes by using a suitably refined mesh. Moreover, Newman [158] used a critical strain to advance the crack, Palazotto and Bednarz [159] proposed a stress criteria to advance the crack, and Nguyen et al. [160] used the cohesive element to simulate the crack growth. The extended FE method (X-FEM) [161] is becoming popular in crack growth simulation. These are considered as more physical-based methods of crack growth simulation [143].

2.9 Identification of the threshold of stress intensity factor range for fatigue crack growth, ΔK_{th}

The identification of the threshold of stress intensity factor range depends on different aspects. These are described in detail in the following sections.

2.9.1 Background to the ΔK_{th}

FCG threshold, ΔK_{th}, is one of the key parameters representing material resistance to fatigue crack growth (FCG). Newman [162, 163] referred to the Federal Aviation Administration (FAA) by mentioning that traditionally, the threshold is used as a limit for the damage tolerance design (DTD). The ΔK_{th} has been used over the past 40 years in numerous FCG models available in the literature [55, 57, 61, 164-169]. However, the identification of ΔK_{th} and its application in a structure's residual life prediction is not quite straightforward, as it varies both qualitatively and quantitatively due to various experimental, numerical and analytical methods and corresponding assumptions used [11]. Whilst FCG curves of physically small cracks and microstructurally small cracks have different shapes [170], FCG can be represented by the sigmoidal curve of the $\log(\Delta K)$ – $\log\left(\frac{da}{dN}\right)$ for long cracks [7] as described before (see Figure 2.4.4). It depicts three regions, region I, region II and region III. Region I

is taken as either a very slow crack growth region or near-threshold region since the SIF range of the sigmoidal curve in this region asymptotically approaches ΔK_{th}. The Paris Law [53] is normally applicable to the crack growth in region II. There are several models available to represent the whole sigmoidal curve covering all three regions. One of the models developed by NASA and represented by Forman and Mettu [166] is the most popular (see Equation 2.4.1).

$$\frac{da}{dN} = C\Delta K^m \frac{\left(1 - \frac{\Delta K_{th}}{\Delta K}\right)^p}{\left(1 - \frac{K_{max}}{K_C}\right)^q} \tag{2.9.1}$$

where, C, m, p and q are material constants, SIF range $(\Delta K) =$ maximum SIF $(K_{max}) -$ minimum SIF (K_{min}) , $K_C =$SIF at fracture and $\Delta K_{th} =$ SIF range at threshold.

Ideally, ΔK_{th} is the value of SIF range, ΔK, below which fatigue crack will not grow [7]. However, it has been shown [171] that cracks propagate even below the large-crack threshold measured by the ASTM test procedure [162, 172]. Therefore, ΔK_{th} is also defined to be a value of ΔK at which the crack growth rate, $\frac{\mathrm{da}}{dN}$ is below 10^{-10} $\frac{\mathrm{m}}{cycle}$ [162, 173]. This is sometimes experimentally determined by extrapolation to $\frac{\mathrm{da}}{dN}$=0 from the lower tail of the sigmoidal curve of raw data when the linear-linear scale is considered [11]. The residual life of a structure can be highly influenced by variation of the ΔK_{th}. As reported by Molent [55] and mentioned by Zerbst and Vormwald [11, 12], a variation in the threshold SIF range of 1 $MPa\, m^{0.5}$ can result in a variation about 18 % of the residual life. This also provides important insights into how relevant and essential it is to determine ΔK_{th} accurately in a DTD approach.

2.9.2 Different methods of determining ΔK_{th}

There are several experimental methods available to determine ΔK_{th}. These are:

- Load reduction method (LRM);

- K_{max} constant method;
- Far-field cyclic compression method [11].

The load reduction method is standardised by American Society for Testing and Materials (ASTM) 647 [172] or International Organization for Standardization (ISO) 12108 [174]. The load is reduced stepwise to find ΔK_{th} in a pre-cracked specimen at a constant R. In the K_{max} method, the same stepwise reduction of the load range is followed, but at the same time R is increased by maintaining the same maximum SIF value. The far-field compression method can be divided into three sub-methods including:

I. Compression pre-cracking constant amplitude (CPCA);
II. Compression pre-cracking load reduction (CPLR);
III. Cyclic R curve method.

A detailed review of all these methods is given by Zerbst in [11].

The ΔK_{th} values obtained with the above mentioned methods can, however, be quite different due to the different mechanisms involved. These mechanisms are related to the plasticity induced ahead of the crack tip as well as the conditions of the fracture surfaces. Comparatively lower threshold values have been found using the far-field cyclic compression method rather than using the load reduction method [162, 163, 175-177]. This is due to the fact that the far-field cyclic compression method is not affected by the compressive yielding at the crack-starter notch and more "steady-state" constant amplitude data in the near threshold regime are achieved with this method [176]. Crack surface roughness and grain size near the crack tip also influence the overall ΔK_{th} [162, 178]. In general, the greater size of grains promotes roughness induced crack closure (RICC), and oxide-induced crack closure (OICC) is enhanced simultaneously [179]. The above phenomena increase the ΔK_{th} values when measured. Consequently, in LR Method crack-faces can produce rough-surface or fretting debris which contributes to the early crack closure and higher ΔK_{th}.

2.9.3 Factors influencing ΔK_{th}

The ΔK_{th} varies with mechanically short and long cracks. Linear-elastic fracture mechanics (LEFM) is normally only applicable in long cracks under small scale yielding conditions. According to Newman [180], the ΔK_{th} is not valid in the giga-cycle fatigue region for short cracks as there is no continuous crack propagation below $\frac{\mathrm{da}}{dN} = 10^{-7}\frac{\mathrm{mm}}{cycle}$, which is smaller than one lattice spacing per cycle [11]. In general terms, it is possible to find in the literature [181] two different ΔK_{th} levels; a microstructural threshold for short cracks and a mechanical threshold for long cracks [182]. The difference is related to the advancement of a short crack at microstructural level and stable propagation of a longer crack having a plastic zone which covers several grains. Moreover, at low SIF, the FCG rate is more sensitive to microstructure, load ratio and environment for long cracks [170]. However, there is a minimum value independent of R, which can be considered as a material property and for this reason it is called the intrinsic threshold, also known as the effective or true threshold [181]. Moreover, the intrinsic threshold can be increased by the increase of stiffness and strength of the material [11, 183, 184]. Another important effect is related to the specimen geometry. ΔK_{th} seems to be lower in an M(T) specimen than a C(T) specimen for the same ΔK condition [185, 186]. The justification should be related to the geometrical constraint or T-stress, which is found to be lower in an M(T) specimen (T-stress<0), compared to C(T) specimen (T-stress>0) even though T-stress has different effects (e.g. PICC) which might contradict this observation. However, the lowest stress triaxiality at the crack tip associated with the M(T) specimen, produces a much bigger plastic zone near the crack tip than the geometry with a high level of the constraint like the C(T) specimen [187].

2.9.4 R ratio effect on ΔK_{th}

As discussed above, the ΔK_{th} value usually decreases with the increase of R [188]. Two types of R-dependency have been reported in the literature [181]. In some cases, ΔK_{th} decreases up to a critical value of R and then it becomes constant beyond that value [11]. In other cases, ΔK_{th} continues to decrease beyond that critical value of R [189]. Klensil and Lucas [164] used the Equation 2.4.4 to identify ΔK_{th} in a steel alloy.However, other approaches have been adopted such as the one reported by Kwofie [190] in which an equivalent stress approach based on the R ratio is used to identify the fatigue threshold value. In general, it has been recognised that crack closure is found to be the controlling factor in this case [54, 55]. For this reason, a different parameter has been introduced ΔK_{thr}, which is an FCG threshold value that depends on R and the crack length value. In the literature, the scatter in fatigue life is explained by the variation of ΔK_{thr} values [55]. Further methods to experimentally identify the threshold condition have been recently developed using plain fretting crack arrest analysis [191]. Here, the dispersion between long crack ΔK_{th} fretting estimations and conventional fatigue data was found to be less than 10 %.

2.10 Electromagnetic treatment (ET) effect on fatigue resistance

The effect of electromagnetic treatment (ET) on metallic materials is reviewed, with focus on fatigue resistance and crack repair of the metallic alloy. While a growing body of literature and research exists focusing on the topic of ET, the mechanisms governing the treatment are not entirely understood. Furthermore, the optimal parameters for ET to enhance fatigue resistance are not yet clearly defined. This review seeks to summarise the existing literature of various ETs used to enhance the fatigue resistance. ET and fatigue resistance will be explained briefly; the parameters of the ET used, the subsequent benefits of fatigue life enhancement of different materials will be highlighted. The rearrangement of the microstructure of the materials and crack healing mechanisms due to ET will also be demystified. In addition, issues related to the effectiveness of this treatment on fatigue resistance and the threats and

challenges of this topic will be discussed. Therefore, the purpose of this section is to help develop a more optimised research method to investigate the effect of electromagnetic treatment (ET) on fatigue resistance of metals in the near future.

2.10.1 Background to electromagnetic treatment effect on fatigue resistance

Fatigue, alongside corrosion and wear, are the main causes of damage in metallic members and structures [192]. If ignored, fatigue can lead to catastrophic failure with financial and economic costs. About 90 % of all metallic failures are estimated to be due to fatigue [193]. In order to deal with this problem, a new concept known as ‘remanufacturing’ [194-198] is becoming adopted in many types of industry, including aerospace and automotive. The idea of ‘remanufacturing’ is to recycle and restore the product to its original manufactured conduction. Remanufacturing is also necessary for the sustainable development of mechanical equipment manufacturing, and it depends highly on the application of fatigue crack repairing [198]. It can potentially save energy, materials cost and as well as avoid the unnecessary pollution [195].

Fatigue is known as an inevitable and irreversible process in metallic components subjected to repetitive stresses over time [7, 43, 199]. These repeated stresses create micro-flaws within the microstructure leading to fatigue damage. It is, therefore, desirable to improve the fatigue life of metallic structures because of the requirement for sustainable raw materials and the high cost of production and processing. Metal fatigue is a problem which is constantly affecting many types of industry including aerospace, biomedical, marine and automotive because it reduces the lifetime of structures. Improving fatigue life can be accomplished by reducing the magnitude of stress the material endures or alternatively by increasing the number stress cycles that the material can withstand. Reducing the magnitude of the induced stress can be easily achieved by increasing the size of the structural component. However, this can cause high production and operational costs, as well as a weight penalty. In the case of a vehicle, for example, this can lead to higher fuel consumption and further greenhouse emissions. Therefore, today’s challenge is to increase the number of

cycles while keeping an optimised structural design and maintaining costs to a minimum.

There is currently growing interest in research on fatigue, to improve the number of stress cycles that a material can endure by altering material properties/characteristics. Such methods include nitriding, carburising, high-frequency quenching and shot-peening which are commonly used in industry. These techniques increase the fatigue life by increasing surface hardness and producing compressive residual stresses at the material surface without added weight penalty [14, 16]. However, some of these methods such as heat-treatment can be expensive and time-consuming [200].

One of the potential developments for improvement in fatigue resistance is the use of electromagnetic treatment (ET) [16, 201-203]. The interaction between electricity and magnetism is known as electromagnetism while the interaction of the magnetic field with electrons (or vice-versa) is known as the electromagnetic effect [204, 205]. Exposing a material to the effects of electromagnetism is known as an electromagnetic treatment (ET). According to Bose [203], Winterton is considered to be the first person to investigate the effect of a saturated magnetic field on the fatigue behaviour of carbon steel in 1959. Since then, there have been intensive investigations using ET in the form of static magnetic fields in metallic materials [206]. The technique has shown to be successful in relaxing stresses, improving fatigue resistance and changing other mechanical properties. ET has also been applied in the form of electropulsing [207] and pulsed magnetic field treatment [13]. Pulsed magnetic field treatment is considered to be more economical in generating a high energy magnetic field than a static magnetic field treatment [206, 208]. High current density can be achieved through the application of electropulsing in the material. The current density can be defined as

$$J = \frac{I}{A} \tag{2.10.1}$$

where, I is current and A is cross-sectional area of the sample.

This high current density has been shown to transfer input energy from the external environment to reorganise the fatigue damage within the microstructure [209]. Troitskii [210, 211] pioneered the use of electropulsing for metallic alloys. Subsequent studies

have shown that electropulsing could enhance the fatigue life of steel [14, 207, 212-215], copper [201], titanium [216, 217] and aluminium alloys [218].

Aeroplanes, high-pressure vessels, steel bridges, engineering machinery and nuclear power plants are some of many structures which need to cope with high fluctuating stresses and are highly prone to fatigue failure. The use of ET looks to be promising for extending the fatigue life of these structures [206, 219, 220]. In comparison to conventional treatments like heat treatment, for example, magnetic field treatment is easy-to-produce and easy-to-control fields [221] and the treatment time is significantly shorter [222].

The improvement of fatigue life by ET has been attributed to various mechanisms including dislocation movement [16], Joule heating [14, 209, 216], stress relaxation [213, 216, 223] and crack healing mechanisms [207, 215, 224]. However, there are also several studies that have shown that the fatigue life can be reduced by the use of ET [215, 225, 226]. To explain this phenomenon, it was suggested that excessive treatment caused melting damage due to overheating. Hence, to maximise the effect of ET on fatigue properties optimum parameters need to be identified and implemented.

Much of the early research on the use of electropulsing and magnetic field treatment took place in the former Soviet Union. Owing to their potential, both techniques are nowadays under investigation in the USA, China and Europe. The present review will outline the benefits of the two techniques as reported in the literature and discuss the mechanism by which the treatment has been reported to affect the fatigue resistance of metal alloys. As a result of its potential importance, the effect of the two treatments on fatigue crack healing will be specifically addressed. In the final section, the challenge that remains before this type of technology is commercialised are discussed.

2.10.2 Quantified electromagnetic treatment and its benefits on fatigue resistance

A number of research investigations have reported that electromagnetic treatment (ET) can have beneficial effects on the fatigue life of metal alloys. These studies have shown that after ET, the fatigue life (average) has substantially increased compared to alloys in the untreated state. An inspection of the literature has revealed that there are two main types of treatment that have been used for this purpose. These are:

I. magnetic field treatment, also in the form of static [16, 199] and alternating [16] (This treatment also referred as eddy current treatment field [224]) and
II. electropulsing [14, 15, 207, 209, 213-217, 223, 227, 228] in which a pulse of high-density current passes through a material.

In some research work, ET has been applied at different stages of the alloy's fatigue life. These research investigations can be further categorised into four types depending on the stage of application of the treatment. These are:

i. Prior to fatigue test testing [216],
ii. at a specific prefatigue level [13-16, 207, 209, 213-217, 223, 227, 228],
iii. at several intervals of fatigue test [13, 218] and
iv. during a period of fatigue test [199].

The prefatigue level can be defined as percentage of prefatigue as shown below

$$\%\, Prefatigue = \frac{Number\ of\ fatigue\ cycles}{Untreated\ fatigue\ life} \times 100 \qquad (2.10.2)$$

A summary of the findings of these investigations showing improvement in fatigue life due to ET is given in the Table 2.10.1.

Table 2.10.1 Summary of the beneficial effect of electromagnetic treatment on fatigue life enhancement.

Alloy name	**ET type**	**ET Parameters**	**ET application period**	**Maximum improvement in fatigue life**	**Ref.**
Low carbon steel	Alternating magnetic field	360 Gs for 210 s	At 50 % prefatigued, and after every 100,000 cycles	Over 2 times at 360 MPa and 420 MPa (Rotating-bending fatigue)	[13]
Medium carbon steel	Alternating magnetic field, static magnetic field	900~3650 Gs for 20~240 min	At 55 % prefatigued	34 % at 549 MPa (Rotating-bending fatigue)	[16]
Steel, AISI 4140	Static magnetic field	800 Gs, 1300 Gs	During 30 %, 30-60 % and 100% fatigue life (untreated)	20 % at 630 MPa (Rotating-bending fatigue)	[199]
Titanium alloy (6.1 % Al, 2.2 % Cr, 2.7 % Mo)	Electropulsing	150 $\frac{MA}{m^2}$, 50 μs	Before fatigue test	25-50 % at 300-600 MPa (Ultrasonic fatigue)	[216]
Austenite steel, 08H18N10T	Electropulsing	8 kA, 20 s (no geometry provided)	At 62 % prefatigued	54 % at 80 MPa (Ultrasonic fatigue)	[213]

Austenite steel, 45G17Yu3	Electropulsing	9.3 kA, 70 s (no geometry provided)	At 69 % prefatigued	76 % at 20 MPa (Ultrasonic fatigue)	[213]
Steel, Fe-0.6C-1Mn-2Si	Electropulsing	290 $\frac{MA}{m^2}$, 15 s	At 70 % prefatigued	54 % at 115 MPa (Ultrasonic fatigue)	[228]
Stainless steel (SUS31)	Electropulsing	82.76 $\frac{MA}{m^2}$, 0.5 ms	At 87 % prefatigued	26% at 115 MPa (Tension-tension fatigue)	[14]
Stainless steel (SUS31)	Electropulsing	92.31 $\frac{MA}{m^2}$, 0.5 ms	At 85 % and 43 % prefatigued	21 % and 6 % At 115 MPa (Tension-tension fatigue)	[227]
Stainless steel, 0.45C17Mn3Al	Electropulsing	232.5 $\frac{MA}{m^2}$, 25 μs	At 49 % prefatigued	72 % at 20 MPa (Ultrasonic fatigue)	[223]
Medium carbon steel, steel 40 & steel 45 and titanium alloy, VT1-0	Electropulsing	280 $\frac{MA}{m^2}$, 0~135 s	Prefatigued samples	28 % at 20 MPa (Ultrasonic fatigue)	[217]
Cast hot work die (CHWD) steel	Electropulsing	54 $\frac{MA}{m^2}$, 120 μs	80 % prefatigued (Thermal fatigue)	140 % (Thermal fatigue)	[214]

2.10.2.1 Magnetic field treatment

There has been a considerable amount of research to suggest that magnetic field treatment has extended the fatigue life of various alloys. Fahmy et al. [13] treated low carbon steel using an alternating magnetic field strength of 360 Gs for a total of 210 s. The fatigue tests were conducted, using a rotating-bending fatigue machine, at 360 MPa and 422 MPa stress amplitude. At the lower stress amplitude, an alternating magnetic field treatment was applied at half the estimated fatigue life. For the higher stress amplitude, the treatment was applied at 100,000 cycles intervals. Due to this treatment, the fatigue life of low carbon steel increased by more than two times in comparison to the untreated samples. Despite achieving substantial improvement in fatigue life, the authors did not analyse experimentally the exact mechanisms, which contributed the fatigue life increase. Furthermore, this study only suggested some possible explanations for the increase in fatigue life due to magnetic field treatment and did not attempt to estimate the exact magnitude of the increased fatigue life. According to these explanations, the magnetic field had some effect on the strain (i.e. magnetostriction which is a property of ferromagnetic materials that causes them to change their shape or dimensions during the process of magnetisation) and the dislocation motion and/or the dislocation density of the steel alloy. On the other hand, Bao-Tong et al. [16] used a comparatively higher magnetic field intensity to treat medium carbon steel after a prefatigue level of 55 %. Both alternating and static magnetic fields were used in this study. Their study showed that the alternating magnetic field was found to be more effective than static magnetic field in improving the fatigue life. This study revealed that the correct combination of treatment intensity and treatment time are critical parameters for achieving the optimal fatigue life enhancement. For example, when a static magnetic field was used for 60 $mins$, a magnetic field intensity of 900 Gs had no effect at all, while at 1350 Gs an increase in the fatigue life by 34 % was reported. However, application of 3650 Gs increased fatigue life by only 14 %. This indicates that there was a possible saturation effect due to the excessive magnetic field treatment. This study also suggested that the improvement in the fatigue life was due to the effect of magnetostriction, which has good agreement with the proposed mechanism by Fahmy et al. [13]. To explain the deterioration of fatigue damage, Boa-Tong et al. [16] referred to the heavy oxidisation

effect which can be caused as a result of excessive heat generated by the eddy current. However, these authors presented no microstructural evidence for this.

Celik et al. [199] used a slightly different technique from other authors [13, 16] to treat AISI 4140 steel. The alloy was exposed to a static magnetic field treatment with a treatment intensity higher than that of Fahmy et al. [13] while the fatigue test was ongoing. It was observed that the magnetic field treatment was more effective at initial stage when applied during first 30 % prefatigue. However, the treatment was not as effective when applied at the later stage of the fatigue life. This study also suggested that the length of the fatigue life was enhanced when the magnetic field intensity increased to 1300 Gs from 800 Gs. Using Atomic force microscopy (AFM), alignment of the magnetic domains was observed in a treated alloy that has been exposed to a magnetic field treatment of 800 Gs. It was proposed that the alignment of the domain walls reduced the obstacles for dislocation movement and assisted the dislocation motion. Therefore, the time for the formation of slip bands was prolonged and this consequently delayed fatigue crack initiation. Recently, an analytical model of the S-N Curve was proposed by Zhao-Long et al. [229] to correlate the fatigue life with magnetic field intensity [229]. This model was developed by using the non-equilibrium statistical theory of fatigue fracture. The obtained curves were consistent with the experimental data [13, 199]. These studies argued that the fatigue life increased with increasing magnetic field intensity. However, the work was focused entirely on the use of static magnetic field treatment and did not consider any possible adverse effects by the treatment due to the application of excessive treatment intensity.

2.10.2.2 Electropulsing effect

Levitin et al. [216] examined the effect of electropulsing on the fatigue resistance of titanium alloy (Ti - 6.1 %, Al - 2.2 %, Cr - 2.7 % Mo). The specimens had been treated using ultrasonic frequency to produce compressive residual stresses on the surface and then electropulsed before the fatigue testing. By using this approach, the fatigue life was reported to increase by 25-50 %. For this treatment, the electric pulse generated was from an electric capacitor of 200 mF. A current density of 150 $\frac{MA}{m^2}$ was recorded with pulse time of 50 μs. To investigate the improvement further, Levitin et

al. [216] measured the macroscopic residual stress, the microscopic stress and the resistivity of the sample before and after the treatment. The results showed a decrease in the macroscopic residual stress. In addition, a decrease in the resistivity was observed and this was proposed to occur via homogenisation of the microstructure. An increase in the microscopic stress was also recorded due to stress relaxation of the material. The combination of all these effects was thought to aid restoration of the fatigue damage.

Sosnin et al. [213] researched the fatigue life of austenitic stainless steels 08H18N10T and 45G17Yu3 using electropulsing. They applied the electropulsing treatment, at prefatigue levels of 62 % and 69 %, respectively. The study found that using a treatment of 8 kA for 20 s on 08H18N10T austenitic stainless steel, the fatigue life improved by 54 % at a stress amplitude of 80 MPa. However, with the 45G17Yu3 austenitic steel there was a higher improvement of 76 % at a stress amplitude of 20 MPa using 9.3 kA for 70 s. The current density was not identified as the geometrical details of the sample are not provided in this study. To examine the healing effect of electropulsing, the authors used scanning and transmission electron microscopy. In the case of 08H18N10T austenitic stainless steel, electropulsing improved fatigue resistance by retarding dislocation substructure growth, curbing the development of martensitic transformation, [$\gamma \rightarrow \varepsilon$ or, austenite (Face-centred cubic) to martensite (body-centred tetragonal) transformation], inducing disintegration of the solid solution by precipitation of TiC particles, and reducing the internal field stress amplitude. For the 45G17Yu3 austenitic steel, electropulsing enhanced the fatigue life by (i) stress relaxation due to the combined effect of reconstruction of grain structure; (ii) the annihilation of dislocation, and reconstruction of dislocation substructures; (iii) formation of micro-twins (probably as the result of thermal-stress); (iv) healing of stress concentrator; and (v) suppressing martensitic transformation.

A further study [228] from the same authors involved the use of electropulsing at 70 % prefatigued notched steel (Fe-0.6C-1Mn-2Si). The current density applied to the specimens was 290 $\frac{MA}{m^2}$ for 15 s. The recorded improvement in the fatigue life was 54 %. The microstructural analysis showed that the fatigue life increased due to relaxation of stress concentrators through the dissolution of cementite particles at grain boundaries. As a result, there was a state change of the interphase boundaries

between the matrix and second-phase particle. This caused the mean and maximum subcritical crack length for fatigue to increase. The layer of the steel which was involved in the strain of the material and the zone of fatigue crack growth, also enhanced.

Tang at al. [14] recently investigated the effects of electropulsing on the restoration of fatigue damage on a notched stainless steel (SUS31) plate with a focus on the time to crack initiation (i.e. the number of cycles required for the crack to grow) at the notch area using a tensile-tensile fatigue test. The study showed that at a stress level of 115 MPa, the crack initiation period delayed by 26 % due to electropulsing of 82.76 $\frac{MA}{m^2}$ for 0.5 s after 87 % of the crack initiation period of the sample. According to this study, electropulsing led to a decrease in the residual plastic strain parallel to the loading direction (ε_{yy}) and in the dislocation density. The reduction in the dislocation density is accompanied with a decrease in the microhardness to the nominal level in order to restore fatigue damage. In another study, the same authors [227] varied the prefatigue level to examine its effect on the amplitude of the fatigue crack initiation period (crack growth up to 25 μm). By using a current density of 92.31 $\frac{MA}{m^2}$ for 0.5 ms was used. They observed that treatment at the fatigue crack initiation period of 85 % and 43 %, improved the fatigue crack initiation period by 21 % and 6 %, respectively. They further investigated the effect of electorpulsing treatment on dislocation and slip band. From TEM observations, it was concluded that the delaying effect of the electric current on the fatigue crack initiation period was related to the decrease of the dislocation density. It was also observed that when the treatment was applied at 85 % of the crack initiation life, the dislocation density reduction was greater than that for treatment at 43 % of the crack initiation period. This also supported the fatigue crack initiation model of Tanaka and Mura [230] which attributes the delay of fatigue damage to the reduction of the dislocation density. The AFM results indicated that the step height of the slip bands formed during the cyclic loading was decreased following electropulsing. Dislocation motion due to electron wind drag and thermal stress due to high-speed heating were suggested to be the reasons behind these changes. However, in this study, the authors could not explain why the treatment was more prominent when applied at a later stage of the fatigue crack initiation life. Electropulsing has also been shown to enhance the fatigue life of stainless steel

(0.45C17Mn3Al) by Konovalov et al. [223]. A treatment of 232.5 $\frac{MA}{m^2}$ for 25 μs, at a prefatigue level of 49 % produced an increase in fatigue life by 72 %. Diffraction electron microscopy was used to investigate the effects of electropulsing. The study revealed that the electropulsing treatment led to one of the most powerful stress concentrators in the crystal lattice structure to relax and this was thought to delay fatigue crack initiation. In another study, the same researchers [217] varied the pulse time of the treatment from 0-135 s to examine the effect of the duration of the treatment of the fatigue resistance. Using a current density of 280 $\frac{MA}{m^2}$, the electropulsing treatment was applied to prefatigued samples of medium carbon steel (steel 40, steel 45) and titanium alloy (VT1-0). The maximum increase in the fatigue life of steel 45 was recorded at 28 %, when the pulsing time was set to between 45-70 s. The authors suggested that the electro-plastic effect was most prominent when the treatment duration reached 70 s. However, when increasing the treatment time to 135 s, the fatigue life decreased by 10 %. This observation was attributed to the increase in the thermal effect. Electropulsing was used as a means to enhance the thermal fatigue life of cast hot work die (CHWD) steel by Zhao et al. [214] . Using a lower current density of 54 $\frac{MA}{m^2}$ at a pulse time of 120 μs and treating at 80 % fatigue crack initiation life, there was an improvement of 140 % in the fatigue crack initiation life. In this study, electropulsing induced a circular heat affected zone (HAZ) at the notch root of the sample due to high-speed heating and cooling, in other words, high-speed quenching took place. The microstructures of the HAZ was composed of superfine martensite and of a fine-grained carbon compound. It was proposed that this microstructural change could promote the energy required for crack nucleation and supress crack growth. However, the authors did not study the temperature rise due to electropulsing ; this would have been useful to predict the energy required to induce the HAZ and optimise this treatment.

2.10.3 Mechanisms of electromagnetic treatment on fatigue resistance

A variety of mechanisms have been documented in the literature to explain the increase in fatigue life using electromagnetic treatment (ET). These are based on quite complex phenomena, which take place due to this treatment, and depend on the ET intensity, the extent of prefatigue damage, material properties, etc. These mechanisms are mostly explained by a single factor or combination of factors including dislocation movement [13, 14, 16, 199], Joule heating [14, 216], stress relaxation [216, 223, 228], homogenisation of microstructure [214, 216], phase transformation [209, 214, 228], restoration of hardness [14, 209, 214], and healing of slip bands [14].

It was proposed that electro-magneto-plasticity influences the dislocation movement based on the magneto-plastic theory [231] and electro-plastic theory [232]. In the case of the pulsed magnetic field treatment, it can provide a condition for dislocation depinning to occur in alloys. It has been well-documented that magnetic field treatment can cause a magnetostriction effect in steels and enable dislocation movement to occur. This dislocation movement can thus initiate a delay in fatigue crack initiation by increasing the time to form slip bands within the alloy [13, 16, 199] and as a result, fatigue resistance can be enhanced. It has also been reported that magnetic domain walls affect the plastic flow by hindering dislocation movement [13, 225]. In magnetostriction, the magnetic domains rotate and the domain walls shift in such a way that the orientation randomness decreases. Consequently, resistance to dislocation motion by domain walls is reduced [13, 16, 199, 225]. The movement of dislocation has been reported by Babutskyi et al. [233] who examined the effect of pulsed magnetic field treatment on titanium alloy (TA2). Using transmission electron microscopy (presented in Figure 2.10.1), it was shown that the dislocations became untangled and uniformly dispersed within the alloy.

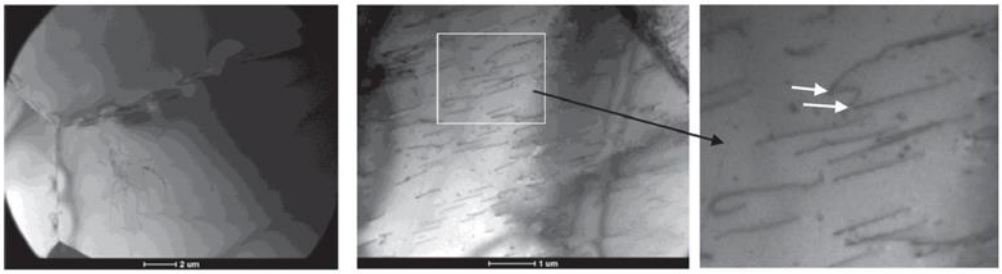

Figure 2.10.1.Transmission electron microscope (TEM) micrograph of untreated (a) and treated (b,c) samples [233].

The alignment of magnetic domains at 800 Gs magnetic field treatment was shown by Celik et al. [199] using atomic electron microscopy. Due to the magnetic domain alignment the weakly pinned dislocations were relieved in the process of magnetostriction [16, 232]. The application of a magnetic field led to the disappearance of densely populated areas of dislocations and the dislocation distribution became more uniform [199]. Apart from this, the application of magnetic field increased the energy of dislocations [199, 234] thus enabling dislocations to overcome obstacles. By this means the application of magnetic field can increase the dislocation motion [199, 235].

Electropulsing has also been observed to alter the dislocation substructure and thus help improve fatigue life [14, 213, 217, 223, 227, 228]. Tang et al. [14, 227] observed a reduction in the dislocation density following electropulsing. According to their studies [227], the electron wind force generated by electropulsing assisted in the annihilation of dislocations and eventually caused healing of the slip bands formed during the fatigue process and restored the microhardness to values prior to fatigue loading. Electropulsing also led to healing of the fatigue damage near the notched area of the sample due to the current becoming concentrated at the vicinity of the defect [216]. This process causes Joule heating to occur leading to a heat release at the crystal lattice defects because of the high electrical resistance of the defects. As the surrounding unheated area constrains the heated area, thermal compressive stresses occur. Eventually, this heals the microstructural defects. It was also proposed that stress relaxation takes places due to a decrease in the electric current resistance caused by the high current density imposed by electropulsing [216, 236, 237]. This

stress relaxation helps enhance the fatigue life. The phase transformed heat affected zone (HAZ) near the notch of a steel sample due to electropulsing has been shown to be able to delay fatigue crack initiation [209, 214]. This HAZ contains a more homogeneous microstructure with higher hardness compared to the other parts of the material and also has high ductility and wear resistance. All these factors increase the energy required for the crack to nucleate. The electropulsing treatment has been reported to relieve residual stresses, on a macro level [238-241] which can lead to the higher fatigue life of material.

2.10.4 Electromagnetic treatment effect on fatigue crack repairing

The effect of electromagnetic treatment (ET) on fatigue crack repairing or healing has been investigated by a number of researchers. A recent study by Jung et al. [218] examined the effect of electropulsing on the fatigue crack growth behaviour of aluminium alloy 6061-T6 using two different current density pulses of 90 $\frac{MA}{m^2}$ and 150 $\frac{MA}{m^2}$ of duration of 0.5 ms. The treatment was applied at a prefatigue level of 70 % and was further applied at 10 % intervals. The 90 $\frac{MA}{m^2}$ treatment with yielded the maximum fatigue life improvement with a 55 % increase in the fatigue life. However, at the higher current density of 150 $\frac{MA}{m^2}$, the fatigue life decreased by 10 % compared to the untreated specimens. The use of scanning electron microscopy (SEM), showed that crack propagation with cyclic slip deformation in the untreated sample appeared to start from the surface of the specimen. However, in the treated specimen with a current density of 90 $\frac{MA}{m^2}$, there were sites of local melting near the crack tip. This induced the crack shielding effect [242] effect which enabled crack growth retardation. It was also proposed that the healing process occurred in two steps by:

i. The high-density electric current concentrated around the crack tip followed by
ii. Joule heating caused by the electric current which led to local melting and thus healed the fatigue crack.

In the case of the treated sample at 150 $\frac{MA}{m^2}$, brittle fracture was observed in addition to the melted sites. The authors suggested that the electric current became too high and thermal damage occurred at the crack tip hence causing the reduction in fatigue life. Another interesting observation made suggested that the effect of electropulsing in fatigue crack growth retardation existed only at the lower maximum stress intensity factor, K_{max}. The results indicated that when K_{max} became larger than 0.91 $MPa\sqrt{m}$, the concentration of current was not high enough to induce the melting effect. In a different study by Yang et al. [224], the eddy current treatment was used to treat a fatigue crack in 1045 steel. Induction heating caused by the treatment was used to treat the fatigue crack in the axial and radial direction. The eddy current treatment was generated using a copper coil connected to a 60 kW high-frequency induction-heating apparatus. The duration of the eddy current treatment varied from 1 s to 3 s and the corresponding fatigue crack healing increased up to 8.4 times compared to the initial improvement at lower treatment duration. The study showed that eddy current treatment led to heating of the fatigue crack along the axial direction, while there was no healing of the crack along the radial direction. Observations using optical microscopy revealed that the crack tip along the axial direction healed due to bridging between the crack faces. The authors proposed that for the sample with an axial fatigue crack, crack face bridging occurred due to voltage breakdown [243] and subsequent local melting. In addition, they also suggested that the reason for the radial crack not being unaffected by the eddy current treatment was due to the lack of electron detouring around the crack surfaces.

Hosoi et al. [15, 207, 215, 226] showed that electropulsing of high current density had a beneficial effect on fatigue crack growth of Austenitic stainless steel (SUS316NG) by investigating several research works. The authors used electropulsing ranging from 0.5-10 kA with a pulse time between 0.5-10 ms to treat pre-cracked specimens [207, 215]. The treatment led to fatigue crack growth retardation, and finally to fatigue crack healing. Like in other two research work [218, 224], it was shown that local melting benefited the crack healing process and crack growth retardation. SEM observations displayed evidence of crack surface bridging, annealing at the crack tip and crack tip blunting. Furthermore, these studies [207, 215] showed that the compressive residual stress due to Joule heating also enabled crack closure to occur which delayed the rate of crack growth. In another study by Hosoi et al. [15], 6-9 kA

electropulsing for 2-3 ms with 20-30 applications were used to repair fatigue cracks. It was also demonstrated that by using 4 kA for 2 ms with 12 applications, cracks would gradually heal after each application and repaired between 75-97 % of the original crack [226]. In the research work of [215], crack growth behaviour by measuring the stress intensity factor, K, using the digital image correlation (DIC) method. A drop in the stress intensity factor range, ΔK, also reported due to the crack closure effect, while the crack growth rate slowed down. However, there was evidence of crack growth acceleration when a long crack was treated by electropulsing. The reason for this observation was proposed to be due to higher current density that was caused by the longer crack length leading to excessive thermal stress. Once the excessive thermal compressive stress is applied at the crack tip, tensile residual stress is formed due of the restriction of plastic strain around the crack tip created by the unheated elastic area. This tensile residual tensile stress exceeded the compressive residual stress imposed in the crack closure area, and thus, accelerated the crack growth.

Electropulsing also showed promising effects on the crack growth retardation and fatigue life improvement during thermal fatigue of cast hot work die (CHWD) steel [209, 214]. The average current density used by Lin et al. [209] was 80 $\frac{MA}{m^2}$ at pulse discharge duration of 100 ms, 120 ms and 140 ms. The results showed that the crack growth propagation rate decreased with discharging duration up to 120 ms. However, when the discharging duration increased to 140 ms the effect of retardation was less compared to 120 ms discharging time. Using both X-ray diffraction analysis and SEM observation, it was shown that the subgrain refinement due to the formation of superfine martensite and an otherwise unidentified fine grained carbon compound in the heat affected zone (HAZ) resulted in the reduction of the fatigue crack growth rate. In the case of discharging duration of 140 ms, there was evidence of melting damage at the surface ahead of the notch of the sample due to the conversion of excessive electric energy to heating energy. In this study, an increase in microhardness and dislocation density was observed which was made linked to the enhanced fatigue resistance. However, there was no further explanation given on how the increased dislocation density can help improve the fatigue resistance. On the other hand, Zhao et al. [214] used 54 $\frac{MA}{m^2}$ at a pulse duration of 120 μs in order to retard fatigue crack growth in addition to the delay of fatigue crack initiation for CHWD steel, leading to a

reduction in crack propagation velocity by 1.9 times. From the optical microscopy observation, it was suggested that the superfine martensite and fine grain carbon compound formation was the reason behind the crack growth retardation. This observation was similar to that reported by Lin et al. [209]. Furthermore, an analytical study by Zhao-Long et al. [244] revealed that the average crack length decreased with the increase of magnetic field intensity.

2.10.5 Mechanism of electromagnetic treatment on fatigue crack repairing

The mechanisms by which electromagnetic treatment can lead to improvement in fatigue resistance have been the subject of several investigations. The main mechanisms that have been identified for fatigue enhancement can be classified as follows:

I. Crack healing [15, 207, 215, 224, 226],
II. Crack closure [207, 215],
III. Crack arrest [198, 245] and
IV. A variety of microstructural changes leading to enhanced yield strength and microhardness [209].

The beneficial effect of electromagnetic treatment on metal fatigue resistance can be related to the phenomenon of the natural concentration of current in the vicinity of a crack tip and to subsequent Joule heating at that location. Joule heating plays a key role in healing fatigue cracks [15, 207, 226]. In addition, as a result of Joule heating, the material in the vicinity of the crack tip expands permanently which leads to crack closure. Microscopic analysis has shown that due to electropulsing, the current density formed at the crack tip caused Joule heating to occur [218]. The heating led to melting around the crack tip and this enables the crack healing by crack shielding and bridging. This Joule heating can help retard crack growth as a result of sub-grain refinement in the circular/elliptic heat affected zone (HAZ) formed ahead of the notched tip [209]. Electropulsing has been shown to lead to fatigue crack arrest in UNS S 31600 stainless steel [198, 245]. The electron detour effect and Joule heating by

electropulsing treatment introduced an elliptical hole formed ahead of the crack tip. Local recrystallization occurred in fusion zone and heat affected zone (HAZ) around the crack tip, and around the radius of the curvature of the hole. The curvature of the hole along with thermal compressive stress led to fatigue crack arrest. Due to electropulsing, there was an enhancement in the yield strength and microhardness of the material. As a result, these improvements increased the resistance to plastic slip formation, and inevitably resisted crack initiation and propagation [209]. The enhancement of fatigue crack growth retardation by electromagnetic treatment can also be explained by other factors such as structure-phase states, the evolution of dislocation substructures and partial restoration of resource durability [228]. Furthermore, fatigue crack can also be repaired by local recrystallization, local homogenisation, refinement of grains around the crack tip [246, 247] and disappearance of slip bands [248].

Hosoi et al [15] presented a schematic illustration of the fatigue crack repairing process as shown in Figure 2.10.2 and the corresponding result on steel is shown in Figure 2.10.3. When high-density current flows around the fatigue crack surface, it causes a concentration of current at the crack tip (Figure 2.10.2(a)). This concentration of current causing Joule heating (Figure 2.10.2(b)) leads to rapid expansion of the area around the crack tip (figure 2.10.2(c)). However, the area away from the crack tip remains intact as there is no concentration of current. Eventually, the restricted expanded area along with its thermal compressive stresses triggers crack closure (Figure 2.10.2(d)). This further forms bonding between the crack surfaces near the crack tip due to energisation (Figure 2.10.2(e)). As a result, after several pulses of high-density electropulses the crack tip shifts to the opposite direction of the crack growth (see Figure 2.10.3).

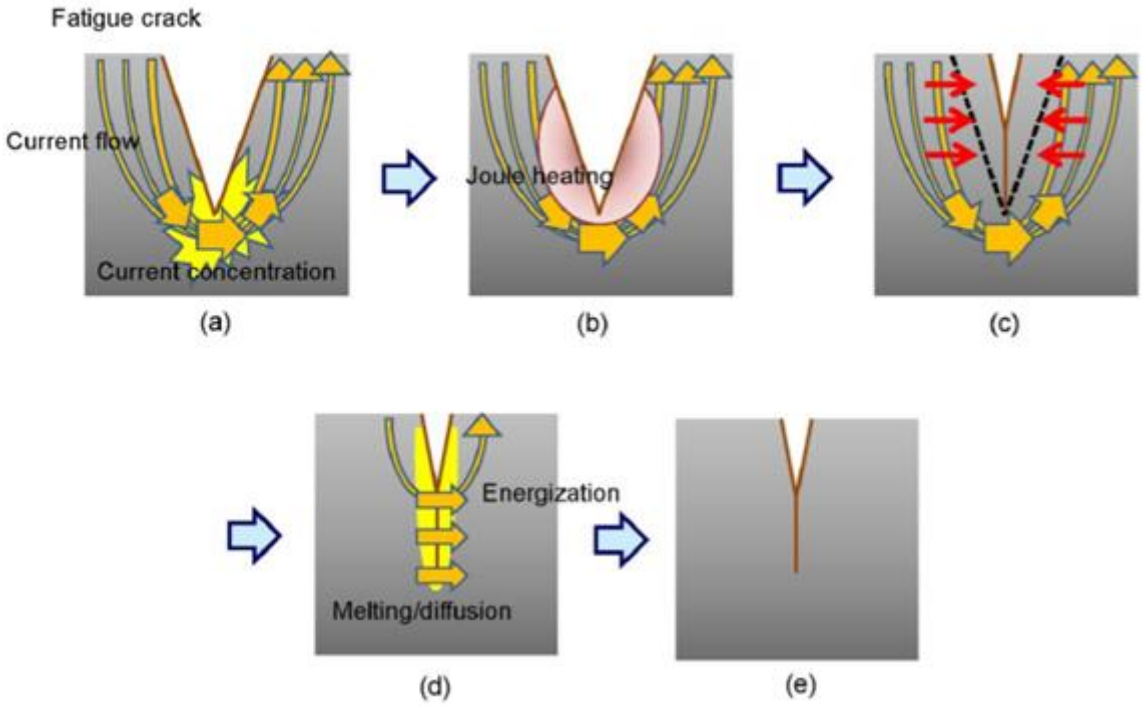

Figure 2.10.2 Schematic illustration of fatigue crack healing process due to electropulsing: (a) high-density current concentration, (b) Joule heating, (c) rapid expansion of crack faces in the vicinity of the crack tip, (d) crack closure and (e) bonding of the crack [15].

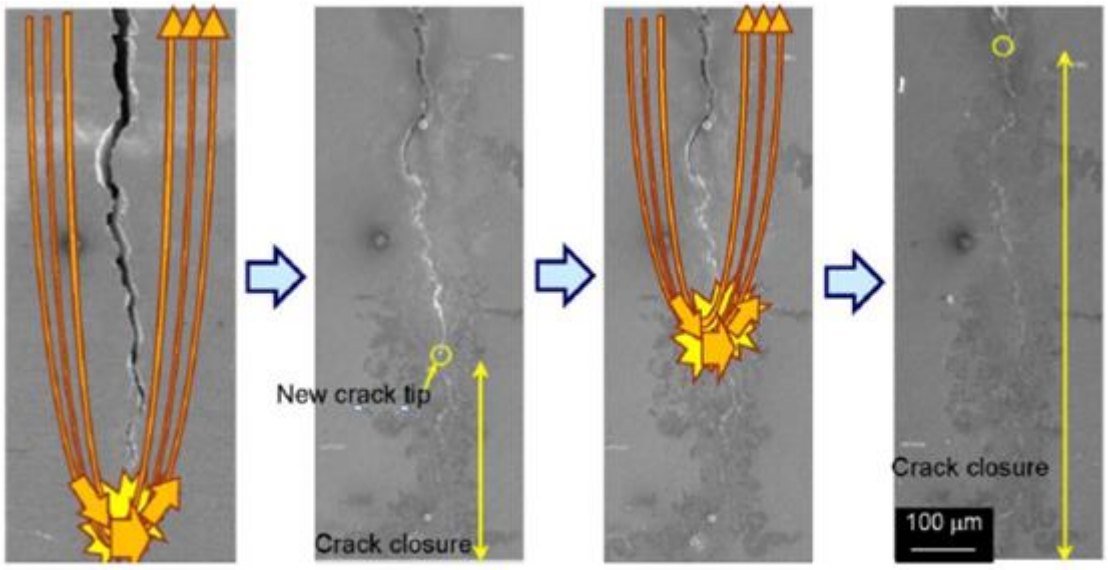

Figure 2.10.3 Progressive crack healing due to continued application of electropulsing [15].

This study [15], has shown that electropulsing can lead to both crack growth retardation and crack growth acceleration. In one experiment, electropulsing of 8 kA with 4 ms was applied for 20 times, and fatigue crack was grown at constant amplitude (CA) loading of stress intensity factor range, ΔK = $25MPa\sqrt{m}$ and load ratio, R=0.05. The crack growth rate decreased to $3.01 \times 10^{-8} \frac{m}{cycle}$ from 4.171×$10^{-8} \frac{m}{cycle}$ right after the application of the electropulsing. Then, crack growth gradually returned to the pre-electropulsing condition. However, when electropulsing of 6 kA of 2 ms was applied for 25 times and the fatigue crack was grown at constant amplitude (CA) loading of stress intensity factor range, ΔK = $15MPa\sqrt{m}$ and load ratio, R=0.05, the result was the opposite. After the application of electropulsing crack growth rate increased to $1.46 \times 10^{-8} \frac{m}{cycle}$ from 1.03×$10^{-8} \frac{m}{cycle}$ before it gradually reverted to the pre-electropulsing condition. Yang et al. [224] reported a quite similar process of crack healing by eddy current detouring due to eddy current treatment as shown in Figure 2.10.4. An additional mechanism is introduced here if compared to the previous one [15] which is the bridging in several areas between the crack surfaces due to a voltage breakdown effect [243].

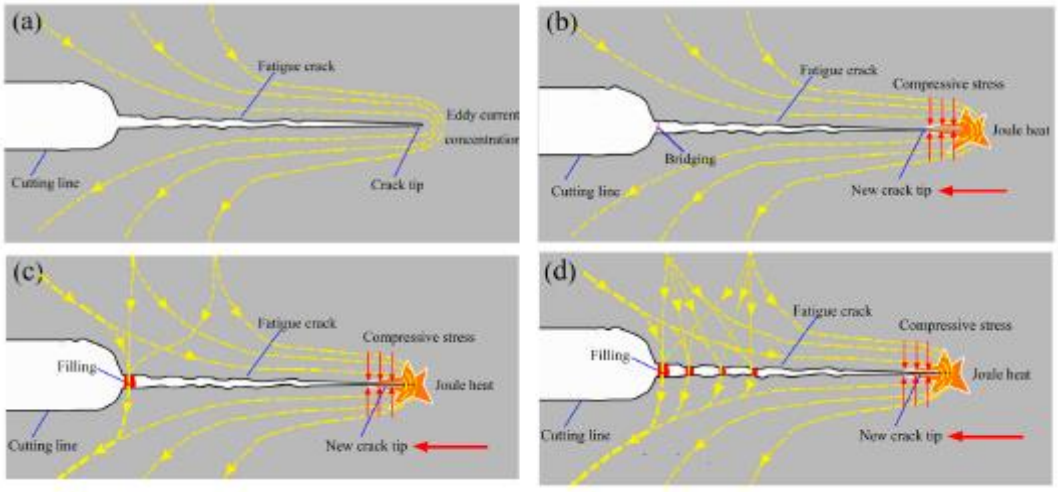

Figure 2.10.4 Schematic illustration of fatigue crack healing process due to eddy current treatment: (a) the detour of eddy current, concentration, (b) appearance of compressive stress and crack face bridging (c) appearance of voltage breakdown and the crack tip healing, (d) crack closure and (e) continuous crack healing [224].

Yang et al. [224] explained that the breakdown voltage (u) effect depended on the gap between been the crack surfaces and become more effective when the gap was lower. As a result, bridging was only found in the fatigue crack where there is less gap compared to the cutting line (slit) used to initiate fatigue crack. According to this study, thermal compressive stress aided reduction in the fatigue crack length. The same study has mentioned the 'skin effect' [249] which is explained as the penetration depth of the electric current increases higher with the intensity of the electric current in a conductor. This also contributes to the effectiveness of the fatigue crack repairing.

2.10.7. Threats and challenges in the electromagnetic treatment to enhance fatigue resistance

Despite the many positive impact of electromagnetic treatment (ET) outlined in this literature review, there are still concerns with regard to the correct treatment parameters that need to be addressed. Furthermore, the main question concerning many researchers in this field is:

- Does the application of an external magnetic or electric energy improve the fatigue of metals and alloys [199, 250, 251]?

While several investigations have indicated that ET can extend fatigue resistance, there is also evidence in the literature that detrimental effects are possible due to ET [13, 213, 218, 224, 225, 252]. The observation of adverse effects has been attributed by some researchers to the excessive time and level of ET intensity. while others have argued that exceeding a critical point during treatment can lead to microstructural damage and reduced fatigue life. Some studies have also shown that ET can only repair fatigue damage if the initial damage prior to the treatment does not exceed same critical level or the intensity of the treatment does not approach a certain "saturation limit" [16, 199, 225, 253]. There is also evidence that the treatment needs to reach a minimum level or threshold point [16, 225] before it starts to extend fatigue life. It is also important to know about the optimum level of treatment [16, 225] in order to maximise the fatigue life. Therefore, the real issue faced is to identify the ideal

parameters of treatment regarding type, intensity, time, number of applications and frequency, etc. for the optimisation of fatigue resistance of a given alloy.

There have been reports in the literature that have documented adverse effects of both magnetic field treatment and electropulsing on the fatigue life of metal alloys. For example, there was a reduction of 10 % in the fatigue life of low carbon steel specimens following magnetic field treatement [16]. The samples were exposed to a higher alternating magnetic field treatment at 3200 Gs for 20 $mins$. The explanation given was that excessive overheating took place by the resulting eddy currents which caused heavy oxidation leading to the deterioration of the fatigue properties of the material. There was also decrease in fatigue life of mild steel as the magnetic field increased [13]. In another study, electropulsing was applied to aluminium alloy 6061-T6 using a current density of 150 $\frac{A}{mm^2}$ [218]. This treatment led to the decline of fatigue life by 10 % which was caused by melting damage or thermal damage due to excessive current density. This study also indicated that at a higher maximum stress intensity factor, K_{max} of 0.91 $MPamm^{1/2}$, the current density of 90 $\frac{A}{mm^2}$ did not have any effect on fatigue life. The reason was given that the current density was not sufficient high enough to achieve melting.

Zhipend et al. [254] have reported that the effects of magnetic field treatment may be related to the field orientation. Applying a magnetic field perpendicular to the direction of maximum stress has the potential to release more residual stresses. Thus, this can be useful for fatigue life enhancement. The fatigue life has a minimum value when the magnetic field reached or exceeded the critical field strength and induced magnetic saturation as mentioned before. This behaviour has further led to crack tip plastic deformation which accelerated the fatigue crack growth and diffusion of carbon to the free surface for steel [13, 225]. This has caused surface defects and fatigue crack initiation. Levitin et al [216] have compared the direct current effect with electropulsing effect on fatigue resistance of titanium alloy and found no effect of direct current on fatigue life of titanium alloy.

Celik et al [199] found that prefatigue level has an substantial effect on the effectiveness of ET. The fatigue life of AISI 4041 steel did not improve when the magnetic field was applied between 60 % and 100 % of the untreated fatigue life in AISI 4041 steel. It was explained that when fatigue crack propagation plays the leading

role in controlling fatigue life in a notched specimen, there was no effect of the application of magnetic field treatment. Tang et al. [227] observed that by electropulsing at 43 % of fatigue crack initiation with 3 kA for 5 μs, there was only 6 % improvement in fatigue crack initial life. However, when it was applied at 85 % of the fatigue crack initiation life, there was 21 % improvement in the fatigue crack initiation life. In their work, the time of treatment plays an important role in improving the fatigue life. For instance, when an electropulsing treatment of 280 $\frac{MA}{m^2}$ was applied for a duration of 135 s instead of 70 s, the beneficial improvements of the fatigue life in titanium alloy were reversed. The study found that the fatigue life was reduced by 10 % due to the excessive time of treatment [217]. Hosoi et al. [15] showed that for a high number of electropulses crack acceleration took place. It was mention that electropulsing can lead to crack growth acceleration by inducing tensile residual stress around the crack tip [215]. No beneficial effect was observed on fatigue crack repairing when eddy currents were applied in the radial direction of fatigue crack as there was no eddy current detouring effect [224]. This observation indicated that the treatment works best when applied perpendicular to the crack defect within the material. All these results suggest that there is a need for controlling the ET parameters to achieve fatigue life enhancement.

The research works demonstrate that the increase in the magnitude of ET can introduce a desirable fatigue resistance in metals. However, very little research has been carried out which isolates variable parameters, such as the intensity of treatment, the number of treatment applications and the pre-treated conditions of the alloy. Isolating the variable parameters would establish how the factors and mechanisms within the ET change the properties of the metal. By varying the parameters associated with ET, a relationship between the variables and fatigue resistance may be derived to identify the optimal treatment parameters. Another factor not mentioned in literature that need to be consider are the alloys initial condition. Understanding if the treatment works best for alloys that are annealed, cold worked or pre-stressed are key points that must be considered when trying to determine the optimal treatment parameters.

2.10.6 Summary

In the light of the findings mentioned from this review, it seems that there are several types of electromagnetic treatment (ET) used and with varying parameters. The results have mainly shown beneficial effect of ET on fatigue properties of the metallic alloys. However, the problems now faced with ET is the understanding of the optimal treatment parameters, e.g. current density, pulse time, the number of applications of pulses, which will produce the maximum fatigue improvement of a given alloy. As mentioned in this review, excessive treatment can cause premature failure in fatigue life of the metallic alloy. Other factors such as treatment during the different stages of the fatigue life need to be taken into consideration as this may accelerate fatigue failure of the alloys. In terms of treatment for fatigue cracks, the orientation of the crack relative to the ET is crucial for achieving crack closure and crack retardation. There seems to be a maximum stress intensity factor, K_{max}, up to which ET can heal cracks. Consequently, a comprehensive investigation is required to understand fatigue damage that occurs due to excessive treatment intensity. Furthermore, a reliable correlation is needed to be established between fatigue resistance and microstructural characterisation, microhardness, thermodynamics, residual stress, dislocation density, etc. due to ET. Isolation of different parameters is also required to investigating individual parameter effect along with the specific mechanism of fatigue resistance related to it. Hence, this review can be considered as a stepping stone for summarising the different treatment parameters, its effect on several stages of fatigue life and the changes in the materials characteristics.

3 Research Strategy

The aims of this PhD project are to further understand and develop capability of fatigue crack growth assessment and fatigue life enhancement of engineering aluminium alloys. To achieve these aims, a research strategy has been taken in consideration which will be discussed in this chapter. The purpose of the chapter is to give the reader a brief view of the research method used. Furthermore, the feasibility and rationality of the research methods is highlighted. The more detailed technical aspects including the experimental setup, construction of the models and analytical analyses are explained in their corresponding chapters.

3.1 Flowchart of research strategy

A research strategy was adopted to conduct a series of investigations based on the coordinated experimental, numerical and analytical approaches as shown in the flowchart (Figure 3.1.1). A brief description of these approaches is given in the following sections.

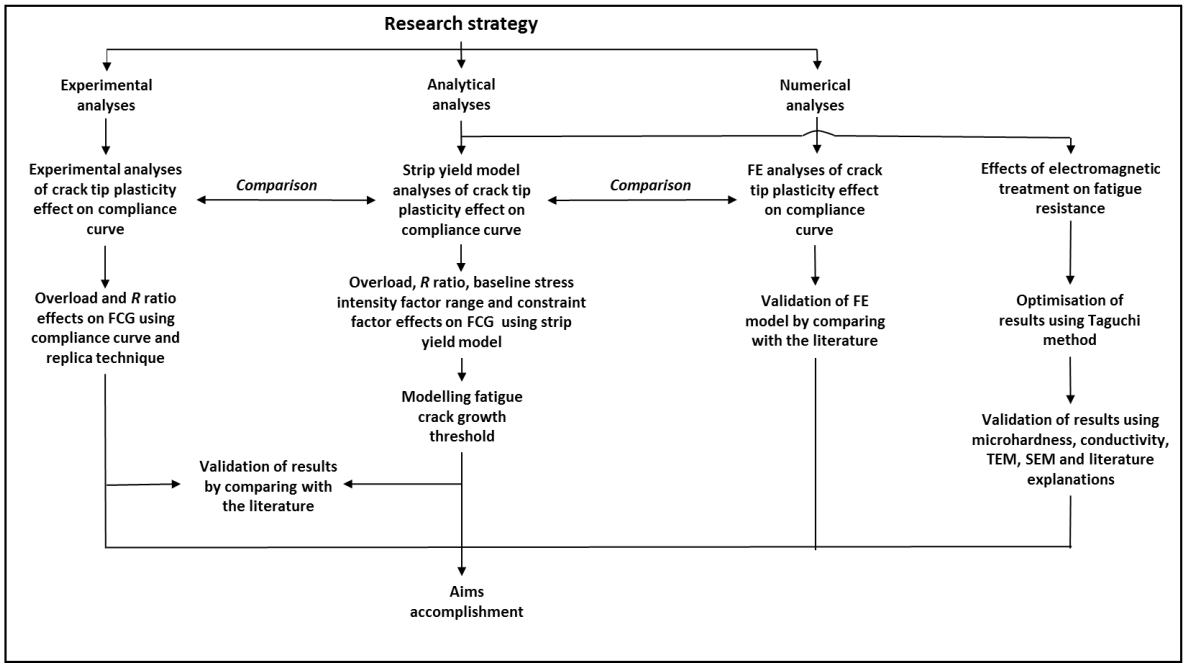

Figure 3.1.1. Flowchart of research strategy used for this project.

3.2 Analytical approach

From the literature review, it can be seen that overload can lead to fatigue crack growth retardation. The plasticity induced crack closure (PICC) can be used to rationalise the overload transient fatigue crack growth behaviour. The reliability of plasticity induced crack closure (PICC) depends on the accuracy of the crack closure measurement. Loading and geometrical effects can also control the PICC. Furthermore, the fatigue crack growth threshold, ΔK_{th} can influence the overall estimation of fatigue crack growth life.

The first purpose of the analytical approach was to investigate fatigue crack growth under variable amplitude (VA) loading using the strip yield model. To achieve this, only one-quarter of the centre cracked tension (CCT) specimen was considered. The nonlinearity of the compliance curve without the fatigue crack growth was investigated and compared with the experimental and numerical results using the material properties of aluminium alloy 6082-T6. The crack profiles, overload ratio (OLR), R ratio, baseline stress intensity factor range, $(\Delta K)_{BL}$, and constrain factor, α, effects were also investigated using the material properties of aluminium alloy 2024-T4. These results were further validated by comparing them with the literature. FORTRAN code was developed to perform strip yield modelling for this purpose.

Secondly, an analytical model was optimised to identify the fatigue crack growth threshold, ΔK_{th}, of different aluminium alloys including aluminium alloy 2024-T3, aluminium alloy 2024-T351 and aluminium alloy 7075-T6. Here, different experimental databases were used to fit the analytical fatigue crack growth curves. Finally, the obtained analytical fatigue crack growth threshold, ΔK_{th}, values were compared with the literature in order to provide the validation. Matlab was used to write and run the code of the model.

3.3 Experimental approach

One of the purposes of the experimental approach was to investigate the fatigue crack growth behaviour under variable amplitude (VA) loading. For that, the effect of plastic deformation on the compliance curve based crack closure measurements were analysed. Overload ratio (OLR) and R ratio effects on fatigue crack growth were also analysed. In this study, a servo-hydraulic fatigue test machine along with strain gauges, PicoScope, plastic replica and microscope were used. The replica technique was utilised to measure the crack during fatigue loading. The crack length from the plastic replica was measured under a microscope. The crack closure was measured using the compliance technique. These compliance curves were obtained from the strain gauge measurement around the fatigue crack tip. Centre cracked tension (CCT) specimens of aluminium alloy 6082-T651 were chosen for these analyses which were designed using CATIA V6 and manufactured using the machining and fabrication lab facilities at the university. These were prepared from metal sheet. The samples were also polished when required. The results obtained were compared with the numerical results and also with the literature where necessary to validate it.

The other purpose of the experimental study was to investigate the beneficial effect of electromagnetic treatment (ET) on fatigue resistance. For this, the samples were prepared by designing of the samples using CATIA V6, manufacturing using computer numerical control (CNC) machine, and polishing using the rotating polishing rig. Some of the parts of the ET rig including the specimen holder embedded in the circuit of ET rig were also designed and manufactured. The ET was conducted using that ET rig along with a voltage generator built at the university. Fatigue tests were conducted using a rotating bending fatigue machine. Aluminium alloy 2011-T6 and 2014-T6 were chosen as the materials for hourglass-shaped samples. These were prepared from the bar materials. The fatigue life of the treated and untreated samples were compared to establish the increase in fatigue life due to ET. The Taguchi method was used to optimise the treatment parameters including pulsed electromagnetic treatment intensity, pulse time and the number of pulses based on the experimental results. Here, Minitab 17.0 software was used to implement the Taguchi method. A baseline stress vs number of cycles (S-N) curve was also generated for the untreated samples of aluminium alloy 2014-T6 in order to make it comparable with the fatigue life of the

treated samples for different stress ranges. The microhardness test rig and conductivity measurement device were also utilised to measure the microhardness and conductivity of the samples, respectively before and after the treatment. The reason behind this was to correlate the effect of the electromagnetic treatment with the microstructural and physical characteristics of the material. The fracture surfaces of the treated and untreated alloy were studied using SEM. The mechanisms of electromagnetic treatment in aluminium alloy 2014-T6 were investigate using TEM technique in order to understand the enhanced fatigue performance of this alloy.

3.4 Numerical approach

The purpose of the numerical approach was to analyse the crack tip plastic deformation effect on compliance-based crack closure measurement. Finite element (FE) based numerical analysis was performed using commercial-off-the-shelf (COTS) software Ansys 16.0. Only one-quarter of the centre cracked tension (CCT) specimen of the material properties of aluminium alloy 6082-T6 was utilised for the FE modelling. Mesh density studies were performed and the model was built using the options which are comparable to the literature. Finally, the FE results were compared with the experimental and analytical results in order to validate them.

4 Experimental analysis of fatigue crack growth under constant amplitude and variable amplitude loading

4.1 Introduction

The overload effect, R ratio effect and crack closure effect on fatigue crack growth have already been explained in lthe iterature review. The aim of this chapter is to investigate experimentally the crack closure effect, overload effect and R ratio effect on aluminium alloy 6082-T6. Here, the overload effects with OLRs of 1.3, 1.6 and 2.1 were taken into consideration at R=0.1. The overloads were applied for fatigue cracks of different length. Additionally, the effect of stress ratio on the fatigue crack growth at constant K_{max} condition were also investigated at R ratios of 0.1, 0.4 and 0.7. The crack closure effect during constant amplitude (CA) loading and variable amplitude (VA) loading was also analysed. Two types of technique were utilised during the experimental analysis; the replica technique to monitor crack growth and the compliance technique to measure crack closure.

4.2 Material selection

The fatigue crack growth test was carried out on a centre cracked tension (CCT) specimen. The material chosen was aluminium alloy 6082-T6 which is a solution heat treated and artificially aged automotive grade alloy. The chemical composition and material properties of this alloy are shown in Tables 4.2.1 and 4.2.2.

Table 4.2.1 Chemical composition of aluminium alloy 6082-T6 [315].

AL	Mn	Fe	Mg	Si	Cu	Zn	Ti	Cr	Other (Each)	Others (Total)
Balance	0.4-1.0	0.0-0.5	0.6-1.2	0.7-1.3	0.0-0.1	0.0-0.2	0.0-0.1	0.0-0.25	0.0-0.05	0.15

Table 4.2.2 Material properties of Aluminium alloy 6082-T6 [315].

Density	$2.7\frac{g}{cm^3}$
Melting Point	555°C
Thermal Expansion	$24 \times 10^{-6}\ K^{-1}$
Thermal Conductivity	$180\ \frac{W}{m.K}$
Electric Resistivity	$0.038\ \times 10^{-6}\ \Omega.m$
Ultimate Tensile Strength	$310\ MPa$
Yield Strength	$268\ MPa$
Young's Modulus	$71\ GPa$

Due to its high strength, aluminium ally 6082-T6 is replacing aluminium alloy 6061-T6 [255]. It has good weldability, machinability [255] and corrosion resistance [256]. Typical use of this alloy is in highly stressed applications such as truss, bridge and transport applications [256].

4.3 Methodology

4.3.1 Specimen geometrical details

The fatigue crack growth test was carried out on a centre cracked tension (CCT) specimen. The specimen was 400 mm in length, 150 mm in width and 1.6 mm in thickness. A photograph of the saple is shown in Figure 4.3.1.

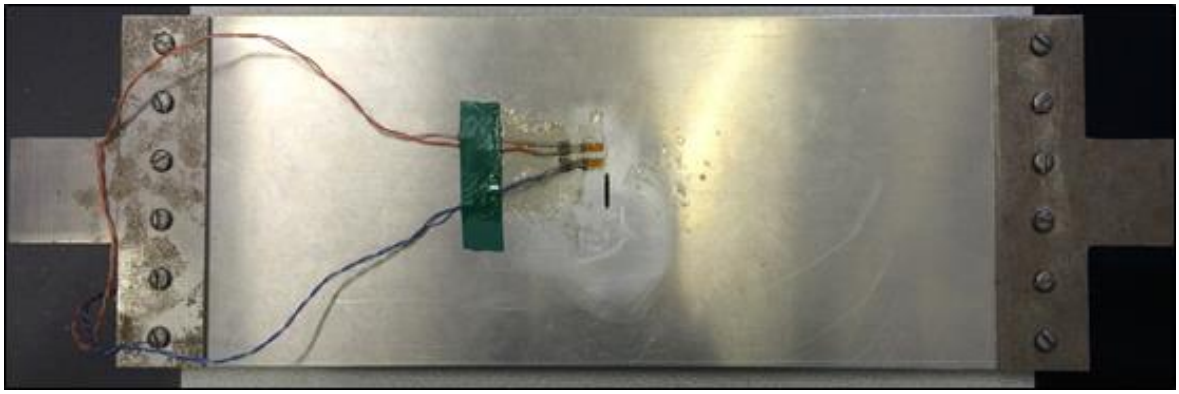

Figure 4.3.1 The test sample with steel clamps.

The length was taken in the longitudinal direction. This is also known as the rolling direction or extrusion direction or axis of forging. A 16 mm slit representing an initial crack was introduced with L-T (longitudinal-Transverse) fracture path [257] and 45° notch angle. The thickness of the slit was 2 mm. There were six holes of 6 mm diameter at each end with 20 mm offset from the edge to attach the specimen with the clamp. This clamp was able to withstand the fatigue loading without damaging the CCT sample.

4.3.2 Fatigue crack growth test setup

A hydraulic fatigue machine (Servotest 200) was used to run the fatigue crack growth test. The actual view of the set-up is shown in Figure 4.3.2 and the schematic view is shown in Figure 4.3.3.

Figure 4.3.2 Actual test set-up.

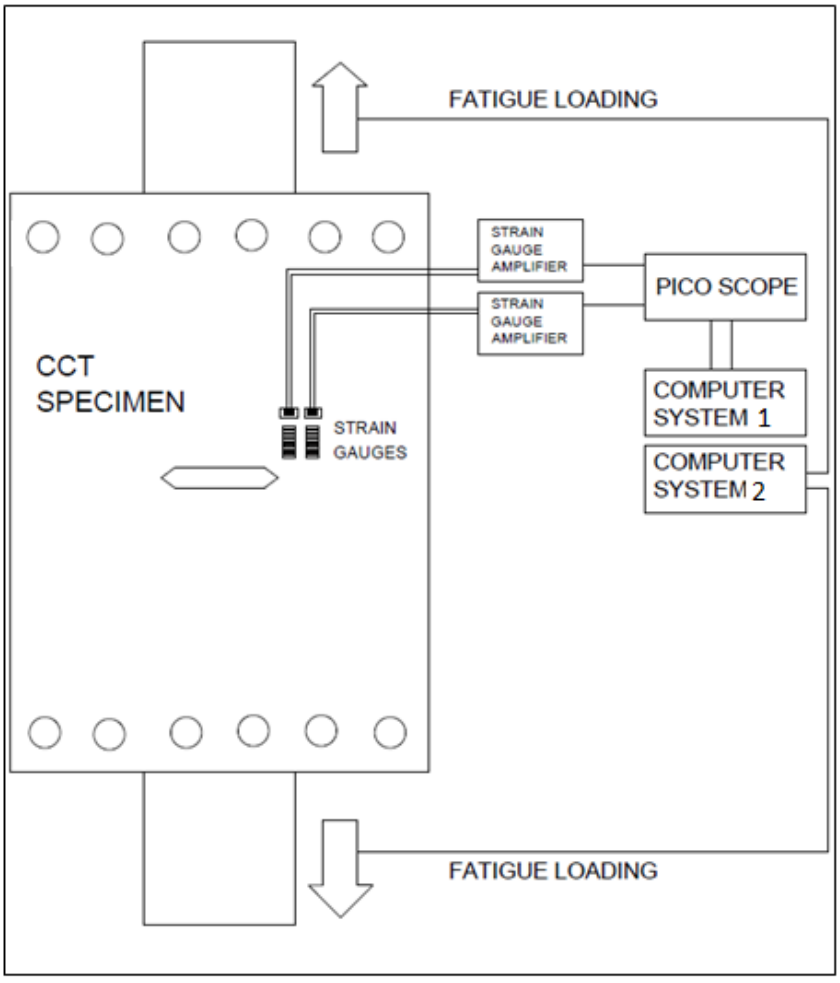

Figure 4.3.3 Schematic diagram of fatigue crack growth test set up.

The clamped sample was installed within the grip of the fatigue test machine. The gripping force was controlled so that the grip was sufficient to hold but not to damage the sample. The fatigue load spectrum was generated and controlled using the MTS software (MTS 793) in the computer system 2. Mode I loading (Figure 4.3.3) was applied during the test. Two strain gauges were installed to measure the strain near the crack tip and these were connected with computer system 1 through a strain gauge amplifier and PicoScope. The strain gauges and nearby wires were protected by the plastic glue and tape to avoid any damage caused during the test. It is to be noted here that 5 Hz cyclic loading was used in this test.

4.3.3 Fatigue crack growth monitoring

To monitor crack growth, the crack length was measured using the replica technique. The fatigue crack grew during the test, and the test was paused periodically to measure the crack length. The surface of the plastic replica was dipped into acetone and quickly pressed onto the crack tip area for a couple of minutes. Then, the plastic replica was removed and measured under a conventional travelling microscope. Figure 4.3.4 shows the plastic replicas and a microscope, which were used to measure crack length.

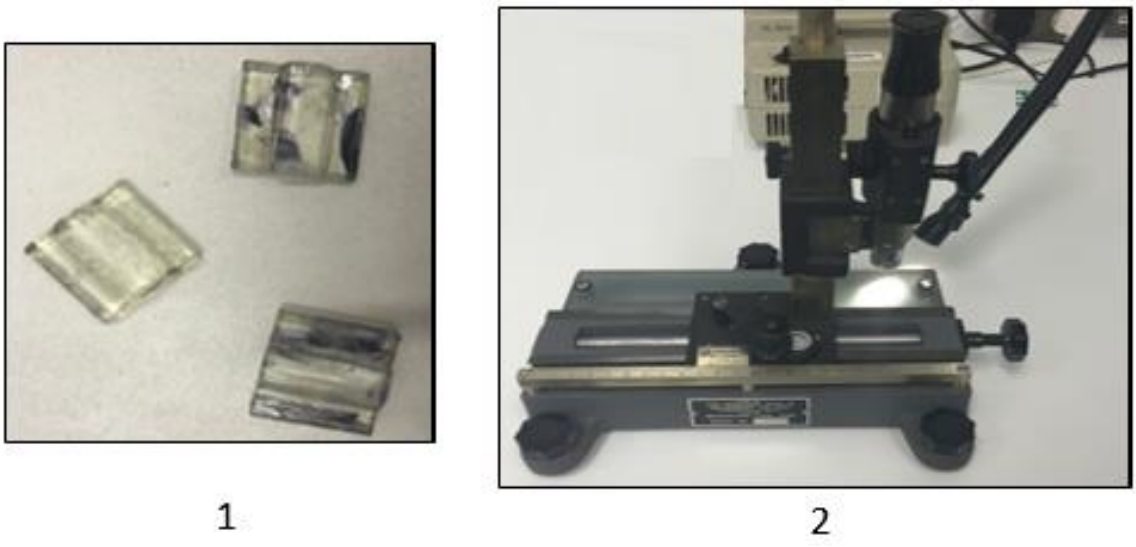

Figure 4.3.4 (1) Plastic replicas and (2) microscope to measure crack length.

During the measurement, the sample was kept under low tension so that the crack tip was open and copied onto the plastic replica surface. The advantage of measuring the crack with this technique is that it gives an accurate representation of the physical crack length, which can then be measured under a microscope.

Another technique known as the compliance technique was also implemented to monitor crack closure. In this case, the crack growth test was paused, and the crack was loaded and unloaded between the minimum and maximum fatigue load. The loading and corresponding strain values were used to obtain the compliance curve. The schematic view and actual view of the compliance curve and corresponding offset compliance curve are given below in Figures 4.3.5 and 4.3.6. The offset compliance curve was recorded as an offset value from a straight line fit to the upper part of the compliance curve. The offset method which is recommended by ASTM E647 [172] can improve the sensitivity of the non-linearity of the compliance curve. The closure point, P_{op} was identified as the point when the linear line becomes non-linear as shown in figure 4.3.5(2).

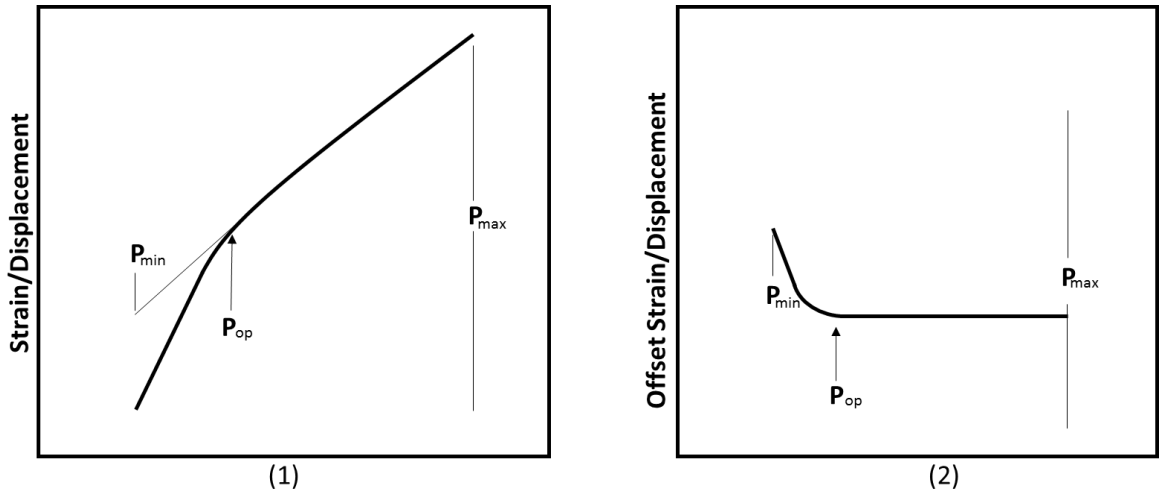

Figure 4.3.5 Schematic view of (1) Compliance curve and corresponding (2) offset compliance curve.

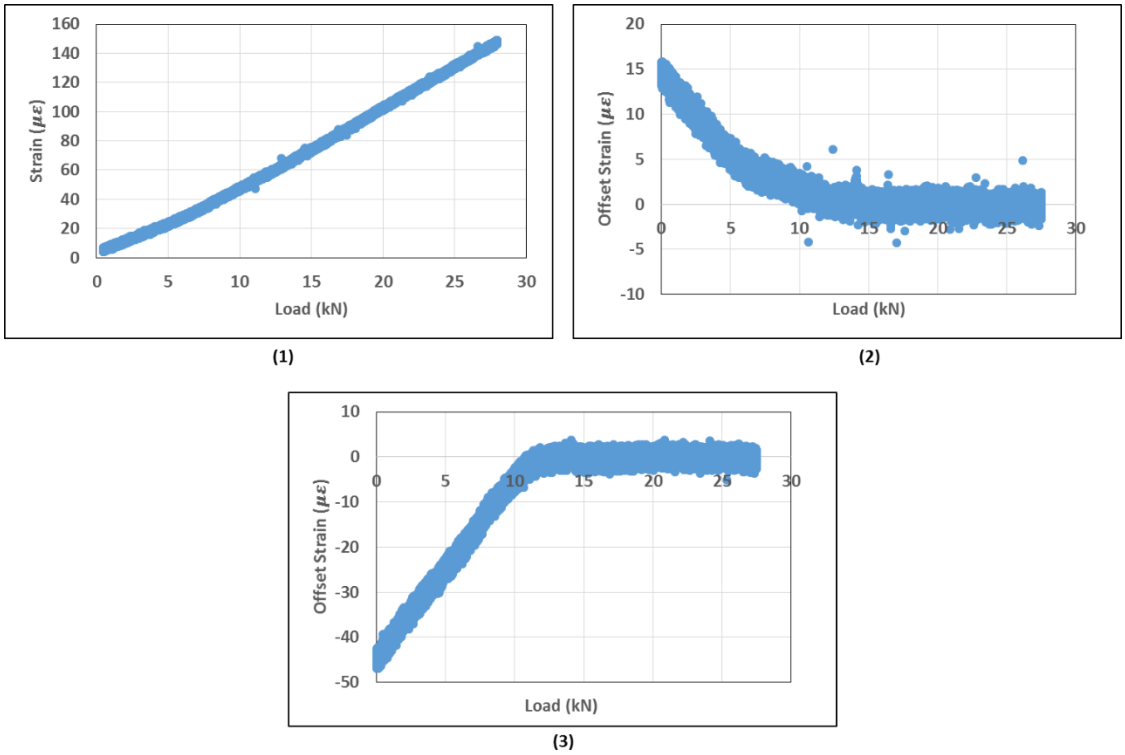

Figure 4.3.6 (1) Compliance curve from strain gauge near the crack tip, (2) offset compliance curve from strain gauge ahead of the crack tip and (3) offset compliance curve from strain gauge behind the crack tip.

4.3.4 Load spectrum used

There were three different types of load spectrum used for fatigue crack growth analysis under variable amplitude (VA) loading as shown in Figure 4.3.7. Fatigue crack growth tests were run with constant amplitude (CA) baseline fatigue load incorporated with overloads. For the investigation of overload effect, different overload cycles with overload of 30 %, 50 % and 100 % (calculated using Equation 2.6.1) were applied during the fatigue crack growth test at load ratio, R=0.1 of the CA baseline fatigue loading with P_{max}=15.03 kN and P_{min}=1.5 kN. For 30 % overload, the maximum level of the overload was P_{OL}=19.54 kN. For 50 % and 100 % overload, the maximum levels of the overload cycles were P_{OL}=22.54 kN and P_{OL}=30.05 kN, respectively. Hence, the corresponding load ratios (OLRs) are 1.3, 1.6 and 2.1 (calculated using Equation 2.4.7), respectively.

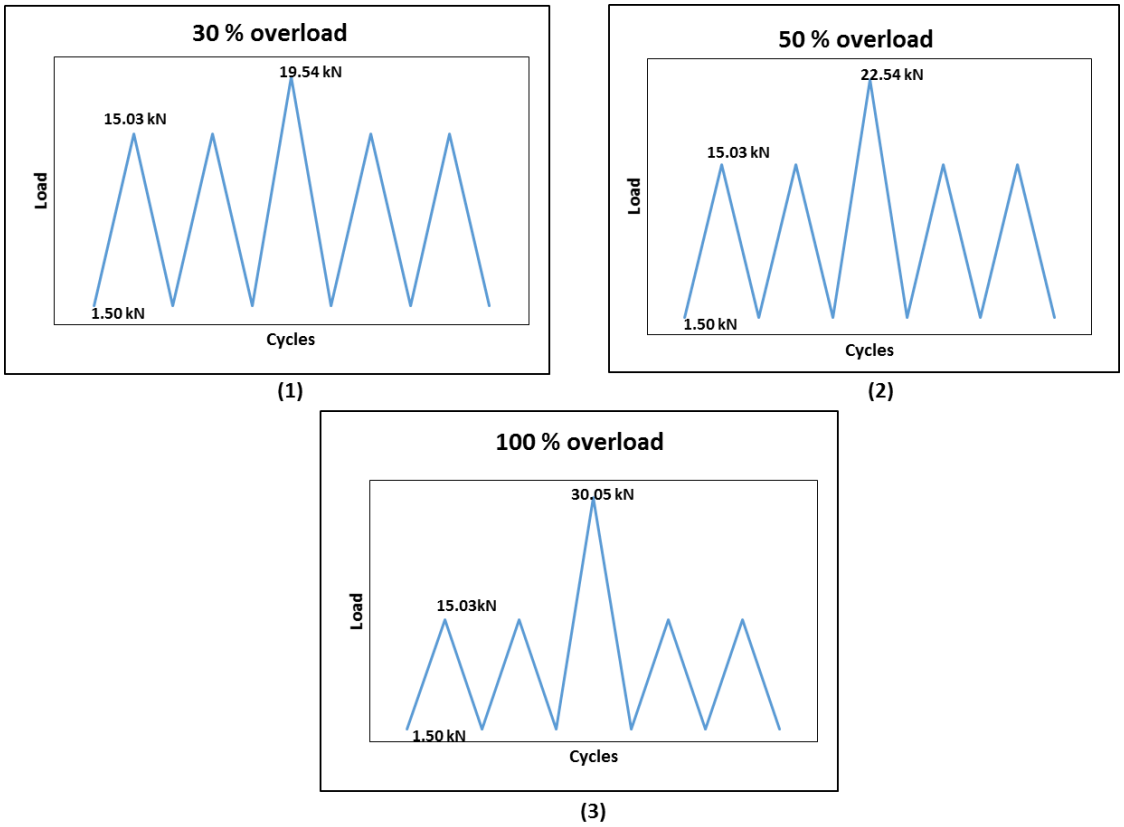

Figure 4.3.7 Load spectrum for (1) 30 % overload, (2) 50 % overload and (3) 100 % overload.

For analysis of the baseline R ratio effect, there were three load spectrum used as shown in Figure 4.3.8. Three different R values were used during CA loading; these were 0.1, 0.4 and 0.7. In this instance, to consider the different load ratio effect, the maximum load was kept unaltered, but the minimum load was changed to a nominal value of 1.5 kN, 6.01 kN and 10.52 kN to achieve a load ratio, R of 0.1, 0.4 and 0.7, respectively.

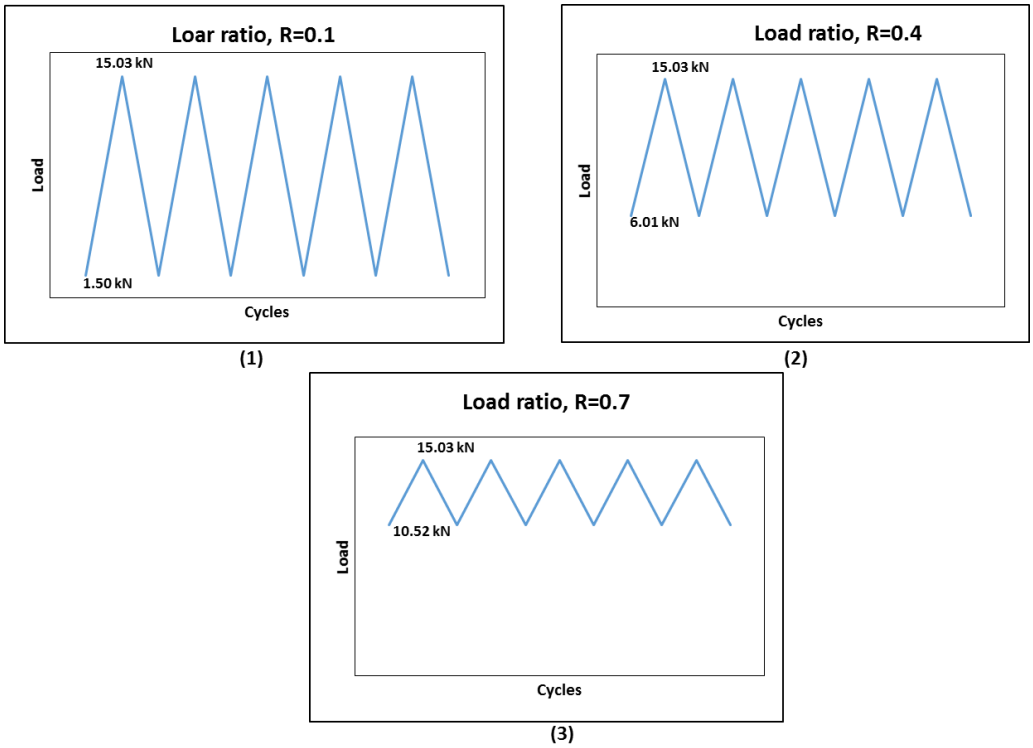

Figure 4.3.8 Load spectrum for (1) R=0.1, (2) R=0.4 and (3) R=0.7.

4.4 Results and analyses

4.4.1 Crack growth retardation under single overloads

The single overload effect was investigated by applying different level of overloads incorporated with constant amplitude (CA) loading. Graphs of crack length vs number of cycles are plotted accordingly in Figure 4.4.1.

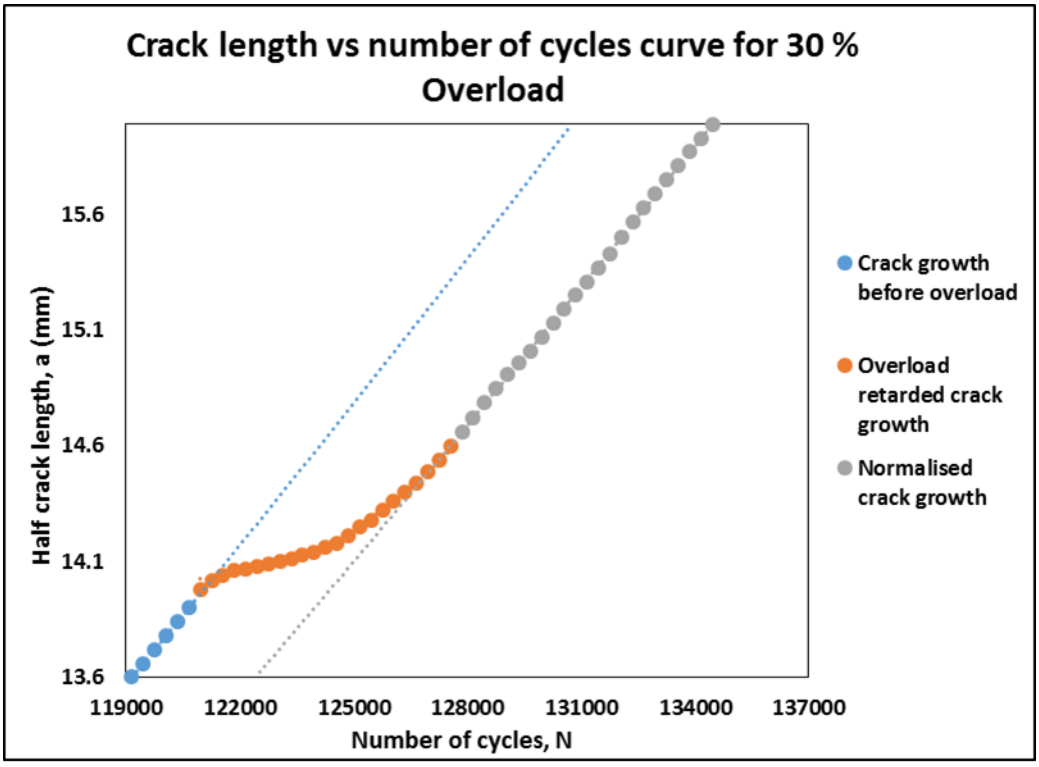
Crack length vs number of cycles curve for 30 % Overload
Half crack length, a (mm)
15.6
15.1
14.6
14.1
13.6
119000
122000
125000
128000
131000
134000
137000
Number of cycles, N
Crack growth before overload
Overload retarded crack growth
Normalised crack growth

(a)

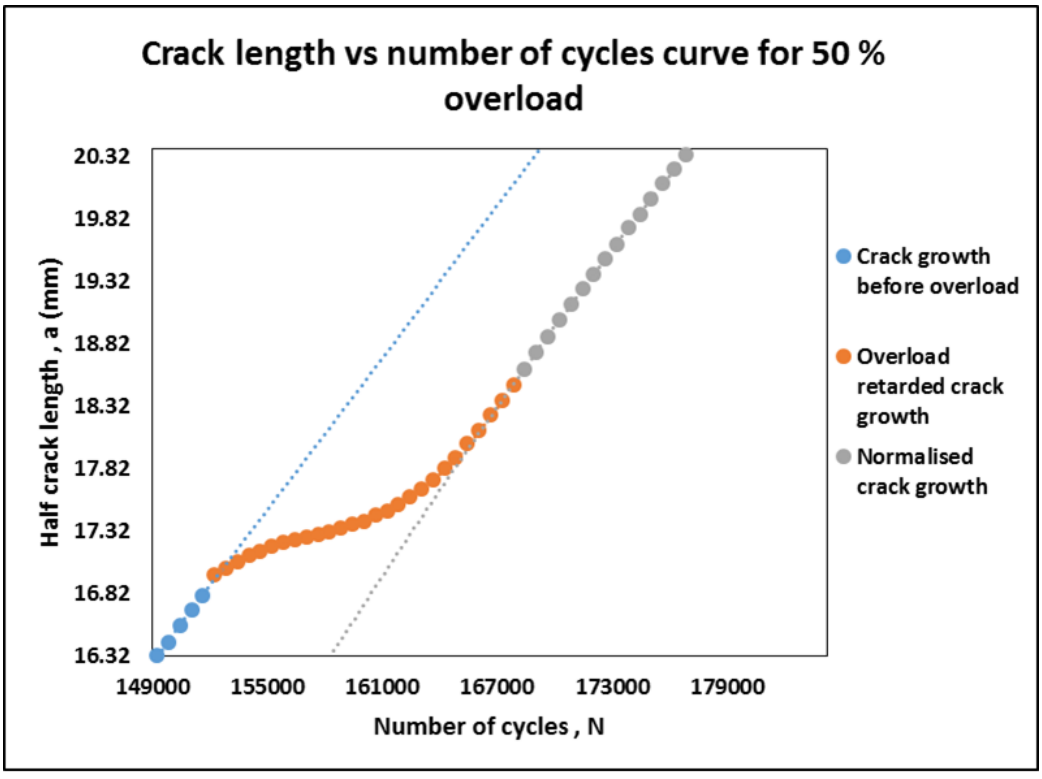
Crack length vs number of cycles curve for 50 % overload
Half crack length , a (mm)
20.32
19.82
19.32
18.82
18.32
17.82
17.32
16.82
16.32
149000
155000
161000
167000
173000
179000
Number of cycles , N
Crack growth before overload
Overload retarded crack growth
Normalised crack growth

(b)

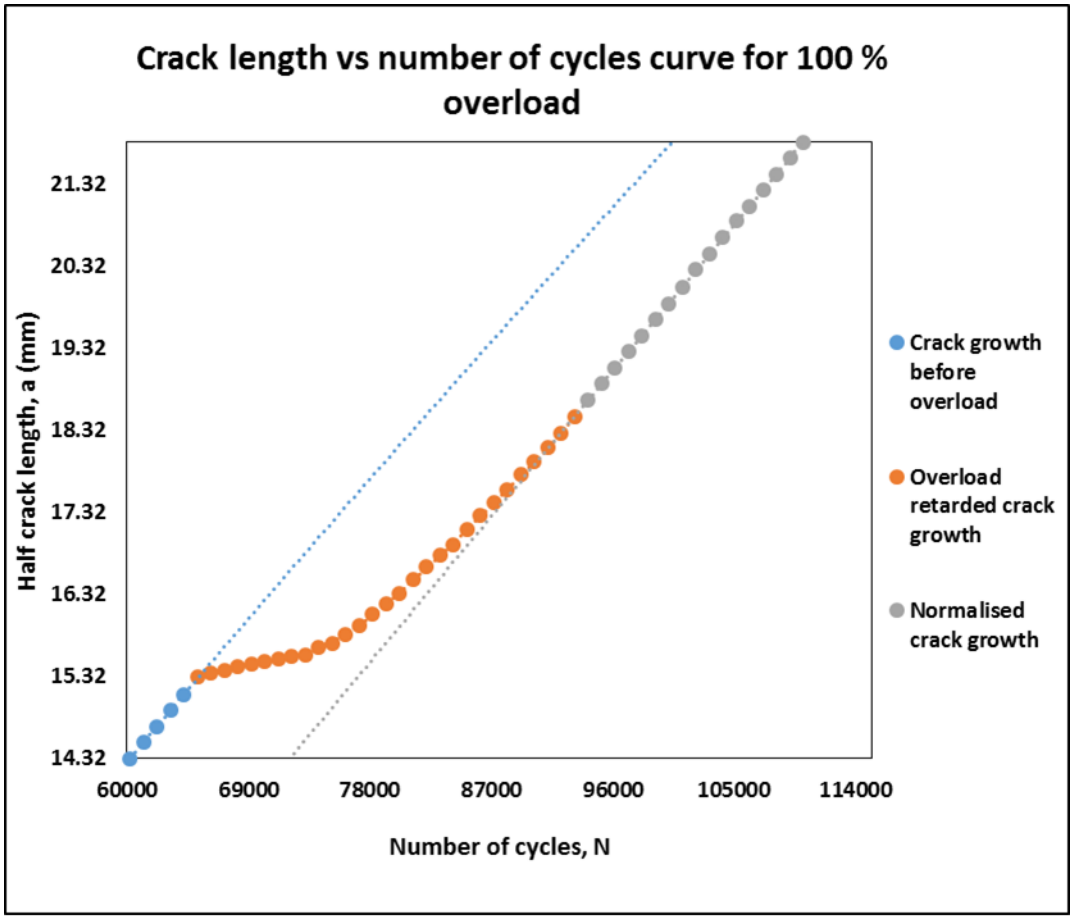

(c)

Figure 4.4.1 Half crack length vs number of cycles curves: (1) for 30 % overload, (2) for 50 % overload and (3) for 100 % overload.

From figure 4.4.1(1), it was observed that for a CCT specimen of aluminium alloy 6082-T6, when the fatigue cycles were 119157, the half-crack length was 13.6 mm. The fatigue crack grew steadily upto a length of 13.9 mm for 120957 cycles before a 30 % overload was applied. After the application of the 30 % overload, there was a retardation of fatigue crack growth for some period of cycles, and then it returned to the pre-overload fatigue crack growth at a length of 14.6 mm at 127557 cycles. The stress intensity factor range, ΔK was 19.8 $MPa\sqrt{m}$ in this case. Due to this overload effect, the delay distance, a_D was 0.7 mm and number of delay cycles N_D was 11492 cycles. These, a_D and N_D are defined later in Figure 4.5.1.

From Figure 4.4.1(2), It is seen that the fatigue crack grew steadily from 16.32 mm at 14972 cycles to 16.8 mm at 151672 cycles in the same sample. After application of an

overload of 50 %, the crack growth was retarded until it reached 18.56 mm at 168172 cycles. Then, the crack growth returned to a similar trend of preoverload fatigue crack growth. Here, the stress intensity factor range, ΔK was 23.04 $MPa\sqrt{m}$. For a 50 % overload, the a_D was 0.86 mm and the N_D was 20000 cycles.

In Figure 4.4.1(3), for a different CCT sample of aluminium alloy 6082-T6, crack growth started steadily from 14.32 mm at 60203 cycles and it continued growing in the similar fashion before the overload of 100 % was applied when the crack length was 15.1mm at 64203 cycles. After the application of the overload there was retardation in fatigue crack growth, and then the crack growth returned to the trend of pre-overload fatigue crack growth when the crack length was 18.49 mm at 93203 cycles. Here, the stress intensity factor range, ΔK was 31.27 $MPa\sqrt{m}$ as the crack length within this sample was diffent from the previous one. For this 100 % overload, the a_D was 3.18 mm and the N_D was 40500 cycles.

4.4.2 Overload ratio (OLR) effect on fatigue crack growth

The overload ratio (OLR) effect in terms of % OL on fatigue crack growth rate is shown in Figure 4.4.2. Here, 30 % OL, 50 % OL and 100 % OL correspond to OLRs of 1.3, 1.6 and 2.1, respectively.

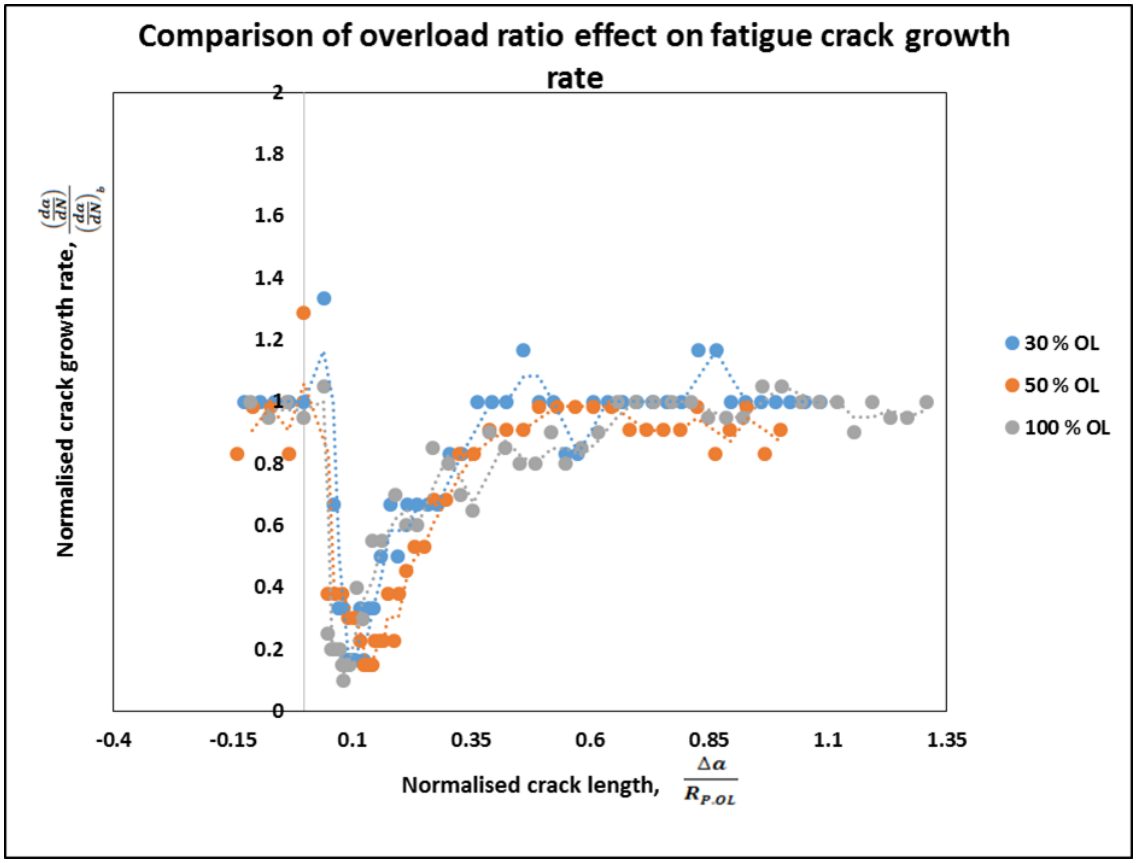

Figure 4.4.2 Comparison of overload ratio effect on fatigue crack growth rate.

The crack growth rate, $\frac{da}{dN}$ was normalised by the baseline crack growth rate at CA loading, $\left(\frac{da}{dN}\right)_b$. The crack length increment, Δa was normalised by the overload plastic zone size, $R_{P.OL}$ at the crack tip. In every case, the fatigue crack was growing steadily before the overload was applied. When the overload was applied, there was an instant acceleration for a small period followed by a prolonged retardation period. Finally, the fatigue crack growth rate normalised to the baseline fatigue crack growth rate. For a 30 % overload, the maximum retardation in fatigue crack growth was reached at 10 % of the overload plastic zone, and the retardation period finished at 36 % of the overload plastic zone. For a 50 % overload, the maximum retardation in fatigue crack growth reached at 14 % of the overload plastic zone, and retardation period finished at 50 % of the overload plastic zone. Finally, for a 100 % overload, the maximum retardation point and retardation length were 8 % and 67 % of the plastic zone, respectively. In the experimental study of [63], the maximum retardation point was between 4-42 % of

overload plastic zone size. The magnitude of the retardation in fatigue crack growth increased with the increase of OLRs.

4.4.3 Overload ratio (OLR) effect on fatigue crack growth driving force

The overload ratio (OLR) effect was analysed on effective fatigue crack growth driving force, ΔK_{eff} which was identified using the offset compliance method [172] (Figure 4.3.5(2)) and normalised by the fatigue crack growth driving force of the constant amplitude (CA) loading, $(\Delta K)_b$ and shown in Figure 4.4.3. In this study, the fatigue crack crack length increment Δa, was normalised by the overload plastic zone size, $R_{P.OL}$. The crack closure concept was taken into consideration to identify the crack growth driving force. It can be seen that the fatigue crack growth driving force followed the same trend as the fatigue crack growth rate. The crack growth driving force was nearly constant during CA loading before overload was applied. After the overload, there was prolonged retardation following a temporary acceleration in the fatigue crack growth driving force. Eventually, the fatigue crack growth driving force returned to the pre-overload crack growth driving force level when the OLR effect was over. The maximum retardation points were 15 %, 12 % and 10 % of the overload plastic zone size for 30 %, 50 % and 100 % OL, respectively. The retardation lengths were 41 %, 53 % and 66 % of overload plastic zone size. The magnitude of the retardation in fatigue crack growth driving force increased with the increase of OLR.

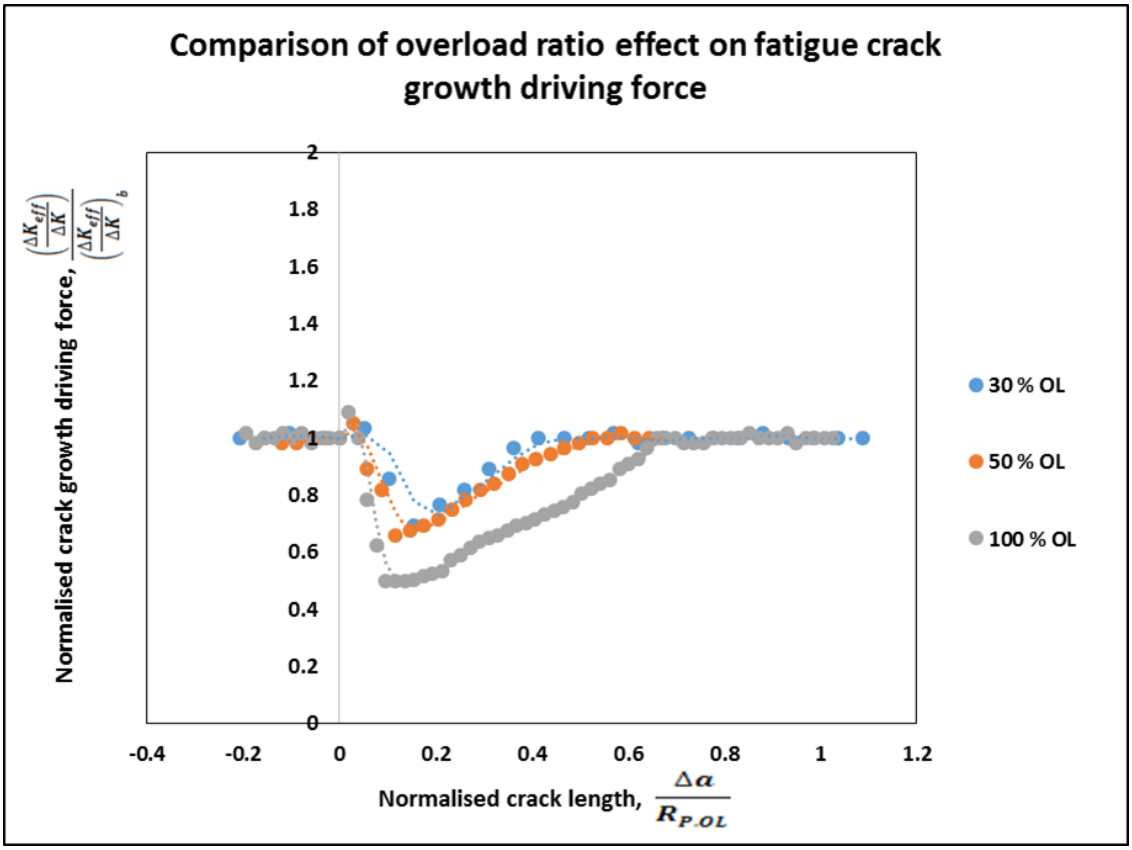

Figure 4.4.3 Comparison of overload ratio effect on fatigue crack growth driving force.

4.4.4 R ratio effect on fatigue crack growth rate

To investigate the R ratio effect, fatigue crack growth tests were run with R ratios of 0.1, 0.4 and 0.7 at constant K_{max} condition in a CCT specimen of aluminium alloy 6082-T6. The crack grew from 19.55 mm to 20.8 mm at R=0.1, from 20.8 mm to 21.65 mm at R=0.4 and from 21.65 mm to 21.9 mm at R=0.7. The corresponding log-log plots of crack growth rate, $\frac{da}{dN}$ vs. stress intensity factor range, ΔK are shown in Figure 4.4.4. It was observed that with the increase of R, the crack growth rate data shifted to the left. This observation is consistent with earlier results by [258]. Therefore, the crack growth rate reduced as the R ratio increased. This may appear to contradict findings in literature where crack growth rates are increased at higher R ratios [259]. It should, however, worth noting that the current crack growth test is conducted under fixed K_{max}. The higher R ratio is achieved by the increase of K_{min}, which effectively reduces the stress intensity factor range, ΔK. As such, the reduction in the crack

growth rate is caused by the reduction of the stress intensity factor range, not the conventional increase of the R ratio.

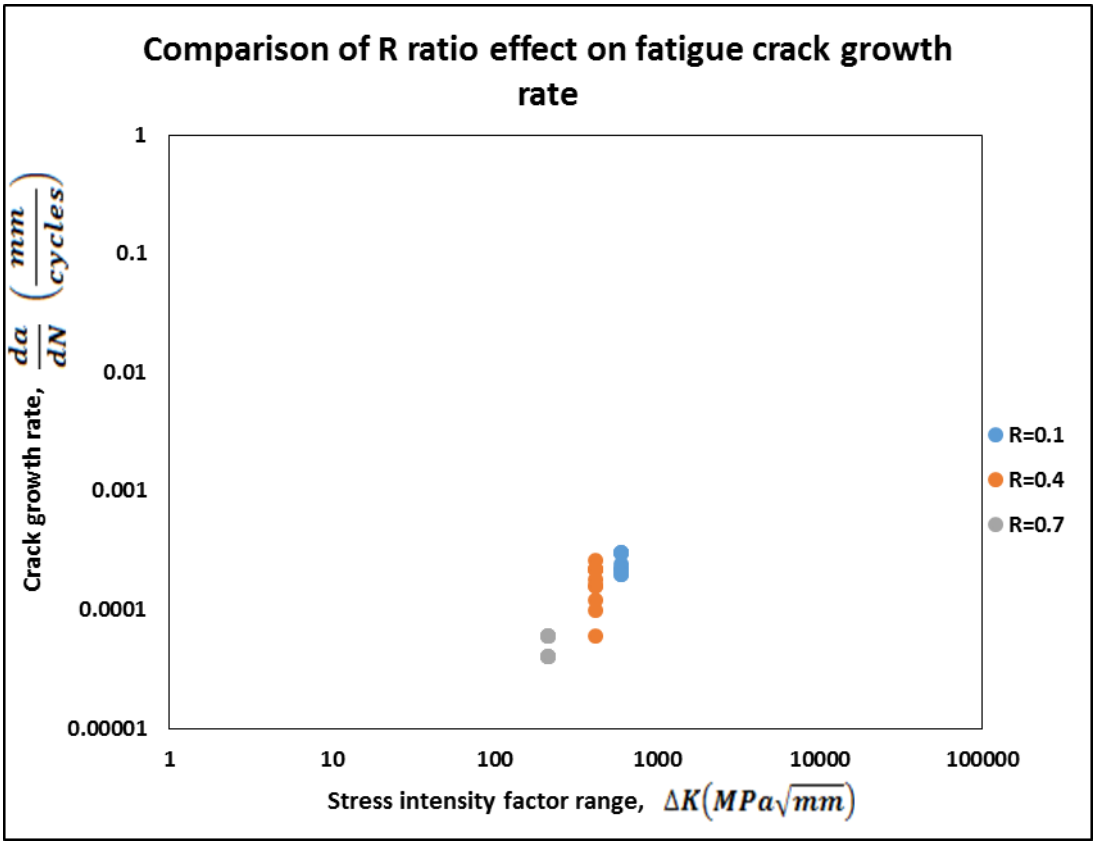

Figure 4.4.4 Comparison of R ratio effect on fatigue crack growth rate (all plots are in log-log scale).

4.4.5 Crack closure effect on crack growth rate for different R ratio

The crack closure effect was considered to explain the R ratio effect. This also explained the necessity of the crack closure effect on fatigue crack growth. The corresponding log-log plot of crack growth rate, $\frac{da}{dN}$ vs effective stress intensity factor range, ΔK_{eff}, was shown in Figure 4.4.5. By considering the crack closure for R ratio values of 0.1, 0.4 and 0.7, the effective stress intensity factor range ratio, U, became 0.56, 0.67 and 1, respectively. So, the crack growth rate both for R=0.1 and R=0.4 shifted to the left with a lower factor of 0.56 and higher factor of 0.67, respectively and

got closer to the crack growth rate data for R=0.7. The distance between these two crack growth rate data of R=0.1 and 0.4 also decreased. The crack growth rate data for R=0.7, did not move because there was no crack closure effect. If the data of Figure 4.4.4 and Figure 4.4.5 are compared, then all three crack growth rate data for the effective stress intensity factor range were closer to each other, than the three crack growth rate data for the stress intensity factor range without considering the effect of crack closure. Therefore, the R ratio effect can be explained by the crack closure effect and the crack growth rate data contained less scattering when the effective stress intensity factor range was considered.

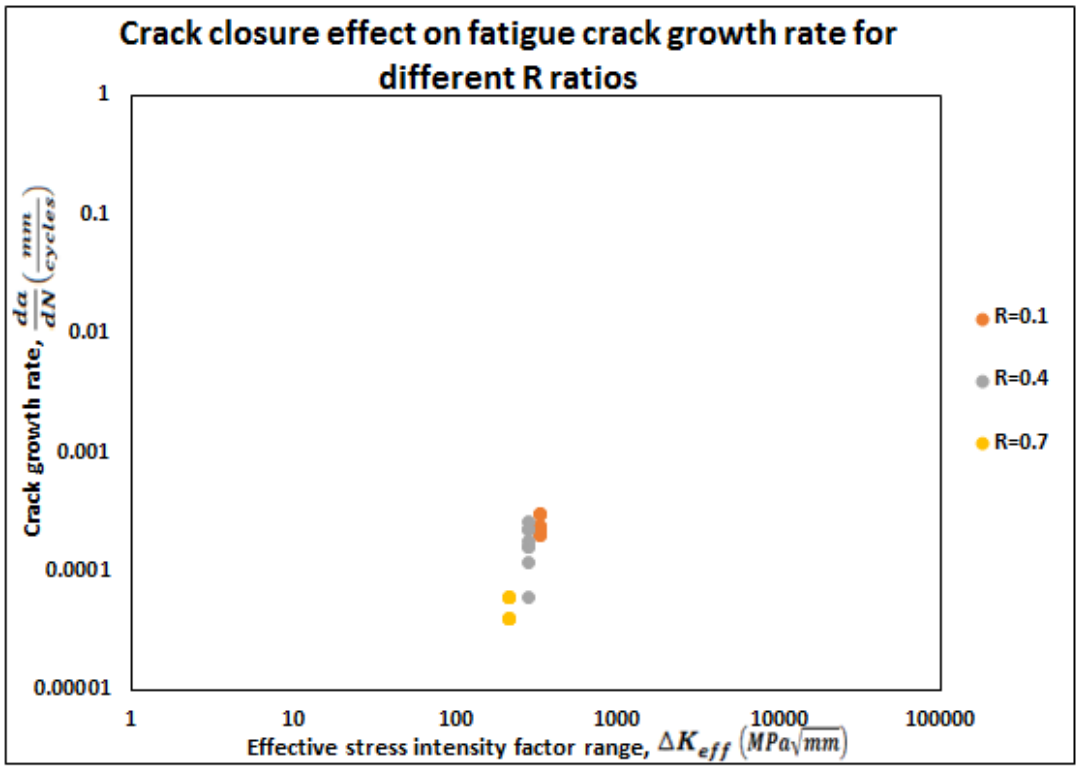

Figure 4.4.5 Crack closure effect on fatigue crack growth rate for different R ratios in log-log scale.

4.5 Discussion

From the replica technique of crack growth monitoring, it was clear that fatigue cracks propagated steadily during constant amplitude (CA) loading. Then, there was an acceleration of fatigue crack growth right after the overload. An overload retardation period was observed afterwards. Finally, the crack growth returned to the same rate as in the preoverload crack growth period. This type of transient overload effect was also overserved in other studies [62-66]. The delay distance, a_D and number of delay cycles, N_D also increased with the OLR as suggested in other research work [63]. The delay distance, a_D and number of delay cycles, N_D are defined in Figure 4.5.1. The crack closure measurement using compliance curve also suggested the same trend of transient overload effect. Here, crack growth driving force reduced due to the enhanced crack closure after the overload. Therefore, crack closure can be used to explain the overload effect.

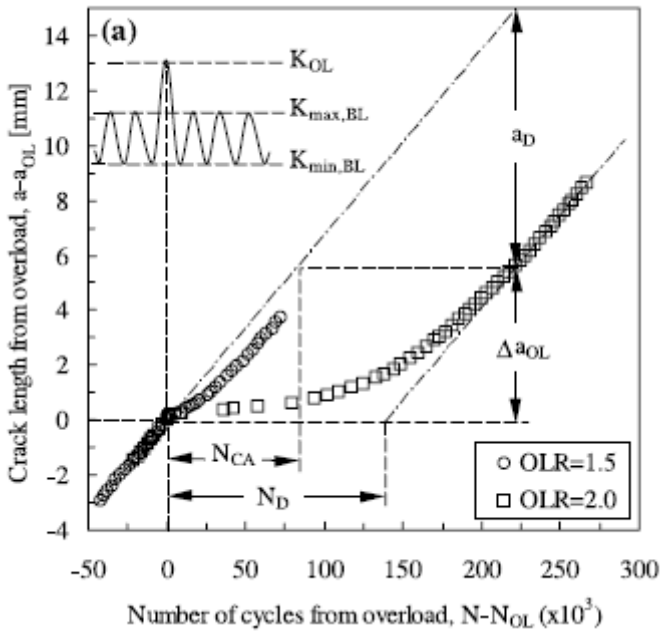

Figure 4.5.1 Showing the delay distance, a_D and the number of delay cycles, N_D due to overload effect [63].

From both the replica technique and the compliance technique, it can be seen that with the increase of the overload ratios (OLRs), the magnitude and extent of crack growth retardation increased. This change in crack growth retardation due to OLR effect was also found in another study in the same material (aluminium alloy 6082-T6) [63]. The retardation distance for all three OLRs including 1.3, 1.6 and 2.1, were less than one overload plastic zone size. According to the Wheeler model [8, 57, 74] the crack growth retardation is within the fraction of the overload plastic zone. When the current plastic zone size reaches the edge of the overload plastic zone, crack growth retardation ends. The post-overload crack length increment for maximum crack growth retardation (known as 'delayed retardation' [81]) can be found between one eighth to one quarter of the overload plastic zone as suggested by [81, 112]. However, it was also found between 6-42 % of the overload plastic zone size [63] as mentioned before. In this study, the delayed retardation varied between 8-15 % of the overload plastic zone size.

The crack growth rate data shifted to the left with the increase of the R ranging from 0.1, 0.4 and 0.7 when the stress intensity factor range, ΔK, was considered. However, when the effective stress intensity factor range, ΔK_{eff}, was taken into account based on crack closure effect, there was a shift of the crack growth rate data to the left. Crack growth rate data for the R of 0.1 and 0.4 shifted to the left and nearly merged together with the crack growth rate data of R=0.7 at constant K_{max} condition. As a result, the scattering of the crack growth rate data reduced when effective stress intensity factor range, ΔK_{eff} was considered. It is clear that R ratio effect can be explained by the crack closure effect as suggested by other research work [33, 64, 260, 261]. There was no sign of crack closure when the crack was propagated at stress ratio of 0.7. Experimental effective stress intensity factor range ratios, U for R of 0.1 and 0.4 are quite consistent with the Elber model [78], the Shijve model [80] and the ASTM model [172, 262] as shown in figure 4.5.2. In these models, U is a function of R which is obtained from experimental fatigue crack growth data of aluminium alloy 2023-T3, however, these models can be extended to other materials as well. For example, [262] used these models to obtain U for P355NL1 steel. Therefore, in this study, the comparison of the experimental U for aluminium alloy 6082-T6 with these models is also valid.

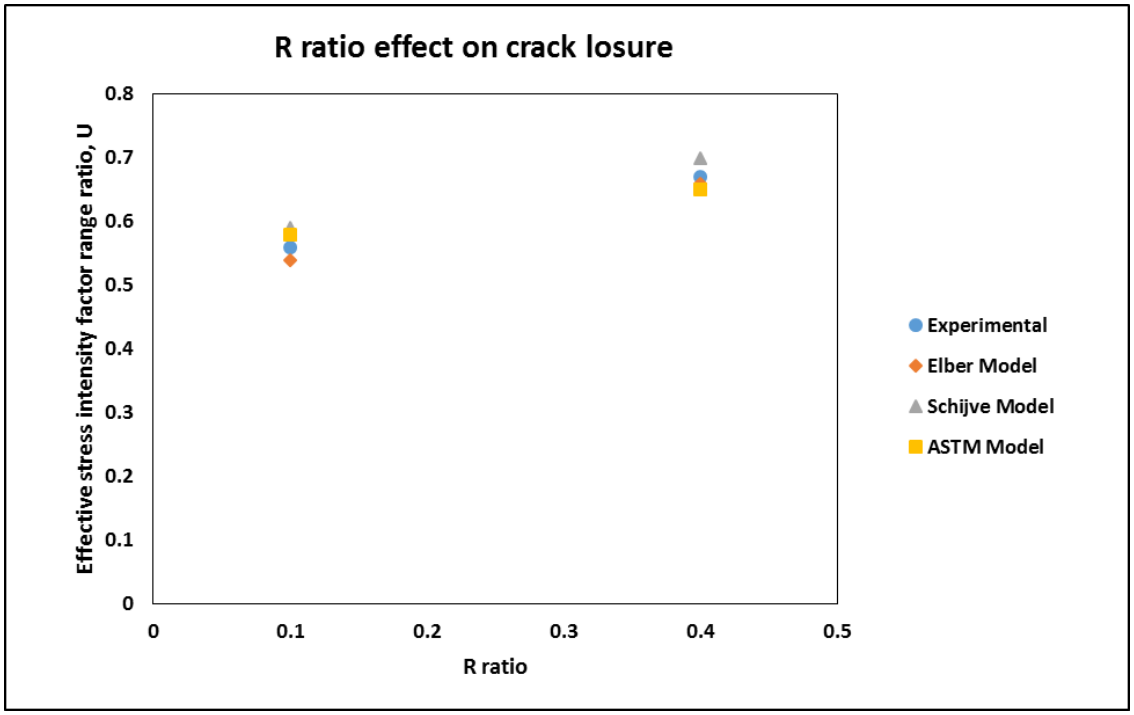

Figure 4.5.2 Comparison of R ratio effect on crack closure for different aluminium alloys.

4.6 Summary

From the experimental analysis, it is clear that the application of the overload retards the crack growth rate. The retardation can be measured by both the replica and the compliance technique. The magnitude and distance of the overload affected zone increased with the increase of overload ratio (OLR). With the increase of R, the crack growth rate data shifted to the left. However, the crack growth rate data merged together when the effective stress intensity factor range was taken into account. As a result, the R-ratio effect can be explained by the crack closure effect. In conclusion, these experimental results will certainly help with the development of new knowledge and understanding of underpinning damage tolerance design (DTD).

5 Analytical analysis of fatigue crack growth driving force under constant amplitude (CA) and variable amplitude (VA) loading

5.1 Introduction

The plasticity induced crack closure (PICC) and its effects on fatigue crack growth driving force under CA and VA loading are explained in detail in the literature review. While there have been many experimental analyses on crack closure under fatigue loading, there have been comparatively lower analytical studies on this area. The development of an accurate analytical model coupled with experimental investigation is highly desirable as it will make prediction of the fatigue crack growth behaviour both cost and time effective.

Various researchers have developed analytical models to investigate crack closure phenomena [83, 263-265]. These are mostly generated by modifying Dugdale's 'strip-yield' model [86]. The modelling of the propagation of the crack into the crack tip plastic zone and the formation of a plastic wake on the crack faces due to this propagation are the basis of these. These models are helpful to understand near-tip crack behaviour in detail. These strip yield based models mostly analyse crack closure in the plane stress condition. However, crack closure in the plane strain condition has also been analysed by this type of model [83, 266] after consideration of the effect of stress state on plastic deformation. FASTRAN code [167], which is based on the 'strip-yield' model, has been developed using 'constraint factor' in order to represent the three-dimensional crack closure effect when considering plane stress and plane strain conditions.

In this chapter, a modified strip-yield model with FORTRAN coding was used and run by Simply Fortran 2 to investigate PICC. It will help understand the fatigue crack growth driving force in detail under CA and VA loading through detailed simulation of the crack opening profile and the contact stress distribution. Xu [9] developed this model based on the physical and mechanical behaviour of centre cracked tension (CCT) samples and validated it with the experimental studies. It has already been used to investigate near-tip crack behaviour and the overload effect in various studies for specific loading conditions [9, 24, 62, 265, 267]. In the present study, this model was

investigated further under various loading conditions. Crack closure and the corresponding stress distributions around the crack tip for different crack lengths have also been investigated.

There is a great demand for reliable assessments of fatigue crack closure under different loading conditions in fatigue research [133, 268, 269]. To fulfil this, a detailed investigation of crack closure and corresponding fatigue crack growth driving forces have been investigated in this chapter using the analytical technique. The properties of aluminium alloy 2024-T351 were considered here. The analysis was performed mainly in the plane stress condition. Constant ΔK loading was selected for this analysis. The strip-yield model was first explained. Near-tip crack behaviour during fatigue crack growth was then evaluated. The overload effect, stress ratio (R-ratio) effect, baseline stress intensity factor range effect and geometrical constraint factor, α effect on fatigue crack growth driving force were also assessed under different loading conditions.

5.2 Methodology

5.2.1 Model Construction

The strip-yield model is based on a modified Dugdale model [86]. It is used to simulate crack closure of a centre cracked tension (CCT) specimen under fatigue loading. Aluminium alloy 2024-T351 was used for this purpose. The length and width of the specimen were 300 mm and 150 mm. Initial crack length was 40 mm. The Young's modulus, yield strength and ultimate strength of the material were 70 GPa, 372 MPa and 483 MPa, respectively. Figure 5.2.1 shows the schematic view of the model.

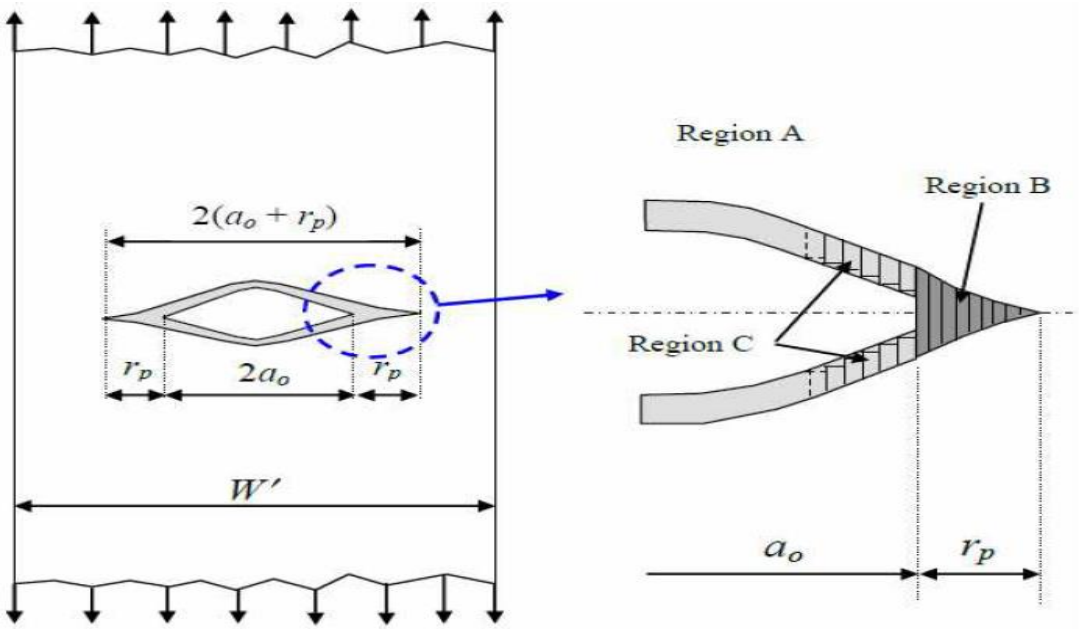

Figure 5.2.1 Schematic view of strip-yield model [62].

This model (Figure 5.2.1) consists of 3 regions including a fictitious crack, $2(a_0+r_p)$, where, a_0 is the half crack length and r_p is the plastic zone size ahead of the crack tip.

1. Region A is the linear elastic region with the Young's modulus of E,
2. Region B is the area of length, r_p ahead of the physical crack tip and
3. Region C is the plastically deformed area along the crack surfaces behind the physical crack tip.

In this model, the plastic zone and the crack surface displacement are obtained by superposition of two tensile stresses: (i) the remote uniform tensile stress, σ_∞, and (ii) the contact stress, σ_i, on a segment of the crack surface as shown in Figure 5.2.2. The segment stress, σ_i, is basically caused by premature contact due to the residual plastically deformed material behind the crack tip, and crack surface roughness and oxide debris (especially at the near-threshold regime).

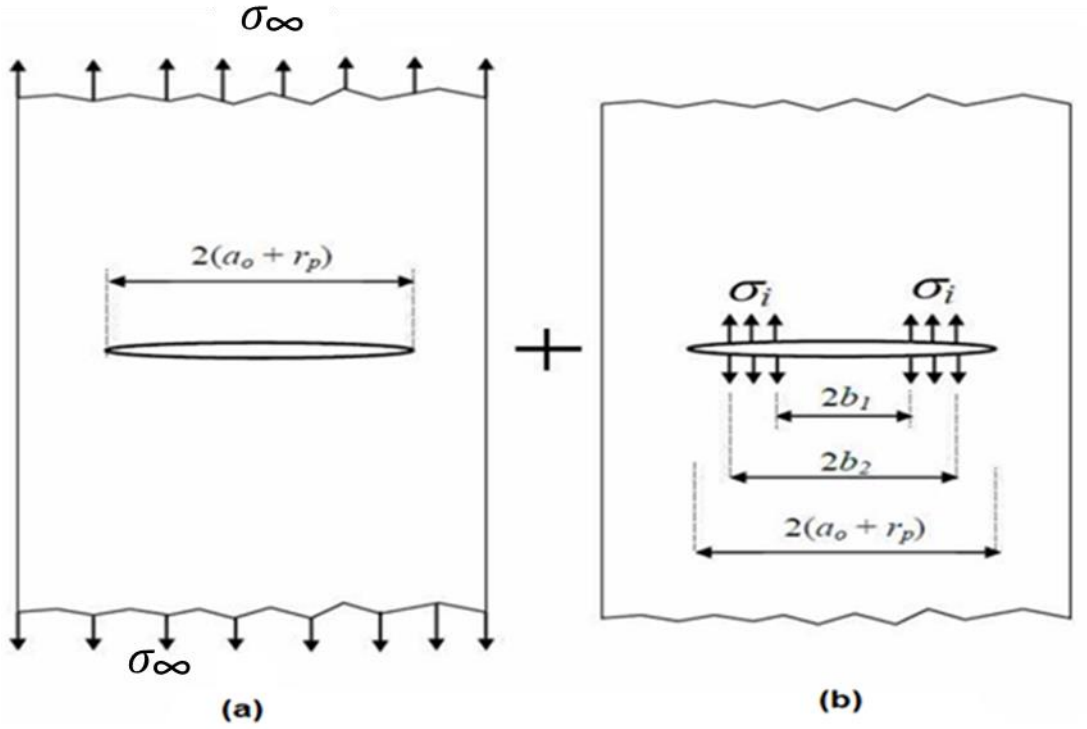

Figure 5.2.2 Superposition of two tensile stresses: (a) remote uniform tensile stress, $\boldsymbol{\sigma}_\infty$ and (b) uniform stress, $\boldsymbol{\sigma}_i$ on a segment of the crack surface [62].

Region B consists of up to 40 elastic-perfectly plastic bar elements whereas region C consists of 60 elements of the same type in order to allow enough space for crack closure formation (Figure 5.2.1). The length of the elements in region B depends on the fictitious crack opening displacement or the plastic zone ahead of the physical crack tip at the maximum level of the cyclic loading. However, the lengths of the elements in the regions C are kept zero initially and then updated with the crack extension. Element widths varied according to their relative positions with the smallest elements being located around the physical crack tip and behind the fictitious crack tip. In this study, the width of the first 40 elements in region C are of $0.11r_P$ each (Figure 5.2.1). The 10 elements that follow are of $0.5r_P$ each in region C, the third group of 10 elements which are behind the crack tip are of $0.01r_P$ each, the fourth group of 10 elements ahead of the crack tip are of $0.01r_P$ each, the fifth group of 10 elements are of $0.03r_P$ each, the sixth group of 10 elements are of $0.05r_P$ each and the final group of 10 elements are of $0.01r_P$ each. As a result, the total element width behind the physical crack tip in region C is increased up-to 5 times of the value of r_p

to properly capture the effect of the plastically deformed material behind the crack tip on crack closure.

5.2.2 Governing equations of the strip-yield model for the computer coding

Figure 5.2.3 shows the Dugdale model [86] used for determination of the plastic zone when the crack is fully open.

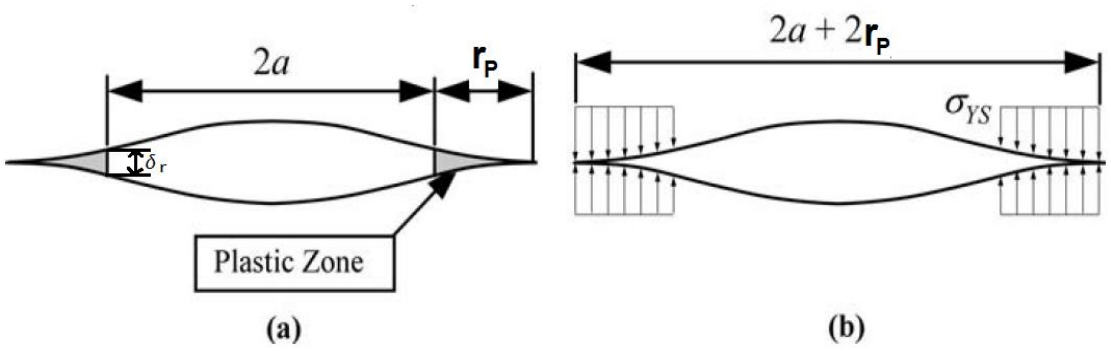

Figure 5.2.3 Dugdale model for the determination of the plastic zone size (a) and corresponding yield stress (b) [7].

Since there is no stress singularity at the fictitious crack tip, the stress intensity factor, K_{σ_∞}, due to remote tensile stess, σ_∞ will be equal to the sum of the stress intensity factor, K_{σ_i} due to uniform compressive stress on element i in region B as shown in Equation 5.2.1.

$$K_{\sigma_\infty} + \sum_{i=1}^{40} K_{\sigma_i} = 0 \qquad (5.2.1)$$

For the solutions corresponding to Figure 5.2.3(a), and Figure 5.2.3(b), approximate finite-width corrections varied with boundary-collocation analyses must be used [83]. The stress intensity factor for Figure 5.2.3(a) is shown in Equation 5.2.2.

$$K_{\sigma_\infty} = \sigma_\infty \sqrt{\pi(a_0 + r_P) \sec\left(\frac{\pi(a_0 + r_P)}{W}\right)} \qquad (5.2.2)$$

where, W is the width of the strip-yield model.

The stress intensity factor for Figure 5.2.3(b) is given in Equation 5.2.3.

$$K_{\sigma_i} = \frac{2\sigma_i}{\pi}\sqrt{\pi(a_0 + r_P)}\left[\sin^{-1}\left(\frac{sin\left(\frac{\pi b_2}{W}\right)}{\sin\left(\frac{\pi(a_0 + r_P)}{W}\right)}\right) - \sin^{-1}\left(\frac{sin\left(\frac{\pi b_1}{W}\right)}{\sin\left(\frac{\pi(a_0 + r_P)}{W}\right)}\right)\right]\sqrt{\sec\left(\frac{\pi(a_0 + r_P)}{W}\right)} \qquad (5.2.3)$$

Only the quarter of the specimen is analysed to simulate crack closure due to the symmetry of the model. Figure 5.2.4 shows the key features of the model.

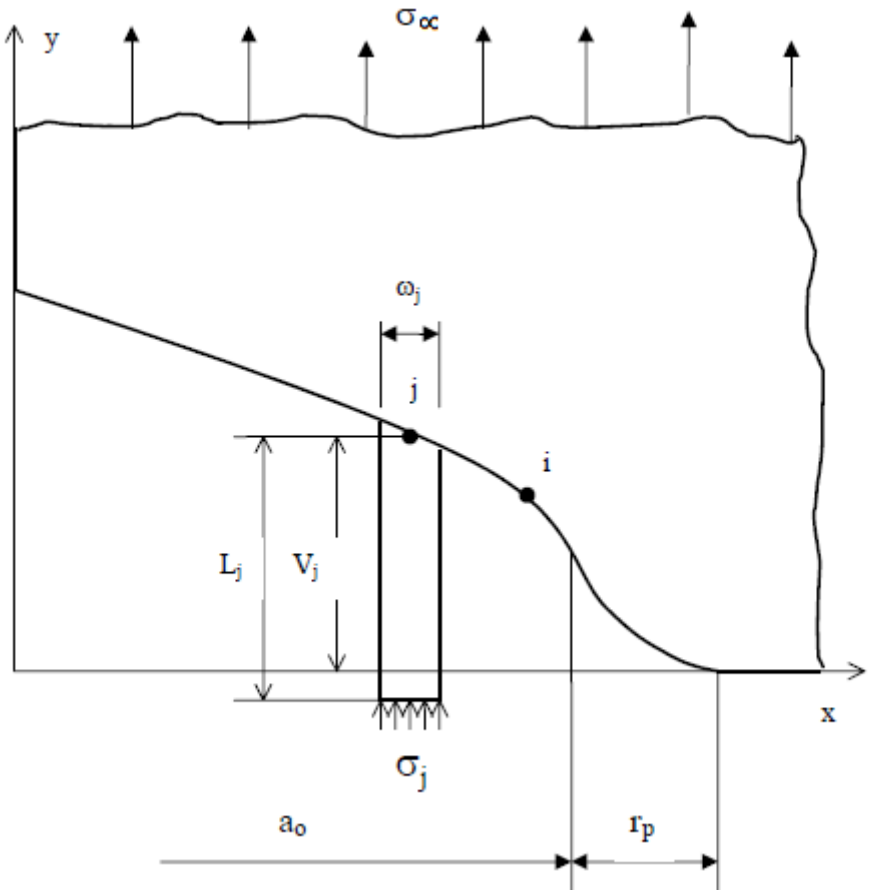

Figure 5.2.4 Key features of the quarter plate model for the crack closure analysis [267].

Element j is connected to the linear elastic region A at point j and subjected to a uniform stress, σ_j, over the element width, ω_j. L_j is the length of element j. V_j is the crack surface opening displacement at point j, which is caused by the remotely applied load and the stress from the bar elements.

The crack surface opening displacement at point i is given by Equation 5.2.4.

$$V_i = \sigma_\infty f(x_i) - \sum_{j=1}^{100} \sigma_j \left[g(x_i, x_j) + g(-x_i, x_j) \right] \; for\; i = 1\; to\; 100 \tag{5.2.4}$$

$f(x_i)$ and $g(x_i, x_j)$ are given by the Equations: (5.2.5) and (5.2.6).

$$f(x_i) = \frac{2(1-\eta^2)}{\pi E}\sqrt{[d^2 - x_i^2]\sec\left(\frac{\pi d}{W}\right)} \qquad (5.2.5)$$

$$g(x_i, x_j) = \frac{2(1-\eta^2)}{\pi E}\left[(b_2 - x_i)\cosh^{-1}\left(\frac{d^2 - b_2 x_i}{d|b_2 - x_i|}\right) - (b_1 - x_i)\cosh^{-1}\left(\frac{d^2 - b_1 x_i}{d|b_1 - x_i|}\right) + \sqrt{d^2 - x_i^2}\left(\sin^{-1}\left(\frac{b_2}{d}\right) - \sin^{-1}\left(\frac{b_1}{d}\right)\right)\right]\left[\frac{\sin^{-1}(B_2) - \sin^{-1}(B_1)}{\sin^{-1}\left(\frac{b_2}{d}\right) - \sin^{-1}\left(\frac{b_1}{d}\right)}\right]\sqrt{\sec\left(\frac{\pi d}{W}\right)} \qquad (5.2.6)$$

where, E is the modulus of the material, and η is the material constant which is zero for plane stress and Poisson's ratio, v for plane strain, $d = a_0 + r_P, b_1 = x_j - \frac{\omega_j}{2}$ and $b_2 = x_j + \frac{\omega_j}{2}$ (Figure 5.2.1), while $B_1$and $B_2$are given by

$$B_i = \frac{sin\left(\frac{\pi b_i}{W}\right)}{\sin\left(\frac{\pi d}{W}\right)} \; for\; i = 1\; or\; 2 \qquad (5.2.7)$$

The crack surface contact stresses used for the calculation of the crack opening stress are solved from the linear system of Equation 5.2.4 using the Gauss-Seidel iterative method [270] with boundary conditions added. The boundary conditions in region B ahead of the current physical crack tip are given in Equations 5.2.8(a-c).

$$If, V_i^{(k)} \geq L_i^{(k-1)}\left(1 + \alpha\frac{\sigma_0}{E}\right) \Rightarrow \begin{cases} L_i^{(k)} = V_i^{(k)}\left(1 + \frac{\alpha\sigma_0}{E}\right) \\ if\ \sigma_i^{(k)} \geq \alpha\sigma_0 \Rightarrow \sigma_i^{(k)} = \alpha\sigma_0 \end{cases} \qquad (5.2.8(a))$$

$$V_i^{(k)} < L_i^{(k-1)}\left(1+\alpha\frac{\sigma_0}{E}\right) \Longrightarrow \begin{cases} L_i^{(k)} = V_i^{(k)}\left(1+\frac{\alpha\sigma_0}{E}\right) \\ if\ \sigma_i^{(k)} \le -\alpha\sigma_0 \Longrightarrow \sigma_i^{(k)} = -\alpha\sigma_0 \end{cases} \quad (5.2.8(b))$$

$$\text{Otherwise,} \begin{cases} L_i^{(k)} = V_i^{(k)} \\ \sigma_i^{(k)} = \sigma_i^{(k-1)} \end{cases} \quad (5.2.8(c))$$

The boundary conditions in region C behind the physical crack tip are given in Equations 5.2.9(a-c).

$$If, V_i^{(k)} \ge L_i^{(k-1)} \Longrightarrow \begin{cases} L_i^{(k)} = L_i^{(k-1)} \\ if\ \sigma_i^{(k)} \ge 0 \Longrightarrow \sigma_i^{(k)} = 0 \end{cases} \quad (5.2.9(a))$$

$$V_i^{(k)} < L_i^{(k-1)}\left(1+\alpha\frac{\sigma_0}{E}\right) \Longrightarrow \begin{cases} L_i^{(k)} = V_i^{(k)}\left(1+\frac{\alpha\sigma_0}{E}\right) \\ if\ \sigma_i^{(k)} \le -\sigma_0 \Longrightarrow \sigma_i^{(k)} = -\sigma_0 \end{cases} \quad (5.2.9(b))$$

$$\text{Otherwise,} \begin{cases} L_i^{(k)} = V_i^{(k)} \\ \sigma_i^{(k)} = \sigma_i^{(k-1)} \end{cases} \quad (5.2.9(c))$$

where, σ_0 is the flow stress or average of the yield strength and the ultimate strength of the alloy, α, is the constraint factor with $\alpha = 1$ representing the plane stress state and the additional superscripts on σ_i, V_i and L_i denote the iteration number of the iterative process solving the linear system Equation 5.2.4. And Equation 5.2.4 is rewritten in the form of Equation 5.2.10.

$$\sigma_i^{(k)} = \frac{\left[\sigma_\infty f(x_i) - V_i - \sum_{j=1}^{i-1} \sigma_j^{(k)} \left(g(x_i, x_j) + g(-x_i, x_j)\right) - \sum_{j=i+1}^{100} \sigma_j^{(k-1)} \left(g(x_i, x_j) + g(-x_i, x_j)\right)\right]}{g(x_i, x_j) + g(-x_i, x_j)} \quad (5.2.10)$$
$$for\ i = 1\ to\ 100$$

Initial assumptions for the value of σ_i are zero and are inserted into the right side of the linear system of Equation 5.2.10. In the Gauss-Seidel iterative method, the newly obtained stress $\sigma_i^{(k)}$ is checked against the boundary conditions of Equations 5.2.8(a-c) and Equations 5.2.9(a-c) once calculated, it is updated accordingly. The newly obtained stresses $\sigma_i^{(k)}$ are always used in Equation 5.2.10 to calculate the remaining unknown stresses, which makes the solving of the linear system of Equation 5.2.10 more efficient. The process is repeated until the changes in all the σ_i, are less than 1 % of the flow stress of the alloy. The crack opening stress, σ_{op}, is calculated based on the following criteria; (i) the applied stress increment ($\sigma_{op} - \sigma_{min}$) is used to effectively remove all the contact stresses (<1 % σ_0) from the bar elements in region C, and (ii) the applied stress increment ($\sigma_{op} - \sigma_{min}$) is used to effectively separate the surface contact ($< 1\ \%\ \delta_{tmax}$), where δ_{tmax} is the physical crack tip opening displacement at maximum load of the loading cycle) behind the physical crack tip. An iterative procedure is again employed in the crack opening stress calculations.

Figure 5.2.5 shows the flow chart of the computer code developed to carry out the above numerical simulations of the crack closure.

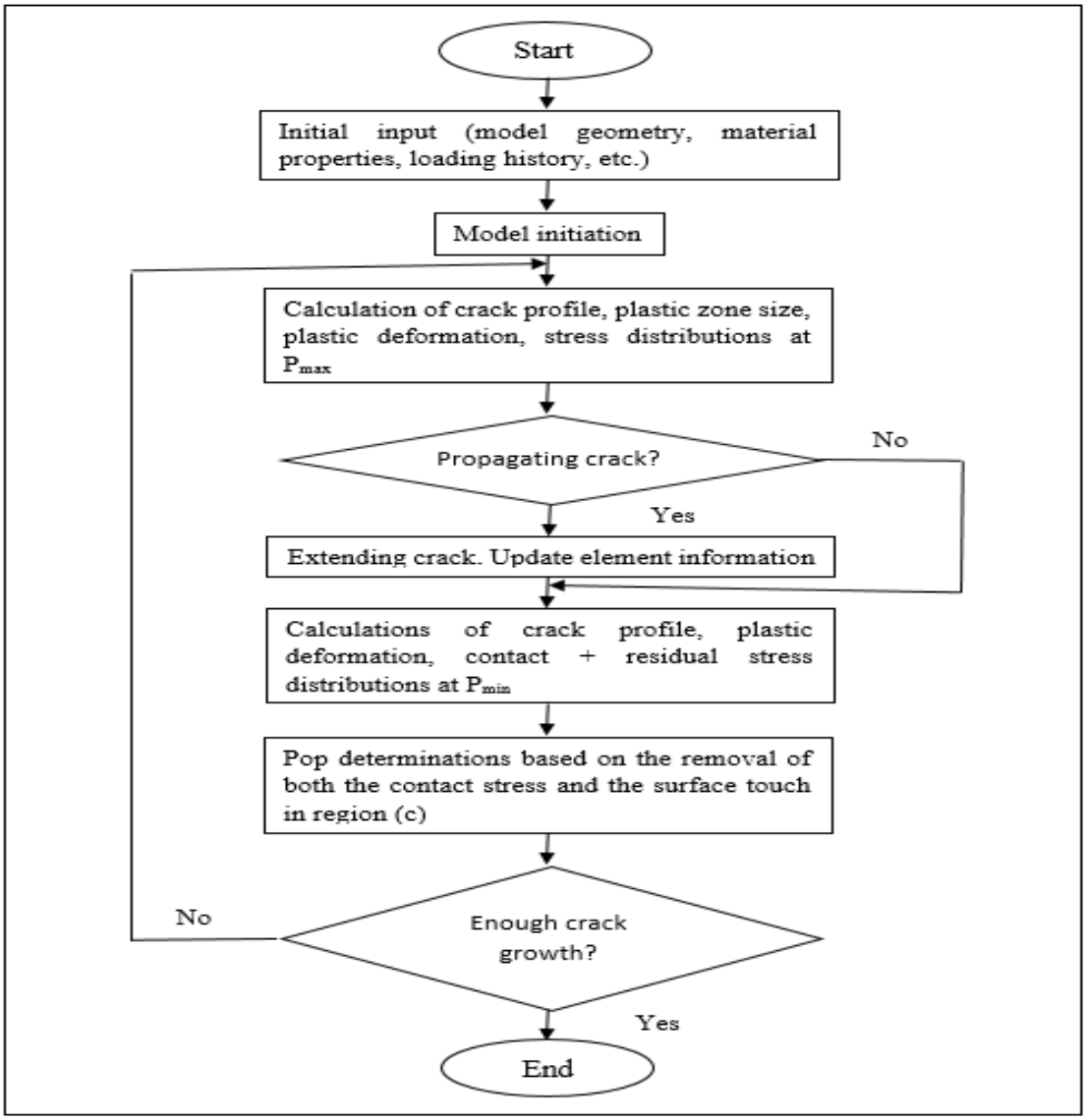

Figure 5.2.5 Flow chart of computer code for crack closure solution using strip-yield model.

5.3 Results and analyses

5.3.1 Near-tip crack behaviour under fatigue loading

The strip-yield model was used to investigate near-tip crack behaviour under both constant amplitude (CA) and variable amplitude (VA) loading. The build-up of crack closure and its influence on fatigue crack growth behaviour are explained here. The variation of cyclic crack tip opening displacement, $\Delta(CTOD)$, plastic zone size, etc. are

used as the parameters to analyse near-tip crack behaviour under the baseline fatigue loading of R=0.

5.3.1.1Near-tip crack behaviour under constant amplitude (CA) loading

Figure 5.3.1(a) shows the crack profiles at maximum and minimum loads of the first load cycle of constant amplitude (CA) loading at stress ratio, R=0, under the plane stress condition. A baseline stress amplitude, $\Delta\sigma$=50 MPa was used to simulate the crack profile. The corresponding ΔK was 12.53 $MPa\sqrt{m}$. For convenience of the comparison, the crack opening displacements, $v(x)$ were normalised by the elastic opening displacement, δ_b at the physical crack tip under the maximum loading, P_{max}, and x coordinates in relation to the physical crack tip of the crack surface were normalised by the monotonic plastic zone size, r_b at P_{max}. The physical crack tip was set at $\frac{x}{r_b}$=0 with an initial half crack length of 20 mm. It was found that the maximum crack tip elastic displacement was $1\delta_b$ and the minimum crack tip elastic displacement was $0.5\delta_b$ which agrees well with the value suggested by [86]. The crack closure level, $\frac{P_{op}}{P_{max}}$ was found to be 0, where, P_{op} is the crack opening load, as no crack growth was introduced. The crack tip opening displacement, $\Delta(CTOD)$ for this fatigue cycle was $0.5\delta_b$. Figure 5.3.1(b) shows the stress distributions along the crack line around the crack tip at P_{max} and P_{min} (minimum loading).The direct stress in the loading direction was normalised by the flow stress of the alloy, σ_0. It was found that, the forward plastic zone size at at P_{max} was $1r_b$ and the reversed plastic zone size due to P_{min} was $\frac{1}{4}$ of the forward plastic zone size (i.e., $0.25r_b$) which agrees well with the Dugdale's model [86].

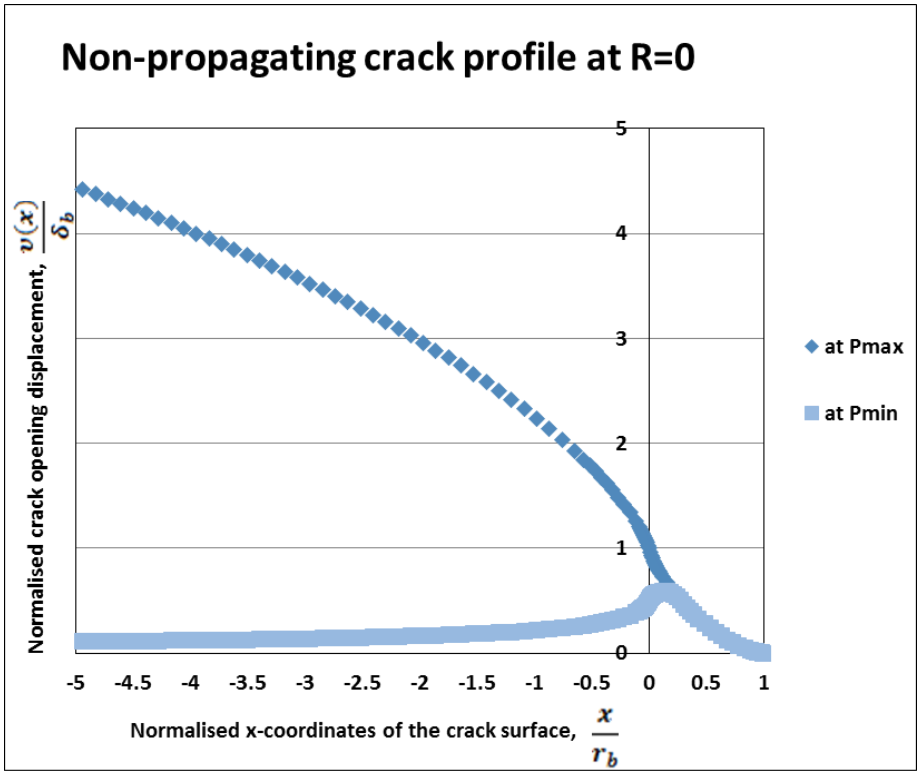

(a)

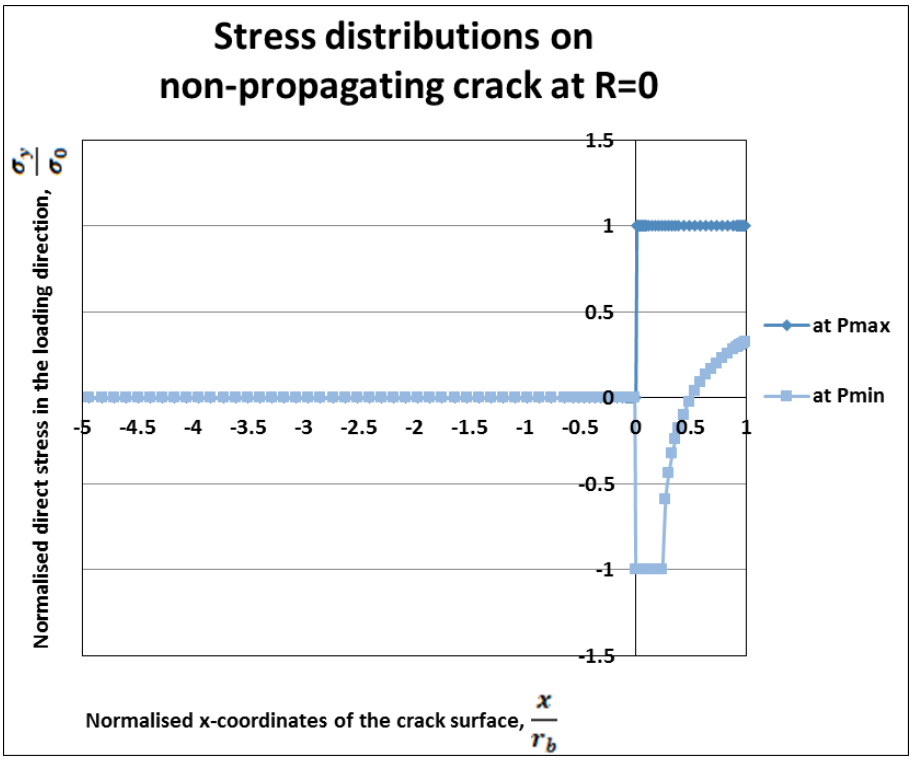

(b)

Figure 5.3.1 First fatigue cycle under constant amplitude (CA) loading of $R = 0$: (a) crack opening profiles, and (b) near-tip stress distributions.

Figure 5.3.2 shows the crack profiles and stress distributions at P_{max} , P_{min} and P_{op} as the crack was grown by one quarter of the baseline forward plastic zone size. The area between the two lines behind the crack tip, $\frac{x}{r_b}$=0, represents the plastically deformed material left behind the crack tip due to crack growth, which causes crack closure. The area between the two lines ahead of the crack tip, $\frac{x}{r_b} = 0$, represents the plastically deformed material or the plastic zone. At P_{max} (Figure 5.3.2(a), the crack tip opening displacement was unchanged from the first fatigue cycle value, $1\delta_b$. At P_{min} (Figure 5.3.2(b)), the elastic opening displacement was $0.817\delta_b$ which was higher than the first loading cycle value, $0.5\delta_b$, because of the formation of crack closure. At P_{op} (Figure 5.3.2(c)), the elastic crack tip opening displacement was $0.821\delta_b$. Crack closure was found immediately behind the crack tip and the crack closure level was $\frac{P_{op}}{P_{max}}$=0.5. The $\Delta(CTOD)$ between P_{max} and P_{min} was $0.183\delta_b$ whereas the $\Delta(CTOD)$ between P_{max} and P_{op} had a slightly lower value, $0.179\delta_b$. In Figure 5.3.2(d), it can be seen that forward plastic zone size at P_{max} decreased to similar to the first loading cycle value, $1\ r_b$ and the reversed plastic zone at P_{min} was decreased to $0.12r_b$ from the first loading cycle value, $0.25r_b$. This was due to the formation of the crack closure or load shielding caused by the load transfer in the wake, which is linked to the reduced fatigue damage associated with the smaller reversed plastic zone size. At P_{op}, the contact stress was removed from the crack wake in region C and residual deformation was raised in region B.

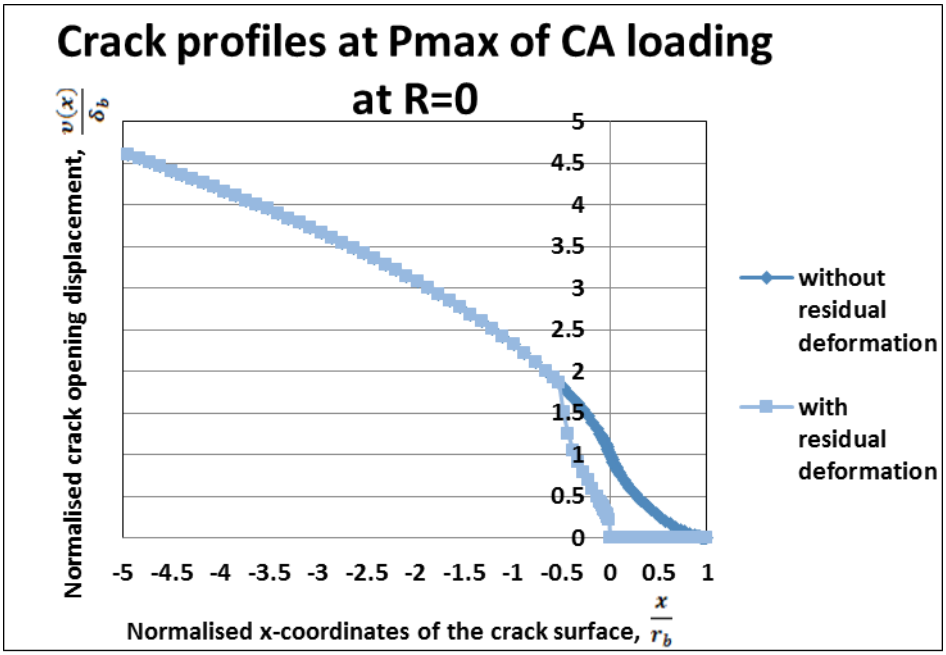
Crack profiles at Pmax of CA loading at R=0
Normalised crack opening displacement, $\frac{v(x)}{\delta_b}$
5
4.5
4
3.5
3
2.5
2
1.5
1
0.5
0
-5 -4.5 -4 -3.5 -3 -2.5 -2 -1.5 -1 -0.5 0 0.5 1
Normalised x-coordinates of the crack surface, $\frac{x}{r_b}$
without residual deformation
with residual deformation

(a)

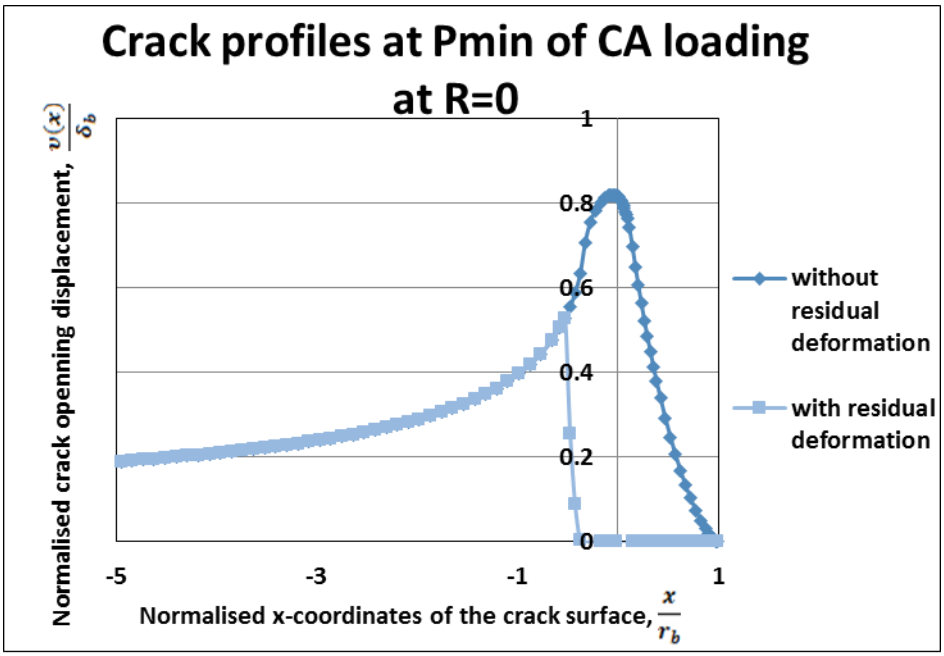
Crack profiles at Pmin of CA loading at R=0
Normalised crack openning displacement, $\frac{v(x)}{\delta_b}$
1
0.8
0.6
0.4
0.2
0
-5 -3 -1 1
Normalised x-coordinates of the crack surface, $\frac{x}{r_b}$
without residual deformation
with residual deformation

(b)

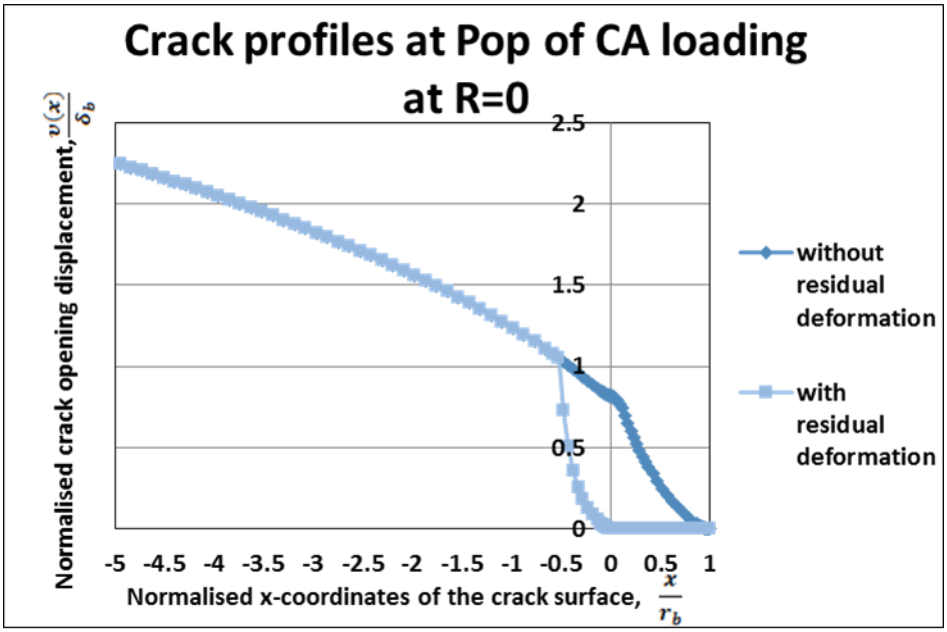

(c)

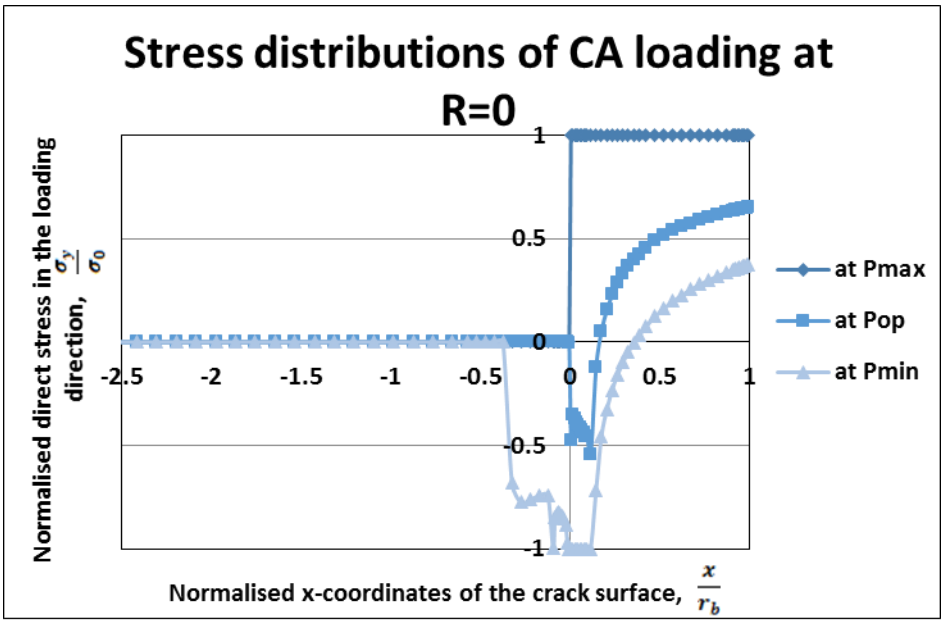

(d)

Figure 5.3.2 Crack profiles (a-c) and near-tip stress distributions (d) after 0.50r_b crack growth under constant amplitude loading of R=0.

5.3.1.2Near-tip crack behaviour under a 90 % single overload

Figure 5.3.3 shows the crack profiles and stress distributions, at P_{max} , P_{min} and P_{op} at 90 % overload cycle. At P_{max} (Figure 5.3.3(a)) the elastic opening displacement was $3.53\delta_b$ which was 3.53 times the first load cycle value, $1\delta_b$, because of the higher P_{max} of the overload cycle. At P_{min} (Figure 5.3.3(b)), the elastic opening displacement was $1.88\delta_b$. The ratio of the opening displacement for minimum and maximum was approximately 0.56, which is quite consistent with the first loading cycle with only 12 % difference. The elastic opening displacement value at P_{op} was the same as for the P_{min} (Figure 5.3.3(c)). This indicates that there was no closure during the overload cycle. This phenomenon can be explained by the overload blunting effect as shown in Figure 5.3.3. From Figure 5.3.3(d), it is apparent that the forward plastic zone size at P_{max} was $3.7r_b$ which was 3.7 times higher than the first loading cycle because of the greater plastic deformation ahead of the crack tip due to the higher load applied. The reversed plastic zone size at P_{min} was $0.8r_b$ which was higher than the first loading cycle, indicating greater fatigue damage of the overload cycle. However, the the ratio of the plastic zone size for minimum and maximum loading was 0.22 due to the absence of crack closure with 12 % difference compared with the 1st loading cycle. At P_{op} , the plastic zone size is similar to the reversed plastic zone size as no crack closure exists behind the crack tip.

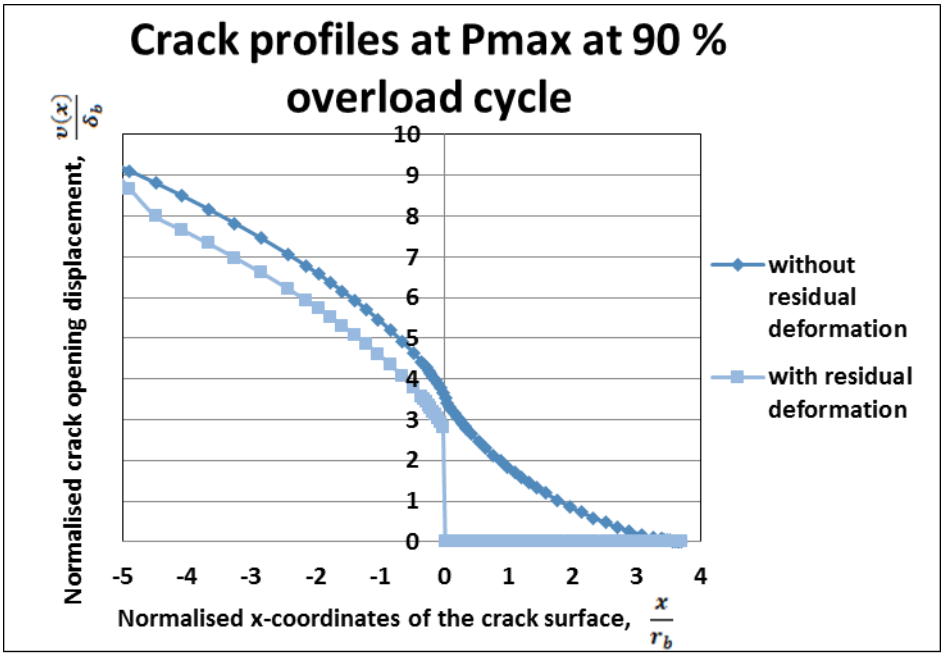
Crack profiles at Pmax at 90 % overload cycle
Normalised crack opening displacement, $\frac{v(x)}{\delta_b}$
10
9
8
7
6
5
4
3
2
1
0
-5 -4 -3 -2 -1 0 1 2 3 4
Normalised x-coordinates of the crack surface, $\frac{x}{r_b}$
without residual deformation
with residual deformation

(a)

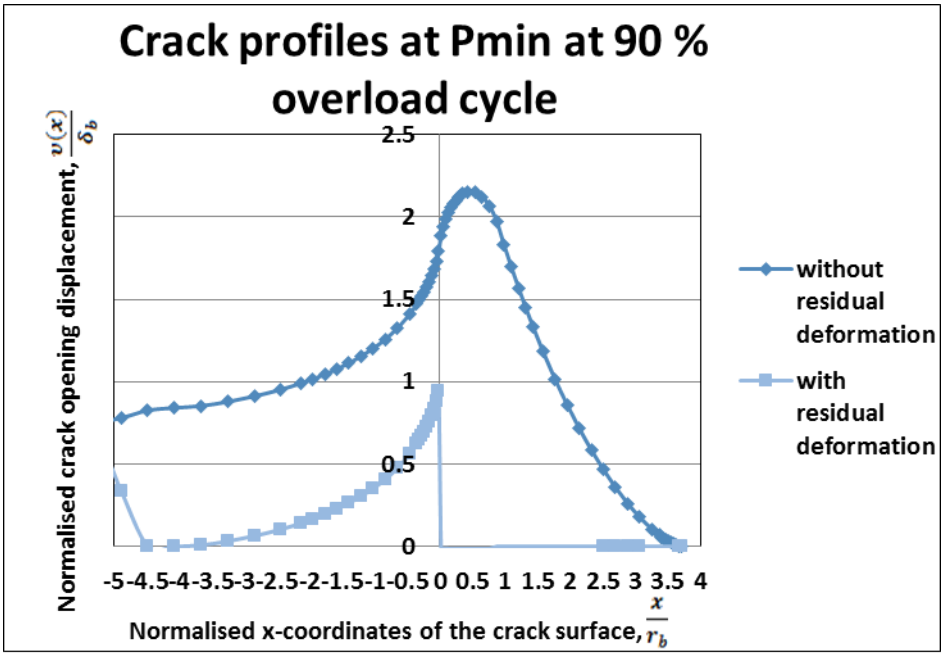
Crack profiles at Pmin at 90 % overload cycle
Normalised crack opening displacement, $\frac{v(x)}{\delta_b}$
2.5
2
1.5
1
0.5
0
-5 -4.5 -4 -3.5 -3 -2.5 -2 -1.5 -1 -0.5 0 0.5 1 1.5 2 2.5 3 3.5 4
Normalised x-coordinates of the crack surface, $\frac{x}{r_b}$
without residual deformation
with residual deformation

(b)

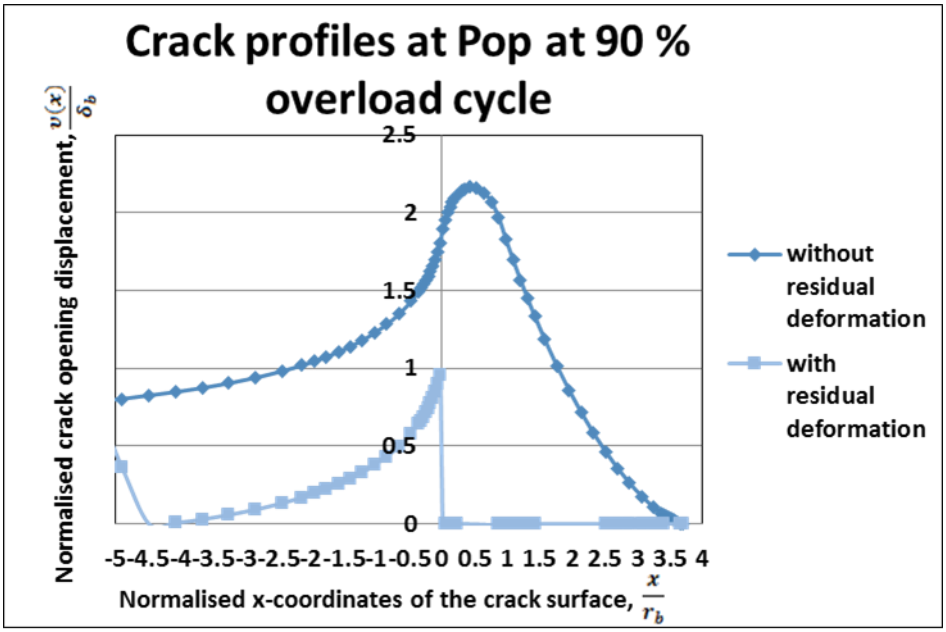

(c)

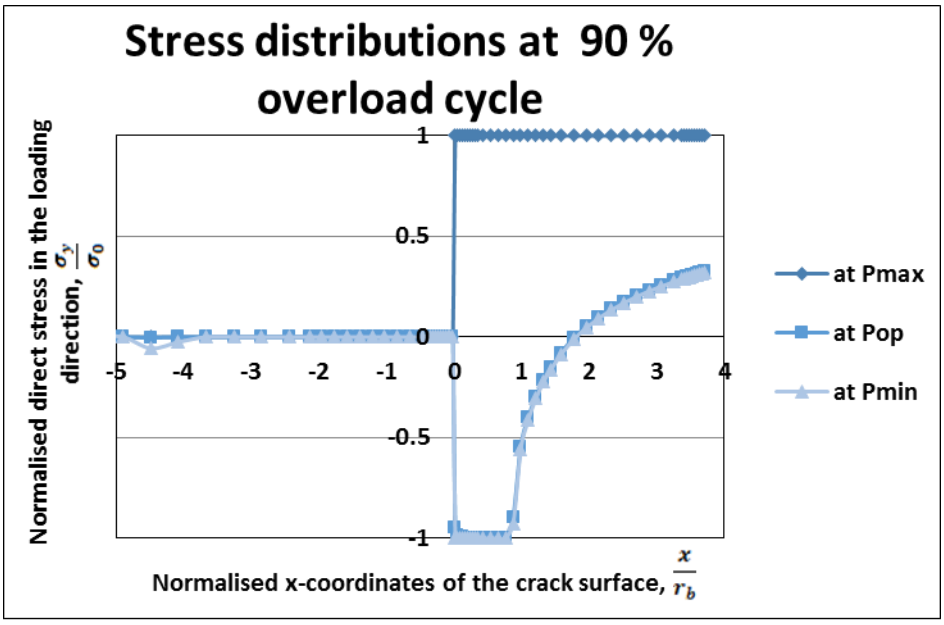

(d)

Figure 5.3.3 Crack profiles (a-c) and near-tip stress distributions (d) of a 90% single overload cycle under plane stress condition.

Figure 5.3.4 shows the crack profiles and stress distributions at P_{max} , P_{min} and P_{op} after crack was grown into the overload plastic zone by $0.63r_{overload}$. The elastic opening of the physical crack tip at P_{max} was $1\delta_b$ in Figure 5.3.4(a), which was similar to that of under CA loading. At P_{min} (Figure 5.3.4(b)), the elastic opening of the physical

crack tip was 0.95δ_b, which was quite similar to the elastic opening of the physical crack tip value, 0.96δ_b at P_{op} (Figure 5.3.4(c)). Again, This value was of the same order of the value at P_{max} with 5 % difference. This difference can be explained by the excessive plastic deformation left in the crack wake as shown in Figure 5.3.4. The $\Delta(CTOD)$ between P_{max} and P_{min} was 0.05δ_b whereas the $\Delta(CTOD)$ between P_{max} and P_{op} was slightly lower value, 0.04δ_b. Both were lower than the values found under CA loading. Here, the crack closure was 0.69 and it was higher than the CA loading condition. This crack closure can be used to explain the delayed crack growth retardation after the application of overload. From Figure 5.3.4(d), it is observed that there was a small forward plastic zone, 0.25r_p at P_{max}, but there was no sign of the reversed plastic zone at P_{min} and P_{op} due to the large extent of the load transfer behind the crack tip on the crack face.

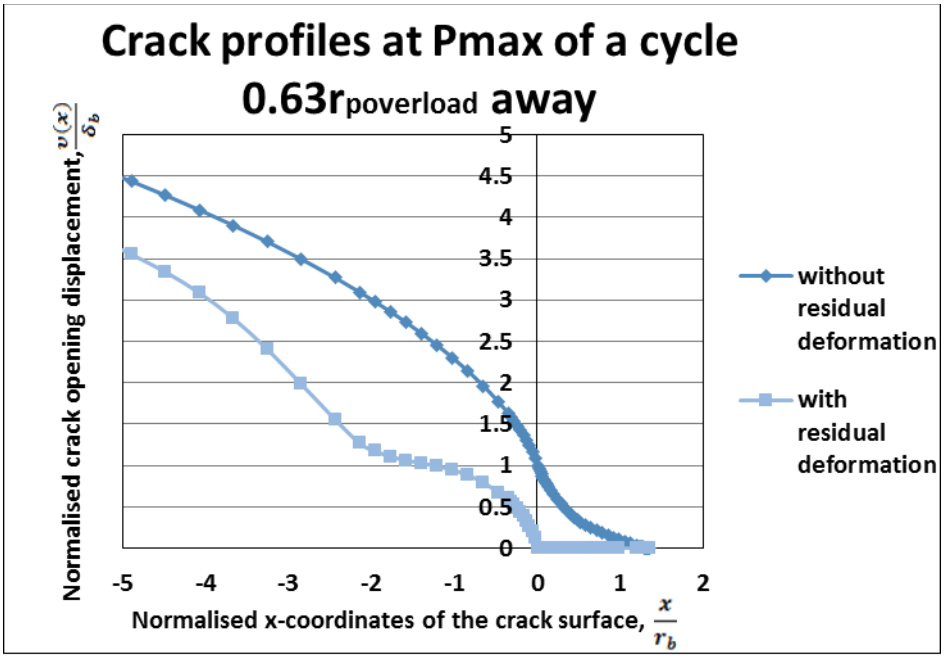

(a)

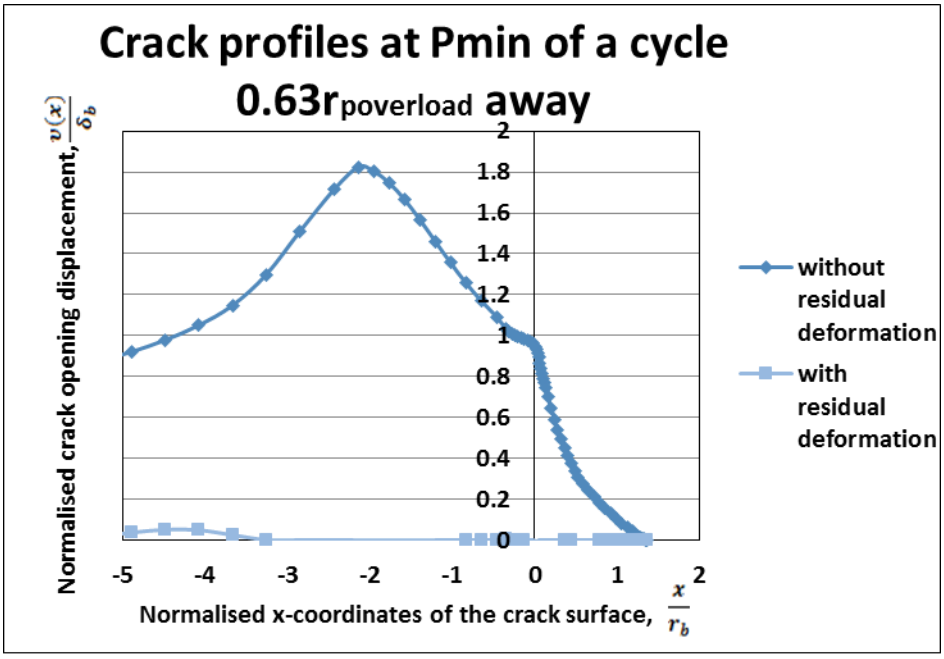
Crack profiles at Pmin of a cycle
0.63rpoverload away
Normalised crack opening displacement, $\frac{v(x)}{\delta_b}$
2
1.8
1.6
1.4
1.2
1
0.8
0.6
0.4
0.2
0
-5
-4
-3
-2
-1
0
1
2
Normalised x-coordinates of the crack surface, $\frac{x}{r_b}$
without residual deformation
with residual deformation

(b)

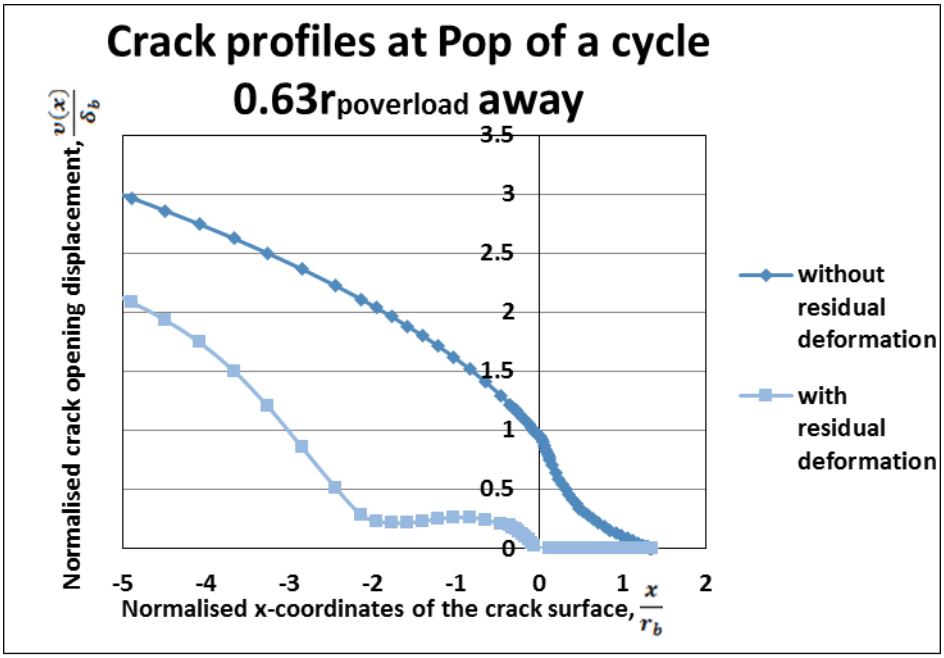
Crack profiles at Pop of a cycle
0.63rpoverload away
Normalised crack opening displacement, $\frac{v(x)}{\delta_b}$
3.5
3
2.5
2
1.5
1
0.5
0
-5
-4
-3
-2
-1
0
1
2
Normalised x-coordinates of the crack surface, $\frac{x}{r_b}$
without residual deformation
with residual deformation

(c)

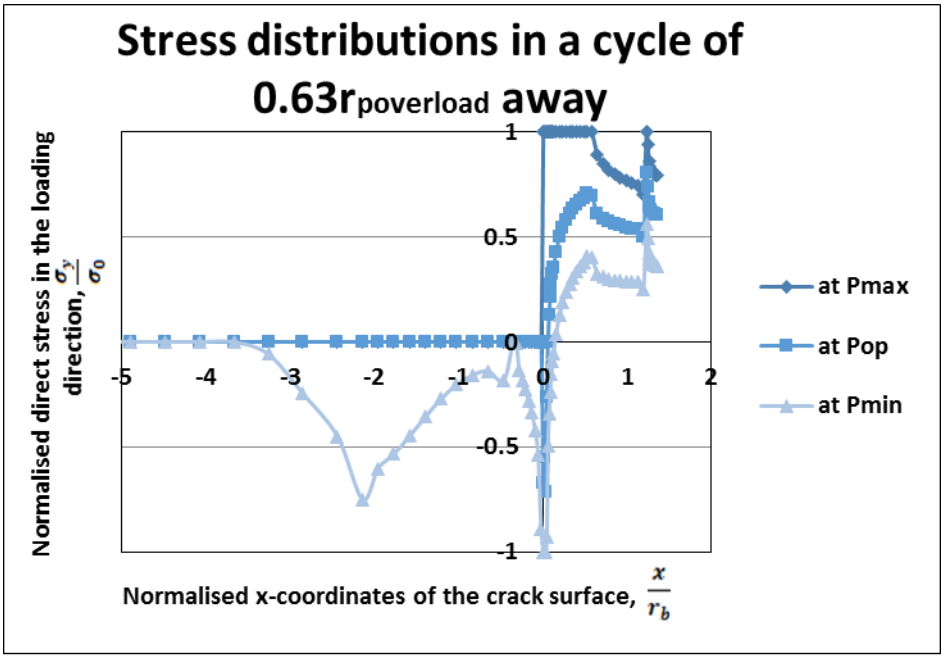

(d)

Figure 5.3.4 Crack profiles (a-c) and near-tip stress distributions (d) of a cycle 0.63$r_{poverload}$ away from the application of a 100 % single overload under the plane stress condition.

5.3.2 Crack growth driving force under a 90 % single overload

Figure 5.3.5 shows a variation of crack growth driving force based on the crack closure effect. Here, with a baseline constant amplitude (CA) loading of R=0 and $(\Delta K)_{BL}$=12.53$MPa\sqrt{m}$, single overload of 90 % (overload ratio, OLR=1.9) was applied at $\frac{\Delta a}{(r_p)_{OL}}$=0. The overload plastic zone was $(r_P)_{OL}$=1.36 mm (calculated using Dugdale's model shown in Table 2.2.1). The crack growth, Δa, was normalised by overload plastic zone size, $(r_P)_{OL}$, and the post-overload transient crack growth driving force, $\frac{\Delta K_{eff}}{\Delta K}$, was normalised by the baseline crack growth driving force, $\left(\frac{\Delta K_{eff}}{\Delta K}\right)_{CA}$. It was observed that the crack growth driving force stabilised initially to 1 prior to the application of the overload. It increased to 2.5 immediately after the application of overload and then reached a minimum level of 0.33 when the crack was propagated by a length of 0.25$(r_p)_{OL}$. It then started to climb up gradually and it recovered to its

pre-overload level as the crack propagated about one overload plastic zone size, $1(r_p)_{OL}$.

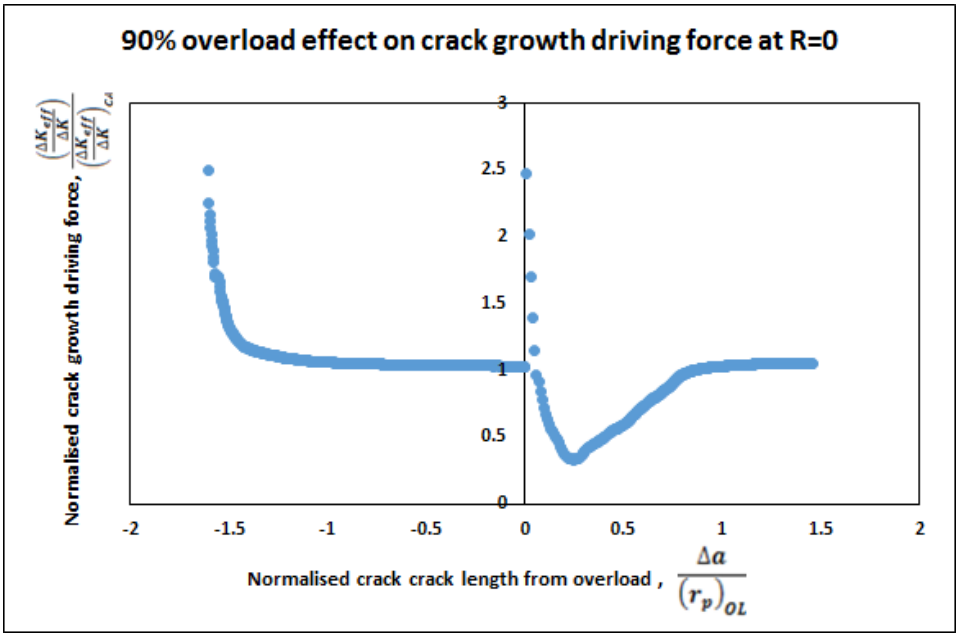

Figure 5.3.5 Variation of the crack growth driving force due to the application of 90 % overload.

The results indicated that crack growth occurred in four stages which are: a constant opening level period corresponding to the constant CA crack growth before the overload, a very short immediate acceleration period just after the overload, followed by prolonged overload period and finally the stabilised opening level period similar to the pre-overload condition. All these are consistent with the results reported in the literature [62-66].

5.3.3 Overload ratio (OLR) effect on crack growth driving force due to single overload

Figure 5.3.6 shows the variation of crack growth driving force with respect to the overload with different overload ratios (OLRs) of 1.4 (% OL=40%), 1.9 (% OL=90 %)

and 2.4 (% OL=140 %). Here, the stress ratio was fixed to R=0. The normalised overload affected distance remained constant at $1(r_P)_{OL}$ for all three OLRs. Here, the crack growth driving force became a minimum value at $0.25(r_P)_{OL}$ for OLR of 1.4 and 1.9. However, for OLR of 2.4, closure level reached 1 at a lower than $0.25(r_P)_{OL}$ due to that the fact that the normalised crack growth driving force reached zero at that distance. Therefore, the crack arrest occurred where the effective crack growth driving force was reduced to zero for OLR of 2.4. It is also evident that with the increase of OLR, the crack growth driving force decreased. For, 1.4, 1.9 and 2.4 OLR, the normalised minimum crack growth driving force decreased down to 0.74, 0.33 and 0, respectively.

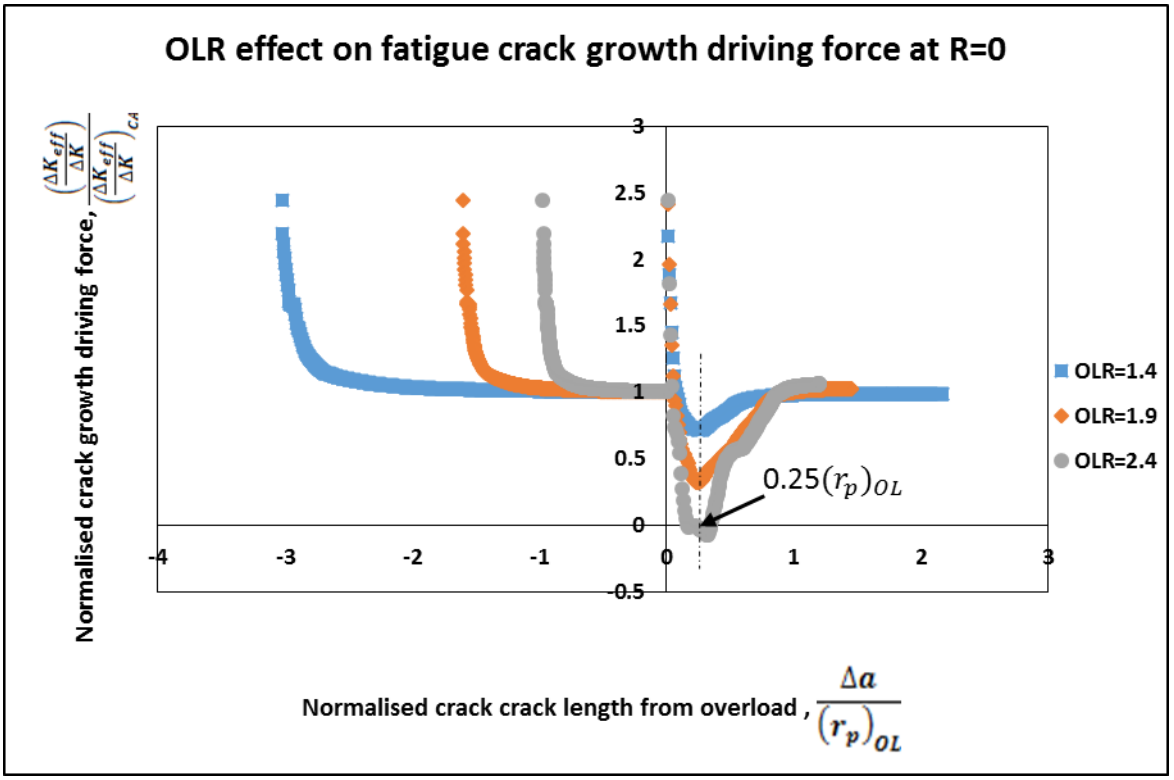

Figure 5.3.6 Variation of crack growth driving force due to the application of overload with different OLRs.

5.3.4 Stress ratio (R-ratio) effect on fatigue crack growth driving force during single overload effect

Figure 5.3.7 shows the R ratio effect on the fatigue crack growth driving force after the application of 90 % single overload. It is seen that, with the increase of R, crack growth driving force increased, which is linked to the lower crack closure level at higher stress ratios. The overload affected distance remained at $1(r_P)_{OL}$ independent of the R ratio effect. However, maximum closure distance shifted to the left with the increase of R. Here, for R ratio of 0.0, 0.1 and 0.3, maximum closure distance points were $0.25(r_P)_{OL}$, $0.21(r_P)_{OL}$ and $0.16(r_P)_{OL}$, respectively. For R of 0, 0.1 and 0.3, the normalised minimum crack growth driving force were 0.33, 0.38 and 0.46, respectively.

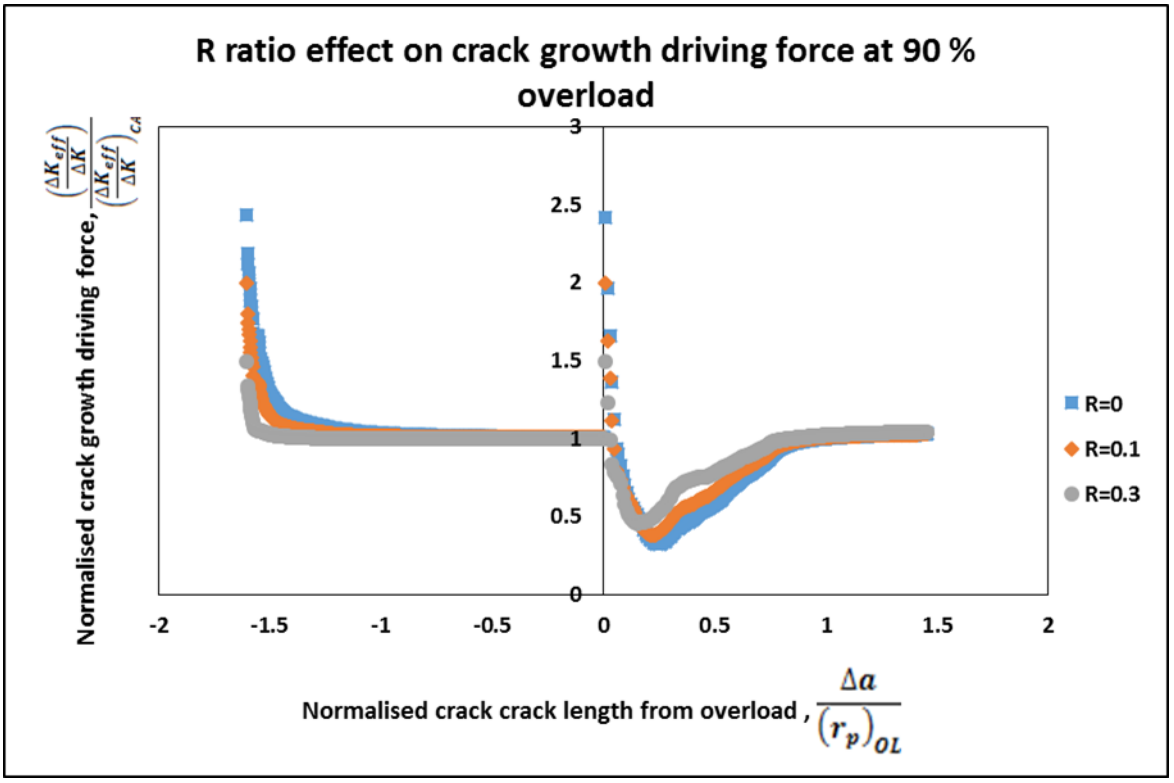

Figure 5.3.7 Variation of crack growth driving force due to 90 % overload at different R ratios.

5.3.5 Baseline stress intensity factor range effect on fatigue crack growth driving force during a single overload

Figure 5.3.8 shows the baseline stress intensity factor range, $(\Delta K)_{BL}$ effect on the fatigue crack growth driving force under a single overload effect. Here, fixed OLR=1.9 (% OL=90 %) and R=0 were used. Firstly, it is apparent that, with the increase of $(\Delta K)_{BL}$, the crack growth driving force decreased. The closure affected distance and maximum closure distance remained independent of the $(\Delta K)_{BL}$ effect, this observation is similar to the effect of R and OLR. Here, for the baseline stress intensity factor range, $(\Delta K)_{BL}$ of 7.52 $MPa\sqrt{m}$, 10.03 $MPa\sqrt{m}$ and 12.53 $MPa\sqrt{m}$, the normalised crack growth driving force were 0.74, 0.58 and 0.32, respectively.

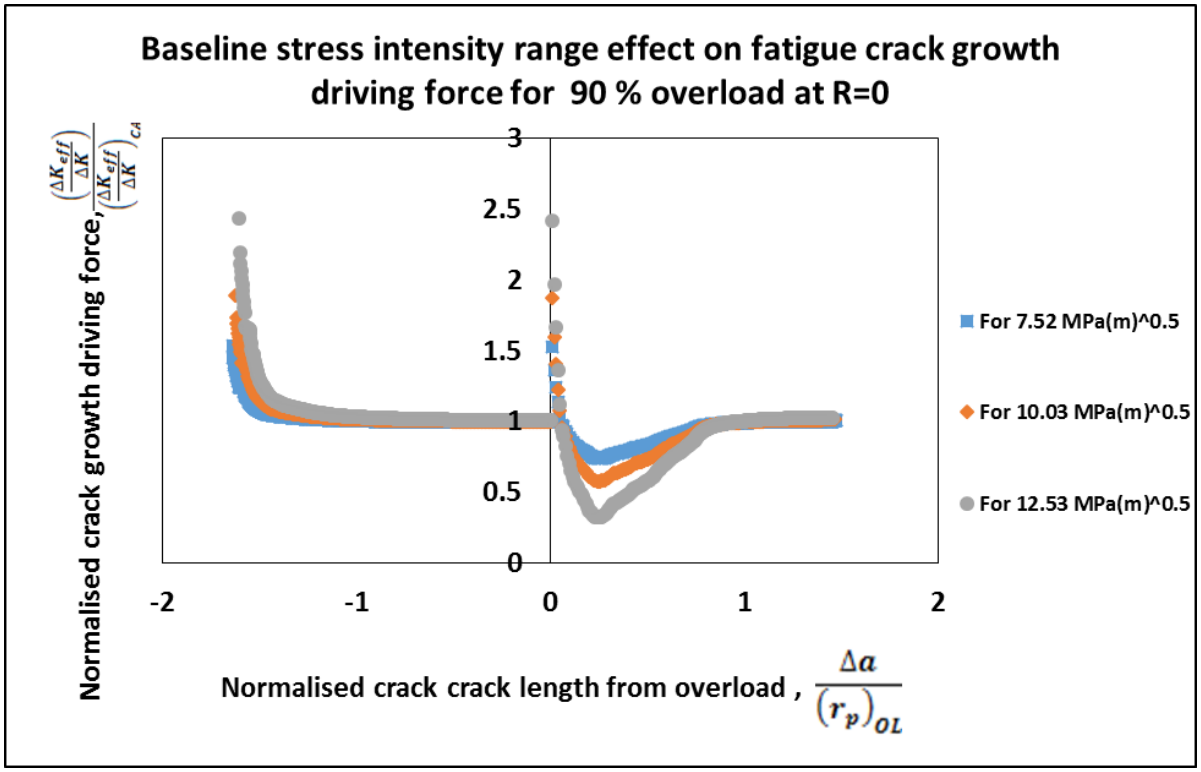

Figure 5.3.8 Variation of crack growth driving force due to the application of overload 90% at different baseline stress intensity factor range with R=0.

5.3.6 Constraint factor effect on fatigue crack growth driving force during single overload

Figure 5.3.9. shows the effect of the constraint factor, α on the fatigue crack growth driving force under a single overload. Here, a fixed value of OLR=1.9 (% OL=90 %) and R=0 were used. With the increase of the α value, the crack growth driving force increased, which is consistent with the decreased crack closure under higher deformation contraint. For an α value of 1.0, 1.5 and 3, the normalised minimum crack growth driving force were 0.34, 0.52 and 0.8, respectively.

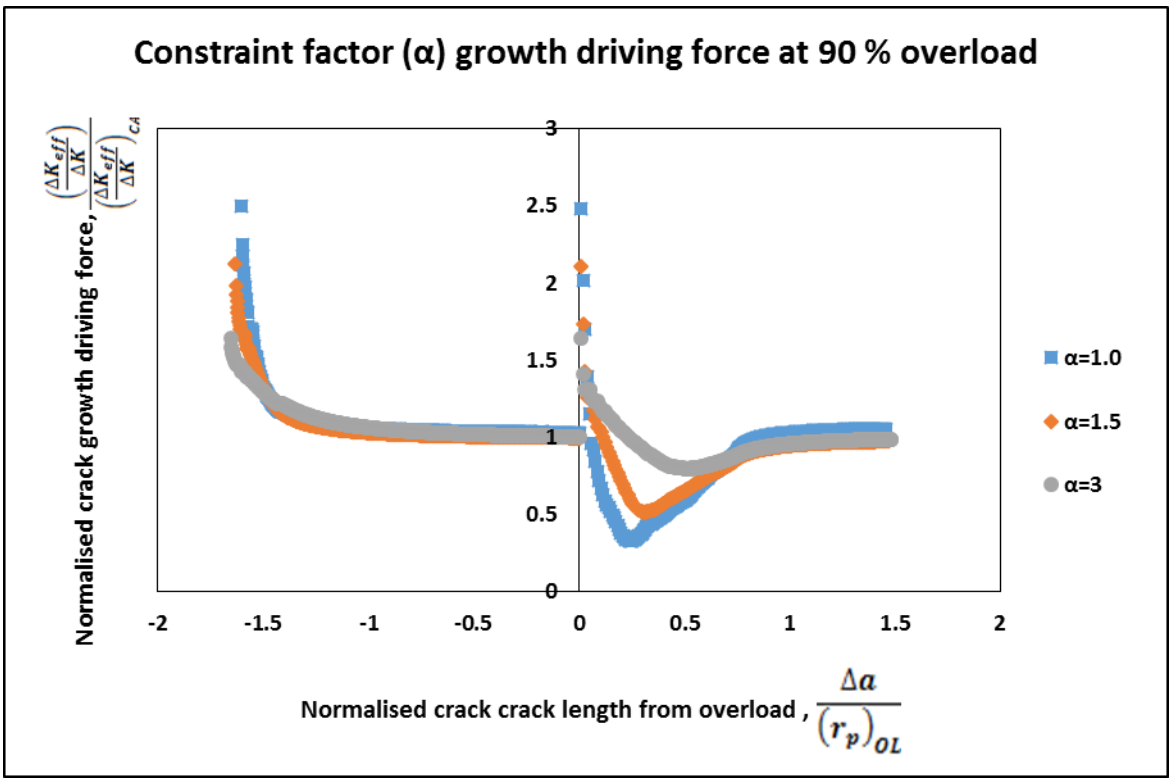

Figure 5.3.9 Variation of crack growth driving force due to the application of 90 % overload at different constraint factor, α with R=0.

5.4 Discussion

At the first loading cycle, the crack profile and stress distribution in front of the crack tip were quite consistent with those predicted by Dugdale model [86]. The ratio of the elastic crack tip opening displacements for minimum and maximum loading was 0.5, while the ratio of crack tip plastic zone sizes under the minimum and maximum loading was 0.25. No crack closure exists for the first fatigue cycle as there is no plastically deformed material left behind the crack tip. When the crack grew to a certain distance, the stabilised crack closure was developed under CA fatigue loading. Here, due to the effect of the plastic wake and crack closure, the ratio of the elastic crack tip opening displacements for minimum and maximum loading decreased. The ratio of plastic zone size decreased due to load transfer behind the crack tip caused by the crack closure.

In the presence of an overload, the crack profile and stress distribution exhibit distinctive post-overload transient behaviour. Crack tip blunting was also clearly observed for the overload cycle, which led to a short period of crack growth acceleration after the overload. When the crack grew into the overload plastic zone, the reduction in the ratio of the elastic crack tip opening displacements of minimum and maximum loading was increased compared with that of CA loading condition, which led to the delayed overload retardation on crack growth. This can be explained by the higher crack closure effect caused by the overload.

The Crack growth driving force remained steady at a constant level before the overload, but it increased after the application of the overload due to the crack tip blunting mentioned earlier. It then started to decrease while the crack propagated inside the overload plastic zone. It finally went back to the preoverload level as the crack propagated to the edge of the overload plastic zone. This correlated with the crack growth retardation effect due to the overload. This overload effect on fatigue crack growth is consistent with other studies [62-66].

With the increase of the overload ratio (OLR), the crack closure also increased, but the crack growth driving force decreased. Therefore, the OLR had a positive effect in reducing the fatigue crack growth driving force. This is also supported by other research works [62, 63, 71] where the overload retardation effect gets prominent with higher OLR. In this present study, an OLR of 2.4 led to crack arrest. On the other hand,

the R ratio had a negative effect on reducing the fatigue crack growth driving force. Borrego et al. [63] also found a decreasing overload retardation effect with the increase of R ratio. In the present study, at constant k_{max}, crack closure effect decreased with the increase of R ratio which eventually led to a decrease in the transient overload retardation effect. It is also worth noting that, the maximum overload retardation point also shifted to the left with the increase of R as reported in the literature [63].

The baseline stress intensity factor range, $(\Delta K)_{BL}$ also had a positive effect on the fatigue crack growth driving force within the overload affected zone. This can be demonstrated by Figure 5.4.1 where the change in the minimum crack growth driving force with the change of the baseline stress intensity factor range for different R and OLR values is shown. The minimum crack growth driving force decreased as the baseline stress intensity factor range increased. This result is also supported by previous research work [63]. Therefore, the minimum crack growth driving force is a function of the OLR, R ratio and baseline stress intensity factor range.

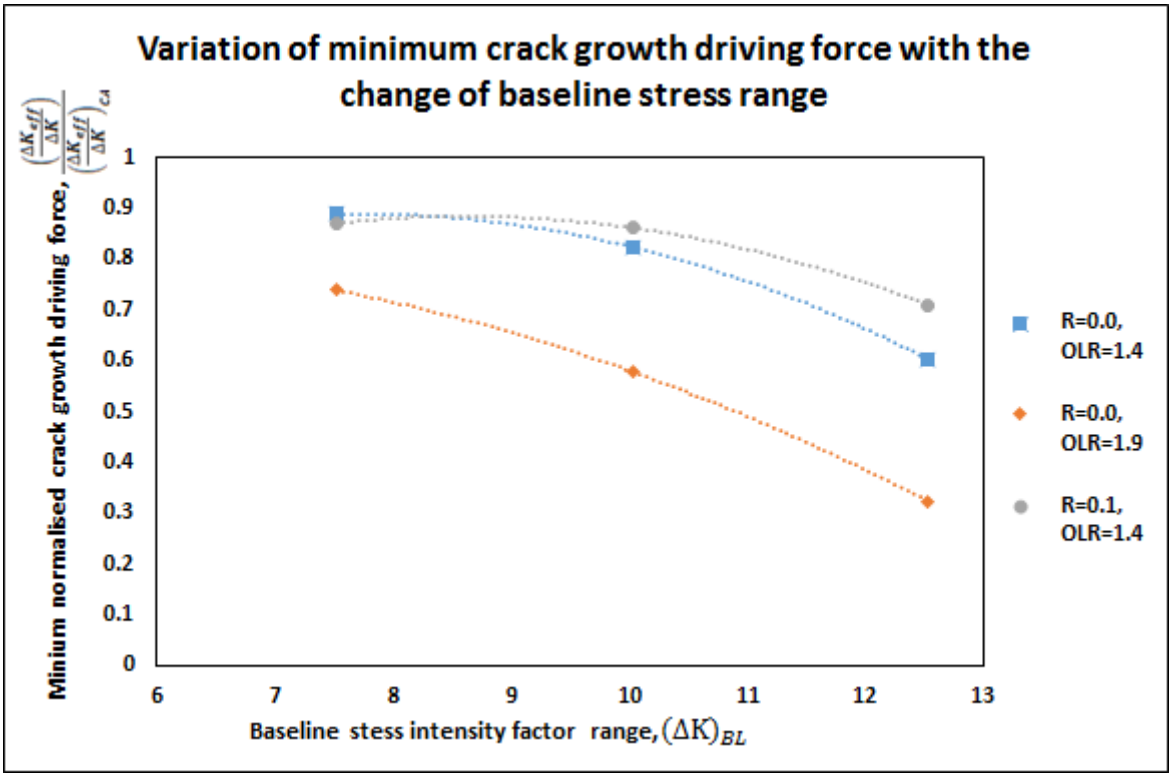

Figure 5.4.1 Variation of minimum crack growth driving force with the change of baseline stress range at different R ratio and OLR.

The size of the overload affected distance was found to have the same size for all cases investigated and this size is equal to the overload plastic zone size. The literature results are not conclusive on this as some research has shown that the overload affected zone is equal to one overload plastic zone [71, 271] and others found it to be much larger than the overload plastic zone [67, 151]. It has been reported [63] that the size of the overload affected zone is dependent on the specimen and loading conditions. In the present work, the maximum closure distance was a quarter of the overload plastic zone size for different OLR and baseline stress intensity factor range conditions. However, it gradually shifted to the left as the R ratio increased. This kind of shift with the increase of *R* was also observed in other studies [63, 67]. In addition, the present study showed that the fatigue crack growth driving force increased and crack closure decreased with the increase of constraint factor, α. As such, this constraint factor, α can be used to explain three dimensional plasticity induced crack closure (PICC) including plane stress, plain strain and mixed of plane stress and plane strain conditions.

5.5 Summary

This strip yield model was proven powerful to simulate and predict the near-tip crack opening profile and the stress distribution around the crack tip. The crack closure effect due to variable amplitude (VA) loading can be explained in detail using this model. The OLR and baseline stress intensity factor had a positive effect on retarding the crack growth driving force by increasing the crack closure. The R ratio at constant k_{max}, had a negative effect on retarding the crack growth due to the reduction of the crack closure. The maximum crack growth retardation point was also found to shift left as the value of R increased. The results also showed that the constraint factor, α can be effectively used to explain three dimensional plasticity induced crack closure (PICC) effect.

6 Effect of plastic deformation on compliance curve based crack closure measurement

6.1 Introduction

The damage tolerance design (DTD) approach is regarded as an improved design philosophy which was introduced in the 1970's due to the limitation of previous approaches including fail-safe, and safe life design approaches [19, 22, 24]. Under this design approach, a crack may remain in the structure. However, the crack growth rate is monitored based on the fracture mechanics approach and an inspection program is set up so that the crack does not go beyond the critical limit starting from the initial detectable crack length. At the moment, this design philosophy remains conservative in its nature [7]. The inclusion of the crack closure concept for accurate fatigue crack growth life prediction will make the damage tolerance design more practical and reliable.

It is generally accepted that the crack growth driving force can be influenced by intrinsic and extrinsic factors occurring around the crack tip. Intrinsic behaviour is affected by deformation heterogeneity, and crack tip plasticity in relation to grain size, secondary phase particle separation and/or dislocation cell size. Extrinsic factors include crack tip shielding processes (e.g. crack closure), environment and loading conditions which may not depend on the microstructure of the material.

Fatigue crack closure is the phenomenon which is widely considered to cause reduction in the fatigue crack growth driving force due to the premature contact of crack faces at positive load levels during cyclic loading. The concept of crack closure has been successfully used to rationalise various types of crack growth behaviour such as overload retardation, underload acceleration, and load sequence effect under variable amplitude loading [9, 10, 24, 81, 100, 108, 109, 272]. There are different types of crack closure mechanisms available in the literature such as plasticity induced crack closure (PICC), roughness induced crack closure (RICC), oxide induced crack closure (OICC), etc. [87, 179, 273-276]. Various microstructural and micromechanical factors influence the premature contact of the crack surface or crack closure. It is evident that separation of intrinsic and extrinsic behaviour in terms of isolating the crack closure

effect from the crack tip plasticity effect can further improve the crack growth life prediction model. According to Singh et al. [277], it is found that the crack-tip nonlinear parameters including the range of cyclic plastic strain, crack tip opening displacement, size of reversed plastic zone and total plastic dissipation per cycle are influenced by the crack closure mechanism. To obtain these nonlinear parameters accurately, crack closure needs to be isolated, and the effective stress intensity factor should be utilised. On the other hand, near-tip plasticity may have an influence on crack closure level. Hence, discretisation of crack closure and crack tip plasticity will yield more accurate fatigue crack growth life prediction.

In 1970, Elber [78] first observed the crack closure effect on striation of fatigue crack growth. The details of this effect are given in Equation 2.5.1. Crack closure measurement methods can be divided into four groups: (i) direct observation of the crack tip, (ii) indirect observation derived from crack growth observations, (iii) indirect observation derived from physical compliance measurement and (iv) indirect observation derived from mechanical compliance measurement [9, 133, 265]. Among them, mechanical compliance measurement is the most widely used method where crack closure/opening point (P_{cl}/P_{op}) is identified at the initial deviation of the linearity in a given compliance curve of the cracked sample. Figure 6.1.1. illustrates a widely used method for crack closure measurement where the crack closure point is identified as the transition point of the linear part (solid line) representing a fully open crack and the non-linear part (dotted line) representing a gradually closed crack.

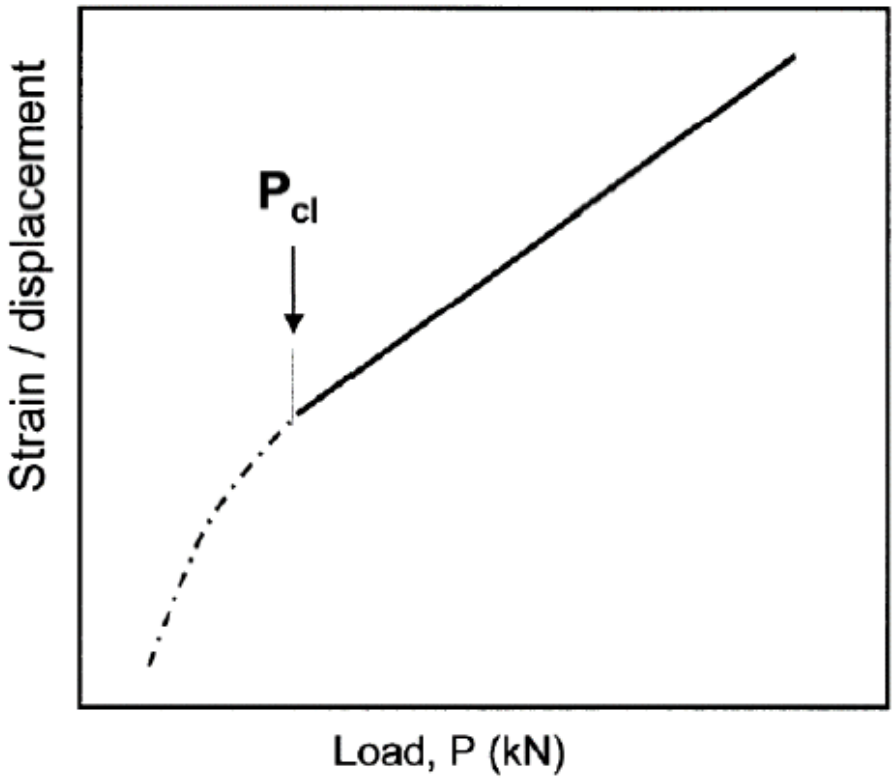

Figure 6.1.1 Schematic illustration of compliance curve based crack closure measurement.

The identification of this P_{cl}/P_{op} is affected by the material, loading and measurement technique used [9, 24, 278, 279]. It is perhaps not surprising that there is a large discrepancy in the results reported in the literature on crack closure measurement. Given the importance associated with the identification of a closure point, it is essential to make the mechanical compliance measurement technique more systematic, accurate and reliable. More detailed investigation of the compliance curve and factors affecting the change in the compliance are therefore needed.

Fatigue crack growth behaviour depends on localised stress-strain behaviour around the crack tip. Many micromechanical and microstructural factors control extrinsic and intrinsic behaviour of fatigue crack growth resistance. Plasticity induced crack closure is considered as the extrinsic behaviour widely used to rationalise fatigue crack growth resistance during variable amplitude (VA) loading. An accurate qualitative and quantitative analysis of crack closure is essential for fatigue crack growth prediction and damage tolerance design (DTD). On the other hand, crack tip plasticity is often controlled by material microstructure and hence related to the intrinsic behaviour of

the material. It is therefore possible that the plasticity-induced crack closure detected based on the mechanical compliance curve may be influenced by the intrinsic plastic deformation at the crack tip. This chapter presents an investigation of the effect of crack-tip plasticity on the non-linearity of the compliance curve in the aluminium alloy 6082-T651. An Experimental technique as well as finite element (FE) modelling and Strip yield modelling have been used to demonstrate the non-linearity of the compliance curve in the absence of crack closure. The result can be adopted to quantify crack closure more accurately when a compliance-based measurement technique is used.

6.2 Material and geometry specifications

Damage tolerant aluminium alloy 6082-T651 has been used in this study. The detail of this material has already been given at Section 4.2 in Chapter 4. A centre-cracked tension (CCT) specimen has been used, with width, W, of 150 mm, gauge length, L, of 400 mm and thickness, t, of 1.6 mm. The half crack length, a, was 8 mm.

6.3 Methodology

6.3.1 Experimental setup

A hydraulic fatigue machine was used to load the specimen from 0 to 19.2 kN gradually. Two near crack-tip strain gauges located at 2 mm ahead from the crack tip, G_1, and 8 mm ahead from the crack tip, G_2, and one crack mouth strain gauge, G_3, were used to capture strain during the loading. The schematic view of the test rig set-up is given in Figure 6.3.1 and the actual view is similar to Figure 4.3.2.

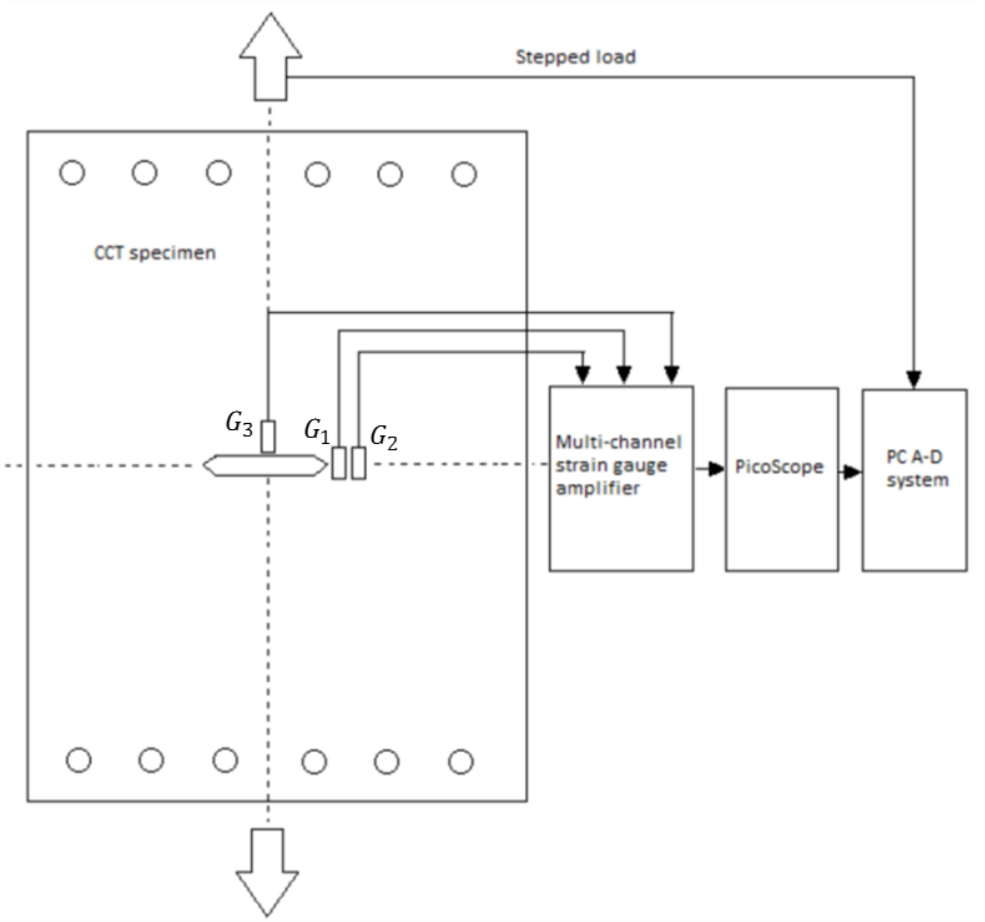

Figure 6.3.1 Schematic view of the test set-up.

6.3.2 Finite element (FE) model construction

For the FE analysis, Ansys 16.0 was used. The FE modelling procedure was the same as in earlier reported work [24, 110]. The following material properties were chosen; Young's modules, E=70 GPa, Yield strength, σ_{ys}=268 MPa, Poisson's ratio, v=0.33 and kinematic hardening modulus (bilinear model), H=0, corresponding to aluminium alloy 6082-T651 properties. Different values of H could possibly be used once this model has been developed as a crack closure model to increase the accuracy of the closure level as suggested by [280].

Only one-quarter of the specimen was considered due to the symmetry of the model in plane stress condition. Figure 6.3.2 shows the schematic view of the FE model. Q4

(4 node quadrilateral) elements were used for cracked specimen modelling as suggested by [10, 24, 81, 99, 101, 105]. Higher order elements are computationally expensive, and their use might not improve the accuracy of the result as crack tip zone modelling is governed by the element size and convergence analysis [272, 281].

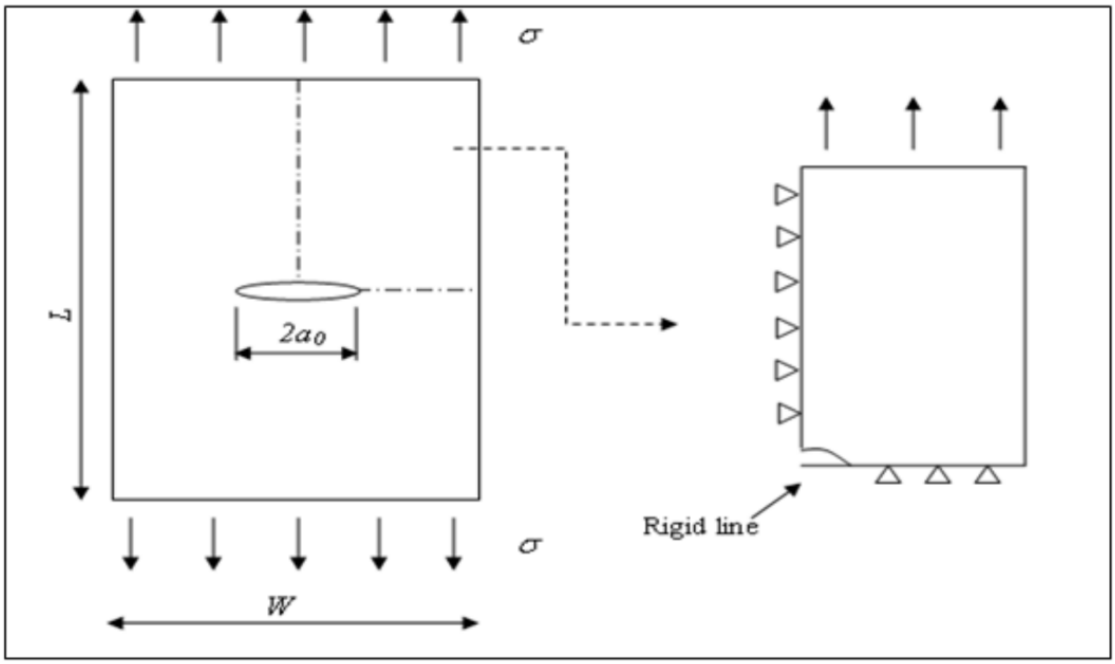

Figure 6.3.2 Schematic view of the FE model [110].

To capture the stress singularity near the crack tip, a dense mesh was used near the crack tip and a coarse mesh was used away from the crack tip (Figure 6.3.3.). After performing a mesh density study, the element size around the crack tip was selected as 24 μm which fulfils the criterion, $\frac{E_p}{R_p} \leq 0.1$ (where E_p=Element size around the crack tip, R_p=forward plastic zone size at the crack tip) as adopted in previous research works [10, 99, 101, 105, 110] according to which this approach is expected to produce a more accurate model of crack tip field which is a primary concern for this study.

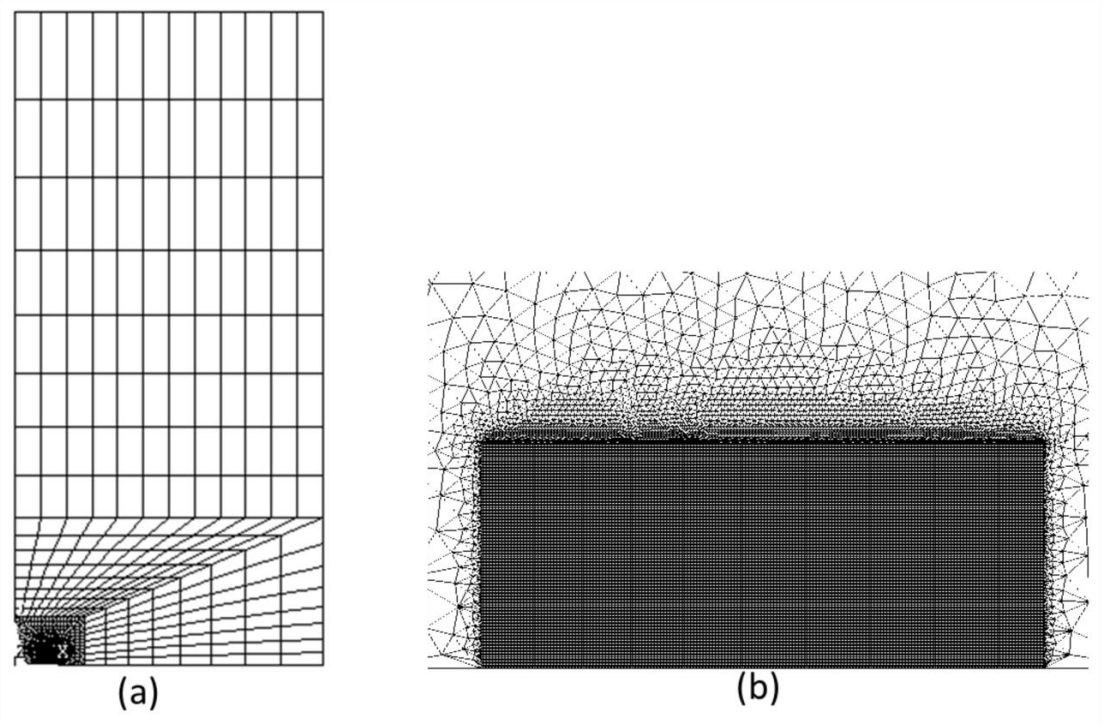

Figure 6.3.3 FE: (a) Mesh of the quarter model, (b) dense mesh around the crack tip.

The specimen was loaded from 0 kN to 19.2 kN, and corresponding strains were measured at four nodes: three near crack-tip nodes including 2 mm ahead of the crack tip, N_1, 0.4 mm ahead of the crack tip, N_2, 7.6 mm ahead from the crack tip, N_3 and one crack mouth node, N_4.

6.3.3 Strip yield model construction

The strip yield model is based on the modified Dugdale model [62, 86, 133]. It is used to simulate crack closure of a centre cracked tension (CCT) specimen under fatigue loading [9, 62, 90, 282]. Aluminium alloy 6082-T651 with similar geometry and material properties as in the FE study was used. The details of the model are given in Section 5.2.2 in Chapter 5.

The model was loaded up to 19.2 kN with an initial load of zero and corresponding vertical displacements at different increments of loading were measured at the near crack-tip point, P_1 0.002 mm ahead of the crack tip. Crack closure was absent as no

crack growth was considered and plane stress condition is considered to keep it comparable with the FE model.

6.4 Results and analyses

6.4.1 Experimental analysis of nonlinear compliance curve

Figure 6.4.1. shows the compliance curve and offset compliance curve of strain gauge, G_1. It was evident that, these curves were not quite linear. The shape of the non-linearity was a 'sagging' type. The compliance curve showed a lower gradient of 0.0874 $\left(\frac{\mu\varepsilon}{N}\right)$ at lower levels of the loading and a higher gradient of 0.0928 $\left(\frac{\mu\varepsilon}{N}\right)$ at higher levels of loading (Figure 6.3.1(a)). The gradient difference was 0.0054 $\left(\frac{\mu\varepsilon}{N}\right)$. From the offset compliance curve, the non-linearity was quite clear (Figure 6.4.1(b)). A 'transition point' was found at 6 kN loading, where the curve significantly changed its direction (initial deviation) from its initial linearity of zero strain. The compliance curve found in the presence of closure has also this type of 'transition point' which is considered as a 'closure point' [78]. It should, however, be noted that this non-linearity and the 'transition point' similar to the 'closure point' has nothing to do with crack closure. There is no crack closure for a stationary crack and the nonlinearity is caused by the crack-tip plasticity as G_1 is very close to the crack tip plastic zone.

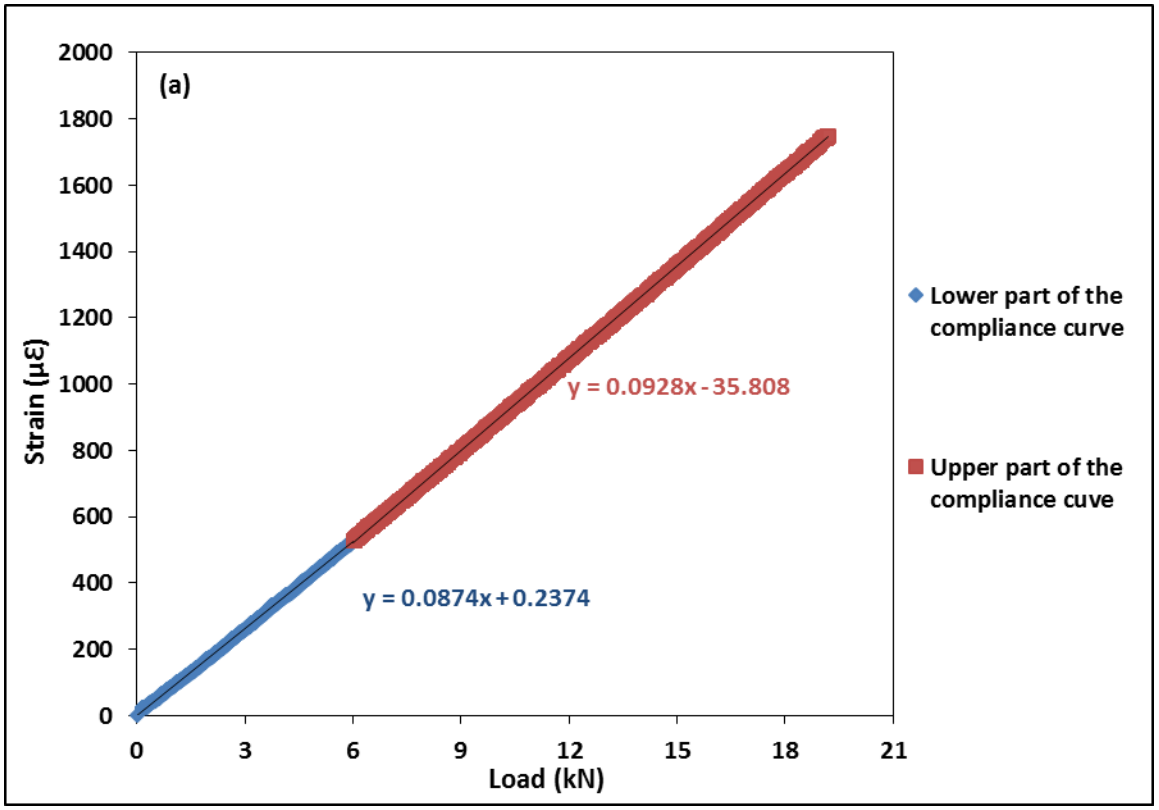

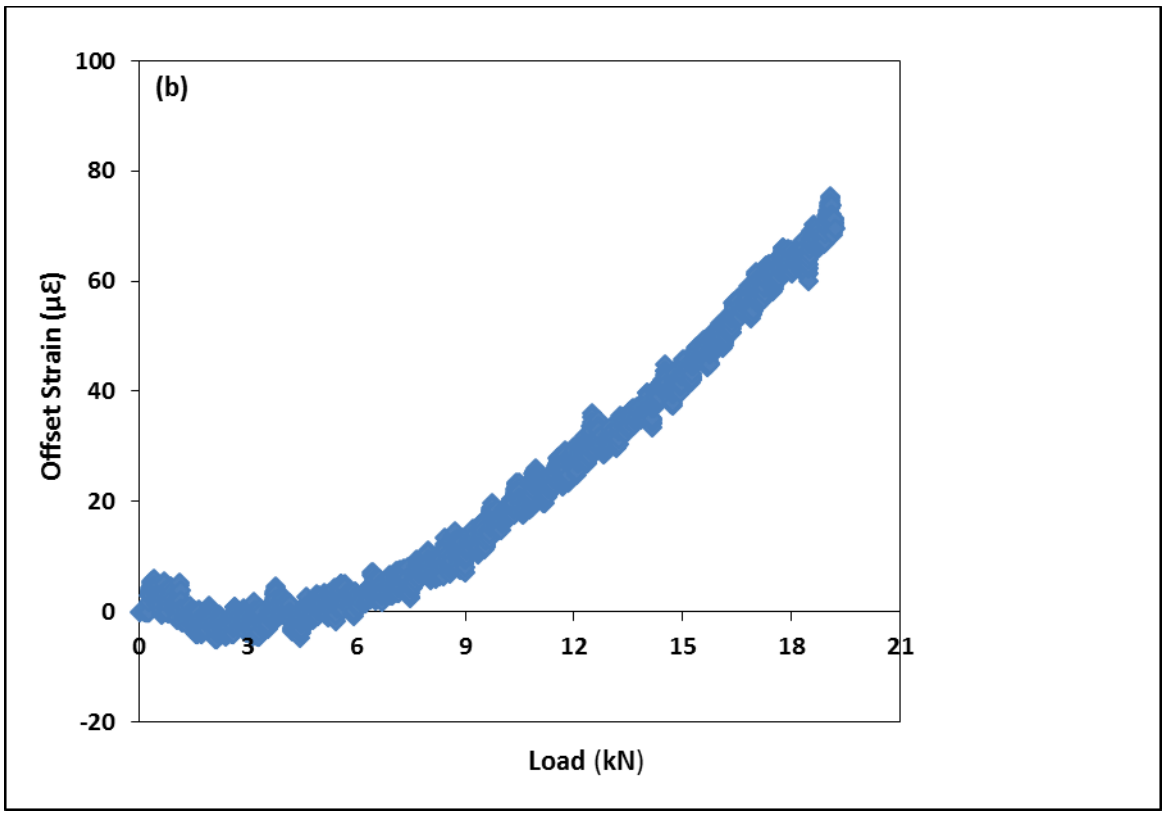

Figure 6.4.1 (a) Compliance curve of near crack-tip strain gauge, G_1, 2 mm ahead of the crack tip, (b) offset compliance curve of near crack-tip strain gauge, G_1, 2 mm ahead of the crack tip.

Figure 6.4.2. shows the compliance curve and offset compliance curve of G_2. These curves were found to be nonlinear as well with a similar 'sagging' shape. [133, 265] also showed non-linearity in the compliance curve in strain gauges away from crack-tip when crack closure was considered. The gradients of the lower part and upper parts were 0.0604 $\left(\frac{\mu\varepsilon}{N}\right)$ and 0.0638 $\left(\frac{\mu\varepsilon}{N}\right)$, respectively (Figure 6.3.2(a)). The difference between these two gradients was 0.0034 $\left(\frac{\mu\varepsilon}{N}\right)$, which was lower than the gradient difference of the compliance curve for G_1. As G_2 was away from the crack tip plasticity, the compliance curves were less influenced by the plasticity effect. Non-linearity was visually clear in the offset compliance curve (Figure 6.3.2(b)). The offset compliance curve showed a 'transition point' at 6 kN loading (Figure 6.4.2(b)), which is consistent with the result obtained from strain gauge G_1.

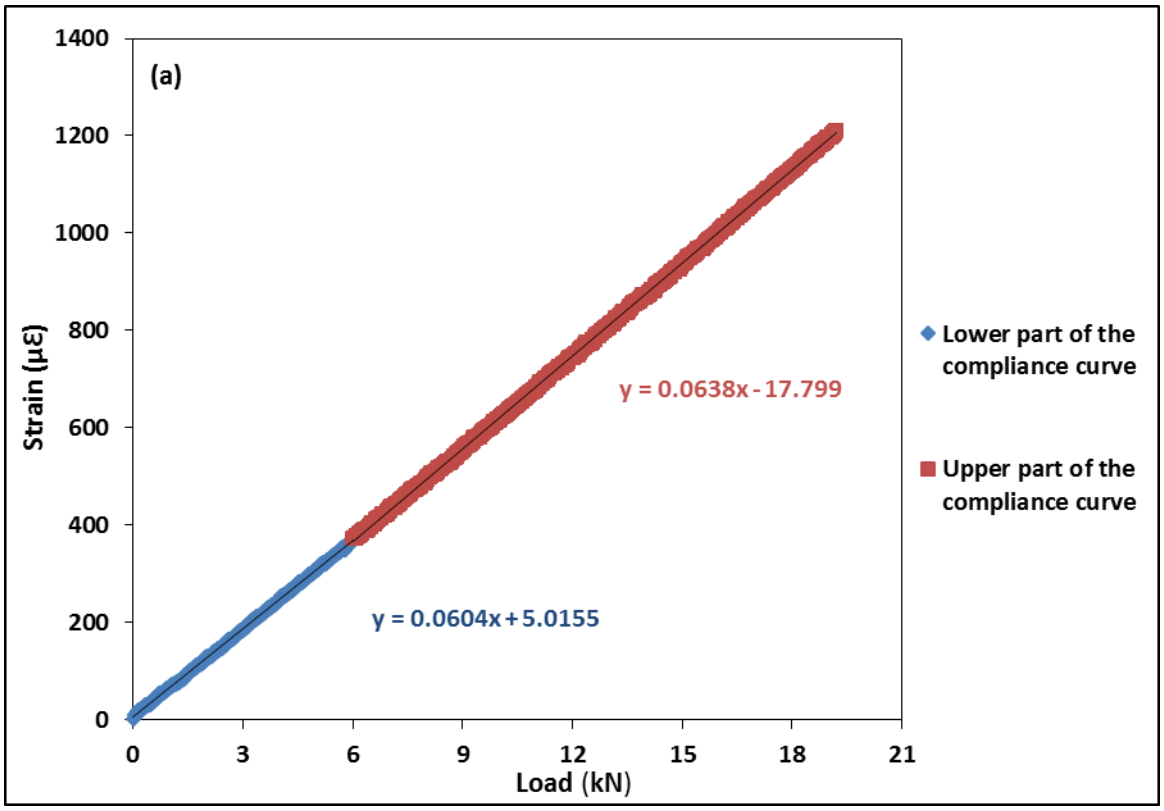

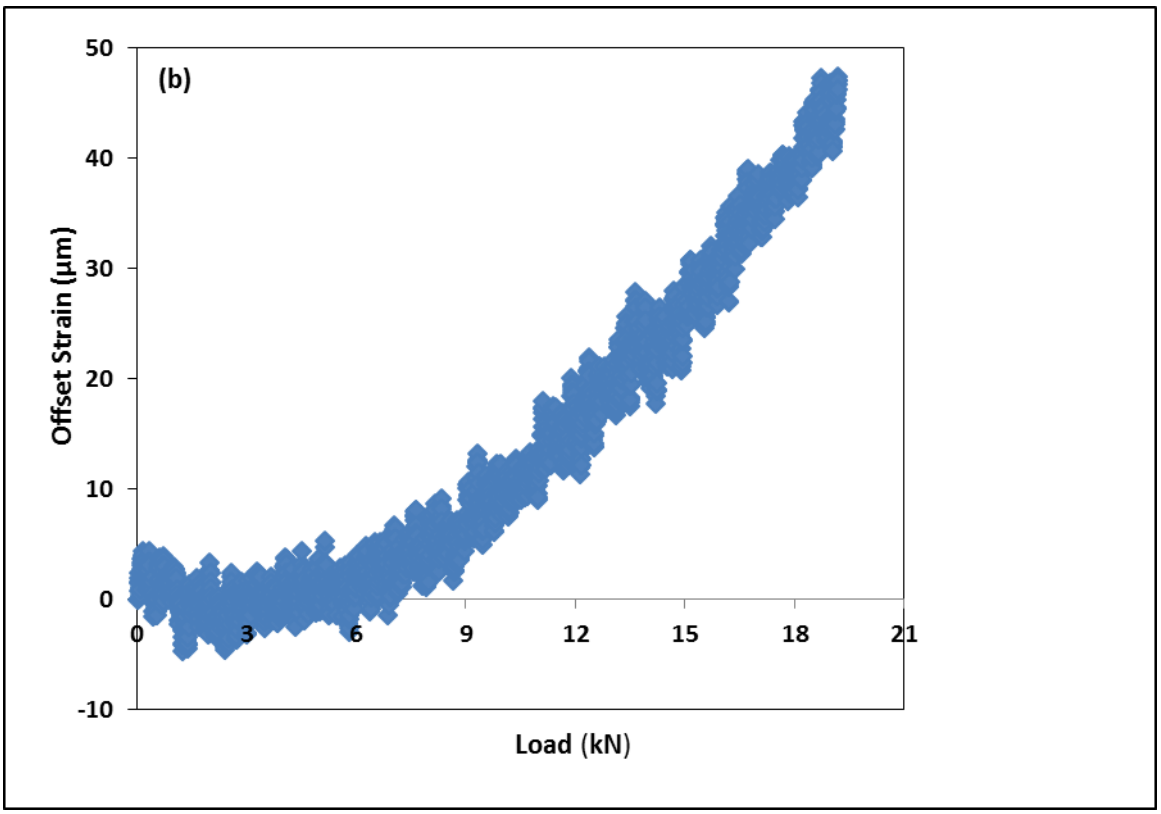

Figure 6.4.2 Experimental: (a) compliance curve of near crack-tip strain gauge, G_2 at 8 mm ahead of the crack tip, (b) offset compliance curve of near crack-tip strain gauge, G_2 at 8 mm ahead of the crack tip.

Figure 6.4.3. shows the compliance curve and offset compliance curve of gauge, G_3. The characteristics of the curves were similar to gauge, G_1 curves in terms of shape. [133, 265] also showed non-linearity in the crack mouth strain gauge when crack closure was considered. In the compliance curve, the gradient of the lower part and upper part were 0.0122 $\left(\frac{\mu\varepsilon}{N}\right)$ and 0.0131 $\left(\frac{\mu\varepsilon}{N}\right)$, respectively (Figure 6.4.3(a)). The difference between the lower part gradient and the upper part gradient was 0.0009 $\left(\frac{\mu\varepsilon}{N}\right)$, which was less compared to other two compliance curves. Therefore, the level of non-linearity was less as it was further away from the crack-tip plasticity zone. The offset compliance curve showed a 'transition point' at 6 kN loading (Figure 6.4.3(b).) which the data obtained from strain gauge G_1 and G_2.

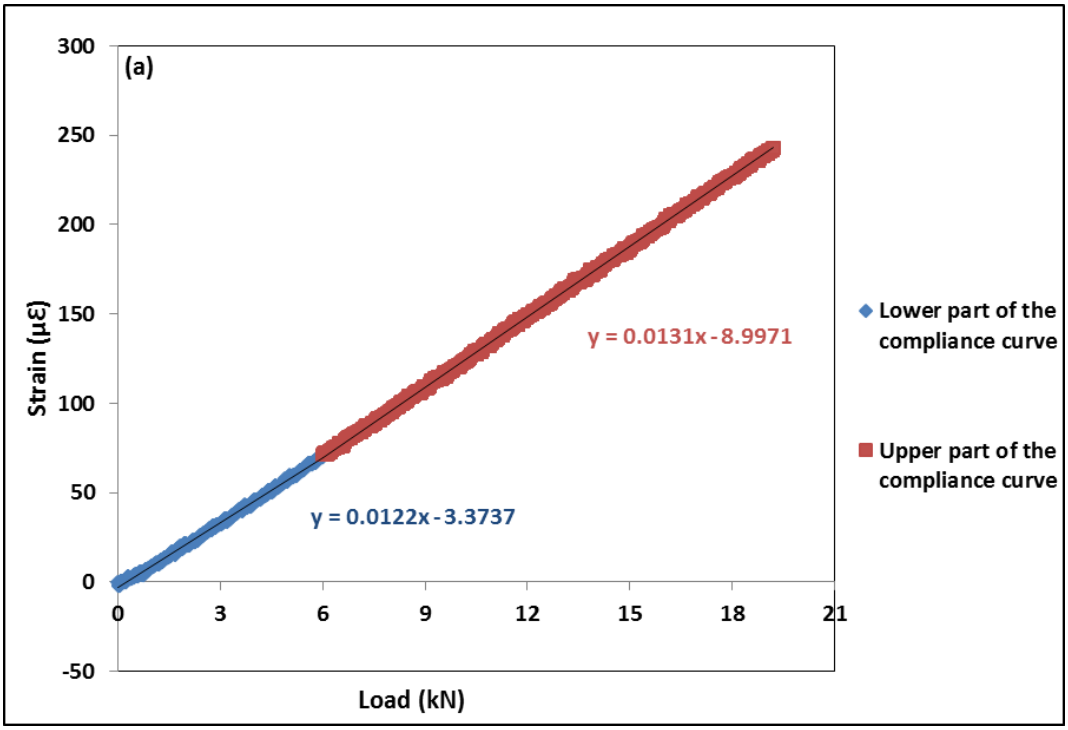

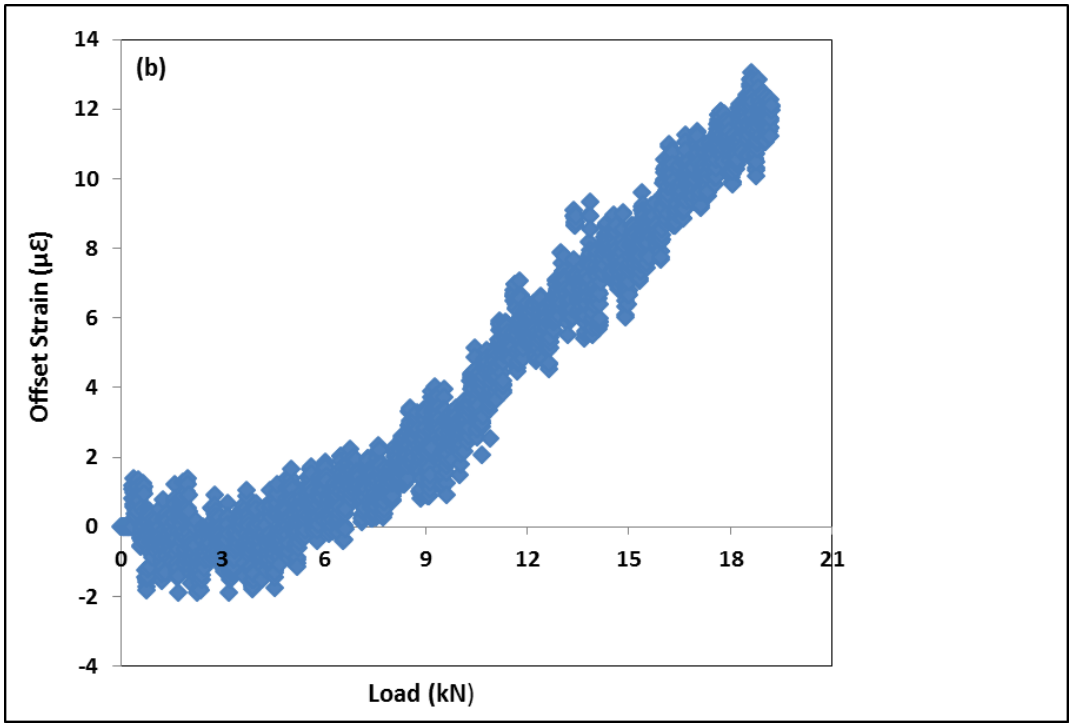

Figure 6.4.3 Experimental: (a) Compliance curve of near crack-mouth strain gauge, G_3, (b) Offset compliance curve of crack-mouth strain gauge, G_3.

6.4.2 Finite element (FE) analysis of non-linearity of the compliance curve

Figure 6.4.4. shows the compliance curve and offset compliance curve of N_1. It was evident that these curves were not quite linear. There was a certain non-linearity existing. A 'sagging' type non-linearity was apparent with a lower part gradient of 0.0864 $\left(\frac{\mu\varepsilon}{N}\right)$ and an upper part gradient of 0.0937 $\left(\frac{\mu\varepsilon}{N}\right)$. The gradient difference was 0.0076 $\left(\frac{\mu\varepsilon}{N}\right)$. This value was quite closer to the experimental value of 0.0073 $\left(\frac{\mu\varepsilon}{N}\right)$ obtained from gauge, G_1. The 'transition point' was at 6 kN loading. This non-linearity in the compliance curves were due to the crack-tip plasticity effect but it was operating quite similar to the plasticity induced crack closure (PICC) around the crack tip.

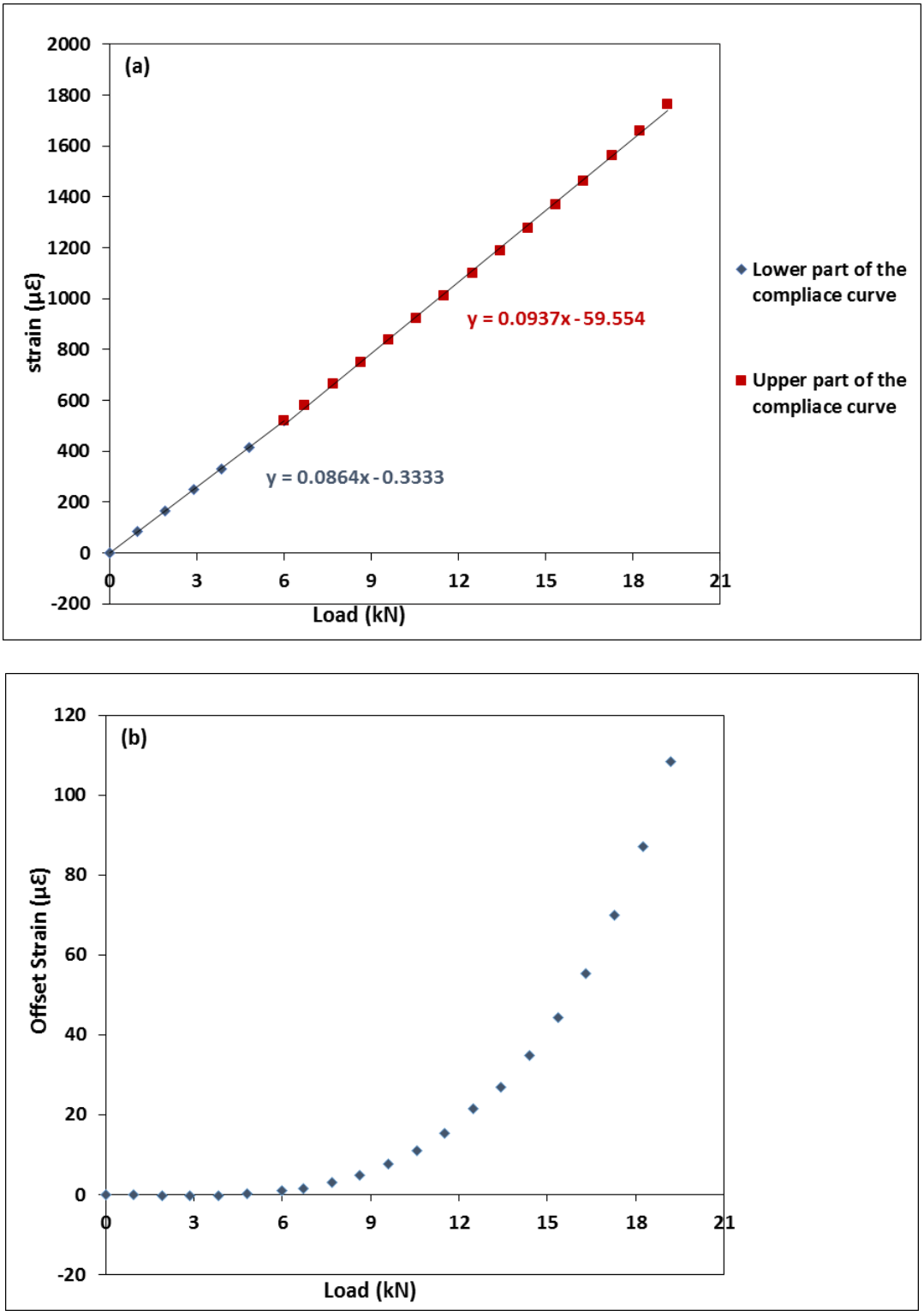

Figure 6.4.4 FE: (a) compliance curve of near crack-tip node, N_1 2 mm ahead of the crack tip, (b) offset compliance curve of near crack-tip node, N_1 2 mm ahead of the crack tip.

Figure 6.4.5. shows the compliance curves of nodes N_2, N_3 and N_4. It was evident that, these curves were linear, except for the compliance curve of node N_2. As node N_2 is within the near crack-tip plasticity zone, it experienced the effect of plasticity (Figure 6.4.5(a).). The shape of the non-linearity was also of the 'sagging' type and the intensity of the non-linearity was also more prominent and visible compared to the gauge G_1 (Figure 6.4.1) and node N_1 (Figure 6.4.4) compliance curves. The other two compliance curves of N_3 and N_4 were not influenced by the crack tip plasticity as these were out of the plasticity zone, which is different to the experimental compliance curves of gauge, G_2 and gauge, G_3 (Figure 6.4.4 (b, c)). It is also worth noting that the 'transition point' identified by N_2 is different to that identified by N_1 2 mm ahead of the crack tip and the strain gauges in the experimental method. The FE method and corresponding assumptions may lead to this difference; only one point was considered to calculate the strain in the FE method while strain gauge provided strain values of a particular area in the experimental method.

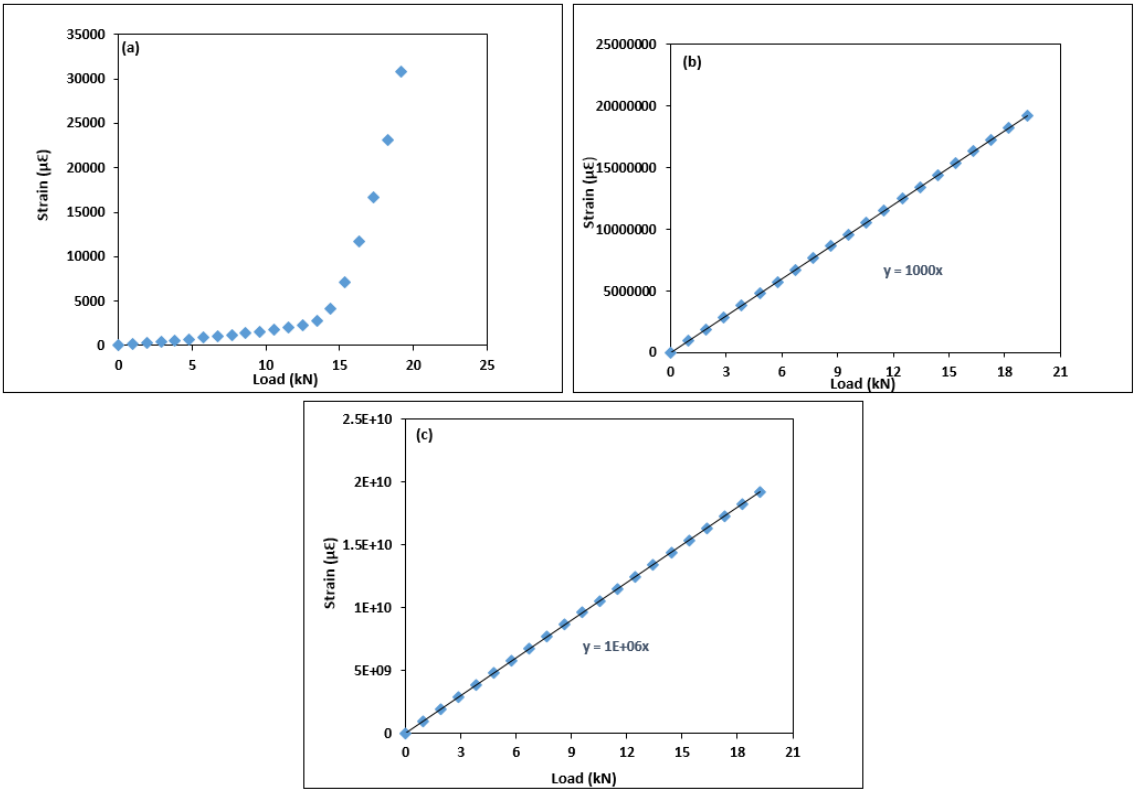

Figure 6.4.5 FE: (a) compliance curve of near crack-tip node, N_2 0.4 mm ahead of the crack tip, (b) compliance curve of near crack-tip node, N_3 7.6 mm ahead of the crack tip and (c) compliance curve of crack-mouth node, N_4.

6.4.3 Strip yield modelling of the non-linearity of the compliance curve

The strip yield model presented in Chapter 5 has been used to obtain the compliance curve of a stationary crack loaded from 0 to 19.2 kN. Figure 6.4.6. shows the compliance curve of a point 0.002 mm ahead of the crack tip. The shape of the curve is of a 'sagging' type and it was quite similar to the compliance curve of N_2, showing a significant level of the non-linearity for material very close to the crack tip. It demonstrates clearly the influence of near crack-tip plasticity on the compliance curve which justifies that the plasticity effect is evident when the point is taken within the plasticity zone and it gets more significant as this point of interest gets closer to the crack tip.

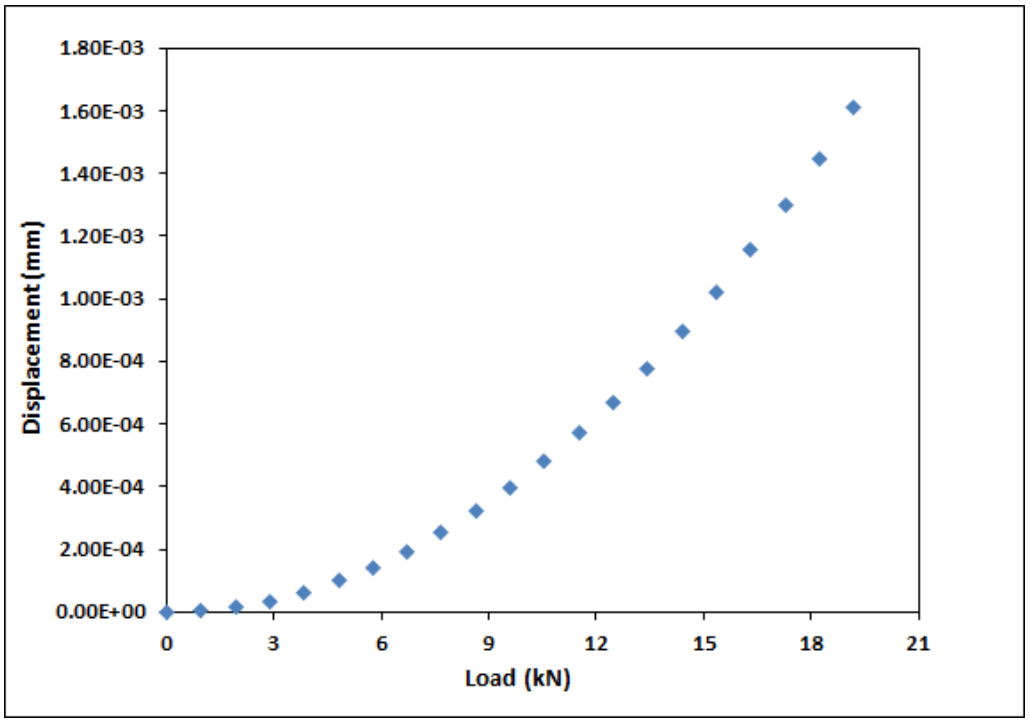

Figure 6.4.6 Strip yield model: compliance curve of near crack-tip node 0.002 mm ahead of the crack tip.

6.5 Discussion

Based on experimental, FE and Strip yield model results, there are a few points, which can be discussed and are stated below:

In the experimental study (Table 6.4.1-6.4.3), all the three strain gauges, including the one near the crack-tip, the one farther away from the crack-tip and the crack-mouth strain gauge, were able to capture the non-linearity of the compliance curve due to crack-tip plasticity even though there is no crack closure for the crack concerned. According to Xu [9], the strain gauge can measure the non-linearity of the compliance curve from a different location aroud the crack tip. In the present study, the near-tip strain gauge was more sensitive to the crack-tip plasticity than the other two strain gauges. It produced more defined nonlinear features in the compliance curve. Here, the ratio of the gradient difference of the lower and upper parts of the compliance curve measured by strain gauges G_3, G_2 and G_1 (Figure 6.3.1) is 1:3.7:6. The offset compliance curve which is of 'sagging' shape was visually more suitable to locate the nonlinear 'transition point'. [7] also suggested that the offset compliance curve technique is more sensitive than the unprocessed compliance curve. This type of offset compliance was quite consistent with the offset compliance curve found due to the closure effect [9]. In that study, a combination of linear and quadratic curve fittings were used.

In FE analysis (Figure 6.4.4), only the near-tip node was able to capture the non-linearity both in the compliance and offset compliance curves. The results of the near-tip node was qualitatively consistent with the experimental results (Figure 6.4.1) in terms of shape, gradient change and 'transition point' although with a few differences in values. The other two nodes including the away crack-tip and crack-mouth nodes were not capable of capturing the non-linearity because of their position being away from the crack-tip plasticity zone. It was not consistent with the experimental result and the reason for that can be explained by the use of different methods and the assumptions made. The node, very close to the crack-tip was more sensitive to the plasticity effect, and it produced a clear nonlinear compliance curve with a 'sagging' shape. It was also determined that as the distance from the crack-tip increased, the sensitivity of the non-linearity reduced and the compliance curve become more linear.

Both the near crack-tip strain gauge in the experimental analysis and the near crack-tip node 2 mm ahead of the crack tip in FE analysis were able to capture the same 'transition point' of the nonlinear curve at 6 kN loading. The experimental and FE compliance and offset compliance curves were approximately overlapping with each other as shown in Figure 6.5.1.

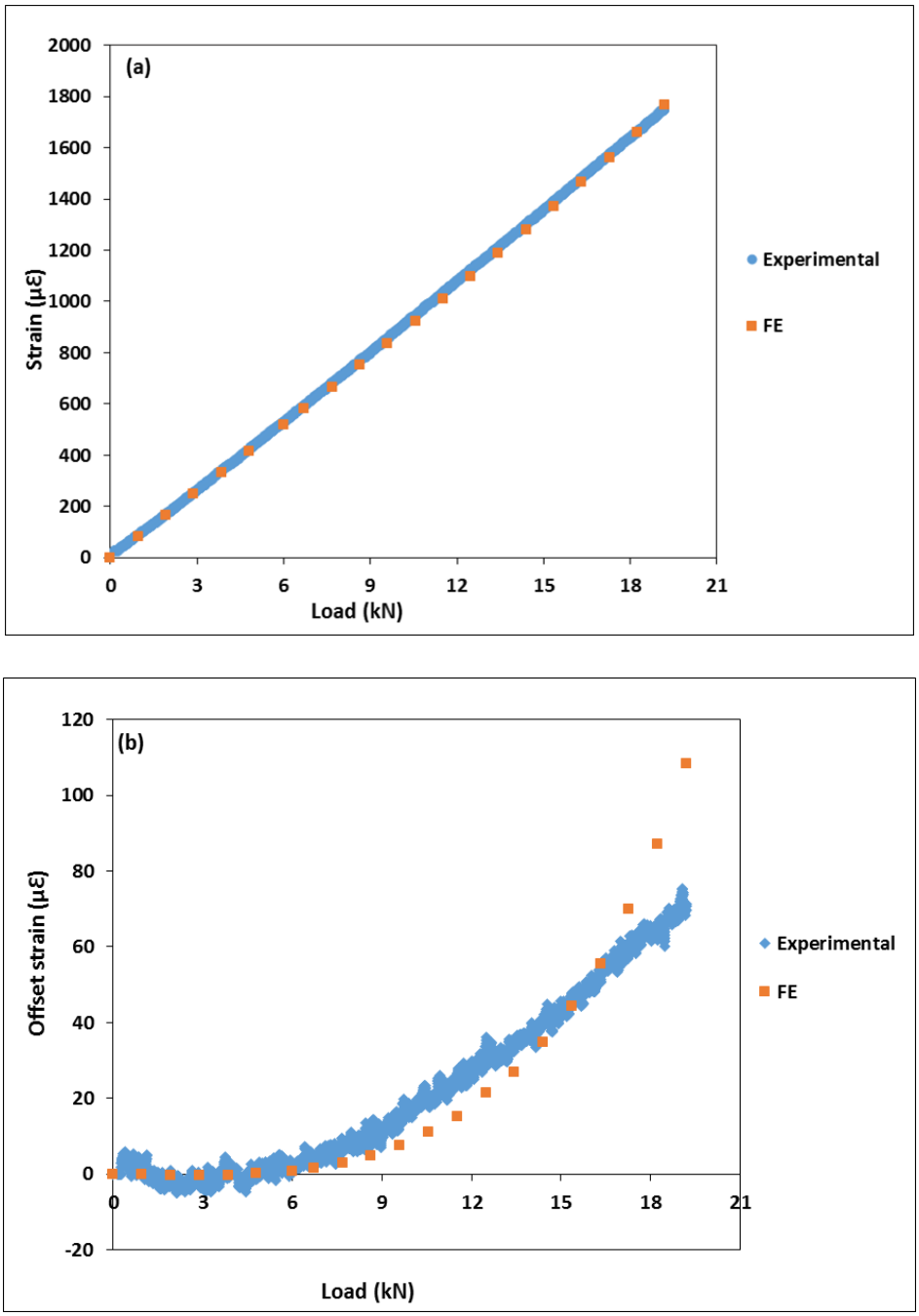

Figure 6.5.1 Comparison of experimental and FE near-tip compliance curves (a) and corresponding offset compliance curve measured 2 mm ahead of the crack tip (b).

In the strip yield model during loading (Figure 6.4.6), the point very near to the crack tip within the plastic zone produced a ‘sagging’ shaped compliance curve which was visually more pronounced. It also verified the FE result which showed quite similar characteristics of higher non-linearity in a node very close to the crack-tip. It is, however, worth noting that, for the stationary crack investigated in the current study, no plastic deformation would be expected behind the crack tip. As such, the non-linearity is not related to the plasticity-induced crack closure, but it is directly linked to the plastic deformation ahead of the notch or crack tip for a fatigue crack. The conventional compliance based crack closure measurement method could therefore identify false crack closure, causing problems in crack growth life prediction. The fact that the compliance curve measured from a node 0.002 mm ahead of the crack tip shows a much higher transition point, demonstrates further that the compliance curve obtained from the near tip strain gauge or node should be carefully evaluated to identify the correct crack closure level.

6.6 Summary

From the discussion above, it was quite evident that crack-tip plasticity has an effect on the non-linearity of the compliance curve in the absence of crack closure. This effect decreases with the increase of the distance away from the crack-tip. The offset compliance curve was visually more useful to identify the non-linearity than the unprocessed compliance curve. This nonlinearity may lead to the identification of a false crack closure when using the conventional compliance curve based crack closure measurement method. The compliance curve actually contains the information of both crack closure and crack-tip plasticity effect. If one of these is isolated, the other will still have an effect on the compliance curve. To calculate the effective fatigue crack growth driving force, plasticity effects need to be considered carefully so that more accurate qualitative and quantitative fatigue crack growth analysis can be achieved. The effect of crack tip plasticity on the non-linearity of the compliance curve should be separated from that of crack closure to obtain reliable crack closure measurement. The results of this study will enable the development of a more accurate crack growth

life prediction for engineering alloys and damage tolerance design (DTD) for the transport industry.

7 An analytical model for the identification of the threshold of stress intensity factor range for crack growth

7.1 Introduction

The value of the stress intensity factor (SIF) range threshold, ΔK_{th}, for fatigue crack growth (FCG) depends highly on its experimental identification. The identification and application of ΔK_{th} are not well established as its determination depends on various factors including the experimental, numerical or analytical techniques used. Different types of identification methods and factors influencing the threshold have been discussed in the literature review.

Due to the high variability of the ΔK_{th} values, the determination of the FCG threshold cannot be certain [11]. Although several models have been proposed to experimentally identify the threshold values, all of them suffer with issues related to the plasticity induced crack closure (PICC) effects. For this reason, threshold values reported in the literature for the same material can vary over a wide range due to the different procedures that were followed. This chapter presents a new analytical model which can fit the raw FCG experimental data to determine ΔK_{th} with high accuracy. The aim of this model is to present a new procedure to identify the FCG threshold value for a long crack; this approach can overcome the problems related to the experimental procedures reported in the literature. The analytical model proposed here makes use of FCG data obtained from K-increasing tests, which are used to derive the FCG properties of the material under long crack condition, allowing this model to identify the three regions of the entire sigmoidal curve, from the threshold condition up to the final value of the crack length.

Considering the fact that it is difficult to separate the extrinsic threshold from the intrinsic threshold using the crack growth data [181], the focus of this chapter is to develop a model which can reliably predict the overall threshold of the material under certain loading conditions. In particular, since the model makes use of raw data generated with a given specimen geometry under certain loading conditions, the

analysis of raw data includes both the load ratio and the T-stress effects. The value identified with the model can be an intrinsic or an extrinsic value depending on the test conditions at which the data has been acquired. A comparison between the threshold SIF range identified by the model proposed and those found in the literature is presented in this Chapter. The accuracy with which the analytical model is able to fit the raw data is also briefly discussed.

7.2 Methodology

7.2.1 Test results for model development

Crack propagation models built on results obtained from a limited number of tests have a validity range closely linked to the particular experimentation carried out [283]. These models are unable to fit all crack growth data with the same accuracy for the entire range of number of cycles for each test. In order to overcome these drawbacks, several FCG data sets obtained with different materials, loading conditions and types of specimens have been collected from the literature. These datasets have been used to verify the suitability of the model in fitting the experimental raw data as well as to identify the ΔK_{th} values of the materials at the corresponding R values. A short description of the datasets collected from literature follows:

Ghonem and Dore [284] data:

Ghonem and Dore [284] carried out tests at room temperature using M(T) specimens made of aluminium alloy 7075-T6 having a thickness of 3.175 mm. The crack direction was perpendicular to the rolling direction and the loading conditions are reported in Table 7.2.1. Sixty specimens were tested under each loading condition to obtain crack growth curves which were used to compare with their mathematical model.

Table 7.2.1 Loading conditions related to Ghonem and Dore [284] tests.

	$P_{max}\ (kN)$	$P_{min}(kN)$	$\Delta P(kN)$	R
Test I	22.79	13.68	9.11	0.6
Test II	22.25	11.13	11.12	0.5
Test III	15.19	6.08	9.11	0.4

Virkler et al. data [285] data:

The experimental activity reported by Virkler et al. [285] was aimed at determining which crack growth rate calculation method yields the least amount of error when the crack growth rate curve is integrated back to obtain the original 'a' versus 'N' curve data. Crack growth tests were carried out on 68 M(T) specimens, made of aluminium alloy 2024-T3 and having a thickness of 2.54 mm. All tests were conducted under the cyclic load with a maximum value of 5.25 kip/23.35 kN and a minimum load of 1.05kip/4.67 kN at R=0.2.

Wu and Ni [286] data:

The experimental work of Wu and Ni [286] was carried out on compact tension C(T) specimens made of aluminium alloy 2024-T351, having thickness, B = 12 mm and width, W = 50 mm. Tests were carried out with variable amplitude (VA) and constant amplitude (CA) loading. The two samples marked by the authors as CA1 and CA2 and composed of 30 and 10 specimens respectively were tested at constant amplitude (CA) loadings reported in Table 7.2.2.

Table 7.2.2 Loading conditions related to Wu & Ni tests [286].

	$P_{max}\ (kN)$	$P_{min}(kN)$	$\Delta P(kN)$	R
CA1	4.5	0.9	3.6	0.2
CA2	6.118	3.882	2.236	0.63

7.2.2 Model implementation

The analysis of experimental data obtained from FCG tests is quite complex due to the scatter nature in the raw data which is amplified by the derivation needed to compute the FCG rate. Several useful formulae to fit the experimental data with the aim of a better, smoother curve have been proposed and reported in the literature. Among those, the use of a polynomial function to fit the raw data gives the ability to obtain a single numerical expression for the crack growth rate valid in the entire data range [283]. The choice of the most appropriate function can be made considering that the crack growth is exponential by nature. In mathematical terms, an exponential correlation can be represented by introducing logarithmic functions for the crack length [287-289]. This linear correlation (log(a) vs N) can be represented on a semi-logarithmic plane as a straight line. There are models proposed in the literature which are developed adopting an exponential structure [290]. However, the trend identified using the experimental FCG data changes as the crack length approaches the failure condition. This consideration is supported by the presence of three different regions in the sigmoidal curve with each of them following a different trend. On the basis of the aforementioned observations, the most suitable formula to fit the whole FCG experimental data points can be deduced by summating the individual effects of the different crack growth regions [291]. Therefore, the following model, on the basis of a trial and error method, could be established.

$$\mathrm{a}(\tau) = \mathrm{h} \cdot \tau^{\mathrm{p}} + \mathrm{a_{th}} \cdot \mathrm{e}^{\left(\frac{\tau^{\alpha}}{\beta - \tau^{\alpha}}\right)} \tag{7.2.1}$$

where $\alpha,\ \beta\ and\ p$ are three parameters to be determined by the least-square method. The procedure to derive the values corresponding to h and a_{th} is described in later parts of this Chapter. The proposed model makes use of a non-dimensional fatigue crack growth life, which makes it more general. Moreover, the non-dimensional fatigue crack growth life allows decoupling the identification of the equation parameters, which are meant to be a material property, from the actual total life for the particular test. The non-dimensional fatigue crack growth life, τ is defined as follows;

$$\tau = \frac{N + N_{th}}{N_f + N_{th}} \tag{7.2.2}$$

The parameter N_{th}, which is identified through a best-fit curve together with the three parameters (α, β and p) reported above, is related to the nucleation phase and hence to the threshold value. N_f is the final value of the experimental crack growth life, which is the number of cycles counted from the initial crack length up to the final failure of the specimen, whilst N is the generic value of the fatigue crack growth life.

Useful formulae can be derived for other parameters in Equation 7.2.2 by considering some specific data points of the crack growth curve. At $N = N_f$, which corresponds to the last experimental data point of the test, the crack length is equal to the value of the crack length, $a_{f,}$ in the corresponding final front just before the failure condition of the specimen. This gives:

$$h = a_f - a_{th} \times e^{\left(\frac{1}{\beta-1}\right)} \tag{7.2.3}$$

Similarly, considering the value of Equation 7.2.3 at $N = 0$, which corresponds to the first experimental data point, the crack length is equal to the value of the crack length, $a_{th,}$ corresponding to the starting point of the test. This gives:

$$a_{th} = \frac{a_0 - a_f \times \left(\frac{N_{th}}{N_f + N_{th}}\right)^p}{e^{\left(\frac{\left(\frac{N_{th}}{N_f+N_{th}}\right)^\alpha}{\beta-\left(\frac{N_{th}}{N_f+N_{th}}\right)^\alpha}\right)} - \left(\frac{N_{th}}{N_f + N_{th}}\right)^p \times e^{\left(\frac{1}{\beta-1}\right)}} \tag{7.2.4}$$

As already stated, the parameter N_{th} is related to the threshold condition and represents the number of cycles needed by the crack to reach the crack length corresponding to the threshold condition. From Equation 7.2.1, the crack length corresponding to the threshold condition is equal to the value of the a_{th} parameter for $N = -N_{th}$.

Equation 7.2.1 is a continuous differentiable function in the range $N_{th} < N < N_f$. It is, therefore, possible to derive the analytical expression of the crack growth rate, $\frac{da}{dN}$ as a function of N. This function (Equation 7.2.5) can be used to represent the continuous propagation process from the threshold region up to the final fast crack growth region.

$$da/dN(N) = \frac{h\left(\frac{N+N_{th}}{N_f+N_{th}}\right)^p p}{N+N_{th}} + a_{th}\left(\frac{\left(\frac{N+N_{th}}{N_f+N_{th}}\right)^\alpha \alpha}{(N+N_{th})\left(\beta-\left(\frac{N+N_{th}}{N_f+N_{th}}\right)^\alpha\right)} + \frac{\left(\left(\frac{N+N_{th}}{N_f+N_{th}}\right)^\alpha\right)^2 \alpha}{\left(\beta-\left(\frac{N+N_{th}}{N_f+N_{th}}\right)^\alpha\right)^2 (N+N_{th})}\right) e^{\frac{\left(\frac{N+N_{th}}{N_f+N_{th}}\right)^\alpha}{\beta-\left(\frac{N+N_{th}}{N_f+N_{th}}\right)^\alpha}} \quad (7.2.5)$$

The parameters in the crack growth rate function are identified by means of linear regression using the FCG raw data. The analytical expression for the crack growth rate is equal to zero at $N = -N_{th}$ according to the assumption that the crack length at this value corresponds to the threshold condition.

The procedure for applying the formulae of the analytical model to derive the threshold SIF range is as follows;

i. The experimental raw data of crack length versus number of cycles are fitted using Equation 7.2.1. The linear regression method has been adopted to fit the model with the experimental data and obtain four parameters: N_{th}, α, β and p minimising the error. In earlier work [291], the model was adopted to assess the accuracy in fitting the raw data produced during FCG tests. In the same work [291], the normal distribution of the residuals as well as the distribution of the equation parameters have been included. The present work is focused on the identification of the threshold SIF range through the use of this analytical model.

ii. After the identification of the values of the four parameters N_{th}, α, β and p, the values of the other two parameters h and a_{th} can be computed.

iii. The values of the six parameters N_{th}, α, β, p, h and a_{th} identified from Equation 7.2.1 are applied to Equation 7.2.5 which represents the crack growth rate as a function of the fatigue crack growth life.

iv. A vector in the range $[-N_{th}; N_f]$ composed of *n* values is then generated. For each value of the vector defined above, the corresponding values of the crack length and the crack growth rate are determined using Equations (7.2.1) and (7.2.5). The crack length values derived from Equation 7.2.1 are used to deduce the SIF range values by means of the expressions in accordance with international standards [172]. This means that the method requires knowledge of the closed form of the SIF for the tested specimen. In this chapter, the expressions reported by the ASTM E647 standard [172] have been used to compute the SIF values.

v. The value of the crack length corresponding to $N = -N_{th}$ is used to derive the value of the threshold SIF range which corresponds to a crack growth rate equal to zero.

The procedure described above has been implemented using a Matlab code to identify the FCG curves and the ΔK_{th} values using the datasets produced by Ghonem and Dore [284], Virkler et al. data [285] and Wu and Ni [286]. A detailed discussion about the capability of the model to properly fit the datasets used in this chapter is given in earlier work [291]. Figure 7.2.1. shows some examples of fitting results with the experimental points related to set I produced by Ghonem and Dore [284].

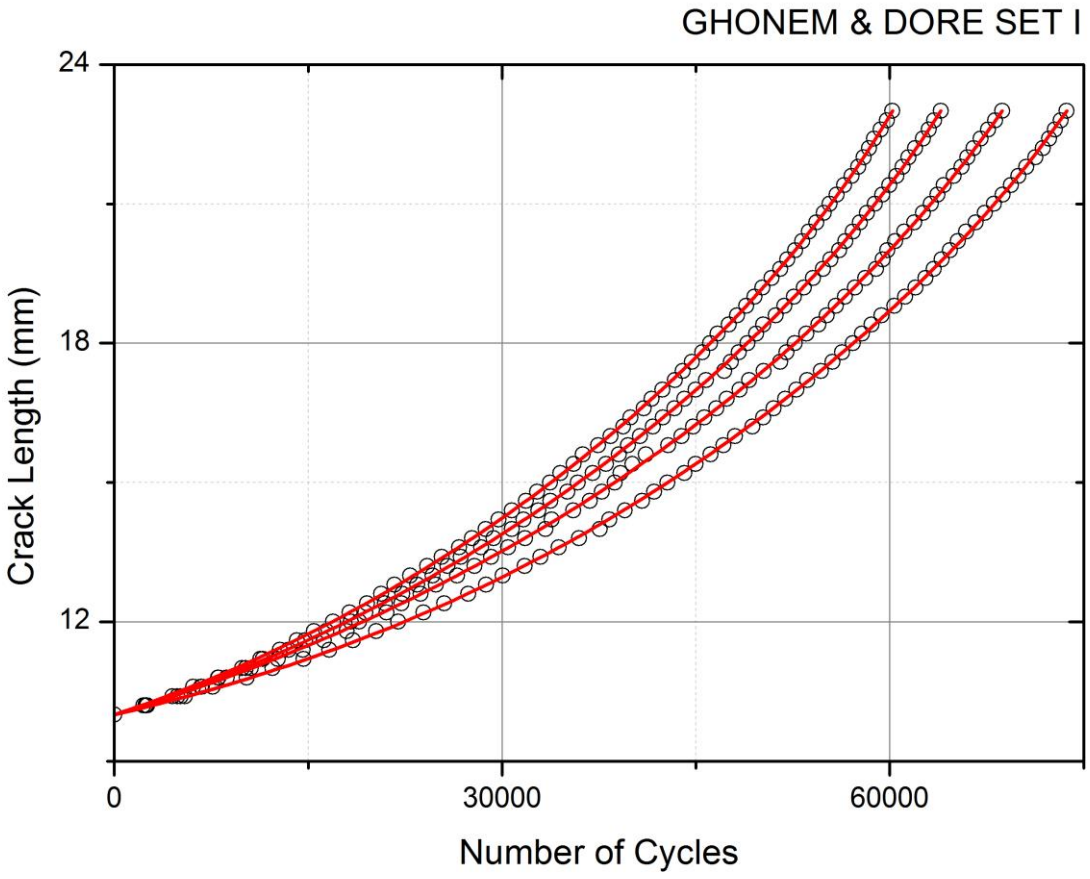

Figure 7.2.1 Four crack growth data from Ghonem and Dore [284] dataset - raw data (dots) analytical model (in lines).

Moreover, the normality of the residuals obtained from each curve has been verified by the χ^2 normality tests and the corresponding residuals frequency histograms have

also been evaluated. In Figure 7.2.2, the two means of the residuals for set I and set III of Ghonem and Dore [284] datasets are shown as an example to highlight that the mean value is equal to zero [291].

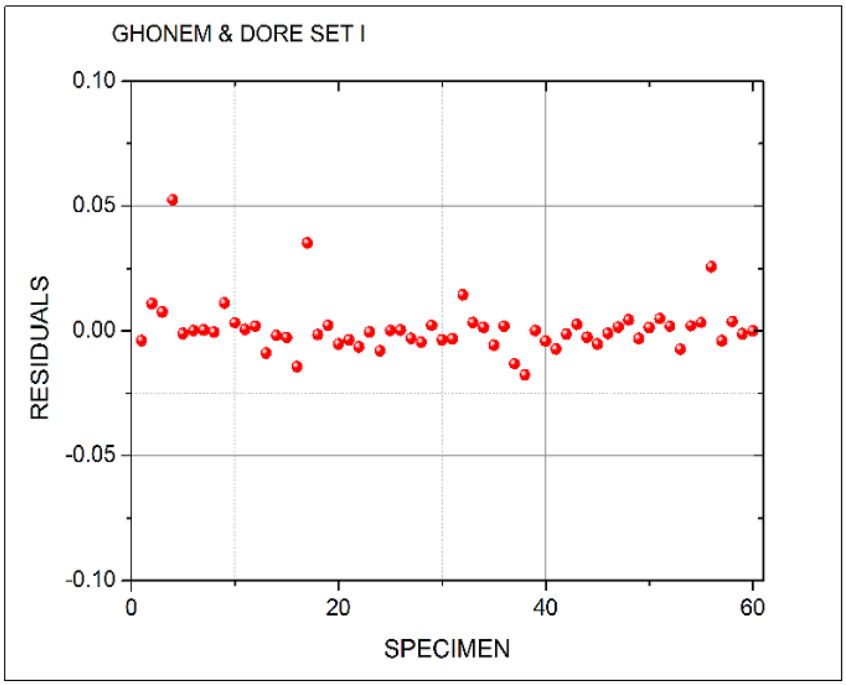

(a)

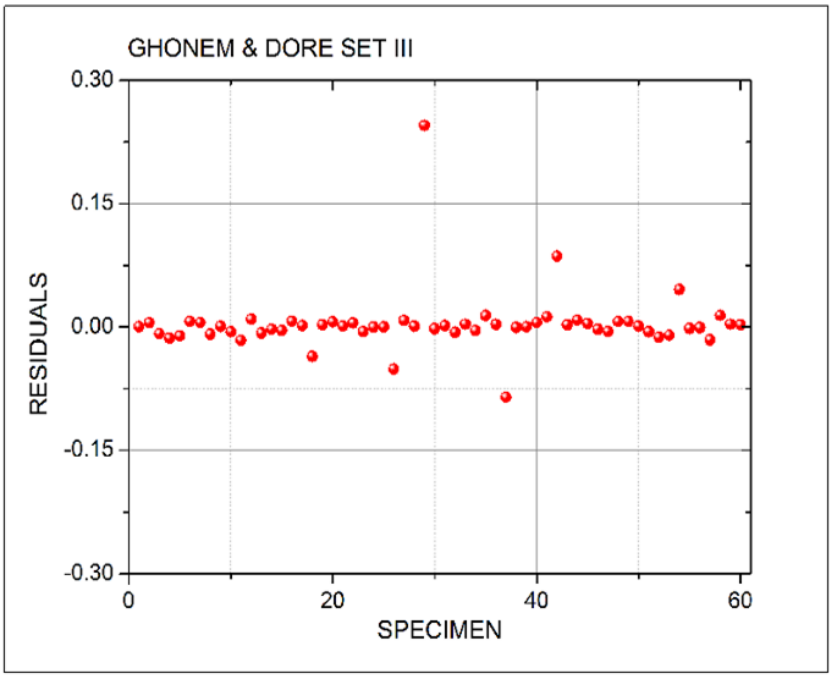

(b)

Figure 7.2.2 Mean of residuals obtained by fitting Ghonem and Dore [284] set I (a) and Ghonem and Dore set III (b).

A further version of the Matlab code, which was already implemented for the fitting curves, was developed in order to identify the values of the FCG rate as well as the SIF range values. In particular, the SIF values in correspondence with $N = -N_{th}$ for each curve of all datasets have been computed in order to estimate the threshold values and compare these with those reported in the literature.

7.3 Results and analyses

The interpolation of the raw experimental data represents the first step of the analysis. The suitability of the equation for fitting the data has been summarised in the above section. In particular, the raw data fitting has an average value of R^2 equal to 0.9998 for all dataset [291]. The values of the parameters obtained for each dataset are shown in Table 7.3.1.

Table 7.3.1 Parameter values for the five datasets.

	α	β	N_{th}	p	h	a_{th}	ΔK_{th} $MPa\sqrt{m}$
Ghonem and Dore dataset no. I *[284]*	1.91	1.34	914314	4.40	6.75	0.81	1.42
Ghonem & Dore dataset no. II *[284]*	1.69	1.33	695502	3.43	6.33	0.72	1.63
Ghonem & Dore dataset no. III *[284]*	4.73	1.53	1635716	4.58	6.38	1.57	1.90
Virkler et al. [285]	2.93	1.28	2211197	6.59	19.84	0.75	2.79
Wu and Ni [286]	58.04	1.85	842999	6.45	21.25	3.65	3.61

The values reported in Table 7.3.1. have been computed as an average of the values obtained over the total number of tests for each dataset.

The crack length as a function of the number of cycles derived in the range $[-N_{th}; N_f]$ is shown for each data set in Figure 7.3.1. In particular, the curve fitting related to the three datasets produced by Ghonem and Dore [284] is shown in the top of Figure 7.3.1 (Set I - Set II - Set III), the curves related to the dataset produced by Virkler et al. [285] and the curves related to the datasets produced by Wu and Ni [286] are shown at bottom row of the Figure 7.3.1. In each dataset, all the fitting curves tended to the same asymptotic value as the number of cycles approaches $-N_{th}$ even though the values are different between the various datasets. Log-linear plots have been used in order to make possible the comparison between the experimental data points and the curves identified by the analytical model.

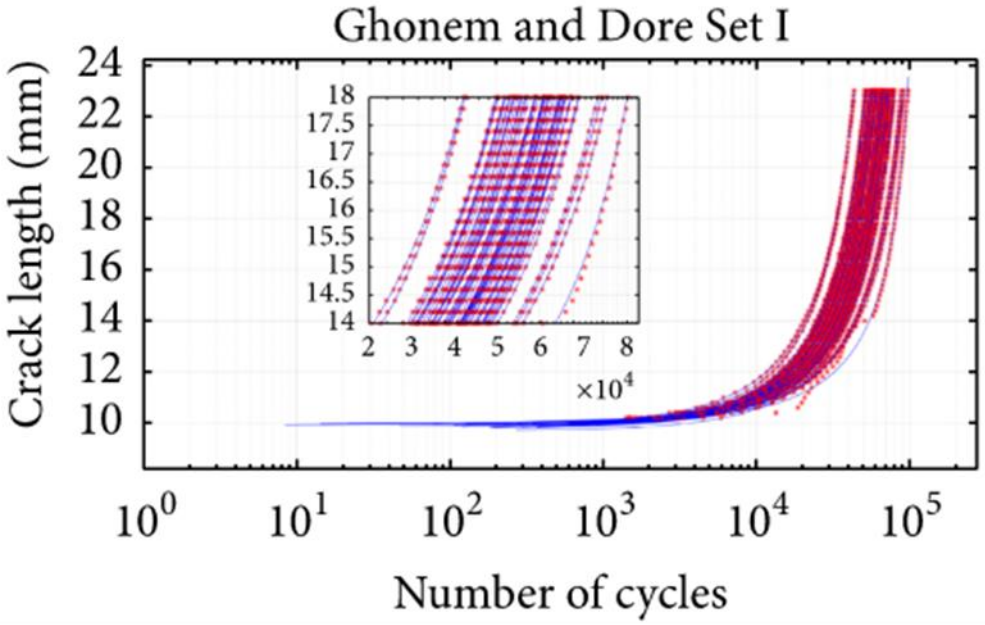

(a)

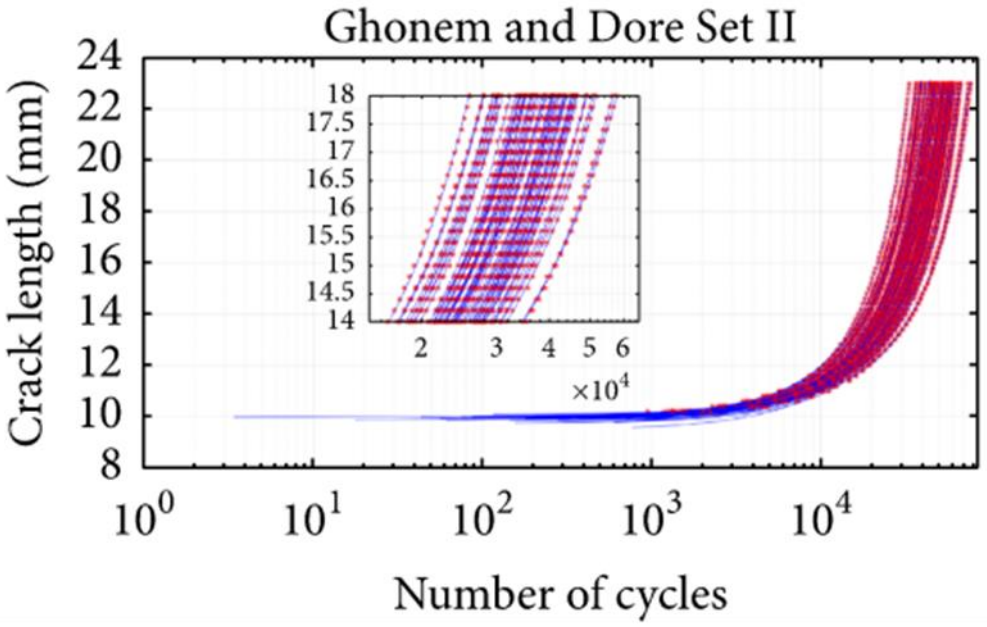
Ghonem and Dore Set II
Crack length (mm)
Number of cycles
×10^4

(b)

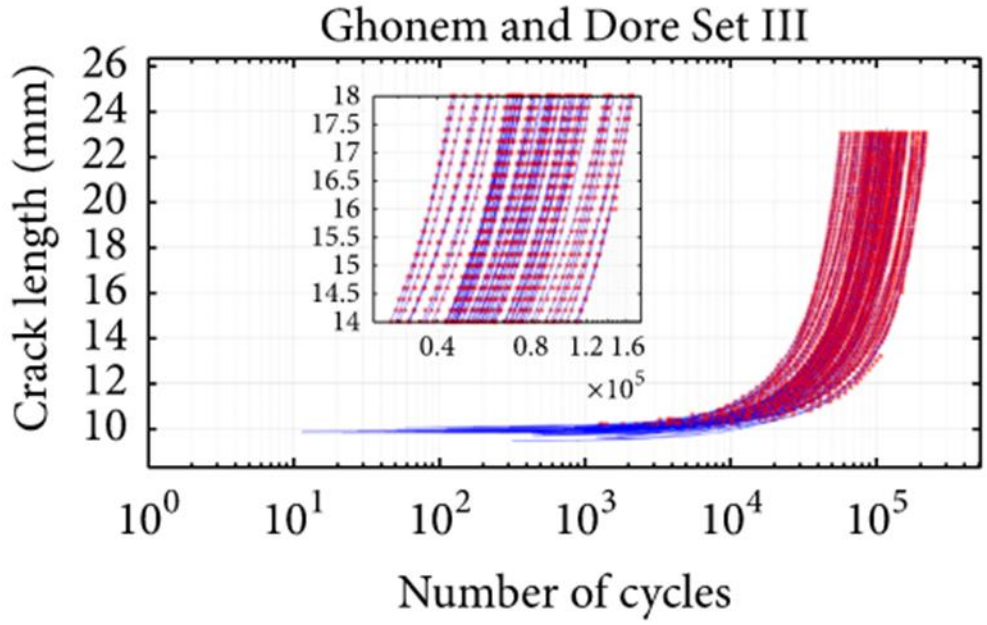
Ghonem and Dore Set III
Crack length (mm)
Number of cycles
×10^5

(c)

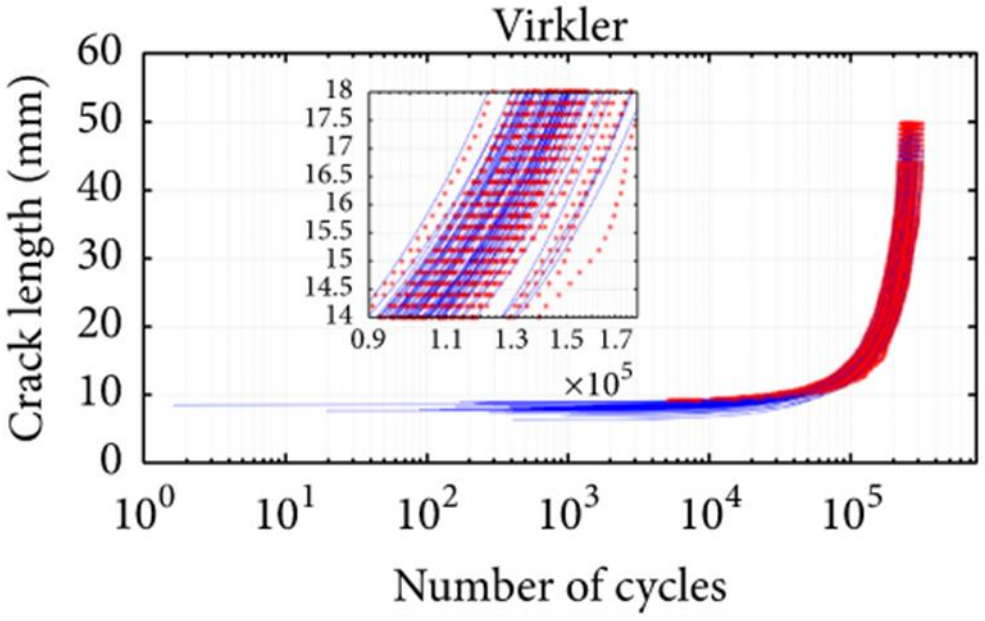

(d)

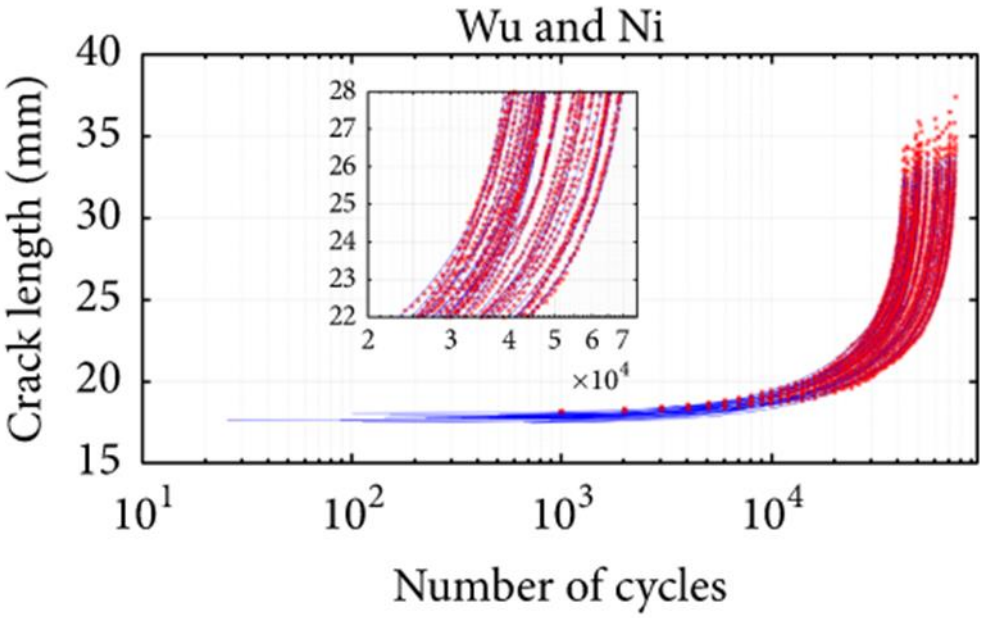

(e)

Figure 7.3.1 Comparison of raw (dots) and analytical (lines) crack length vs number of cycles for the five datasets: Ghonem and Dore dataset (I-III) [284] (a-c), Virkler et al. [285] dataset (d) and Wu and Ni [286] dataset.

In order to draw the FCG curve for the entire range, it is necessary to derive the crack growth rate together with the SIF range for the corresponding values. The curves

shown in Figure 7.3.2 correspond to all of the experimental data of the datasets considered in this chapter. These graphs show clearly that the gradient approaching N=$-N_{th}$ was equal to zero, which reflects the asymptotic behaviour in the a-N curves. As a consequence the FCG rate, as expected, approached zero (Figure 7.3.2).

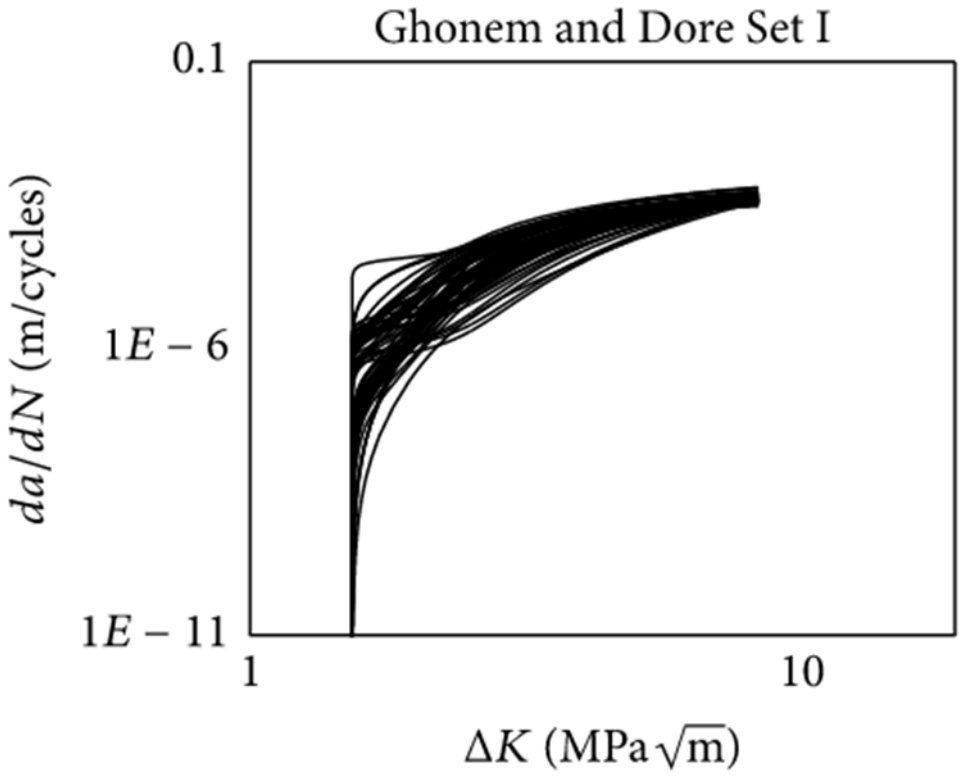

(a)

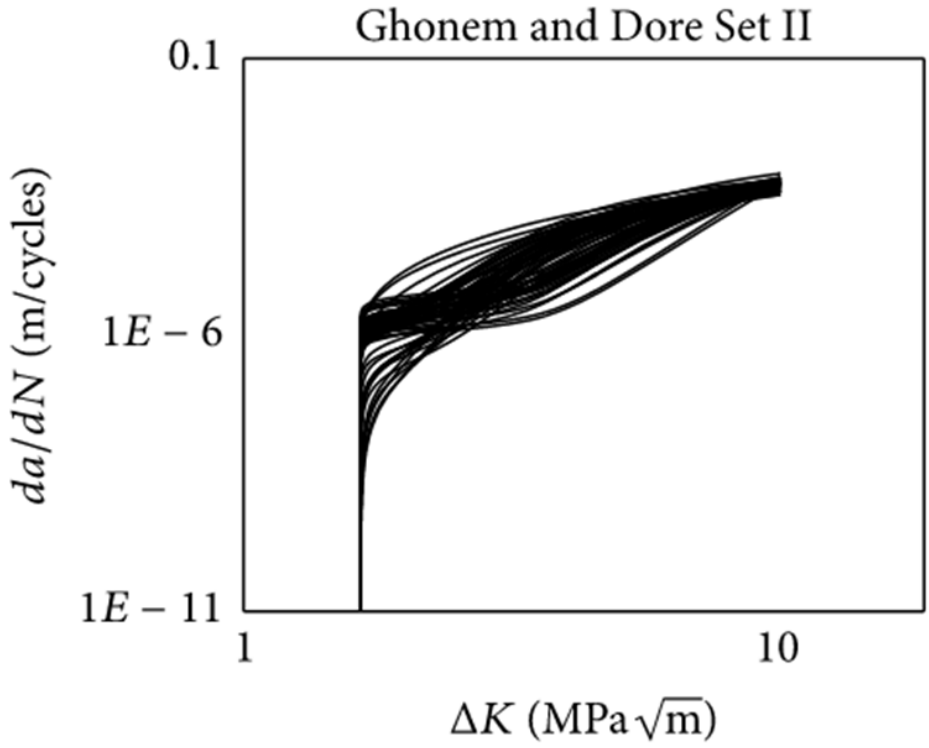
Ghonem and Dore Set II
0.1
1E − 6
1E − 11
da/dN (m/cycles)
1
10
ΔK (MPa√m)

(b)

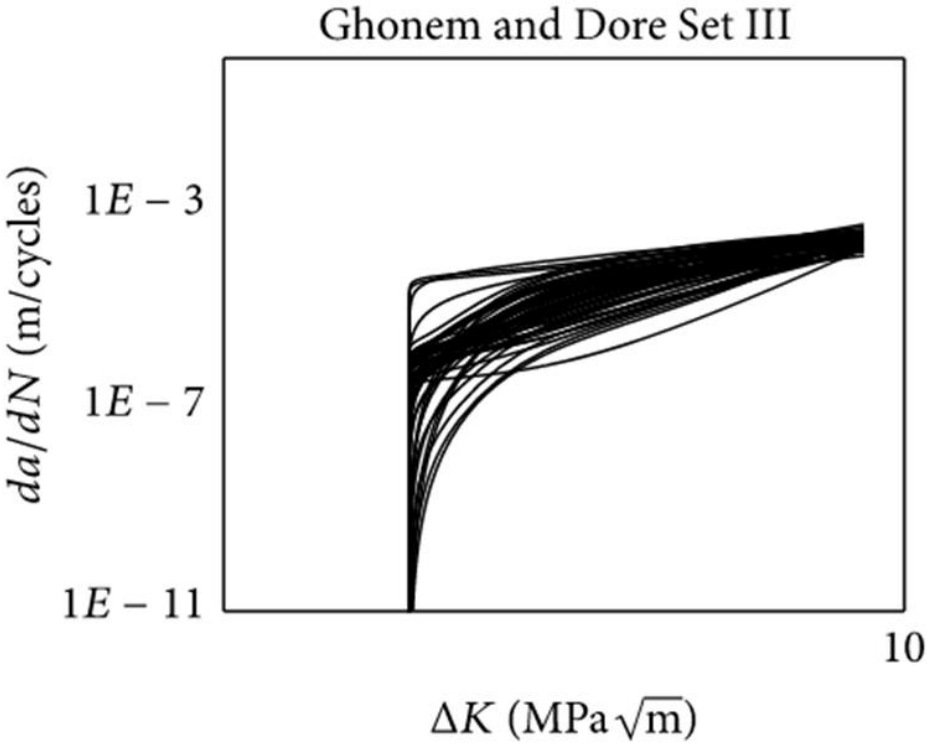
Ghonem and Dore Set III
1E − 3
1E − 7
1E − 11
da/dN (m/cycles)
10
ΔK (MPa√m)

(c)

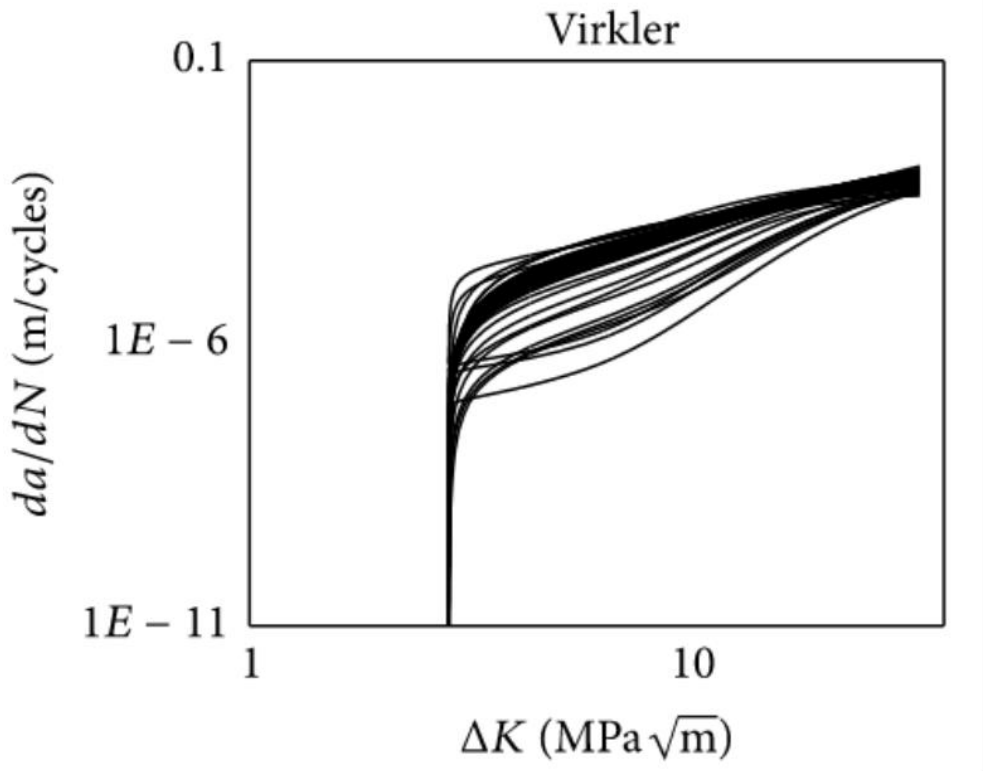

(d)

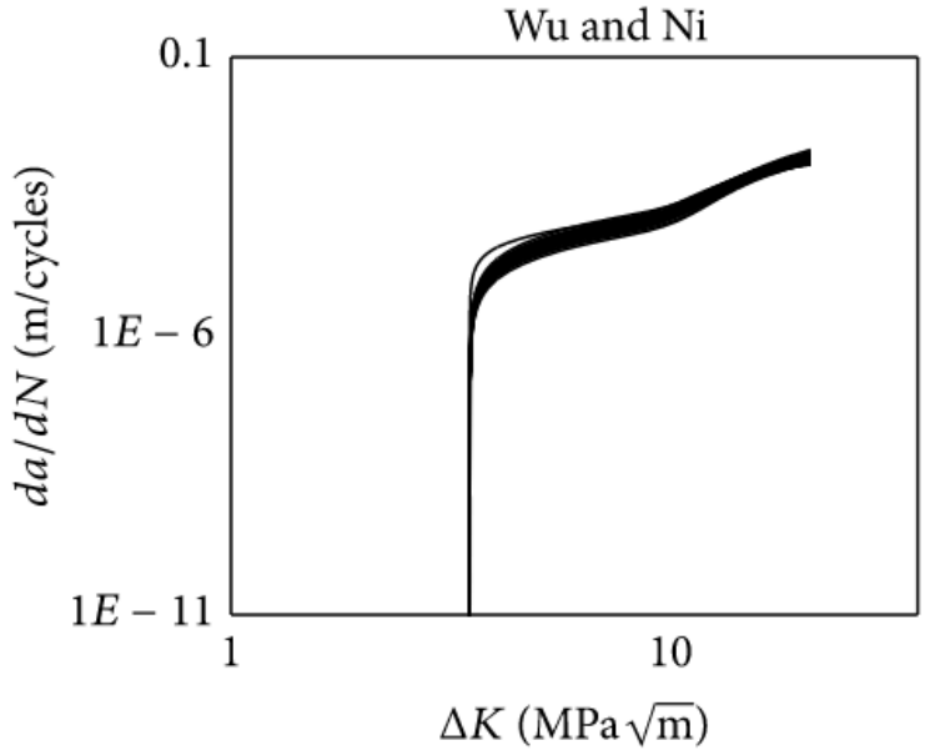

(e)

Figure 7.3.2 FCG curve for the five datasets: Ghonem and Dore dataset (I-III) [284] (a-c), Virkler et al. [285] dataset (d) and Wu and Ni [286] dataset.

This observation can be used to extrapolate the crack growth rate curve from the lower part. The value of the threshold SIF range was found where $N=-N_{th}$. The value of the crack length at $N=-N_{th}$ can be derived from Equation 7.3.1. In Figure 7.3.3, the values of the threshold SIF predicted by the model for each curve of the five data sets analysed in this chapter are shown together with the corresponding values gathered from the literature [54, 188, 190].

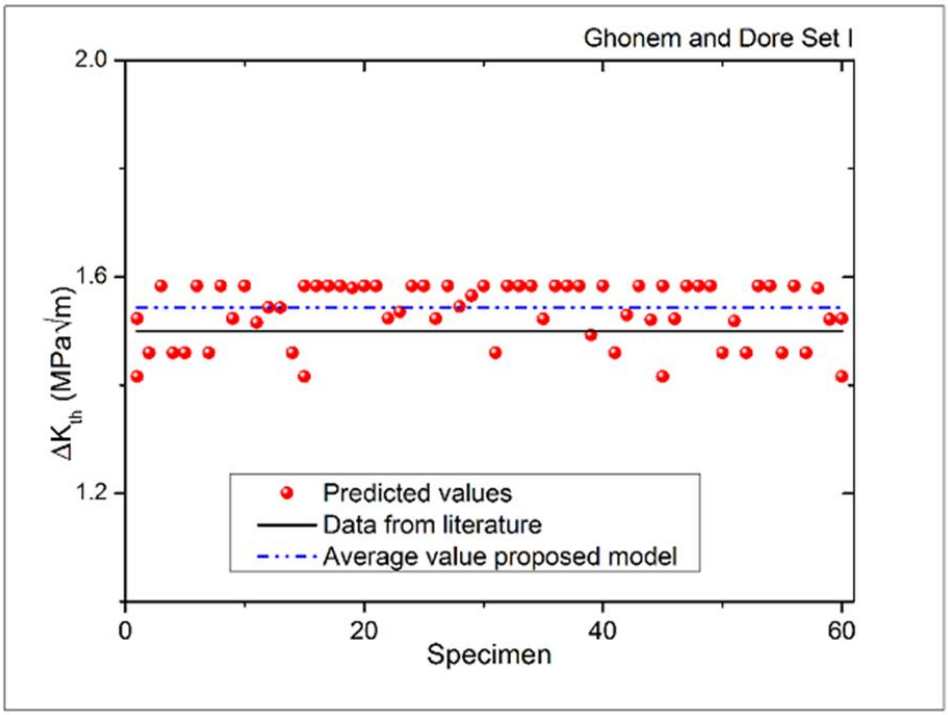

(a)

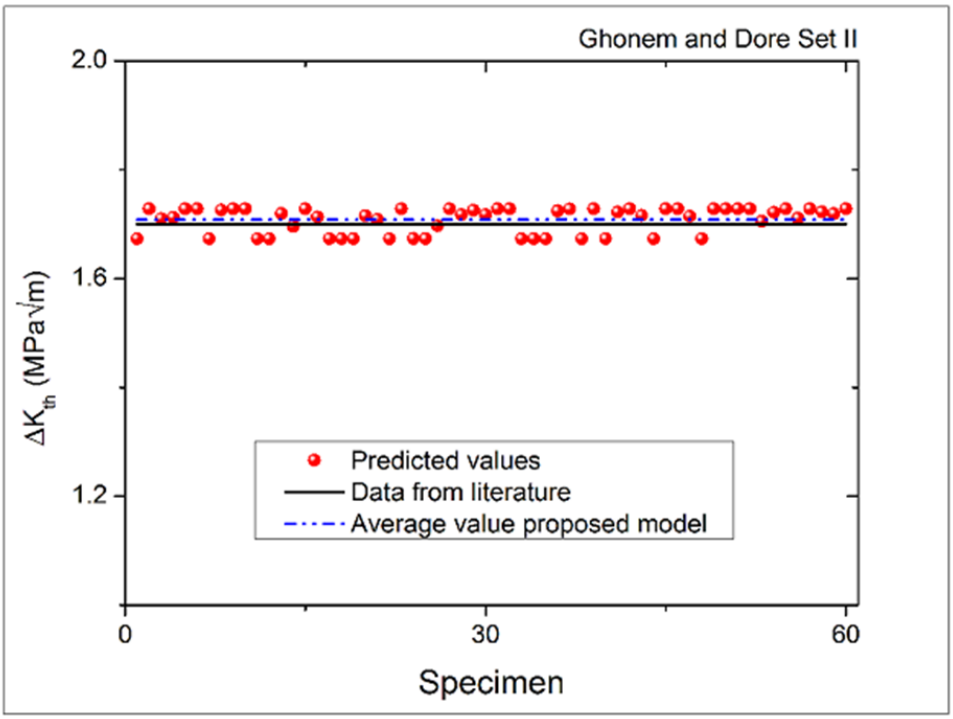
Ghonem and Dore Set II
2.0
1.6
1.2
ΔK_{th} (MPa$\sqrt{m}$)
Predicted values
Data from literature
Average value proposed model
0
30
60
Specimen

(b)

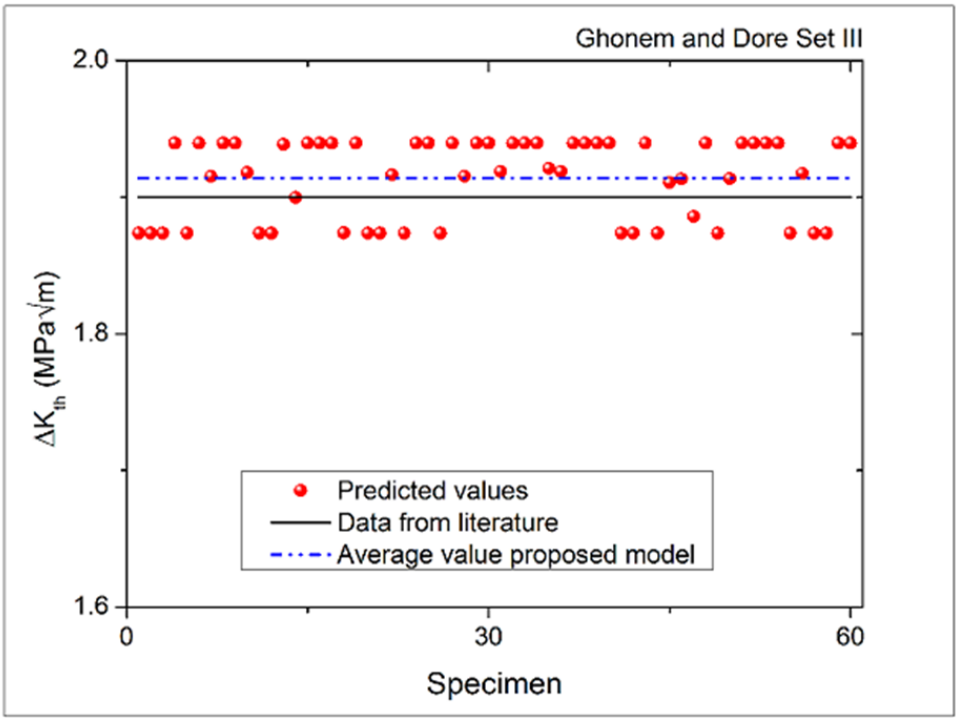
Ghonem and Dore Set III
2.0
1.8
1.6
ΔK_{th} (MPa$\sqrt{m}$)
Predicted values
Data from literature
Average value proposed model
0
30
60
Specimen

(c)

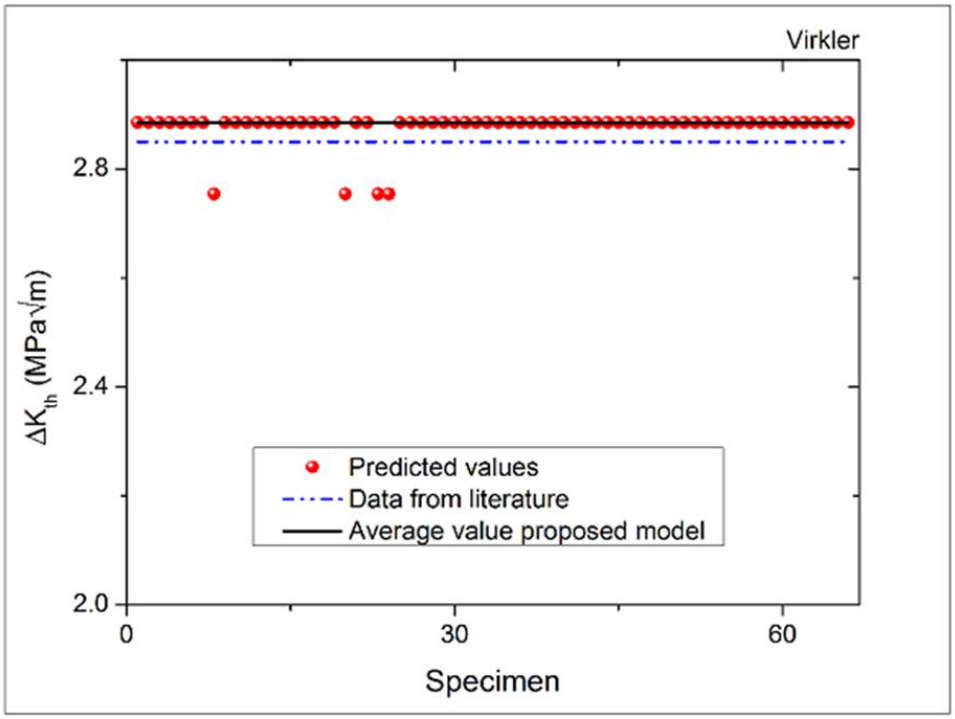

(d)

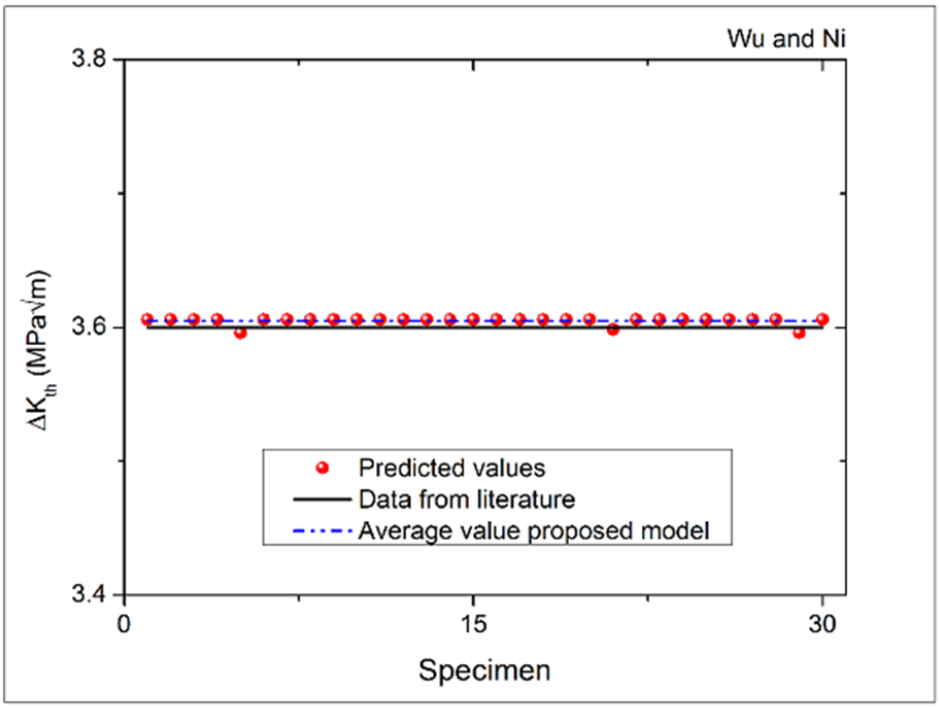

(e)

Figure 7.3.3 Threshold SIF range for the five datasets: Ghonem and Dore dataset (I-III) [284] (a-c), Virkler et al. [285] dataset (d) and Wu and Ni [286]dataset.

7.4 Discussion

The crack length vs number of cycle curves obtained from the model correlated well with the raw data points (see Figure 7.3.1). As shown in Figure 7.3.2 and Figure 7.3.3, in all cases, there was a band of threshold values predicted for the same material with the literature showing the same trends. The threshold vs R graph provided by [188] shows a small range of threshold values with the upper and lower limits indicated for aluminium alloy 2024-T3. Different investigations by Newman and Raschau [162, 163, 175-177] also found a range of threshold values based on different experimental methods used, e.g. load reduction (LR) methods, K_{max} constant methods and far-field cyclic compression methods.

Recently, Molent, et al. [55] used an FCG threshold parameter, ΔK_{thr} to explain the scatter in the fatigue life prediction and this parameter is known as cyclic stress intensity threshold. The ΔK_{thr} is used to explain the dependency of the threshold values on the material properties, R ratio, crack length and loading method. The use of the value of ΔK_{thr}=0 in order to predict the crack growth data has previously been shown to be rather conservative for different aluminium alloys. The fact that there is a range of threshold SIF values for same material can be explained by this concept of cyclic stress intensity threshold, ΔK_{thr}. In these studies, for the material used in generating Virkler et al. [285] dataset, a range of ΔK_{thr} values between $(2.9 - 4.2\ \mathrm{MPa}\sqrt{\mathrm{m}})$ was reported whilst the material related to Wu and Ni [286] dataset , a range of ΔK_{thr} values between $(0 - 4.2\ \mathrm{MPa}\sqrt{\mathrm{m}})$ was reported. Moreover, for 7075-T6 aluminium alloy material at R = -1, a range of ΔK_{thr} values between (0.6 – 1.13 $\mathrm{MPa}\sqrt{\mathrm{m}}$) was obtained. In other published work [292], it has been shown a threshold band; values between (2.8 – 4 $\mathrm{MPa}\sqrt{\mathrm{m}}$) at R = 0.33 for 2024-T351 aluminium alloy. All these values are in good agreement with those estimated by the proposed model.

Figure 7.3.3 shows a comparison between the threshold values obtained using the proposed model and the threshold values found in the literature for different materials. The values considered from the literature are based on ESDU documents [188] for aluminium alloy 7075-T6 (at R = 0.4, 0.5 and 0.6) and aluminium alloy 2024-T3 (at R = 0.2). For aluminium alloy 2024-T351 (at R = 0.2), the literature value is taken based on the ΔK_{th} value provided by [54] and the normalised threshold SIF range against the

R curve provided by [190]. The average threshold value of the model was used for comparison. In Ghonem and Dore (set I-III) [284], Virkler et al. [285], Wu and Ni [286] datasets, the threshold values of the corresponding materials from the literature are 1.5 $MPa\sqrt{m}$, 1.7 $MPa\sqrt{m}$, 1.9 $MPa\sqrt{m}$, 2.85 $MPa\sqrt{m}$ and 3.6 $MPa\sqrt{m}$, respectively. Comparing these values with those predicted by the proposed model, the percentages of error were approximately 5.3 %, 4.1 %, 0.24 %, 2.1 % and 0.3 %, respectively.

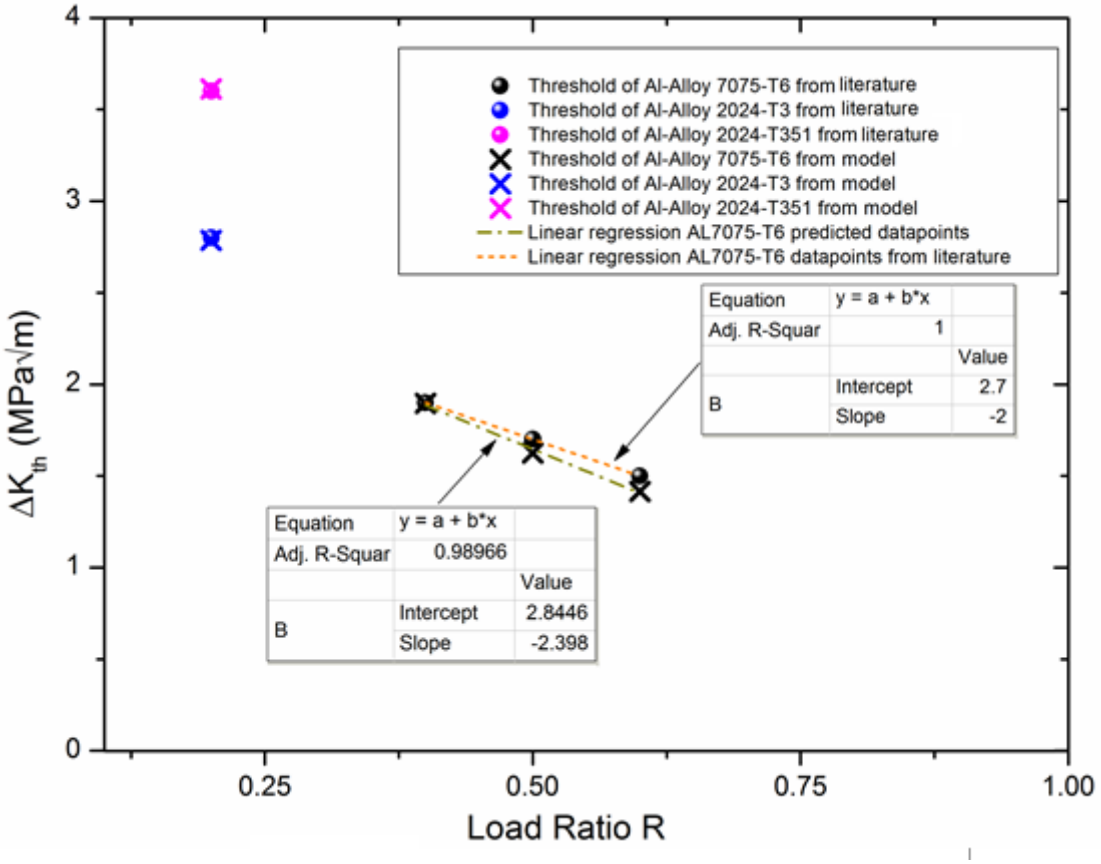

Figure 7.4.1 Threshold vs load ratio data where thresholds of model and literature are compared.

Reporting all the results on the same graph in Figure 7.4.1, it is possible to identify a common trend which is useful to compare the results with the literature values. Firstly, the threshold line found with declined linear pattern or shape in relation to R for the aluminium alloy 7075-T6 was qualitatively and quantitatively consistent with the line found in the literature [188]. The percentage of error ranges between 0.24 % and 5.61 %, which is quite low considering the scattering nature of the fatigue test data. These

two lines should converge at the higher value of R, but it was found that the scatter was getting bigger and reached 5.61 % at R = 0.6. This difference or scatter could be attributed to the different experimental methods used and the corresponding crack closure effects as referred to by [162, 163, 175-177]. All the predicted threshold values of aluminium alloys (7075-T6 and 2024-T6) were lower than the values from literature (see for example [188]) except for the threshold value of aluminium alloy 2024-T351 which overestimated the literature value from [54, 190]. For aluminium alloy 7076-T6, the threshold values from the literature [164] at R = 0.2 is 2.3 $\mathrm{MPa}\sqrt{\mathrm{m}}$, whilst the value derived using the analytical model proposed here was equal to 2.3651 $\mathrm{MPa}\sqrt{\mathrm{m}}$ with an error less than 3 %.

In general, the yield strength of aluminium alloy 2024-T351 (330 MPa) is higher than aluminium alloy 2024-T3 (320 MPa) even though they are the variant of same material [293]. The threshold values obtained from the model for aluminium alloy 2024-T351 and 2024-T3 alloys at R = 0.2, are 3.6 $MPa\sqrt{m}$ and 2.8 $MPa\sqrt{m}$, respectively. This indicated a correlation between the yield strength and threshold of this alloy; the threshold of aluminium alloy increase with the strength of the alloy and vice versa. This supports the statement of previous investigations which found the same type of correlation between the strength and threshold of materials [11, 183, 184].

It should be added that, the values of the a_{th} in Equation 7.2.4 are found to influence the threshold value since it is the crack length corresponding to the fatigue life value equal to $N = -N_{th}$. Therefore, a_{th} values can be further considered to correlate with the material properties, the load ratio as well as the geometry of the cracked component. As stated before, there is a linear relationship between the threshold and the strength of a material [11, 183, 184]. Further research should be carried out to properly address this correlation, which could help in both identifying the parameter values and giving them a more physical understanding.

7.5 Summary

An analytical model for the interpolation of crack propagation data has been developed. The threshold SIF range has been derived for different materials and different specimen geometries. The new model has been shown to fit, with the needed accuracy, to a wide range of experimental data produced with different specimen geometries, different materials and different loading conditions. Moreover, it has been highlighted that it is possible to identify, by means of the above model, the value of the threshold SIF range with an error, as compared to the values reported in the literature, of less than 6 %. The relation between ΔK_{th} and R ratio predicted by the model agrees well with the literature results. The proposed model is, therefore, valuable in identifying the threshold of stress intensity factor range for fatigue crack growth.

8 Electropulsing treatment increasing fatigue resistance of aluminium alloy 2014-T6 and its optimisation

8.1 Introduction

Electromagnetic treatment has been shown to enhance fatigue life of metals. While the research work on this topic is growing with time, the mechanisms of effect of this treatment are not entirely understood yet. The literature review in Chapter 2 summarises the research work on this effect of electromagnetic treatment effect on fatigue life, which include background knowledge of electromagnetic treatment and fatigue resistance, parameters of the electromagnetic treatment, the rearrangement of the microstructure of the materials due to electromagnetic treatment, crack healing mechanisms and fatigue life enhancement. Issues related to the effectiveness of this treatment on fatigue resistance, threats and challenges of this topic were also discussed.

It is well-documented that microhardness can be used to predict the mechanical properties of aluminium alloy [350]. Some authors believe microhardness and fatigue life are proportional to each other [47]. This statement may not be quite correct but the change in microhardness is closely linked to the change in microstructure which has a direct effect on fatigue life. There has been effort by different researchers to enhance fatigue life by increasing the microhardness. For instance, fatigue life of cutting tools made up of 0.4 % carbon steel was enhanced by increasing microhardness and compressive residual stress on the surface [294]. By increasing microhardness using different methods, fatigue life was also improved in steels [295], titanium alloys [296] and aluminium alloys [297, 298]. It is also worth noting that cracks orthogonal to weld line of aluminium alloy 2024-T351 exhibited a lower growth rate due to higher microhardness [297].

Electromagnetic treatment has been used mostly during the casting stage to improve the microhardness of the aluminium alloys [299, 300]. It is described that due to the treatment the microstructure of the material gets more refined and more homogeneous. Thus, the material becomes harder compared to untreated material.

Stoicanescu et al. [301] studied magnetic field treatment effect during artificial ageing of an aluminium alloy (AlCu4Mg1,5Mn alloy) by applying an alternating/stationary magnetic field. They found that this magnetic field treatment, particularly in the form of the alternating magnetic field, enhanced the microhardness. The reason was that the extra energy provided by this treatment promotes diffusion of precipitated phases and the formation of Cu rich Guinier-Preston (GP) zones, fine coherent Al_2Cu precipitate (θ_{II}) and fine semi-coherent Al_2Cu precipitate (θ_I) which cold hardened the microstructure. Herbert [302] used alternating magnetic field treatment on different types of alloys including steel, brass and duralumin. The treatment was applied in different time intervals after quenching. It was observed that the applied alternating magnetic field was able to improve the microhardness. This study attributed the improvement in hardness as the re-arrangement of atoms in the lattice crystal structure of these alloys. Recently, [303] also found increase in hardness in aluminium alloy 2219 due to magnetic field treatment during artificial ageing.

The electrical conductivity of an alloy indirectly provides information about the nature and distribution of precipitates as it is highly sensitive to the microstructure of the alloy [304]. The addition of any alloying element can reduce the electrical conductivity. The alloying of pure aluminium, strain hardening or precipitation hardening which improve mechanical properties can also reduce this conductivity [305]. Salazar-Guapuriche et al. [306] investigated the microhardness and conductivity in aluminium alloy 7010 during natural ageing. The increase in microhardness and the corresponding reduction of conductivity have been related to the formation of precipitates. It has been mentioned that the formation of GP zones and fine coherent and semi-coherent precipitates during natural ageing can decrease the electrical conductivity by scattering the electrons. However, these can enhance the microhardness by increasing precipitate strengthening. This phenomenon is also supported by other research work [304]. Conductivity along with microhardness have been correlated to the mechanical properties of aluminium alloy [304, 306-308].

In the literature, there is no real correlation of different parameters of electropulsing treatment with fatigue life enhancement available. The purpose of this chapter is to correlate electropulsing treatment parameters with fatigue resistance. This treatment is a particular case of electromagnetic treatment when pulsed electric current is passed through the sample during the treatment. The electropulsing treatment

intensity, pulse time and number of treatment have been investigated to find the best possible fatigue life enhancement. Taguchi technique is used to optimise the electropulsing treatment parameters to identify the best parameters, which can improve the fatigue life of aluminium alloy 2014-T6 more efficiently. A baseline stress-number of cycle (S-N) curve of untreated alloy is also presented which has a good correlation with the literature. A systematic approach has been adopted to correlate the conductivity and mechanical properties with the beneficial effect of electromagnetic treatment on fatigue resistance. The comparison of fatigue life of treated and untreated samples is also discussed. The fracture surfaces of treated and untreated sample have been studied using the scanning electron microscopy (SEM). Furthermore, the mechanisms of electromagnetic treatment on improving the fatigue resistance have been investigated using transmission electron microscopy (TEM).

8.2 Aluminium alloy samples

Aluminium 2014-T6 was used in this study. The chemical composition of this alloy is shown in table 8.2.1. The ultimate tensile strength of 2014-T6 is 510 MPa.

Table 8.2.1 The chemical composition of aluminium alloy 2014-T6 [309].

Element	Al	Si	Fe	Cu	Mn	Mg	Cr	Zn	Ti	Others
Weight (%)	Balanced	0.5-1.2	0.7	3.9-5.0	0.4-1.2	0.2-0.8	0.1	0.25	0.15	0.15

8.3 Methodology

8.3.1 Sample preparation for fatigue test

The geometrical details of the hourglass shaped test sample with nominal cross-sectional area at its smallest diameter of 12.57 mm^2 (i.e., 4 mm diameter), are shown in Figure 8.3.1.

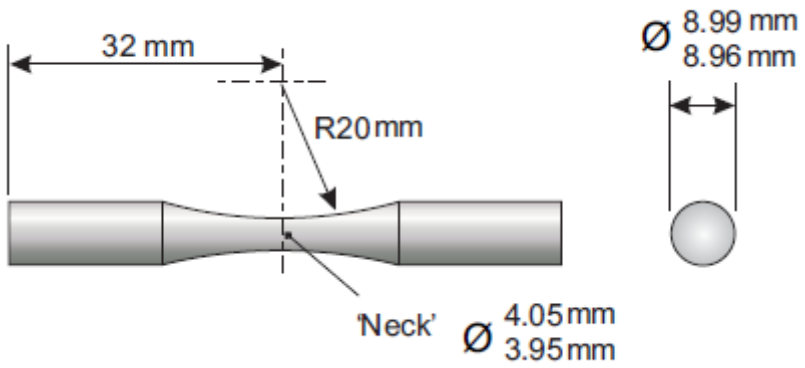

Figure 8.3.1 Geometrical details of the fatigue test samples.

These samples were designed in CATIA V5 and machined using a CNC machine from a metal bar. The neck area was polished by carrying out ten circular rotations using fine (3000) grit silicon carbide paper to reduce manufacturing defects. These samples complied with the requirement of specification RF1020 given by the manufacturer and supplier of the rotating-bending fatigue machine SM1090: TechQuipment Ltd [310].

8.3.2 Sample preparation for microhardness and conductivity test

For the microhardness and conductivity tests, samples similar to fatigue test samples were machined as shown in Figure 8.3.2.

Figure 8.3.2 (1) A sample machined for microhardness and conductivity test and (2) section cut & polished for the microhardness test.

The only difference is that it does not have a radius of curvature of 20 mm although it has a small fillet in the corner. For microhardness test, a section was cut from this sample revealing the $4\ mm$ diameter cross-section, which was further polished (Figure 8.3.2). An automatic polishing machine Motopol 2000 was used to polish the sample to obtain a mirror-like surface with different grits of sand papers and polishing agents. The top surface was ground using 800 and 1200 grit silicon carbide papers, respectively. Then, the surface was gradually polished using 9 μm, 3 μm and 0.05 μm diamond suspensions.

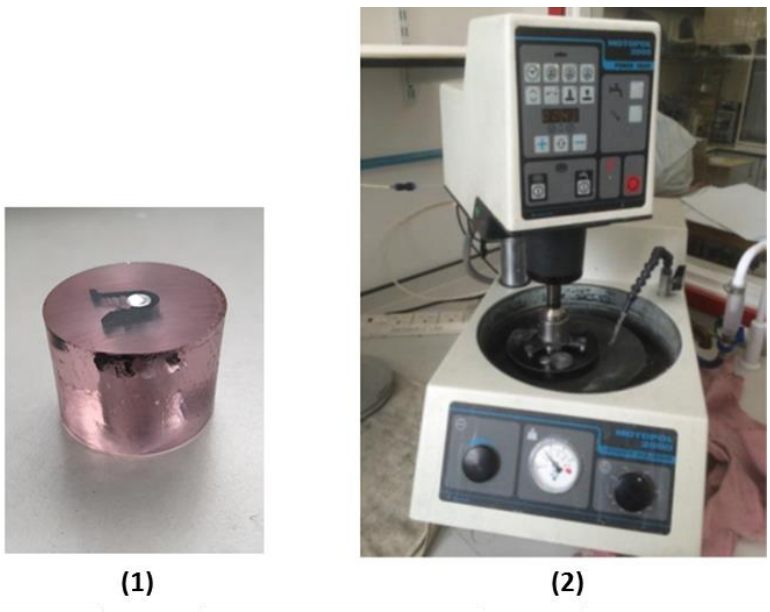

Figure 8.3.3 (1) sample within the casted mould of hardener and resin and (2) polishing device.

8.3.3 Experimental setup rotating bending fatigue test

A SM 1090 rotating-bending fatigue machine was used to undertake the fatigue test. It is shown in Figure 8.3.4. with different parts indicated by numbers and named after these numbers. It applies a load on the free end of the sample as shown in Figure 8.3.5. and the top part undergoes tension, and bottom part undergoes compression. A ball bearing allows the sample to rotate freely while loaded. Tension and compression alter throughout the cross-section resulting in cyclic loading on the sample when the motor of the machine rotates it. A schematic representation of the fatigue loading is shown in Figure 8.3.6.

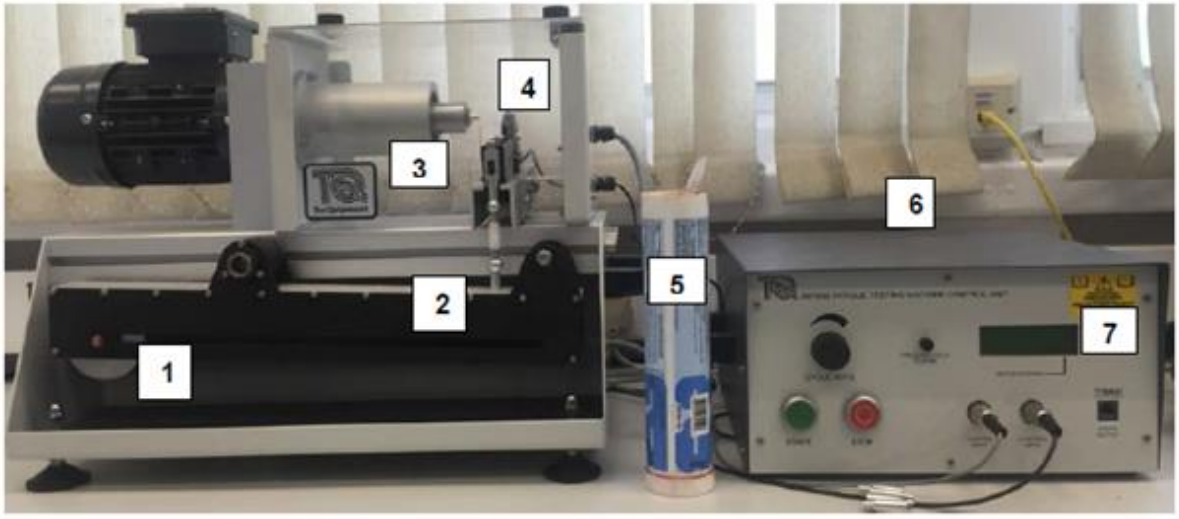

1	Dead weight	5	Bearing lubrication
2	Load arm	6	Control unit
3	Rotating shaft	7	Display board
4	Bearing holder		

Figure 8.3.4 SM1090 rotating bending fatigue test machine with different parts numbered.

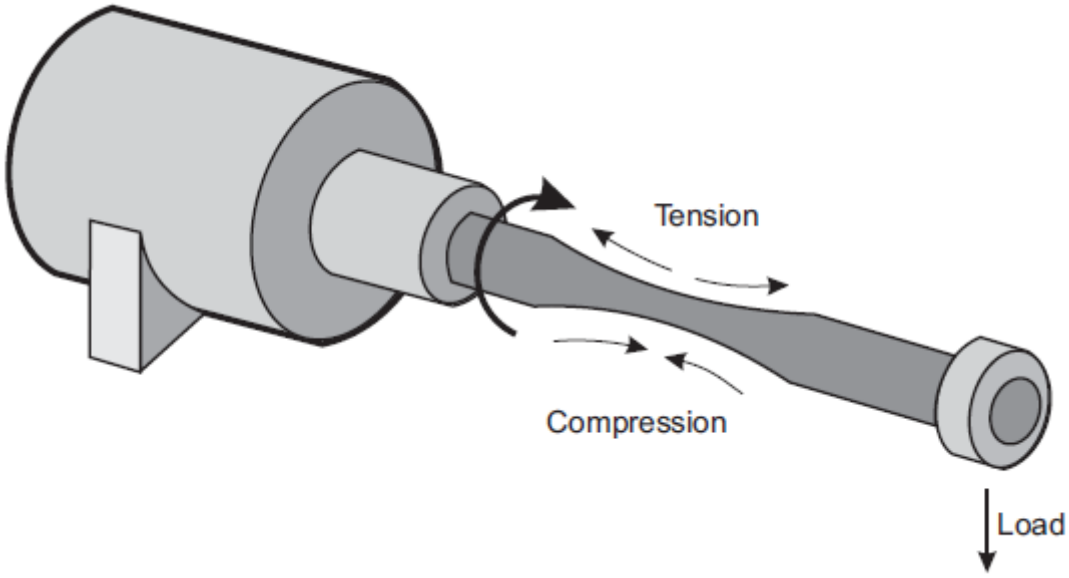

Figure 8.3.5 Rotating-bending cantilever beam [310].

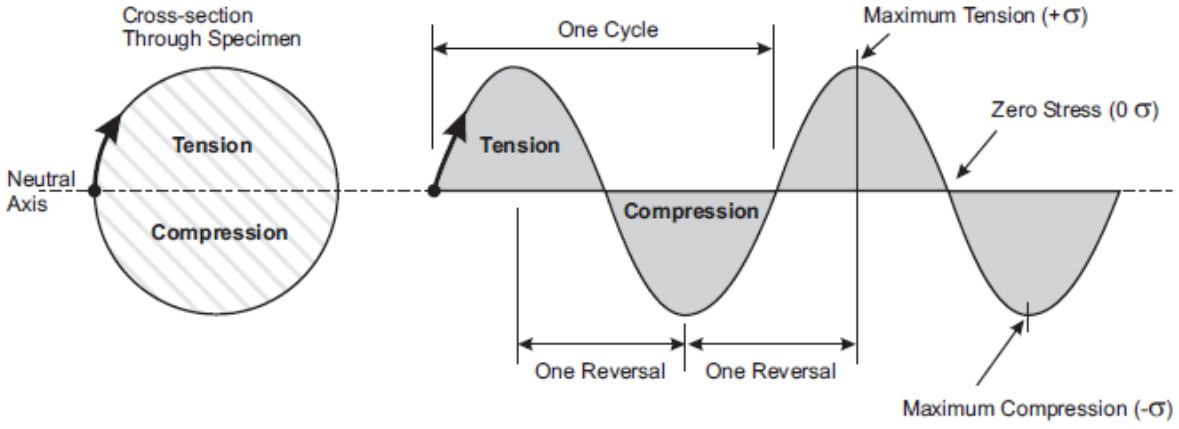

Figure 8.3.6 Schematic illustration of cyclic loading including tension and compression [310].

During the test, the steps of the instructions were systematically followed from SM1090 rotating fatigue machine user guide to reduce test error [310]. Each time, lubrication (Ambergrase EXL) was applied to minimize the friction inside the bearing. The load was applied on the sample by positioning and applying a dead weight at the start of the test. It is to be noted here that this fatigue machine allows a maximum of 80 N at a frequency of 63 Hz. Stress, σ, is the function of the distance to the load, l, shown in

Figure 8.3.7, load, F, and minimum neck diameter, D. It can be calculated using Equation 8.3.1.

$$\sigma = \frac{lF \times 32}{\pi D^3} \qquad (8.3.1)$$

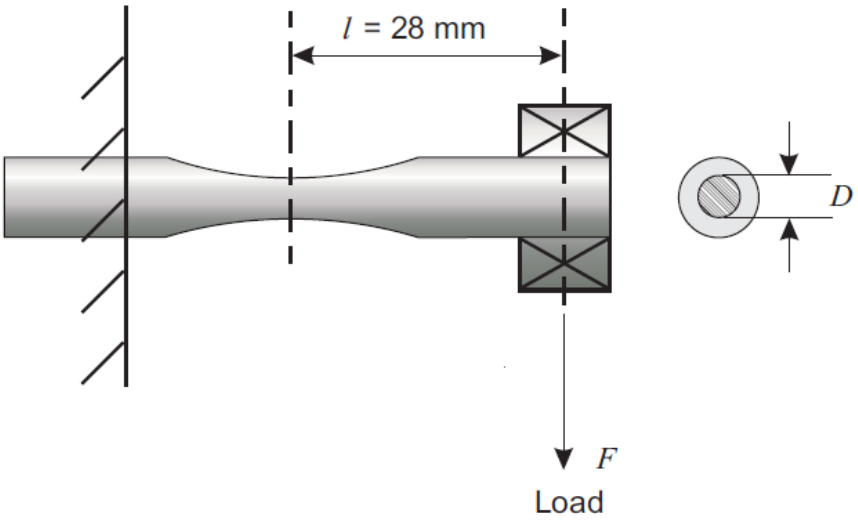

Figure 8.3.7 Distance to load in a standard specimen [310].

For the fatigue test, the frequency of the fatigue loading was f=60 Hz, which was recommended by the Techquipment Ltd [310]. The samples experience fully reversed fatigue loading with a stress ratio of R=-1. Two types of fatigue samples were used for the test including untreated and treated samples. The treated samples underwent electropulsing at prior to the fatigue test. The effect of electropulsing on the fatigue life of aluminium alloy 2014-T6 was investigated by comparing the fatigue life of untreated and treated samples.

8.3.4 Experimental setup for electropulsing treatment

The electropulsing rig is shown in Figure 8.3.8. and the corresponding circuit diagram of the electropulsing treatment is shown in Figure 8.3.9.

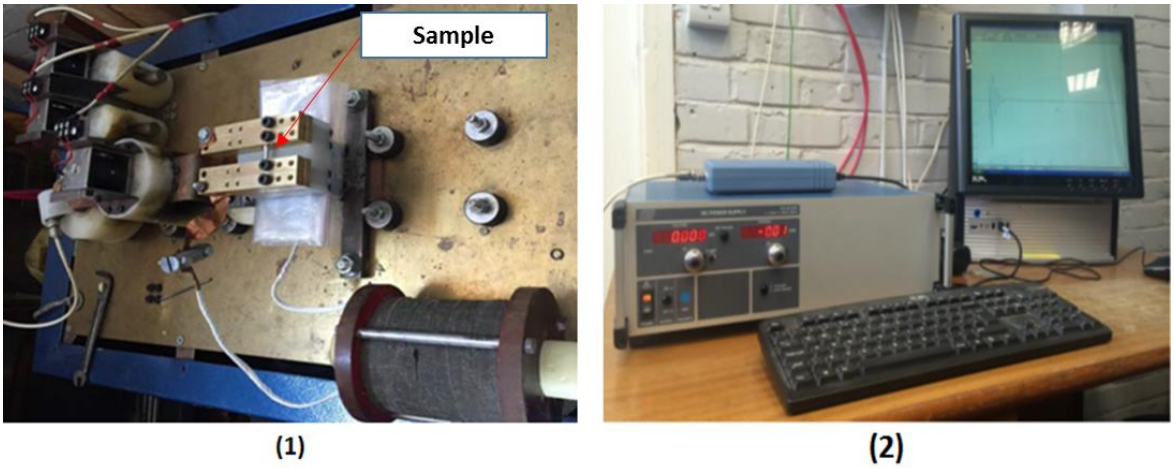

Figure 8.3.8 (1) Actual pulsed electropulsing treatment rig and (2) voltage input and output interface attached to it.

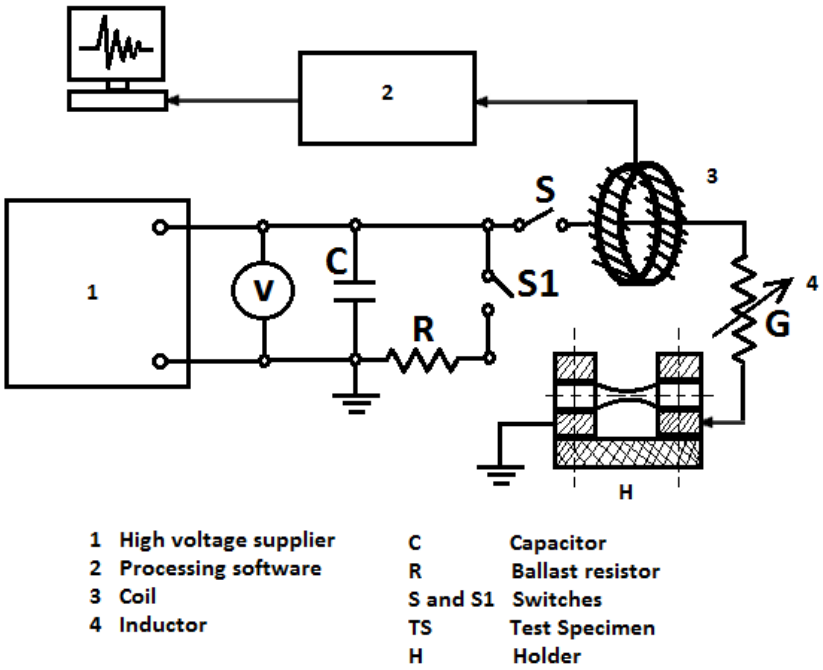

Figure 8.3.9 Pulsed electropulsing treatment circuit diagram.

As shown in Figure 8.3.9, the pulsed electropulsing treatment rig consists of a high voltage supplier which, when switched on, allows the capacitor of 100 μF to collect and hold charge ready to be pulsed through the circuit and induce an electromagnetic field around a sample. Using an analogue to digital converter, software can plot how the voltage alternates. Then the data point is multiplied by Rogovsky belt calibration coefficient (2904.51) to determine the current discharge in the electropulsing. The

current density is calculated using this current value and minimum cross sectional area. Different levels of electropulsing treatment were applied on the sample and a pause of 24 hours or a day was taken before these treated samples were used for fatigue, conductivity or microhardness test. The pause was taken in order to avoid the transient effect caused by the electropulsing treatment. The time will also help settle any precipitation in the aluminium alloy 2014-T6 used in this study.

8.3.5 Experimental setup for microhardness test

The hardness of a solid is the property which measures the resistance of the solid to its local deformation. If the harness is measured using micro-indenter, then it is referred to as the microhardness. Vickers test [362] can be used to measure microhardness of hard metal using square diamond pyramid as the indenter which makes an indent on the surface of the material. It can be expressed in Vickers Diamond Pyramid Hardness Number (DPH or HV). HV is defined as;

$$HV = 1.854\frac{L}{d^2} \qquad (8.3.2)$$

where L =Load in kgf and d=length of diagonal in mm. However,Vicklers hardness (HV) should normally be expressed as a number only without the units $\left(\frac{kgf}{mm^2}\right)$. For microharness test, DURASCAN20 was used. This machine has the capacity to cover complete macro-load ranges around 10 gf -10 kgf (0.098 N-98 N) with a position accuracy of 0.01 mm. For the test in the current study, 10 gf load was used with indententation time of around 15 s. The microhardness test rig and a reading are shown in Figure 8.3.10. The sample was kept under the camera to identify the position of the surface. Auto focus option was used to clearly display the surface. The load was applied to the indenter, which introduced diamond shaped indent. The microhardness was displayed automatically on the display in HV. It allows to manually adjust the measurement when automatic measurement does not work.

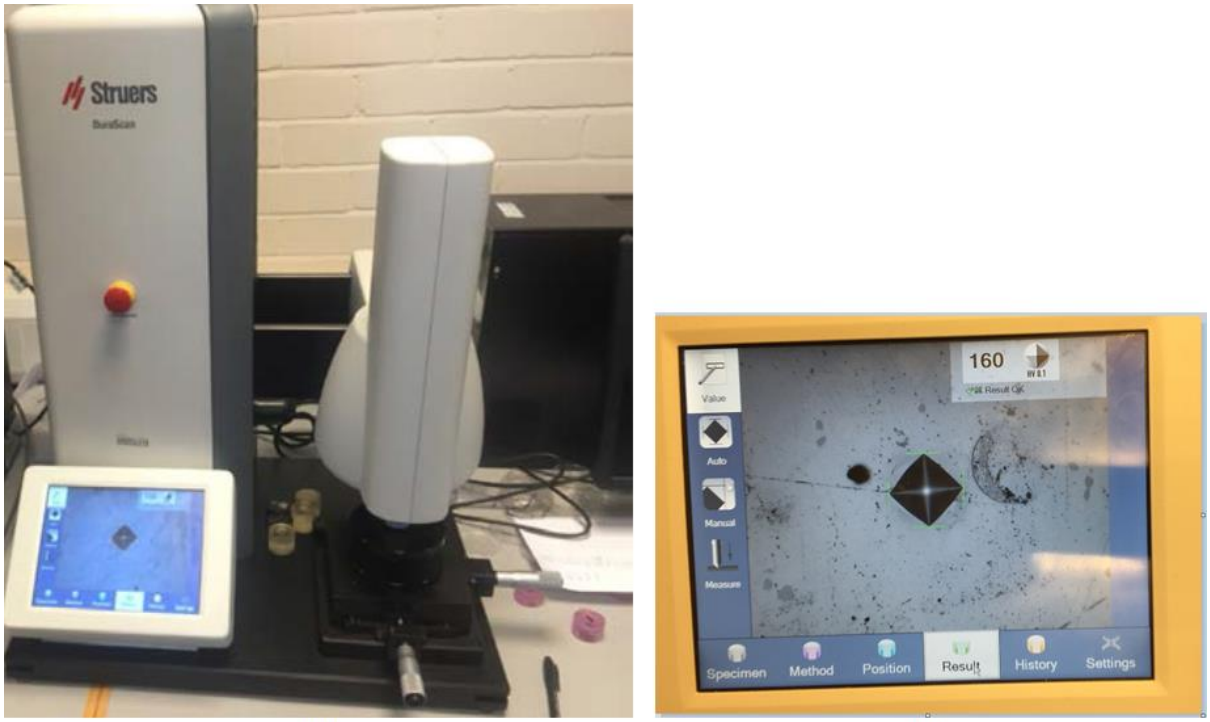

Figure 8.3.10 (1) Microhardness test machine and (2) microhardness result display in HV.

Microhardness was measured for 100 points between outer radius and 0.6 mm depth from the outer surface at 0.05 mm. Enough distance was maintained between two measurement in order to avoid plastic deformation of each dent. The microhadness of the treated and untreated samples were measured in a similar manner.

8.3.6 Experimental setup for conductivity test

In order to measure conductivity, a SIGMATEST 2.069 was used at room temperature as shown in Figure 8.3.11. the accuracy of this equipment is +/- 0.5 % of measured value at 60 kHz. 4 points were selected in equal distance from each other, around the outer surface of 4 mm diameter cylindrical area. The conductivity was measured 5 times in one point before and after the treatment (24 hours) and average value was taken in consideration to analyse the effect of electropulsing on conductivity of the alloy.

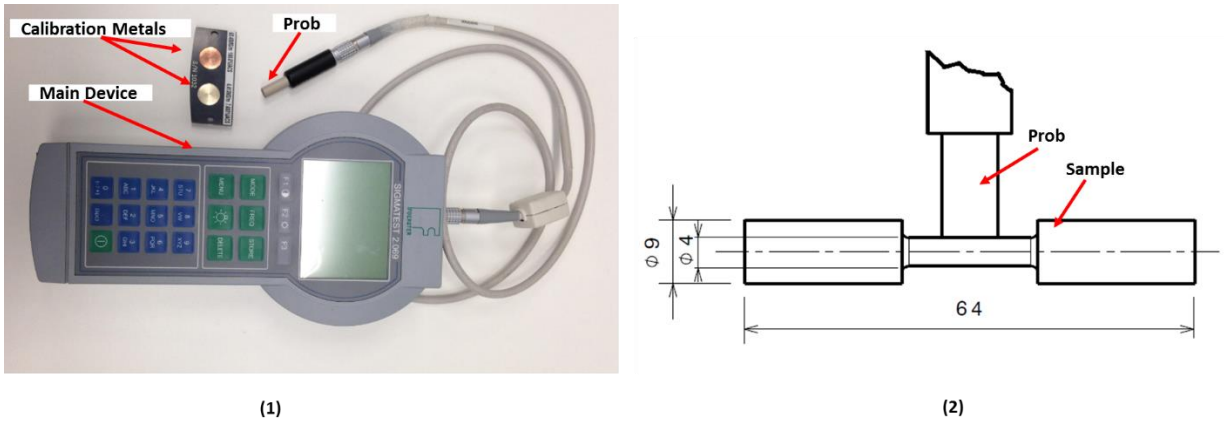

Figure 8.3.11 Conductivity measurement gauge.

8.3.7 Microstructural study using SEM and TEM technique

Microstructural study was carried out using scanning electron microscopy (SEM) and transmission electron microscopy (TEM). For SEM study, JEOL JCM-5700 CarryScope was used to investigate the final fracture surfaces of treated and untreated samples. For TEM study, Phillips CM-20 was used to investigate the microstructure near the surface area of treated and untreated samples. Both thickness and length plane were chosen for this study. The TEM samples were cut using TESCAN LYRA3.

8.4 Results and analyses

8.4.1 Stress vs number of cycles (S-N) curve of aluminium alloy 2014-T6

Stress vs number of cycles curves describe the fatigue behaviour of the material. For improved reliability of the S-N cure, a higher number of test data are required; this is time consuming and expensive. There are several methods available to achieve this curve including a staircase method [311, 312] where a systematic approach is used to define this S-N curve to make it more efficient, reliable, and cost and time effective for this project.

In general, steels have a fatigue limit, but aluminium alloys have no such limits [6]. However, there are industrial approaches to define the nominal endurance limits; some consider the fatigue strength at 10^7 cycles as the endurance limit for aluminium alloys [312, 313] while others [6] considered this number as 500 million cycles. In this study, the fatigue strength for 10^7 cycles is identified as approximately 100 MPa for aluminium alloy 2014-T6 from Engineering Sciences Data Unit (ESDU) document [314] whereas [6] considered the endurance limit of this alloy as 125 MPa as the 500 million cycle was considered for endurance limit.

A sample tested at 75 MPa has a fatigue life greater than 10^7cycles and the test was terminted to save time and reduce cost. Data for this 75 MPa is excluded from S-N curve investigation but shown in Figure 8.4.1.

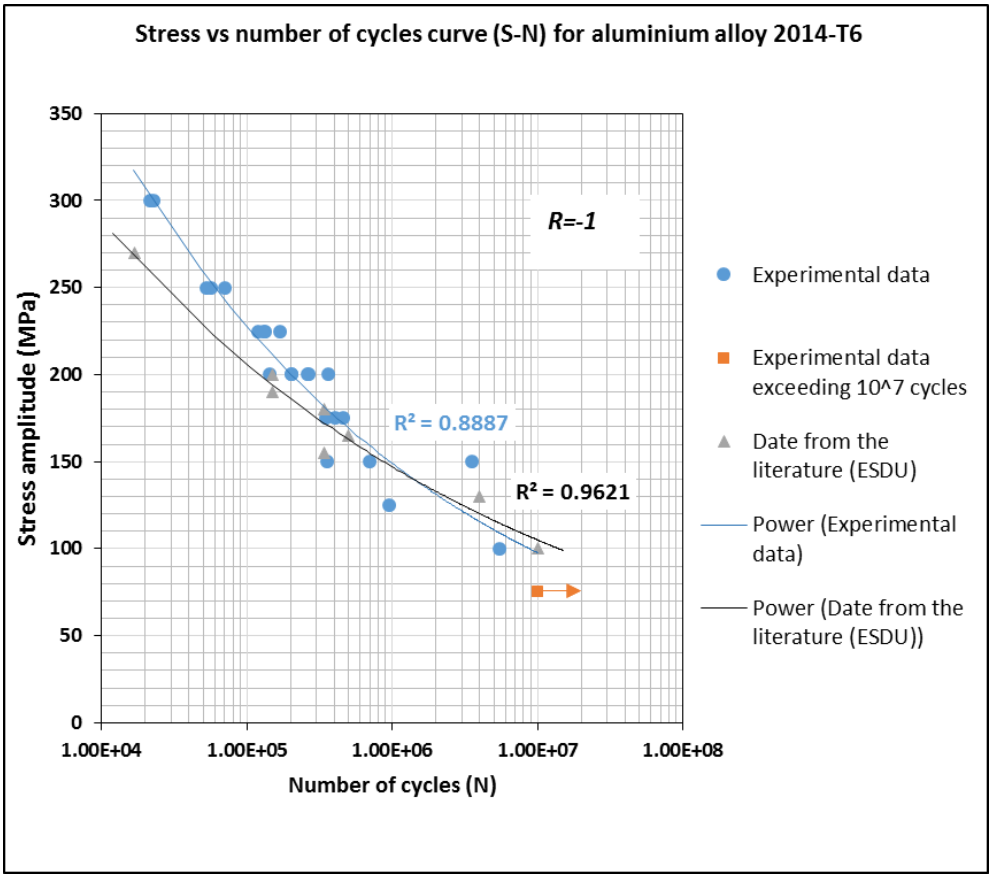

Figure 8.4.1 Stress vs number of cycles curve (S-N) of aluminium alloy 2014-T6.

A range of stress levels were considered for S-N curve determination starting from 100 MPa to 300 MPa. For this, a total of 24 samples were tested at different fatigue stresses and corresponding fatigue life was plotted to generate the S-N curve using the blue circles as shown in the Figure 8.4.1. It can be seen that the curve fits the raw data well with a coefficient of determination, R^2=0.89. It also shows comparatively higher scattering in the lower level of stress which is quite common in S-N curve determination. This experimental S-N curve is compared with S-N curve provided by the literature [314] which used a sample of similar size (minimum neck diameter of 6.4 mm). Both curves show similar shape without any plateau. The difference between the two curves is quite small considering the difference in the size and shape of the sample. So, the same curve fitting procedure of experimental data was used in the analysis of the effect of electropulsing treatment on fatigue resistance. A fatigue stress of 200 MPa which is 39 % of the UTS of the material was chosen as a representative fatigue stress level for the investigation of the effect of electropulsing treatment.

8.4.2 Optimisation of electropulsing treatment parameters for fatigue performance using Taguchi method

The Taguchi method is a systemic approach to design experiments. While the reliability of the test data can be improved by increasing the number of test samples, the Taguchi method optimises the test matrix by using an orthogonal array [315] to reach an optimum with a minimum number of tests at minimum cost. There are several research papers available where this approach is used to optimise relevant parameters for fatigue performance [316-319].

In Taguchi method, the loss function, which represents the variation between the experimental and desired results, is converted into signal to noise ratio $\left(\frac{S}{N}\right)$ [316]. $\left(\frac{S}{N}\right)$ can be based on three different types; the nominal-the best situation, the bigger-the better situation and the smaller-the better situation. To optimise the electropulsing effect on fatigue resistance the bigger-the better situation has been taken in consideration as higher fatigue life was desirable. Minitab 17.0 (statistical package)

was used to implement this. The $\left(\frac{S}{N}\right)$ ratios are shown in Table 8.4.1, which is calculated based on the bigger-the better situation defined by Equation 8. 4.1.

$$\frac{S}{N} = -10log\left[\frac{1}{n}\sum_{i=1}^{n}\frac{1}{y_i^2}\right] \quad (8.4.1)$$

where n is the repeat number and y_i is the measured variable value.

8.4.3 Electropulsing treatment design using Taguchi method

In order to obtain the optimised effect of electronpulsing, Taguchi method has been adopted. Three levels of electropulsing for each treatment parameter were used: low (1), medium (2) and high (3) (Table 8.4.1).

Table 8.4.1 Electropulsing treatment parameters.

Level		Parameters		
		Treatment intensity $\left(\frac{MA}{m^2}\right)$	Treatment time (s)	Number of treatments
		A	B	C
Low	1	58	0.00009	1
Medium	2	83	0.03	2
High	3	96	0.1	4

By combining these different levels of treatment, nine sets of experiments were designed using Taguchi method the as shown in Table 8.4.2.

Table 8.4.2 Orthogonal array, $L_9 = 3^3$ for Taguchi design of experiment (DoE), corresponding experimental fatigue life, average fatigue life and signal to noise ratio $\left(\frac{S}{N}\right)$.

Experiment number	**Factors**			**Fatigue life (cycles)**	**Average fatigue life (cycles)**	**Signal to noise ratio, $\left(\frac{S}{N}\right)$**
	A	**B**	**C**			
i	1	1	1	223245, 260457, 239297	241000	107.640
ii	1	2	2	223873, 298425, 309542	277280	108.858
iii	1	3	3	322360, 401833, 326485	350226	110.887
iv	2	1	2	309125, 249134, 229782	262680	108.389
v	2	2	3	323484, 253510, 393686	323560	110.199
vi	2	3	1	384143, 360730, 312150	352341	110.939
vii	3	1	3	293321, 248464, 229728	257171	108.204
viii	3	2	1	300648, 323873, 262207	295576	109.413
ix	3	3	2	460932, 457860, 448647, 516247, 350492, 597328	471919	113.477

The electropulsing treatment curves used in the above mentioned nine experiments are shown in Figure 8.4.2. These curves were taken using curve fitting of the registered pulsed electric current during the treatment of the samples.

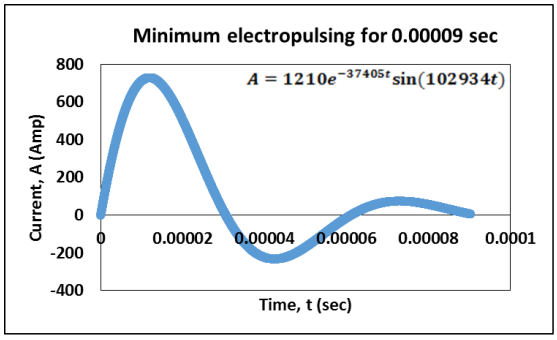

(i)

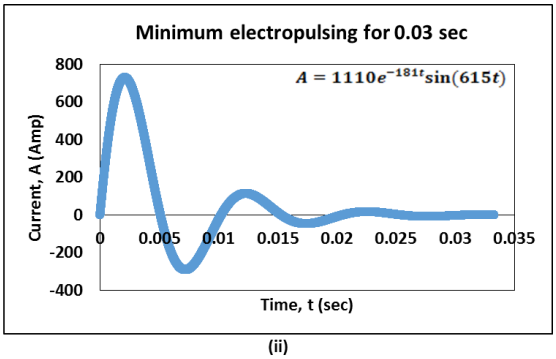

(ii)

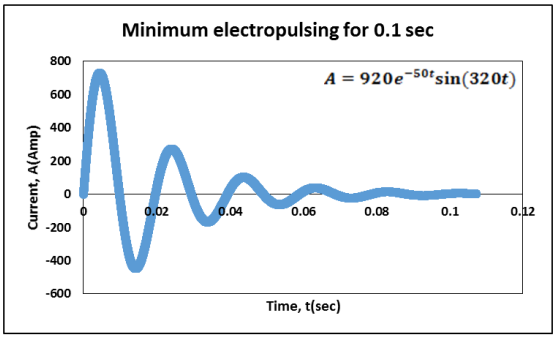

(iii)

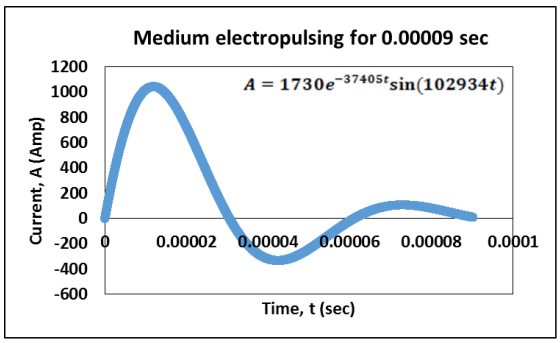

(iv)

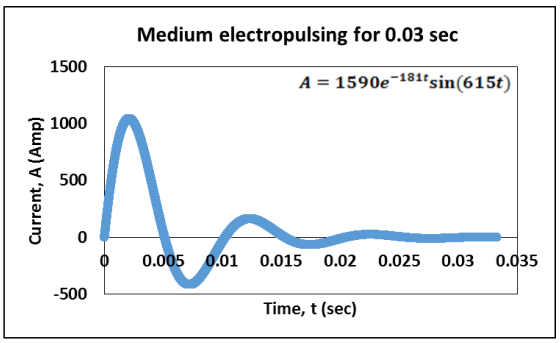

(v)

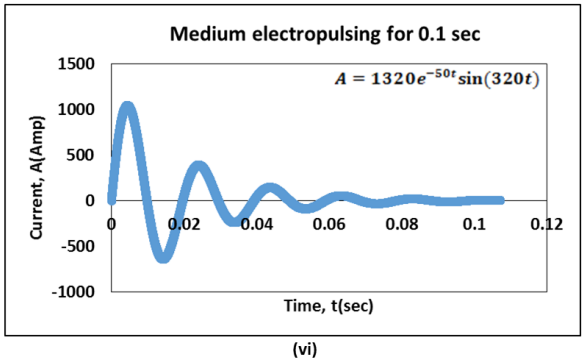

(vi)

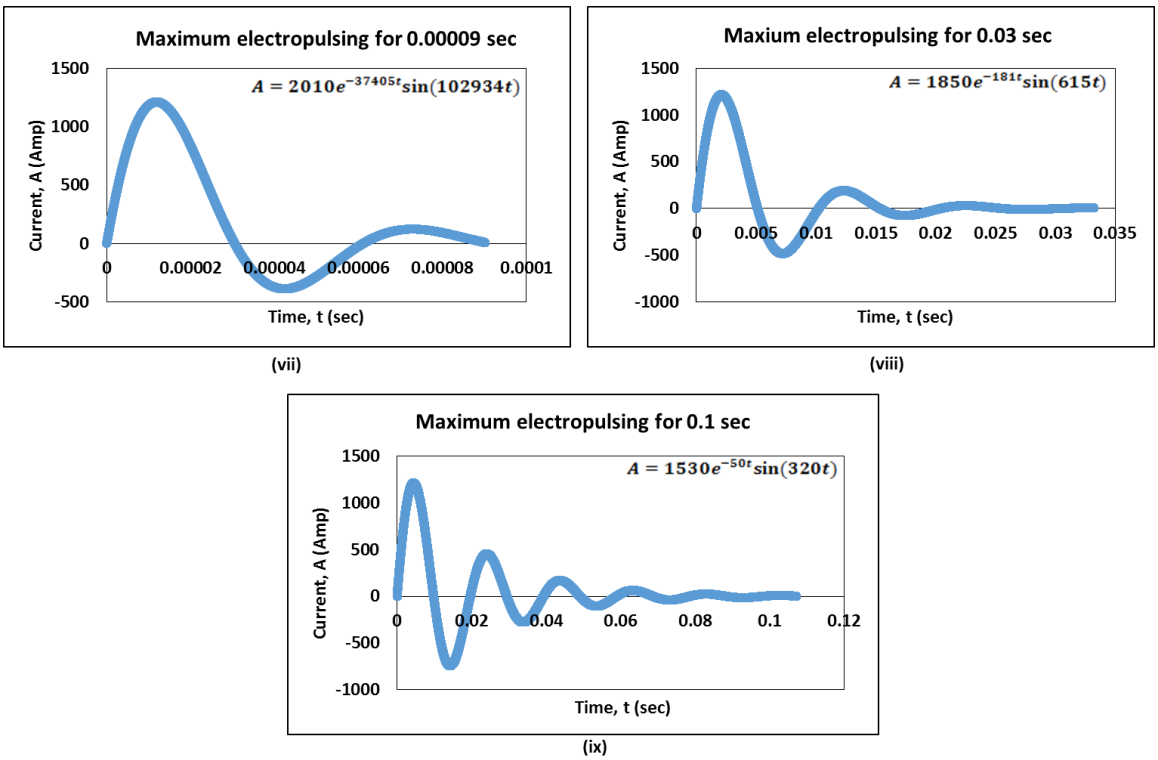

Figure 8.4.2 Electropulsing treatment curves of the nine sets of experiments with their corresponding equations.

Three samples in each category were tested at a stress level of 200 MPa to obtain the average fatigue life which was used to calculate $\left(\frac{S}{N}\right)$ ratio as shown in table 8.4.2. It is to be noted here that the treatment intensity which is represented as pulsed current density in Table 8.4.1. was calculated using the maximum current of the electropulsing process shown in Figure 8.4.3. and the minimum cross sectional area of the sample. The treatment time in terms of pulse time in Table 8.3.1. was also obtained from the electropulsing curves in Figure 8.4.3. The normal probability of residuals of all the experimental fatigue life cycles (FLC) results for treated samples are shown in Figure 8.4.4. This figure demonstrates that for the most part, the data points follow a trend line quite closely. However, there are two very large deviations at the top end and this phenomenon is known as fat tail (i.e. the residuals are still constant mean equal to 0, constant variance and symmetric, etc.). Therefore, for the most part, this distribution here is normally distributed.

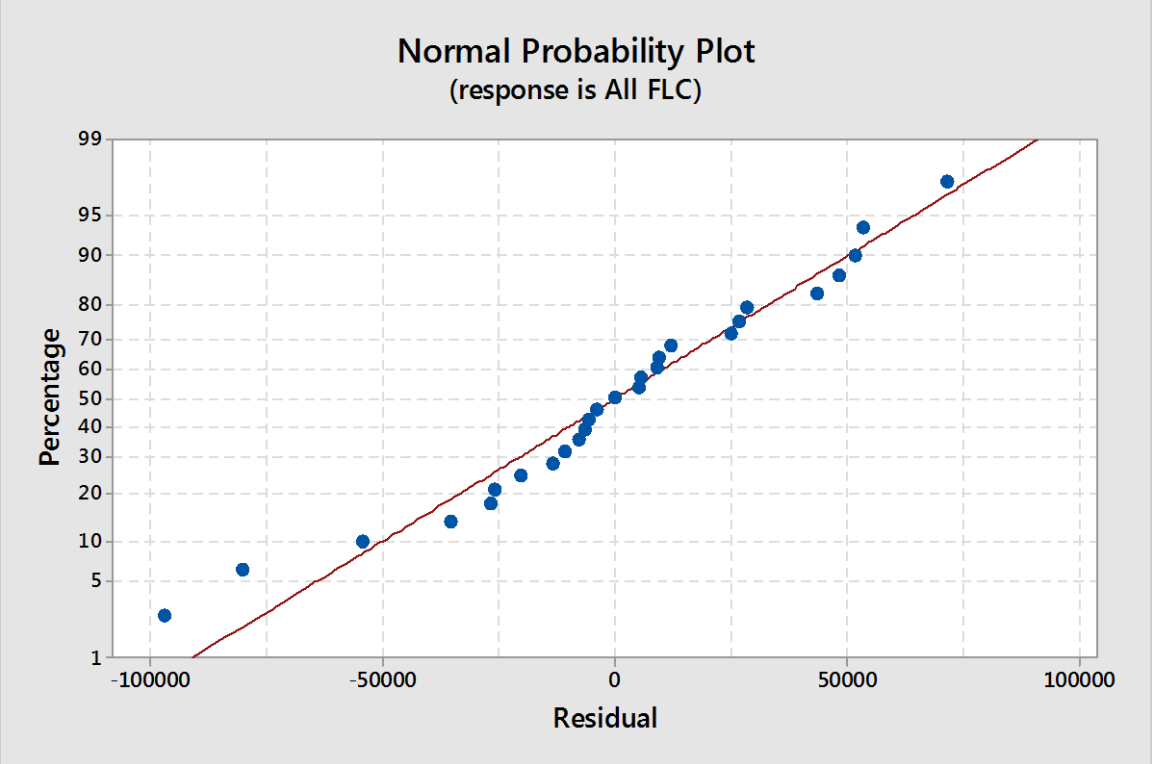

Figure 8.4.3 Normal probability of residuals of all fatigue life cycles (FLC) with best fit line.

8.4.4 Effect of electropulsing treatment parameters on fatigue performance

The $\left(\frac{S}{N}\right)$ ratio can characterise the effect of the parameters of an experiment. To achieve higher fatigue life, this ratio needs to be maximised. The average values of $\left(\frac{S}{N}\right)$ ratio at various parameters at different levels are given in Table 8.4.3. Using these values, in Table 8.4.3, the effect of variation in fatigue life with each parameter level is shown as the response curve for $\left(\frac{S}{N}\right)$ ratio in Figure 8.4.5.

Table 8.4.3 Response for signal to noise ratios, $\left(\frac{S}{N}\right)$ with larger is better criterion.

Factors		A	B	C
Level	1	109.1	108.1	109.3
	2	109.8	109.5	110.2
	3	110.4	111.8	109.8
Delta (Δ)		1.2	3.7	0.9
Rank		2	1	3

It has been seen from table 8.4.3 that Delta (Δ) value (i.g. measures the size of the effect by taking the difference between the highest and lowest characteristic average for a factor) is the highest in level B. As a result, Level B has been ranked (i.g. the ranks in a response table help you quickly identify which factors have the largest effect) 1, and Level A and C are ranked 2 and 3, respectively. Therefore, the time of electropulsing has been identified as the most effective parameter among all three parameters investigated.

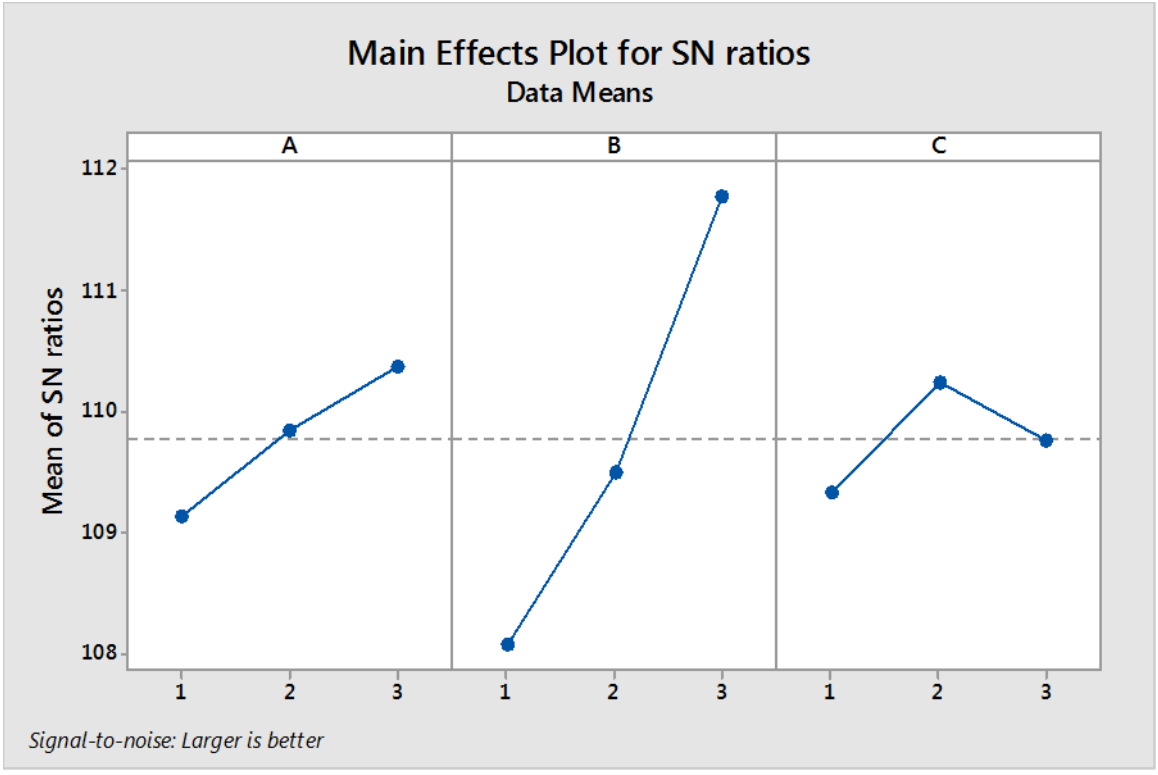

Figure 8.4.4 Main effects plot for signal to noise ratio $\left(\frac{S}{N}\right)$.

Figure 8.4.4 shows that the $\left(\frac{S}{N}\right)$ ratio increases with the increase of levels A and B but factor C has a different effect on this $\left(\frac{S}{N}\right)$ ratio. Factor C increased in levels 2 and 3 compared to level 1, but the increase is lower in level 3 compared to level 2. As such, the beneficial effect of electropulsing increased with the increase of the treatment intensity, the pulse time and the number of applications. However, the beneficial effect of electropulsing reduced when the number of application reached 4. In other words, the 3, 3, 2 array of (see experiment ix in Table 8.4.3) of A, B and C factors appears to be the optimum treatment condition.

To check the statistical significance, $\left(\frac{S}{N}\right)$ ratio was analysed using analysis of variance (ANOVA) test as shown in Table 8.4.4.

Table 8.4.4 Analysis of variance (ANOVA) for signal to noise ratio, $\left(\frac{S}{N}\right)$.

Source	Total degrees of freedom (DF)	Sequential sums of squares (Seq SS)	Adjusted sums of squares (Adj SS)	Adjusted mean square (Adj MS)	F ratio (Adj MSi/Adj MSt)	P	Contribution Percent (%) (SSi/SSt)
A	2	2.312	2.312	1.1558	1.13	0.469	8.76
B	2	20.799	20.799	10.3996	10.19	0.089	78.79
C	2	1.244	1.244	0.6222	0.59	0.621	4.71
Residual Error	2	2.041	2.041	1.0203	0.61		7.73
Total	8	26.396					

In general, a higher value of F ratio [320] and lower value of P [317] refer to the higher importance of the source or factor. Here, it also confirms that factor or source B which is the treatment time is the most important parameter in improving the fatigue performance as it projects the highest F ratio (=10.19) and the lowest P(=0.089) (Table 8.4.4). If α<0.05 is taken as 'statistically significant' value, then P of 0.089> α for factor B is not conventionally or highly significant but approaching a level of significance. On

the other hand, from the F distribution for α<0.05, it is confirmed that F ratio of 10.19 is greater than the critical value of 5.14 (obtained from F-distribution table) which means that the factor B or the treatment time is the most significant parameter among all the parameters used. Moreover, the percentage of contribution of treatment intensity (A), treatment time (B) and number of applications (C) are 8.76 %, 78.79 % and 4.71 %, respectively (taken from Table 8.4.4) which are further graphically represented by the following pie chart (Figure 8.4.5).

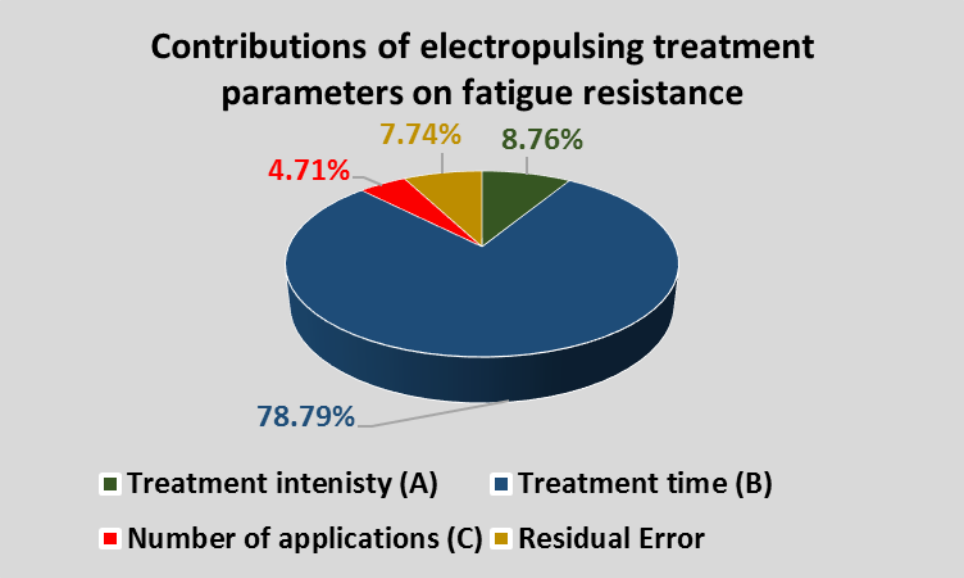

Figure 8.4.5 Contributions of electropulsing treatment parameters on fatigue resistance in percentage.

Therefore, a current density of 96 $\frac{MA}{m^2}$ with 0.1 s pulse time and 2 applications were chosen as the optimum parameters to enhance the fatigue life of aluminium alloy 2014-T6. Also, the corresponding pulse time of 0.1 s was found to be the most significant one among all the parameters used. For all nine sets of electropulsing treatments, the average fatigue life at 200 MPa is higher than the untreated average value of 239095. The average fatigue life of the samples treated with the optimum parameters is 471919 which gives a fatigue life enhancement of 97 % compared to the untreated one. This improvement of fatigue life due to the electropulsing treatment using this optimum parameters will be verified further through the measurement of the microhardness and conductivity of this aluminium alloy.

8.4.5 Electropulsing treatment effect on microhardness of aluminium alloy 2014-T6

The optimum electropulsing treatment which produced the highest improvement in fatigue life was used to investigate its effect on the microhardness. The treatment parameters were: 96 $\frac{MA}{m^2}$ treatment intensity, 0.1 s pulse time and 2 pulses. Figure 8.4.7. shows microhardness results of both treated and untreated sample of aluminium alloy 2014-T6 at points from the surface towards the centre of the minimum cross-section of the sample. The microhardness of the treated sample is higher compared to untreated one. The average value and standard deviation of the microhardness of untreated alloy are 158.10 HV and 4.16 HV, respectively. On the other hand, the increased average value and standard deviation of microhardness for treated alloy are 162.85 HV and 2.88 HV, respectively. Consequently, the coefficient of variations (CV) of the untreated and treated alloys are 2.63 % and 1.78 %, respectively which suggest that the microhardness of untreated sample has more variation relative to its mean than the treated sample. In this study, the improvement in microhardness due to electropulsing treatment was 3 %.

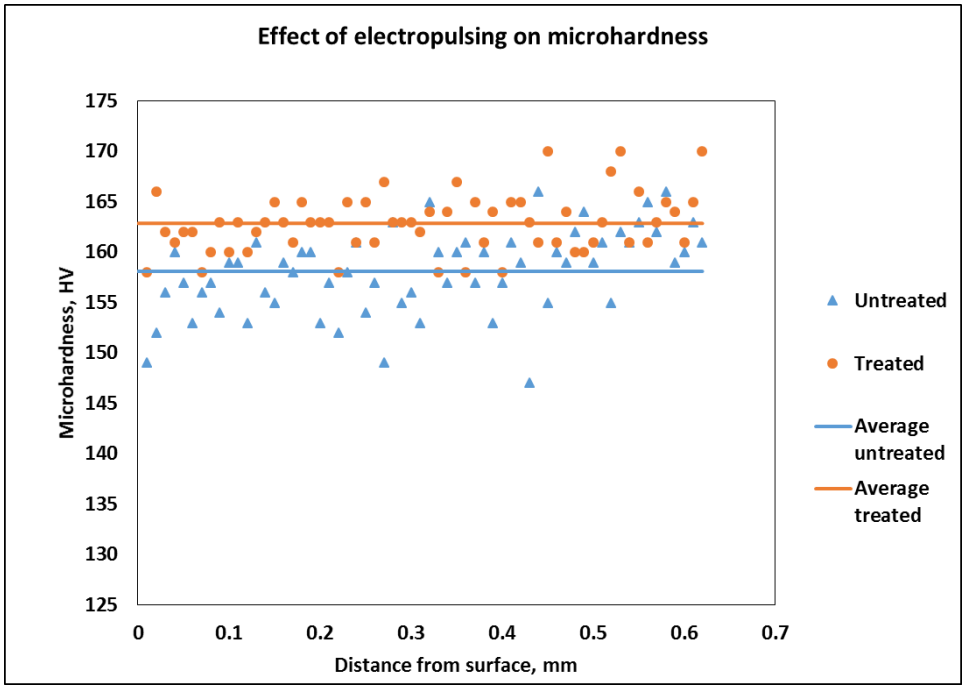

Figure 8.4.6 Electropulsing treatment on microhardness of aluminium alloy 2014-T6.

8.4.6 Electropulsing treatment effect on conductivity of aluminium alloy 2014-T6

The same optimum electropulsing treatment of 2 pulses of current density of 96 $\frac{MA}{m^2}$ with 0.1 s pulse time were used to investigate the conductivity of the sample. The conductivity was measured at 4 reference points A, B, C and D at an equal distance from each other and the results of the average five values at each point and the standard deviation are given in table 8.4.5. However, because of the curvature of the measuring point, the total contact between the overall surface areas of the probe and the sample was not possible. As a result, only partial conductivity of the sample was measured. To address this issue, the experimental conductivity values were normalised by the average conductivity value of point A of the untreated samples. The normalised or relative conductivity values of the untreated and treated sample were compared as shown in Table 8.4.5. The results demonstrate that at every reference point, the conductivity of the treated samples decreased compared to the untreated ones. The maximum reduction of 1.88 % was recorded at reference point C. The overall reduction of conductivity in treated sample was 1.19 % compared to the untreated one.

Table 8.4.5 Electropulsing treatment effect on the conductivity of the aluminium alloy 2014-T6.

Reference point on the surface	Relative conductivity (normalised by the average conductivity of point A of the untreated sample)		Reduction in conductivity due to PEC treatment (%)
	Untreated	Treated	
A	1+/-0.0096	0.9956+/-0.0126	0.41
B	1+/-0.0052	0.9904+/-0.0096	0.97
C	1.0007+/-0.0074	0.9822+/-0.0089	1.88
D	0.997+/-0.0071	0.9874+/-0.0111	1.46
Overall	1	0.9874	1.19

8.4.7 Effect of electropulsing treatment on fatigue fracture characteristics

The features of the final fracture surfaces of the untreated and treated (with optimum parameters) samples were observed with SEM as shown in Figure 8.4. The corresponding fatigue life of untreated and treated samples were 2666446 and 516247 cycles, respectively for a stress level of 200 MPa. In this study, both the aluminium alloy 2014-T6 samples exhibit a mixture of dimple and cleavage fractures (Figure 8.4.7). The treated sample contain more ductile dimple features [321, 322] with diverse sizes (Figure 8.4.7(2). A few quasi-cleavage fractures available in the treated one transformed into the ductile feature called torn edges [323] or peaks [324]. The untreated one, one the other hand, includes more quasi-cleavage fracture [325] throughout the area (Figure 8.4.7(1). The fracture surface of the untreated one also shows more secondary cracks [326] compared to the treated one.

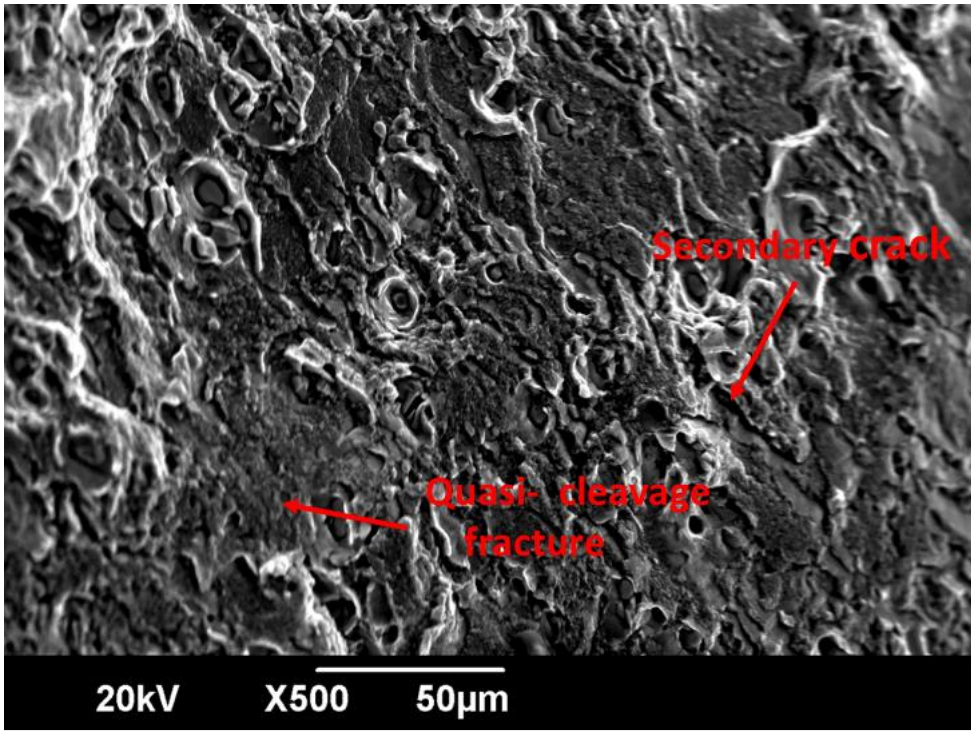

(1)

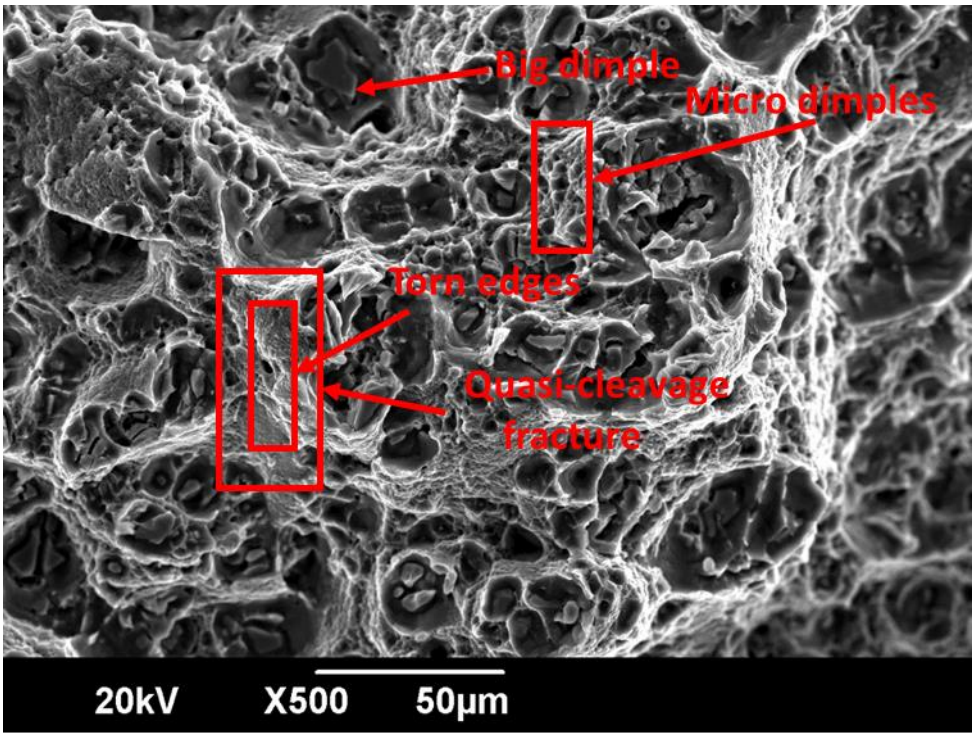

(2)

Figure 8.4.7 Final fracture surfaces during fatigue: (1) untreated and (2) treated (resolution: 5 nm).

The ductile dimple features can mainly be categorised as equiaxed big and micro-dimples (Figure 8.4.7(2)). The increased dimples in the treated sample resulted from uniformly distributed crystal defects, e.g., dislocations and precipitates. The higher amount of precipitates also contributed to this increase. These phenomena further reduced the quasi-cleavage fracture which transformed into ductile torn edges [323] or peaks [324]. A typical mode of quasi-cleavage fracture available in untreated one combines a large number of small and shallow dimples [325] (Figure 8.4.7(1)). The effect of precipitates is to promote ductile fractures and this is explained in the study of [327] which suggests that due to the incompatibility between the precipitates and aluminium alloy matrix, during tensile deformation, the precipitates impede the dislocation sliding, and thus cause stress concentration in the vicinity. When the concentrated stress exceeds a critical value, the interfacial debonding between the precipitates and aluminium matrix or the fracture of precipitates occur. The higher amount of secondary cracks found in the untreated sample can be formed by the dislocation pile-up.

8.4.8 TEM analysis of the effect of electropulsing treatment on dislocations and precipitations

The optimum parameters were also used to treat the material considered in the TEM study. All the photographs (Figure 8.4.8) contain dislocations and as well as precipitates. From (Figure 8.4.8(1) and 8.4.8(3)) it can be observed that, in the untreated samples, dislocations are tangled up forming dislocation pile-up (also known as dislocation cell structure or dislocation wall). Dislocation pinning [328] is also found in the untreated one (Figure 8.4.8(3)). On the other hand, from Figure 8.4.8(2) and 8.4.8(4)) it can be observed that, in treated sample, the dislocations are more spread out throughout the area. Dislocation depinning can be seen in the treated sample (Figure 8.4.8(4)). Precipitation in the treated sample (Figure 8.4.8(2) and 8.4.8(4)) are more pronounced compared to untreated ones (Figure 8.4.8(1) and 8.4.8(3)). These precipitates are relatively uniformly distributed on the area of the treated alloy. Needle-shaped precipitates can be seen only in the treated alloy (Figure 8.4.8(4) which is one of the earlier phases of the precipitates.

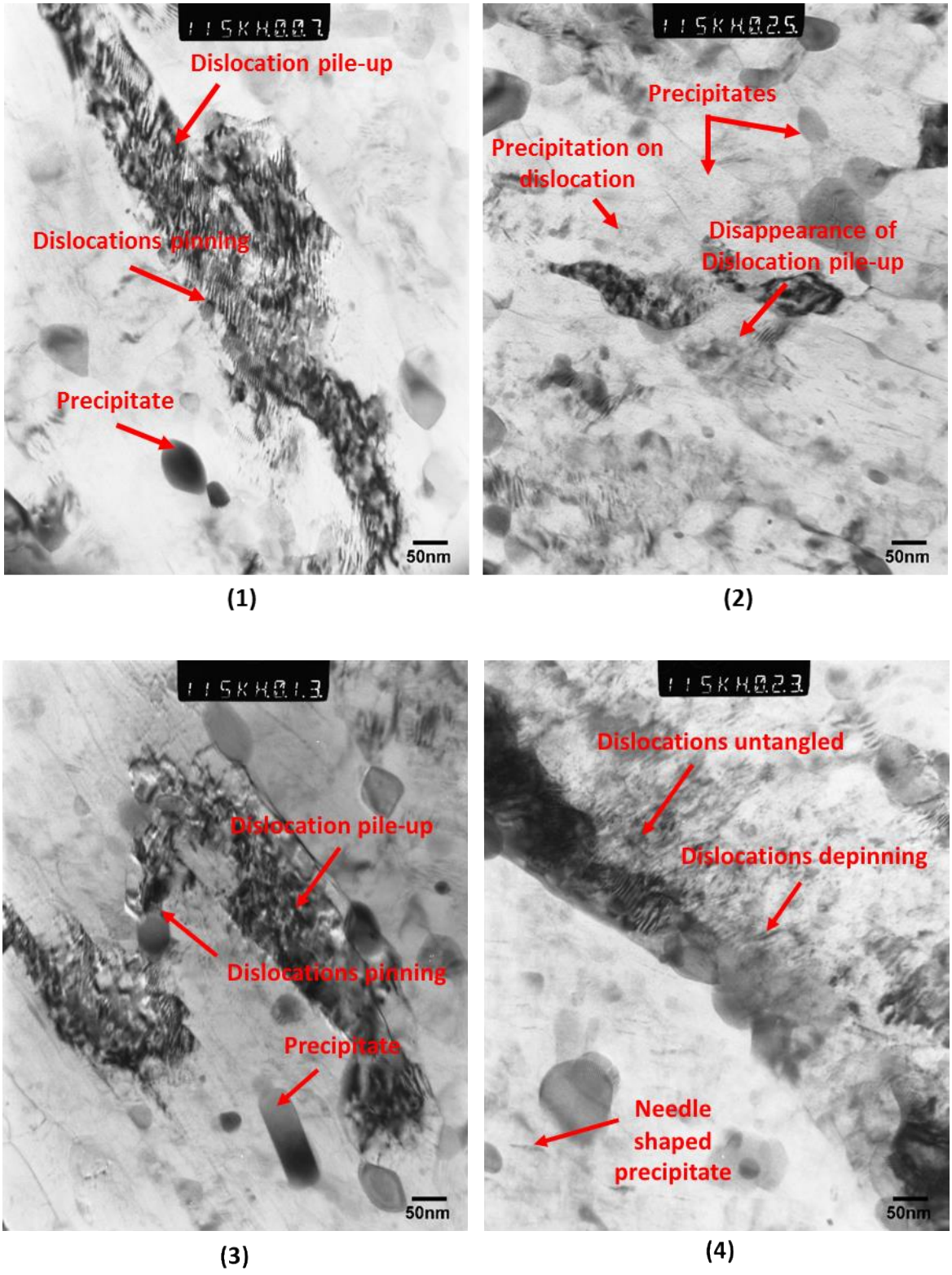

Figure 8.4.8 TEM samples taken from the near-surface area of 4 mm diameter bar on the length plane (1)(2) and thickness plane (2)(3). Here, (1) and (3) are untreated (1)(3) and (2) and (4) are treated.

In the present study (figure 8.4.8), the drift electrons formed during high-density electropulsing treatment applied the extra push force on dislocations which enhanced the mobility of the dislocations. This force is sometimes taken as the athermal effect of electropulsing [329]. The movement of the dislocation further eliminated the dislocation pile-up by untangling the dislocations. The magnetic field and electromagnetic force associated with the electropulsing treatment also contributed in this purpose. Dislocation depinning occurred simultaneously in this process. As a result, the dislocations are dispersed uniformly over the area of the treated sample.

Zhu et al. [330] reported that the total Gibbs free energy has two parts; $\Delta G_{ep} = \Delta G_{thermal} + \Delta G_{athermal}$, where the thermal effect of Joule heating contributes to the $\Delta G_{thermal}$ while the athermal effect contributes to the $\Delta G_{athermal}$. The athermal effect of electropulsing can be 319 times stronger than the thermal effect [330]. Thus, the transfer energy directly from the electrons to the atoms can be more effective than that in the traditional thermal and thermo-mechanical process. The precipitation process of SSS→GBP→ $\theta'' \rightarrow \theta' \rightarrow \theta$ [304, 327] can be considered for this aluminium alloy 2014-T6. The T-phase can also be formed in the 2000 series aluminium alloy [331]. In the present study (Figure 8.4.8), the combination of thermal and athermal effects promoted the growth of precipitates by atomic diffusion. Rahanama [329] also suggests that the athermal effect of electropulsing can remarkably increase the atomic diffusion flux. Moreover, the solute atoms interact better with the dislocations and the dislocations act as a nucleation points of the precipitates [304, 332]. As such, more precipitates were formed on the dispersed dislocations in the present study.

8.5 Discussion

A detailed investigation of the optimisation of the electropulsing effect on the fatigue resistance of aluminium alloy 2014-T6 has been presented in this chapter. Promising results have been achieved in this research.

From the Taguchi method (Table 8.4.3) (Figure 8.4.4), the treatment time was found to be the most effective parameter used to improve the fatigue performance. At the same time, the ANOVA test (Table 8.4.4) established that the treatment time has the

highest statistical significance among all three parameters investigated for the electropulsing effect with 78.80 % contribution. Increasing the treatment intensity and time also led to fatigue life improvement. However, the increase of the number of applications, the improvement in fatigue life did not follow the same pattern as other two. There was a saturation of the beneficial effect of electropulsing when the number of applications was increased. Moreover, if only the treatment intensity (A) and time (B) were considered, the beneficial effect of the electropulsing treatment on the fatigue performance can be simply modelled by using a 3D surface and contour plots as shown in Figure 8.5.1. In the contour plot (Figure 8.5.1(1)), the darker region shows the high fatigue life and the lighter region shows the low fatigue life. This helps identify that the fatigue life was maximum for the current density of 96 $\frac{MA}{m^2}$ with 0.1 s pulse time. From the 3D surface plot (Figure 8.5.1(2)), it is clear that with the increase of treatment intensity and time, fatigue life also increased.

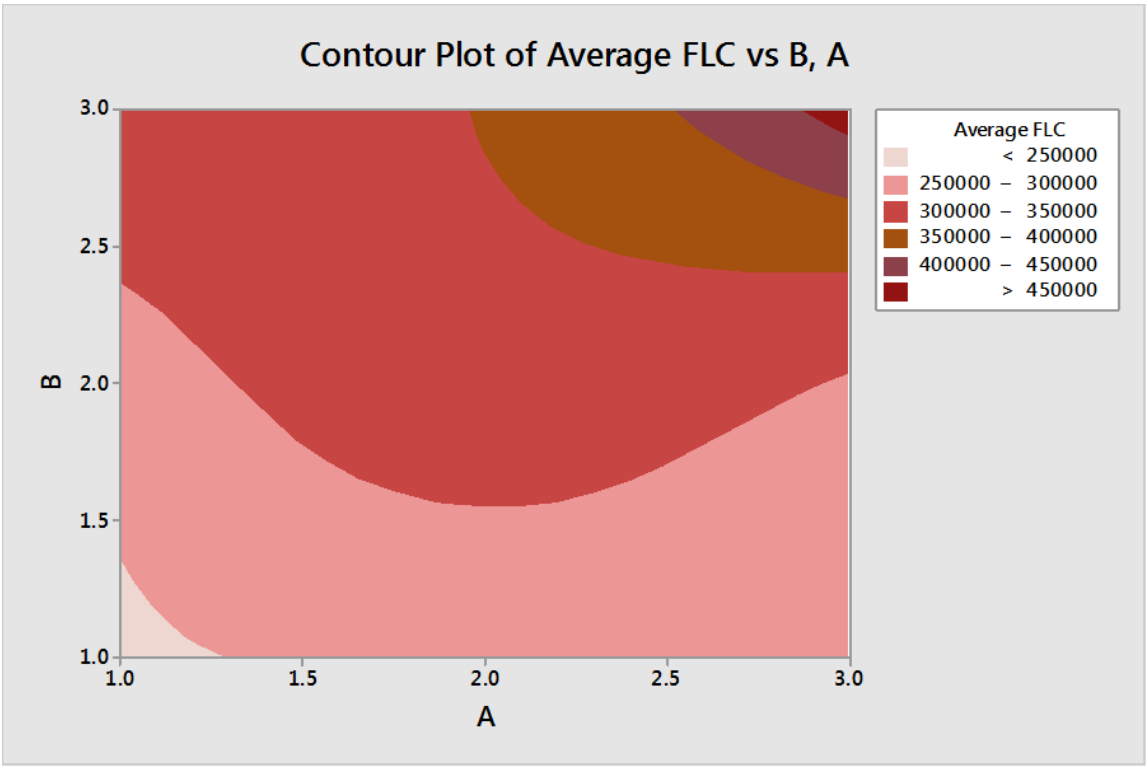

(1)

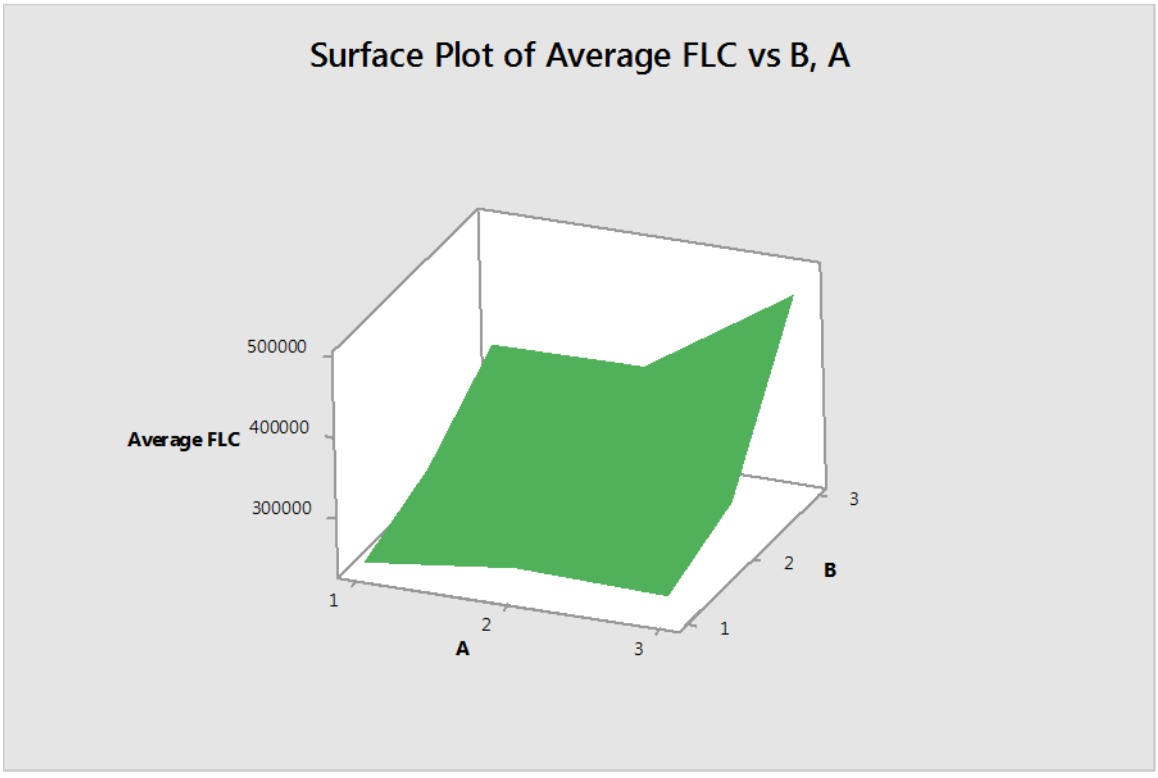

(2)

Figure 8.5.1 Contour (1) and surface (2) plots of average fatigue life cycles (FLC) vs electropulsing treatment intensity (A) and electropulsing treatment time (B).

Apart from the test using the optimum treatment parameters, the effect of electropulsing treatment with various other settings was investigated in the current study. A comparison of fatigue life improvements under different treatment conditions is shown in Figure 8.5.2. It is found that all the treatments were able to improve the fatigue life. 96 $\frac{MA}{m^2}$ with pulse time of 0.1 s and 2 applications was identified as the optimum treatment and gave the highest improvement of 97 %. Second highest improvement was found to be 47 % for 83 $\frac{MA}{m^2}$ with 0.1 s and 1 application. Minimum improvement of 2.41 % was found for 58 $\frac{MA}{m^2}$ with 0.00008 s and 1 application.

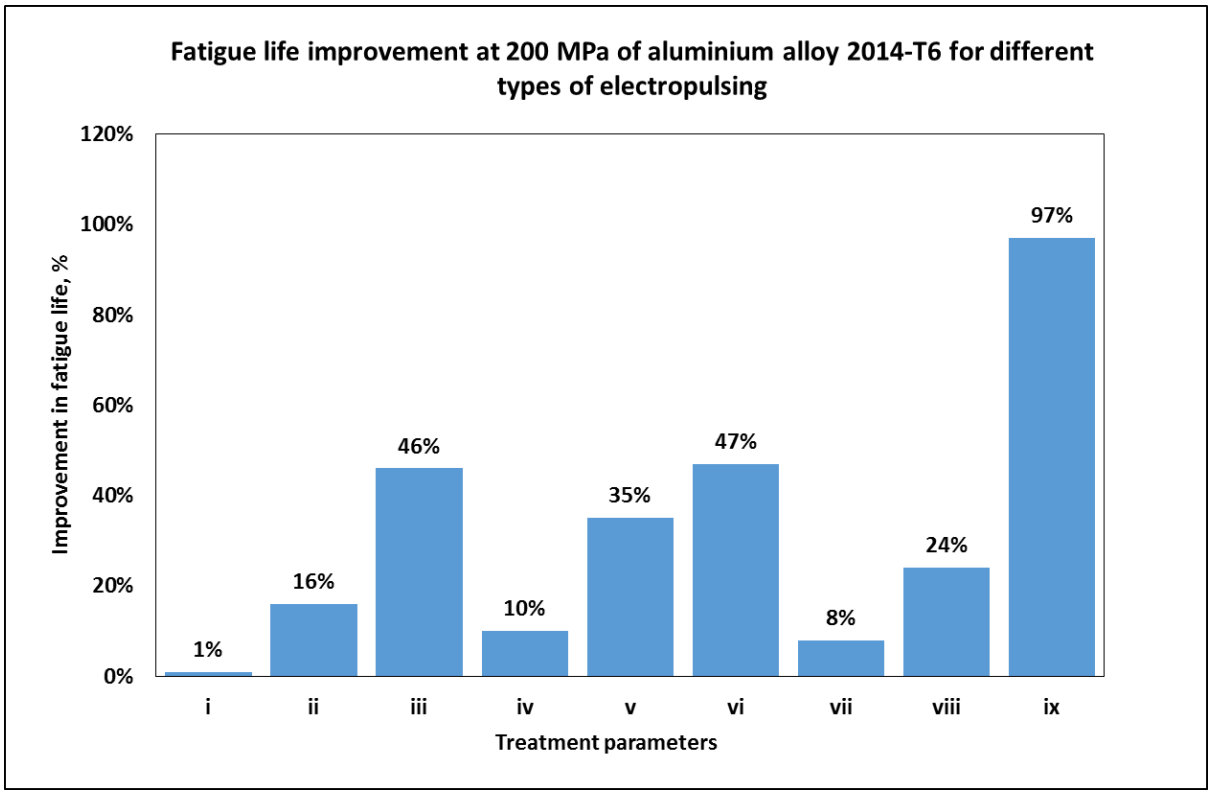

Figure 8.5.2 Bar chart of the fatigue life improvement due to different types of electropulsing treatment.

Microhardness improved by 3 % due to electropulsing of aluminium alloy 2014-T6 in this study(Figure 8.4.6). The microhardness of the treated alloy is less dispersed around the mean value. Electromagnetic treatment has shown improvement in

microhardness in other studies as well [14, 209, 214, 302]. During the rotating-bending fatigue test, maximum fatigue stress occurred near the sample surface and initiated fatigue cracks there. However, the crack initiation was delayed in the treated samples as the hardness was elevated by the effect of electropulsing. The fatigue life of the alloy was, therefore, increased through electropulsing treatment. This is consistent with some other studies which correlated the increase in fatigue life to the improvement of hardness [14, 209, 214, 227].

The effect of electropulsing treatment on microhardness and hence the fatigue resistance of the material can be demonstrated by the effect of the treatment on the conductivity of the alloy. The conductivity of the aluminium alloy 2014-T6 was reduced by 1.19 % after the electropulsing treatment. This can be the indication of enhanced precipitation hardening of the material due to the formation of additional GP zones and fine coherent and semi-coherent precipitates [304-306]. These extra precipitates are capable of scattering electrons further by coherent strain during the current flow and therefore reduce the conductivity of the alloy. The Joule heating [305] associated with the electropulsing treatment can also be responsible for the formation of these precipitates and increase of the microhardness. As a result, there exists a relation between the increase of the fatigue resistance and the reduction of the conductivity of the alloy.

From the fractographic analysis (Figure 8.4.7), it is found that there are relatively more ductile features, e.g. dimples formed due to the well-distributed precipitates and dislocations promoted by the electropulsing treatment. The electropulsing treatment in other studies [331, 333, 334] also increased the ductile features.

The TEM study (Figure 8.4.7) can explain the mechanisms of electropulsing treatment on improving the fatigue life. Due to the effect of the high-density electron flow generated by electropulsing, the dislocations were dispersed through the aluminium alloy 2014-T6 used in this study. The dislocation pile-up also disappeared in this process. The dislocation pile-up can sometimes be considered as the precursor of the fatigue crack initiation. Therefore, the disappearance of dislocation pile-up delayed the fatigue crack ignition and enhanced the fatigue life. This type of dislocation activity was also found in the literature where the electropulsing treatment was found to promote dislocation movement [335], rearrangement of dislocations [336], elimination

of dislocations [227]. The thermal and athermal effect of the present electropulsing treatment also promoted uniformly distributed precipitation and thus enabled precipitation hardening (Figure 8.4.7). From the literature, it is also found that the electropulsing treatment refined and dispersed the precipitates [337] and promoted precipitaion [331, 338] while magnetic field treatment promoted precipitates which were fine and dispersed [339]. Additionally, the combined effect of electric and magnetic field promoted precipitation as well [303]. The strengthening of the aluminium alloy 2014-T6 by precipitation further improved the fatigue resistance by delaying the fatigue crack initiation and its growth.

8.6 Summary

The electropulsing treatment is capable of enhancing the fatigue resistance of aluminium alloy 2014-T6. The treatment intensity, duration of the pulsed current and number of applications of this treatment all can affect the fatigue life enhancement. Among these factors, the duration of the pulsed current is the most influential in boosting fatigue resistance. However, a higher number of applications can lead to the saturation of the beneficial effect of electropulsing on fatigue resistance. The hardness of this aluminium alloy can also be improved by the 2 applications of 96 $\frac{MA}{m^2}$ treatment intensity for 0.1 s pulsed duration which represents the optimum electropulsing parameters to improve fatigue resistance in this study. This increased hardness can also be correlated to the reduction of the conductivity of the treated alloy. The mechanism of effect of electropulsing treatment involved the change in microstructure which enabled the improvement of fatigue resistance and this can be explained by dislocation activity and formation of precipitates. Therefore, the results in this chapter can potentially help understand the optimisation of the electropulsing treatment on fatigue resistance of aluminium alloy 2014-T6.

9 Electropulsing treatment effect on fatigue damage repair of aluminium alloy 2011-T6 and 2014-T6

9.1 Introduction

Electromagnetic treatment has a positive effect on the enhancement of mechanical performance of various prefatigued alloys [13-16, 207, 209, 213-217, 223, 227, 228]. This has already been explained in the literature review and supported by the experimental investigation presented in Chapter 8. This chapter presents an experimental study of the electromagnetic treatment in the form of electropulsing treatment on the enhancement of fatigue life of prefatigued samples of aluminium alloys.

For this, both aluminium alloy 2011-T6 and aluminium alloy 2014-T6 have been used. Electropulsing was applied to 70 % prefatigued 2011-T6 and 56 % prefatigued aluminium alloy 2014-T6 (calculated using Equation 2.10.2). The intensity of the treatment and the number of applications were varied while keeping the pulse time constant. The optimum treatment condition was identified based on the highest improvement of fatigue life of aluminium alloy 2011-T6. This optimum treatment condition was also used for aluminium alloy 2014-T6. The change of the fatigue life due to electropulsing and its effect on the level of prefatigued damage have been explained in detail in this chapter. The possible mechanisms for the change of the fatigue life due to electropulsing have also been discussed.

9.2 Methodology

Two types of aluminium alloys were considered in this study as mentioned above. These were aluminium alloy 2011-T6 and aluminium alloy 2014-T6. The details of the aluminium alloy 2014-T6 have already been described in Chapter 8. The chemical composition of aluminium alloy 2011-T6 is given in table 9.2.1.

Table 9.2.1 The chemical composition of aluminium alloy 2011-T6 [309].

Element	Al	Si	Fe	Cu	Pb	Bi	Zn	Others
Weight (%)	Balanced	0.4	0.7	5.0-6.0	0.2-0.4	0.2-0.4	0.3	0.15

Aluminium alloy 2011-T6 has a high strength and machinability [357] but poor weldability. The ultimate tensile strength (UTS) of this alloy is 395 MPa [373]. Typical uses of aluminium alloy 2011-T6 include fasteners, fittings, artillery and the trim of vehicles.

Fatigue samples of aluminium alloy 2011-T6 were supplied by TecQuipment [361], and aluminium alloy 2014-T6 was machined as described in Chapter 8 Section 8.3.1. The geometry of the sample was as previously described in the same section. The samples were prefatigued before the electropulsing treatment was applied.

9.3 Results and analyses

9.3.1 Baseline fatigue life of untreated aluminium alloys

The baseline fatigue life of untreated samples was defined based on the average value of fatigue life of four samples of aluminium alloys 2011-T6 and 2014-T6 for 225 MPa.

Results of the baseline fatigue life have been presented in Table 9.3.1, and Figures 9.3.1 and 9.3.2. For aluminium alloy 2011-T6, the experimental average fatigue life was 153003 cycles and the standard deviation was 18050 cycles. On the other hand, for aluminium alloy 2014-T6, the experimental average fatigue life of aluminium alloy was 137457 cycles and the standard deviation was 18868.

Table 9.3.1 Experimental fatigue life of aluminium alloys at a particular stress level.

Aluminium alloy	Stress level (MPa)	Fatigue life (cycles)	Average fatigue life (cycles)	Coefficient of Variation (CV) (%)
Aluminium alloy 2011-T6	225	131467, 146497, 152815, 181234	153003	11.80
Aluminium alloy 2014-T6	225	118884, 129599, 132397, 168948	1374572	13.73

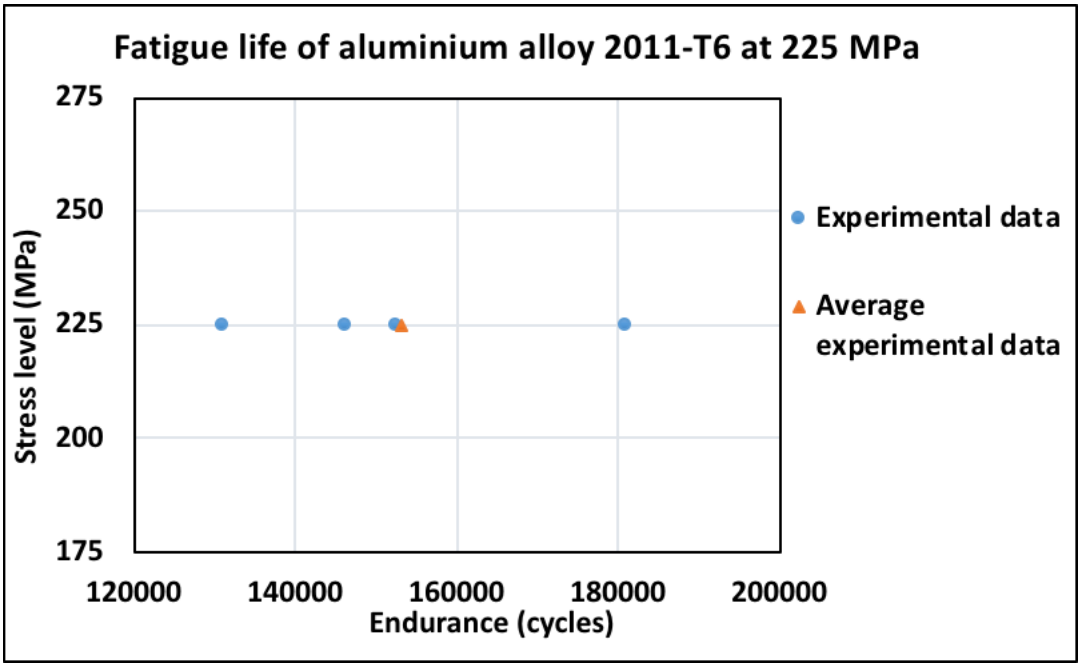

Figure 9.3.1 Graph showing endurance of aluminium alloy 2011-T6 samples at stress level 225 MPa.

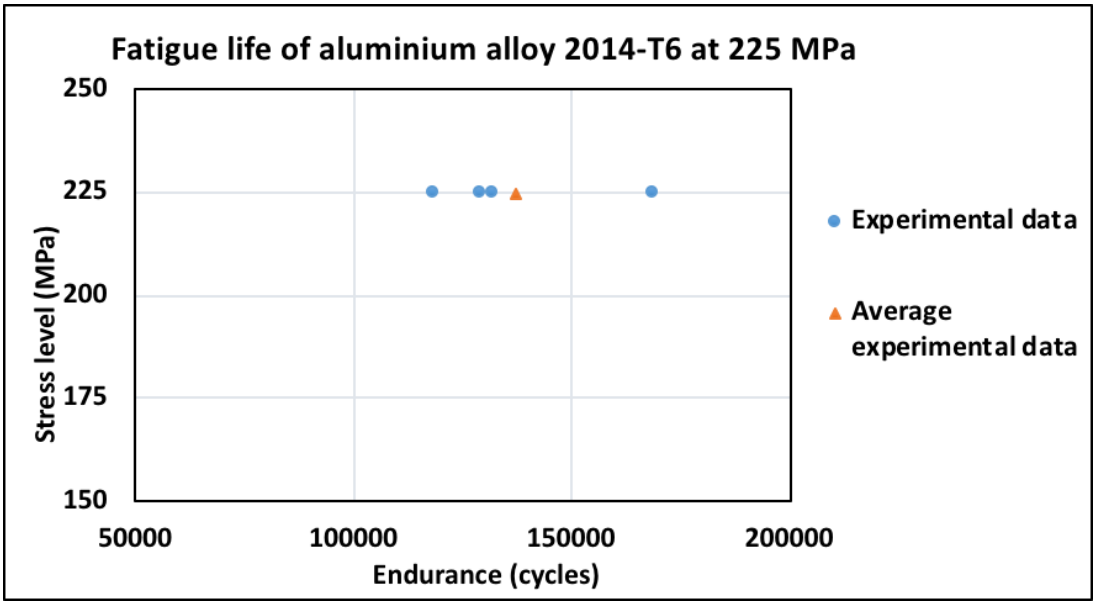

Figure 9.3.2 Graph showing endurance of aluminium alloy 2014-T6 samples at stress level 225 MPa.

9.3.2 Electropulsing treatment effect on prefatigued specimen

Electropulsing treatment effect in terms of the intensity of electropulsing and the number of applications was investigated on the prefatigued specimens; 3 for aluminium alloy 2011-T6 and 4 for aluminium alloy 2014-T6. The work is focused on the damage-repairing ability of the electropulsing treatment based on statistical analysis. All the results are given in Table 9.3.2.

Table 9.3.2 Electropulsing treatment parameters and corresponding fatigue life enhancement.

Aluminium Alloy	Test no.	Stress level (MPa)	ET treatment type	Prefatigue level (%) for treatment	Number of applications	Treatment intensity $\left(\frac{MA}{m^2}\right)$	Treatment time (ms)	Correlation coefficient	Fatigue life (Cycles)	Fatigue life enhancement (%)
Aluminium Alloy 2011-T6	1, 2, 3	225	Electropulsing	70%	3	1091 1391 1691	16	-0.96	202983, 179321, 172123	32.67, 17.20, 12.50
Aluminium Alloy 2011-T6	4, 5, 6	225	Electropulsing	70%	2, 3, 4	1091	16	-0.69	197328, 202983, 183481	28.97, 32.67, 29.92
Aluminium Alloy 2014-T6	7	225	Electropulsing	56%	3	1091	16	-	208787, 224219, 259232	51.89, 63.12, 88.59

Firstly, three different levels of intensity of electropulsing were used to treat prefatigued aluminium alloy 2011-T6. Here, three applications of 1091 $\frac{MA}{m^2}$, 1391 $\frac{MA}{m^2}$ and 1691 $\frac{MA}{m^2}$ with 16 ms pulse time were used. The intensity of the electropulsing was calculated by dividing the maximum current value by the minimum cross-sectional area of 2 mm radius. The treatment curves with their equations are shown in Figure 9.3.3. These curves were taken by filling it with the registered data during the electropulsing treatment. The samples were prefatigued to 107102 fatigue cycles before the electropulsing treatment was applied. This corresponds to 70 % of the fatigue life of the material at 225 MPa.

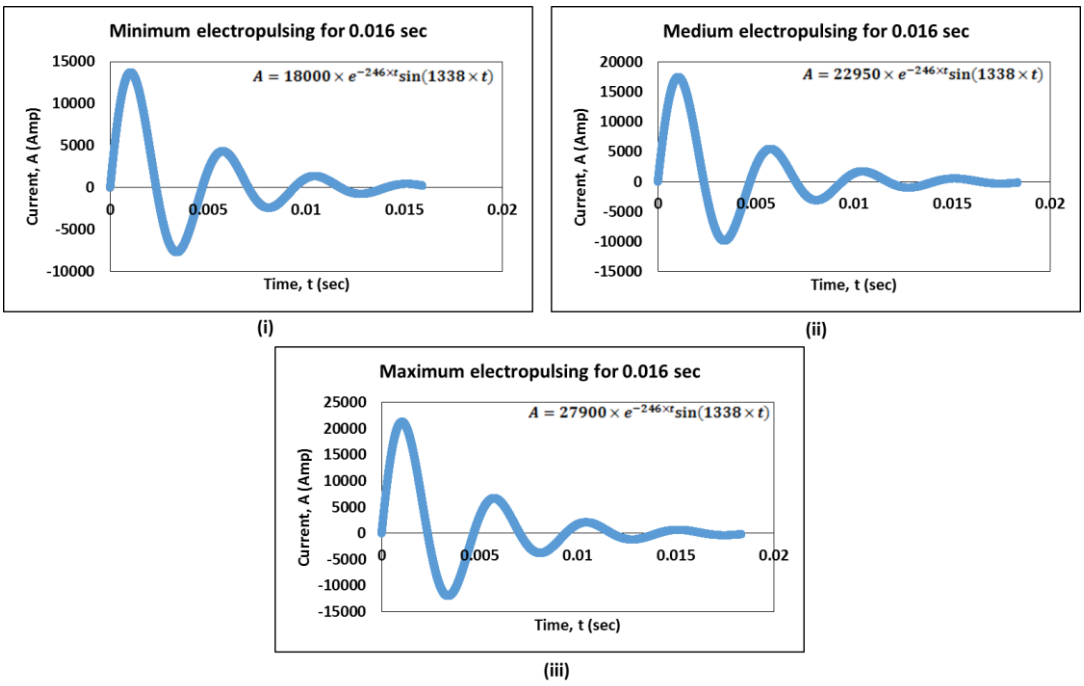

Figure 9.3.3 Electropulsing curves with their corresponding equations.

The electropulsing intensity (current density) effect on fatigue life at 225 MPa is shown in Figure 9.3.4. It has been shown that, in all events, the fatigue life of the treated samples increased compared to that of untreated samples. The treatment with 1091 $\frac{MA}{m^2}$ led to the highest improvement of 32.67 %. The improvement in fatigue life was lower while using higher treatment intensity. For treated samples, the correlation coefficient was r=-0.96 which was close to -1 referring to strong negative linear

correlation between the intensity of the treatment and the fatigue life. From this trend, it can be explained that the beneficial effect of electropulsing can be negatively affected by the higher intensity. This trend also suggest that the sample will get damaged beyond a certain level of electropulsing treatment.

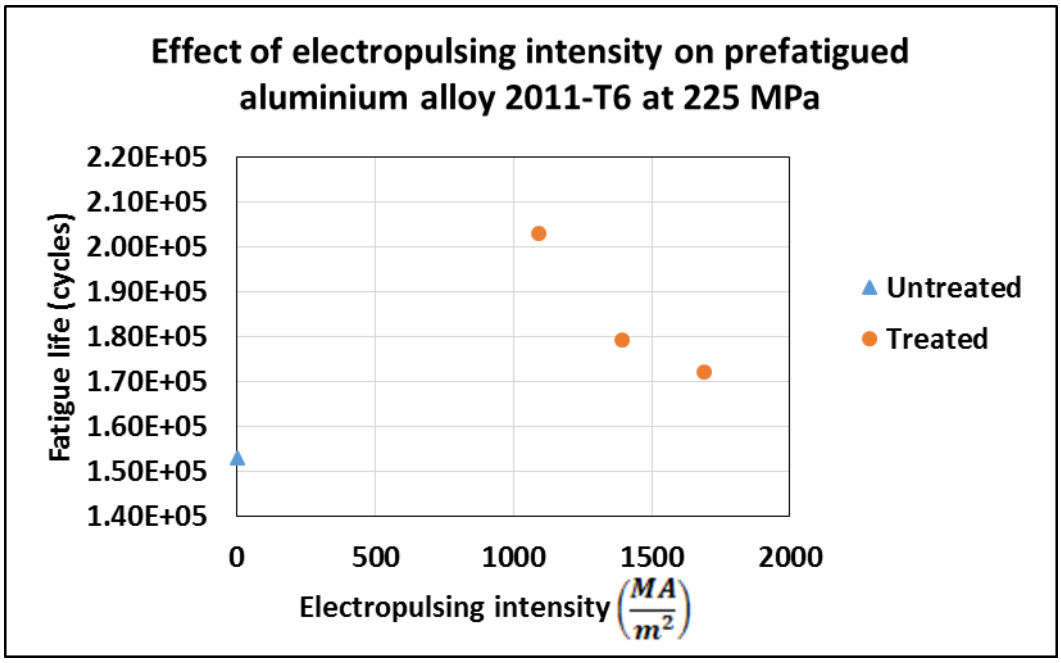

Figure 9.3.4 Electropulsing intensity effect on fatigue life at 225 MPa.

The most effective intensity of 1091 $\frac{MA}{m^2}$ with pulsed duration of 0.016 s was further investigated by changing the number of applications to 2 and 4 in addition to the 3 applications previously used. The results are shown in Figure 9.3.5. Here, all the cases yielded fatigue life enhancement. From the graph, it can be observed that 2 applications gave quite similar improvement to 3 applications. However, the improvement of fatigue life was reduced rapidly for 4 applications. For the treated samples, the correlation coefficient was r=-0.69 which referred to medium negative linear correlation between the number of applications of treatment and the fatigue life. This means that if the number of applications are increased to a certain level the beneficial effect of the treatment will start to decay on fatigue life improvement. Therefore, 3 applications of 1091 $\frac{MA}{m^2}$ pulsed current density with 16 ms pulsed duration appeared to be the optimum treatment condition as shown in Figure 9.3.6.

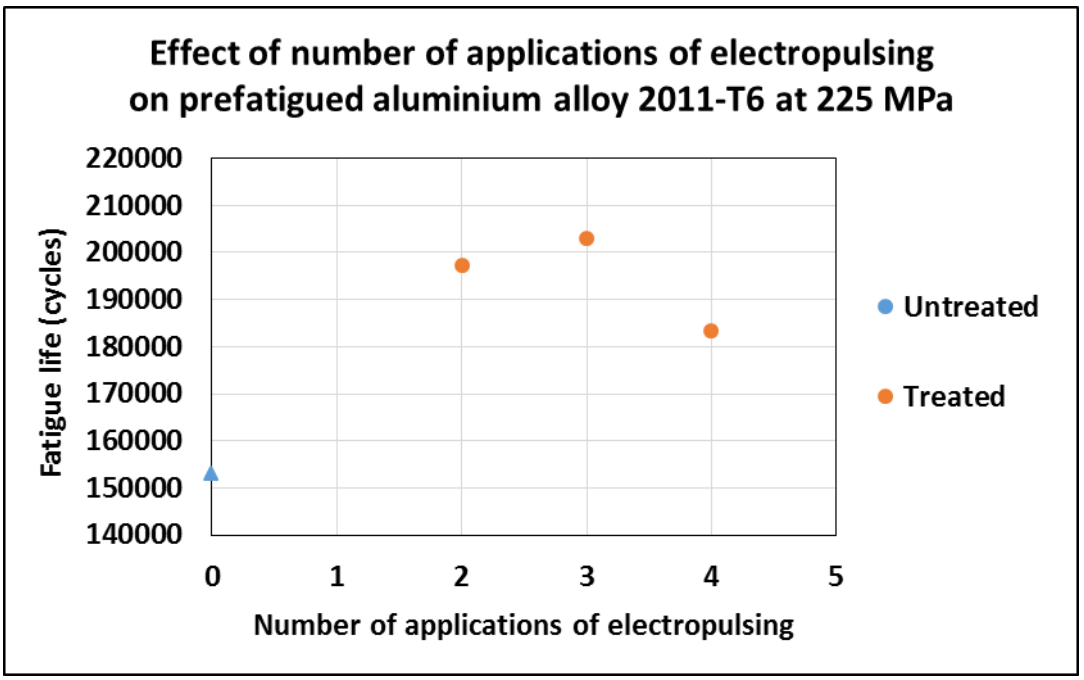

Figure 9.3.5 Effect of the number of applications of electropulsing on fatigue life at 225 MPa.

These optimum treatment parameters were then applied to the prefatigued aluminium alloy 2014-T6 samples. The results are shown in Figure 9.3.6. The treatment was applied after 76975 fatigue cycles which corresponds to 56 % of the fatigue life of this untreated material at 225 MPa. This improved the fatigue life by 67.87 % on average when compared to the untreated average. The highest improvement in fatigue life was 88.59 %.

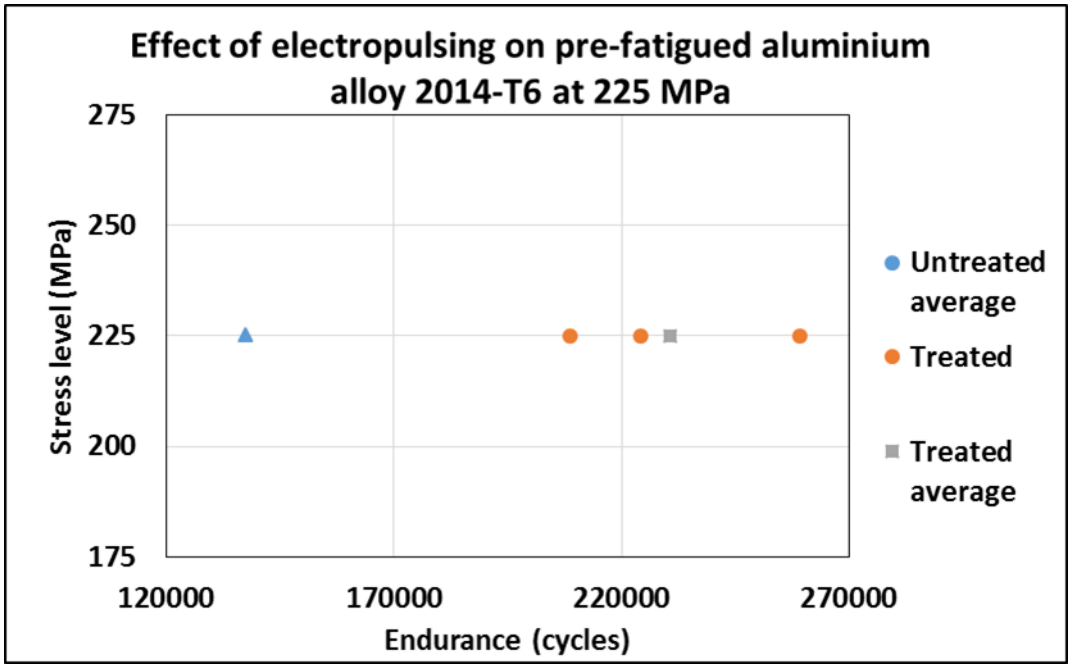

Figure 9.3.6 Electropulsing treatment effect on fatigue life at 225 MPa.

9.3.3 Effect of electropulsing treatment on damage repairing of aluminium alloy

In order to investigate the effect of electropulsing on damage repairing, a parameter $\left(\frac{\Delta D}{D_i}\right)$ referred by the study of Bao-Tong et al. [16] was investigated. According to this study, the initial fatigue damage before magnetic treatment is defined as,

$$D_i = \frac{N_i}{N_f} \tag{9.3.1}$$

where, N_i=Initial number of fatigue cycles before the application of the magnetic treatment and N_f=total fatigue life without treatment.

The residual fatigue life without treatment is denoted by

$$N_r = N_f - N_i \tag{9.3.2}$$

Damage tolerance is defined as

$$D_r = 1 - D_i = \frac{N_r}{N_f} = \frac{N_f - N_i}{N_f} \tag{9.3.3}$$

The difference between the fatigue life of treated and untreated samples is defined as

$$\Delta N_r = N_r' - N_r \tag{9.3.4}$$

Where, N_r'= Residual number of fatigue cycles after the magnetic treatment.

Damage-repairing parameter is defined as

$$\frac{\Delta D}{D_i} = \frac{D_r' - D_r}{D_i} = \frac{N_r' - N_r}{N_i} = \frac{\Delta N_r}{N_i} \tag{9.3.5}$$

where, D_r'= damage tolerance of a sample after magnetic treatment.

$\frac{\Delta D}{D_i}$=0 represents no damage-repairing effect and $\frac{\Delta D}{D_i}$=1 represents the damage is fully repaired.

For this study, It can be observed from the graph shown in Figure 9.3.7 that the damage-repairing was more prominent in aluminium alloy 2014-T6 where only prefatigued level of 56 % was considered compared to aluminium alloy 2011-T6 where a higher prefatigued level of 70 % was considered. The electropulsing treatment used in this study led to the complete damage repairing of aluminium alloy 2014-T6 ($\frac{\Delta D}{D_i}$>1) but partial repairing of aluminium alloy 2011-T6 ($\frac{\Delta D}{D_i}$<1). It can be illustrated from this fact that the higher prefatigued level can cause high damage such as microcracks which can't be fully repaired by this treatment if the damage has exceeded a certain limit. This is consistent with the work reported in other study by [16].

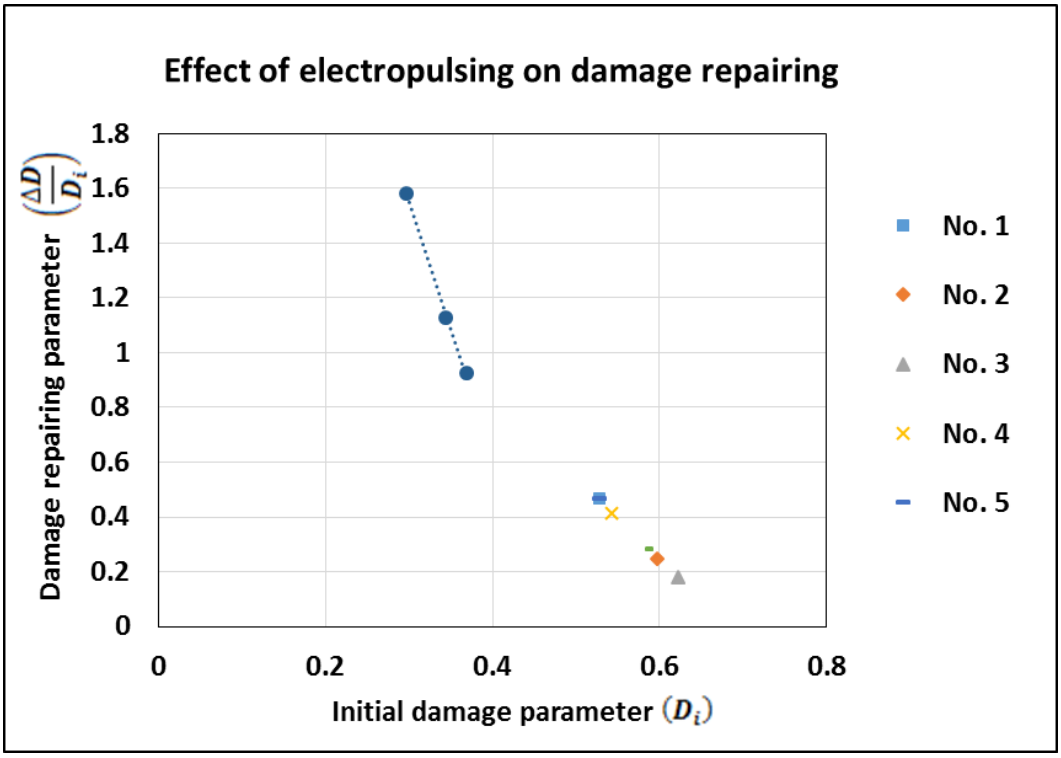

Figure 9.3.7 The relationship of $\frac{\Delta D}{D_i}$ vs. D_i for the specimens with electropulsing treatment (Nos. correspond to the test nos. of Table 9.3.2).

9.4 Discussion

When the effect of treatment intensity on fatigue resistance was considered, the number of applications and the pulse time were kept constant at 3 applications and 16 ms pulsed duration. Here, the electropulsing intensity was varied between 1091 $\frac{MA}{m^2}$, 1691 $\frac{MA}{m^2}$ and 1391 $\frac{MA}{m^2}$ for 70 % prefatigued aluminium alloy 2011-T6 samples. The maximum increase in fatigue life was 33 % which happened to be the treatment with the minimum electropulsing intensity of 1091 $\frac{MA}{m^2}$ (Table 9.3.2). With the increase of the intensity of the treatment, the improvement in fatigue life decreased linearly. This is related to the saturation of the beneficial effect of the treatment when the intensity of the treatment has reached certain level.

On the other hand, when the effect of the number of applications on fatigue resistance was considered, the treatment intensity and pulse time were kept constant at 1091 $\frac{MA}{m^2}$

and 16 ms. Here, the number of applications of the electropulsing varied between 2, 3 and 4 applications at 70 % prefatigued level for aluminium alloy 2011-T6 samples. With the increase of the number of applications, the beneficial effect of electropulsing treatment on fatigue life increased up to 3 applications and then it decreased for 4 applications (Figure 9.3.6). Therefore, The application of three pulses was found to be the optimum choice.

For aluminium alloy 2014-T6, the optimum electropulsing of 1091 $\frac{MA}{m^2}$ pulsed current density with 16 ms pulsed duration and 3 applications was also used at 56 % prefatigued level. Here, the average improvement was found to be 68 % . This was higher than the improvement in 2011-T6. This indicates that the beneficial effect of fatigue life due to electropulsing may depend on the prefatigued level. With the increase of the prefatigued level, the beneficial effect is reduced. This can be quantified from the analysis of damage repairing parameter, $\left(\frac{\Delta D}{D_i}\right)$, (Figure 9.3.8) proposed in [16]. When the damage was small in aluminium alloy 2014-T6, the electropulsing was able to repair the damage fully. However, when the damage exceeded a certain limit which is the case of 70 % prefatigued aluminium alloy 2011-T6 sample, it was only able to partially repair the damage.

The improvement of fatigue resistance can be explained by the damage-repairing mechanism including crack healing. Electropulsing treatment can heal the initial damage by dislocation movement and Joule heating [15, 207, 226]. It can annihilate dislocations by electron drift. Moreover, the damaged area possesses higher electric resistance. When electricity flows around damage, Joule heating is produced due to the current concentration at the damaged area of high resistance. This can repair the slip bands. The heat can also expand and melt crack faces which leads to crack closure and crack healing. The crack growth rate also reduces as a result. On the other hand, excessive treatment can result in overheating. This can cause melting damage [218]. As a result, the beneficial effect of electropulsing on fatigue resistance can be reduced.

9.5 Summary

In this study, it was observed that the electropulsing treatment led to improvement in fatigue life. This improvement varied depending on the change of the electropulsing intensity, duration and number of applications. The intensity and the duration of the electropulsing and the number of applications can be optimised in order to achieve significant improvement in fatigue resistance of aluminium alloy. The effect of treatment also depends on the prefatigued level. The beneficial effect of electropulsing reduced with the increase of prefatigued level. Excessive treatment may lead to saturation or even have a detrimental effect on fatigue resistance. This can be related to the melting damage due to overheating as reported in the literature. Further research is needed to make the best use of this treatment technique for optimum fatigue resistance enhancement.

10 Conclusions and future work

10.1 Conclusions

A comprehensive literature review has been carried out for a better understanding of: fundamental theories of fatigue and fracture mechanics; constant amplitude (CA) and variable amplitude (VA) fatigue crack growth; crack closure effect and measurement; factors affecting the stress intensity factor range threshold for fatigue crack growth; and the electromagnetic treatment and its effect on fatigue resistance.

From the experimental investigation on the transient post-overload crack growth of aluminium alloy 6082-T6, delayed overload retardation widely reported in the literature has been observed. Fatigue crack growth accelerated right after the application of the overload. There was then a prolonged retardation in fatigue crack growth before the fatigue crack growth recovered to the pre-overload level. Both the compliance and the replica techniques were able to identify the transient behaviour. With the increase of the overload ratio (OLR), the magnitude and extent of the overload retardation increased. When the R ratio effect was investigated under CA loading at a fixed maximum stress intensity factor, the crack growth rate was reduced with the increase of the R ratio. This do not contradict findings in literature as the higher R ratio is achieved by the increase of K_{min}, which effectively reduces the stress intensity factor range ΔK. The results prove that the stress intensity factor range rather than the stress ratio is the dominant factor controlling the fatigue crack growth. When crack closure effect is taken into consideration by replacing the applied stress intensity factor range with the effective stress intensity factor range, the R ratio effect can be explained further. These results will help understand crack growth behaviour under various loading conditions and develop more reliable damage tolerance design (DTD) tools.

The analysis of fatigue crack growth of aluminium alloy 2024-T351 using the strip yield model also confirmed the transient overload retardation effect. The magnitude and extent of overload retardation increased with the increase of the OLR and the baseline stress intensity factor range, $(\Delta K)_{BL}$, but decreased with the increase of the R ratio and the constraint factor, α. This α can be used to effectively simulate the plane stress and

plane crack closure condition. These outcomes will help understand the near tip crack behaviour and hence the behaviour of crack growth under variable amplitude (VA) loading in greater detail.

Based on the experimental, finite element (FE) and strip yield model analysis of compliance curves around the crack tip of aluminium alloy 6082-T6, it was shown that crack closure measurement can be influenced by the crack tip plasticity. Clear non-linearity has been identified on the compliance curve at a location close to the tip of a stationary crack for no crack closure should exist. The transition point so identified is related to the crack tip plastic deformation, not to the crack closure. The accuracy of the crack closure measurement can therefore be enhanced if the effect of crack tip plasticity on the non-linearity of the near tip compliance curve could be separated. This is important in defining accurately the effective crack growth driving force for reliable damage tolerance design of engineering components.

The analytical model which was used to predict the threshold stress intensity factor range for fatigue crack growth suggested that ΔK_{th} is a function of material properties and R ratio. With the increase of R ratio ΔK_{th} decreased. This analytical model will help identify the ΔK_{th} for different materials in different loading conditions and improve the fatigue design of engineering components.

Electropulsing was shown to have beneficial effects on the fatigue resistance of aluminium alloy 2014-T6 and aluminium alloy 2011-T6. Among pulsed current intensity, pulse time and number of applications, pulse time is observed to be the most effective parameter to improve fatigue resistance. It has been shown that the electropulsing treatment enhanced the fatigue life by increasing the microhardness which delayed the crack initiation process. By using TEM analysis, the mechanism of the treatment in improving the fatigue life has been explained by dislocation movement and additional precipitation due to the electron wind force produced during electropulsing treatment. The decrease in conductivity also indicated the existence of extra precipitates in the treated alloy. The SEM analysis has shown a higher ductile fracture in the treated alloy. The beneficial effect of electropulsing treatment on fatigue damage repair is dependent on the prefatigued level of the material. The fatigue damage can be fully repaired at a lower prefatigued level and may not be fully

recovered once the prefatigued level exceeds a certain limit. There exists an optimum electropulsing treatment condition for maximum fatigue resistance enhancement.

10.2 Future work

The recommendations for future work are given as follows:

- The experimental study of the post-overload transient fatigue crack growth can be extended to the loading spectrum with multiple overloads, overload/underload combinations, and block loading. This will help understand the interactions among different loading cycles and develop a more reliable damage tolerance design algorithm.
- The strip yield model which is used in this project can be developed further to incorporate other closure effects including roughness induced crack closure (RICC) and oxide induced crack closure (OICC). This will provide an efficient method to determine the effective crack growth driving for reliable damage tolerance design of engineering components under various loading environment.
- The non-linearity of the compliance curve should be investigated further in order to separate the effect of the crack tip plasticity from the effect of crack closure. This will improve the accuracy of the crack closure measurement and hence provide more reliable determination of crack growth driving force.
- The investigation of electromagnetic treatment on the fatigue resistance can be extended to steel, copper and titanium alloys. Different treatment techniques including pulsed magnetic field (PMF) treatment can also be investigated. Effect of electromagnetic treatment on fatigue crack growth can also be investigated.

References

1. Polmear, I., D. StJohn, J.-F. Nie, and M. Qian, *Light alloys: metallurgy of the light metals*. 2017: Butterworth-Heinemann.
2. Djukanovic, G. *Aerospace industry trends & aluminium use*. 2016 [cited 2017 11/04/2017]; Available from: http://aluminiuminsider.com/aersopace-industry-trends-aluminium-use/.
3. Market, C., *Current Market Outlook 2015-2034*. 2015, Boeing.
4. Airbus, A.G.M.F., *Forecast 2015-2034*. 2015.
5. Djukanovic, G. *Aluminium Vs. Steel*. 2015 [cited 2017 11/04/2017]; Available from: http://lmfinternational.com/index.php/markets/590-commodities-shipping/34860-Aluminium-Vs.-Steel.
6. Campbell, F.C., *Elements of metallurgy and engineering alloys*. 2008: ASM International.
7. Anderson, T.L., *Fracture mechanics: fundamentals and applications*. 2005: CRC press.
8. Harter, J., *AFGROW users guide and technical manual: AFGROW for Windows 2K/XP.* Version, 2006. **4**(0011): p. 14.
9. Xu, Y., *Closure assessment and overload transient behaviour in damage tolerant airframe materials*. 2001, University of Southampton.
10. Singh, K.D., *Modelling of combined roughness and plasticity induced closure effects in high strength Al-alloys*. 2005, University of Southampton.
11. Zerbst, U., M. Vormwald, R. Pippan, H.-P. Gänser, C. Sarrazin-Baudoux, and M. Madia, *About the fatigue crack propagation threshold of metals as a design criterion–A review.* Engineering Fracture Mechanics, 2016. **153**: p. 190-243.
12. Vormwald, U.D.-I.M., *Elastic-Plastic Fatigue Crack Growth*, in *Advanced Methods of Fatigue Assessment*. 2013, Springer. p. 391-481.
13. Fahmy, Y., T. Hare, R. Tooke, and H. Conrad, *Effects of a pulsed magnetic treatment on the fatigue of low carbon steel.* Scripta materialia, 1998. **38**(9): p. 1355-1358.
14. Tang, Y., A. Hosoi, Y. Morita, and Y. Ju, *Restoration of fatigue damage in stainless steel by high-density electric current.* International Journal of Fatigue, 2013. **56**: p. 69-74.

15. Hosoi, A., T. Kishi, and Y. Ju, *Healing of fatigue crack by high-density electropulsing in austenitic stainless steel treated with the surface-activated pre-coating.* Materials, 2013. **6**(9): p. 4213-4225.
16. Bao-Tong, L., Q. Sheng-Ru, and S. Xiao-Yan, *Exploration on repairing fatigue damage of steel specimens with magnetic treatment.* Scripta materialia, 1999. **40**(7): p. 767-771.
17. Bristow, J.W. and P. Irving, *Safety factors in civil aircraft design requirements.* Engineering Failure Analysis, 2007. **14**(3): p. 459-470.
18. Ministry of Defence, *Defence Standard 00-970 Part 1 Section 3*, in *Design and Airworthiness Requirements for Service Aircraft*. 2015.
19. Braga, D.F.O., S.M.O. Tavares, L.F.M. da Silva, P.M.G.P. Moreira, and P.M.S.T. de Castro, *Advanced design for lightweight structures: Review and prospects.* Progress in Aerospace Sciences, 2014. **69**(0): p. 29-39.
20. Wanhill, R., *Milestone case histories in aircraft structural integrity* 2002.
21. Blom, A. *Fatigue science and engineering–achievements and challenges*. in *Plantema Memorial Lecture, 21st Symposium of the International Committee on Aeronautical Fatigue (ICAF), Toulouse, France*. 2001.
22. Brot, A. *Developing Strategies to Combat Threats against the Structural Integrity of Aircraft*. in *Presented at the 52nd Israel Annual Conference on Aerospace Sciences*. 2012.
23. Grandt Jr, F., *Damage Tolerant Design and Nondestructive Inspection - Keys to Aircraft Airworthiness.* Procedia Engineering, 2011. **17**(0): p. 236-246.
24. Wang, L., *Load sequence effect and enhanced life prediction under spectrum loading*. 2009, University of Hertfordshire.
25. Downer, J., *When failure is an option: Redundancy, reliability and regulation in complex technical systems*. 2009: Centre for Analysis of Risk and Regulation, London School of Economics and Political Science.
26. Dougherty, J.E., *Recognition of Damage-Tolerance in Civil Airworthiness Standards*. 1978, SAE Technical Paper.
27. Civil Aviation Authority, *Airworthiness Notice 89.* Continuing Structural Integrity of Transport Aeroplanes, 1978.
28. Ramesh, K., *E-Book on engineering fracture mechanics.* IIT Madras, India, 2007.

29. Kirsch, G., *Theory of elasticity and application in strength of materials.* Zeitschrift des Vereins Deutscher Ingenieure, 1898. **42**(29): p. 797-807.
30. Inglis, C.E., *Stresses in a plate due to the presence of cracks and sharp corners.* Transactions of the institute of naval architects, 1913. **55**(219-241): p. 193-198.
31. Griffith, A., *The phenomena of flow and rupture in solids: Phil.* Trans. Roy. Soc. Lond. Ser. A, 1920. **221**: p. 163-98.
32. Irwin, G.R., *Analysis of stresses and strains near the end of a crack traversing a plate.* J. appl. Mech., 1957.
33. Kemp, R., *Fatigue Crack Closure-A Review*. 1990, DTIC Document.
34. Nguyen-Xuan, H., L.V. Tran, C.H. Thai, and C.V. Le, *Plastic collapse analysis of cracked structures using extended isogeometric elements and second-order cone programming.* Theoretical and Applied Fracture Mechanics, 2014. **72**: p. 13-27.
35. Muscat, M., D. Mackenzie, and R. Hamilton, *A work criterion for plastic collapse.* International journal of pressure vessels and piping, 2003. **80**(1): p. 49-58.
36. Westergaard, H., *A problem of elasticity suggested by a problem in soil mechanics: soft material reinforced by numerous strong horizontal sheets.* Contributions to the mechanics of solids, Stephen Timoshenko 60th anniversary volume, 1938: p. 268-277.
37. Irwin, G.R., *Fracture*, in *Elasticity and Plasticity/Elastizität und Plastizität*. 1958, Springer. p. 551-590.
38. Tada, H., P.C. Paris, and G.R. Irwin, *The stress analysis of cracks.* Handbook, Del Research Corporation, 1973.
39. Grandt Jr, A.F., *Fundamentals of structural integrity: damage tolerant design and nondestructive evaluation*. 2003: John Wiley & Sons.
40. NDT Resource Centre, *Dislocaitons*. 2017.
41. NDT Resource Centre, *Fatigue Crack Initiation*. 2017.
42. Agrawal, R., R. Uddanwadiker, and P. Padole, *Low cycle fatigue life prediction.* Int J Emer Eng Res Technol, 2014. **2**(4): p. 5-15.
43. Suresh, S., *Fatigue of materials*. 1998: Cambridge university press.
44. NDT Resource Centre, *Elastic/Plastic Deformation*. 2017.

45. Xin, Q., *2 - Durability and reliability in diesel engine system design*, in *Diesel Engine System Design*. 2013, Woodhead Publishing. p. 113-202.
46. Centre, N.R., *S-N Fatigue Properties*. 2017.
47. Boardman, B., *Fatigue resistance of steels.* ASM International, Metals Handbook. Tenth Edition, 1990. **1**: p. 673-688.
48. Shah, K.P. *The handbook of mechanical maintenance* 2017 [cited 2017 12/03/2018]; Available from: http://practicalmaintenance.net/?p=989.
49. Erdogan, F. and G. Sih, *On the crack extension in plates under plane loading and transverse shear.* Journal of basic engineering, 1963. **85**(4): p. 519-527.
50. Pokluda, J., R. Pippan, K. Slámecka, and O. Kolednik. *Fatigue Crack Growth in Metals under Pure Mode III: Reality or Fiction?* in *FCP2003*. 2013.
51. Sih, G.C., *Strain-energy-density factor applied to mixed mode crack problems.* International Journal of fracture, 1974. **10**(3): p. 305-321.
52. Paris, P.C., M.P. Gomez, and W.E. Anderson, *A rational analytic theory of fatigue.* The trend in engineering, 1961. **13**(1): p. 9-14.
53. Paris, P. and F. Erdogan, *A critical analysis of crack propagation laws.* Journal of Fluids Engineering, 1963. **85**(4): p. 528-533.
54. Jones, R., L. Molent, and K. Walker, *Fatigue crack growth in a diverse range of materials.* International Journal of Fatigue, 2012. **40**: p. 43-50.
55. Molent, L. and R. Jones, *The influence of cyclic stress intensity threshold on fatigue life scatter.* International Journal of Fatigue, 2016. **82, Part 3**: p. 748-756.
56. Donahue, R.J., H.M. Clark, P. Atanmo, R. Kumble, and A.J. McEvily, *Crack opening displacement and the rate of fatigue crack growth.* International Journal of Fracture Mechanics, 1972. **8**(2): p. 209-219.
57. Beden, S., S. Abdullah, and A. Ariffin, *Review of fatigue crack propagation models for metallic components.* European Journal of Scientific Research, 2009. **28**(3): p. 364-397.
58. Wang, W. and C.-T.T. Hsu, *Fatigue crack growth rate of metal by plastic energy damage accumulation theory.* Journal of engineering mechanics, 1994. **120**(4): p. 776-795.
59. Forman, R., *Study of fatigue crack initiation from flaws using fracture mechanics theory.* Engineering Fracture Mechanics, 1972. **4**(2): p. 333-345.

60. Weertman, J., *Rate of growth of fatigue cracks calculated from the theory of infinitesimal dislocations distributed on a plane.* International Journal of Fracture Mechanics, 1966. **2**(2): p. 460-467.
61. Hartman, A. and J. Schijve, *The effects of environment and load frequency on the crack propagation law for macro fatigue crack growth in aluminium alloys.* Engineering Fracture Mechanics, 1970. **1**(4): p. 615-631.
62. Singh, K.D., Y. Xu, and I. Sinclair, *Strip yield modelling of fatigue crack under variable amplitude loading.* Journal of mechanical science and technology, 2011. **25**(12): p. 3025-3036.
63. Borrego, L., J. Ferreira, J.P. Da Cruz, and J. Costa, *Evaluation of overload effects on fatigue crack growth and closure.* Engineering Fracture Mechanics, 2003. **70**(11): p. 1379-1397.
64. Borrego, L., J. Costa, and J. Ferreira, *Predictions by load interaction models in AA6082-T6 aluminium alloy.* Theoretical and Applied Fracture Mechanics, 2016. **85**: p. 67-73.
65. Ding, Z., X. Wang, Z. Gao, and S. Bao, *An experimental investigation and prediction of fatigue crack growth under overload/underload in Q345R steel.* International Journal of Fatigue, 2017. **98**: p. 155-166.
66. Chen, C., D. Ye, L. Zhang, and J. Liu, *Effects of tensile/compressive overloads on fatigue crack growth behavior of an extra-low-interstitial titanium alloy.* International Journal of Mechanical Sciences, 2016. **118**: p. 55-66.
67. Shin, C. and S. Hsu, *On the mechanisms and behaviour of overload retardation in AISI 304 stainless steel.* International Journal of Fatigue, 1993. **15**(3): p. 181-192.
68. Doré, M.J. and S.J. Maddox, *Accelerated Fatigue Crack Growth in 6082 T651 Aluminium Alloy Subjected to Periodic Underloads.* Procedia Engineering, 2013. **66**: p. 313-322.
69. Cho, G., *Fatigue: Core Research from TWI*. 2000: Woodhead Publishing.
70. Silva, F., *Fatigue crack propagation after overloading and underloading at negative stress ratios.* International Journal of Fatigue, 2007. **29**(9): p. 1757-1771.
71. Tsukuda, H., H. Ogiyama, and T. Shiraishi, *Transient fatigue crack growth behaviour following single overloads at high stress ratios.* Fatigue & fracture of engineering materials & structures, 1996. **19**(7): p. 879-891.

72. Skorupa, M., *Load interaction effects during fatigue crack growth under variable amplitude loading—a literature review. Part I: empirical trends.* Fatigue & fracture of engineering materials & structures, 1998. **21**(8): p. 987-1006.
73. Shuter, D. and W. Geary, *Some aspects of fatigue crack growth retardation behaviour following tensile overloads in a structural steel.* Fatigue & fracture of engineering materials & structures, 1996. **19**(2-3): p. 185-199.
74. Wheeler, O.E., *Spectrum loading and crack growth.* Journal of basic engineering, 1972. **94**(1): p. 181-186.
75. Willenborg, J., R. Engle, and H. Wood, *A crack growth retardation model using an effective stress concept*. 1971, Air Force Flight Dynamics Lab Wright-Patterson Afb Oh.
76. Gallagher, J. and T. Hughes, *Influence of yield strength on overload affected fatigue crack growth behavior in 4340 steel*. 1974, AIR FORCE FLIGHT DYNAMICS LAB WRIGHT-PATTERSON AFB OH.
77. NASA Johnson Space Center, *Fatigue crack growth computer program NASGRO version 4.11-Reference manual*. 2004, Houston, Texas.
78. Wolf, E., *Fatigue crack closure under cyclic tension.* Engineering Fracture Mechanics, 1970. **2**(1): p. 37-45.
79. Wolf, E. *The significance of fatigue crack closure*. in *Damage Tolerance in Aircraft Structures: A Symposium Presented at the Seventy-third Annual Meeting American Society for Testing and Materials, Toronto, Ontario, Canada, 21-26 June 1970*. 1971. ASTM International.
80. Schijve, J., *Fatigue of structures and materials*. 2001: Springer Science & Business Media.
81. Singh, K.D., M.R. Parry, and I. Sinclair, *Variable amplitude fatigue crack growth behavior—a short overview.* Journal of mechanical science and technology, 2011. **25**(3): p. 663-673.
82. Roychowdhury, S. and R.H. Dodds Jr, *Effect of T-stress on fatigue crack closure in 3-D small-scale yielding.* International Journal of Solids and Structures, 2004. **41**(9–10): p. 2581-2606.
83. Newman, J., *A crack-closure model for predicting fatigue crack growth under aircraft spectrum loading*, in *Methods and models for predicting fatigue crack growth under random loading*. 1981, ASTM International.

84. Newman, J., *Prediction of fatigue crack growth under variable-amplitude and spectrum loading using a closure model*, in *Design of Fatigue and Fracture Resistant Structures*. 1982, ASTM International.
85. Newman Jr, J., *Crack growth under variable amplitude and spectrum loading in 2024-T3 aluminum alloys*. 1997, The Minerals, Metals and Materials Society, Warrendale, PA (United States).
86. Dugdale, D., *Yielding of steel sheets containing slits.* Journal of the Mechanics and Physics of Solids, 1960. **8**(2): p. 100-104.
87. Suresh, S. and R. Ritchie, *A geometric model for fatigue crack closure induced by fracture surface roughness.* Metallurgical Transactions A, 1982. **13**(9): p. 1627-1631.
88. McClung, R., *Crack closure and plastic zone sizes in fatigue.* Fatigue & fracture of engineering materials & structures, 1991. **14**(4): p. 455-468.
89. Riemelmoser, F. and R. Pippan, *Mechanical reasons for plasticity-induced crack closure under plane strain conditions.* Fatigue & fracture of engineering materials & structures, 1998. **21**(12): p. 1425-1433.
90. Budiansky, B. and J. Hutchinson, *Analysis of closure in fatigue crack growth.* Journal of Applied Mechanics, 1978. **45**(2): p. 267-276.
91. Hill, R., *The Mathematical Theory of Plasticity, The Oxford Engineering Science Series*. 1950: Oxford.
92. Malvern, L.E., *Introduction to the Mechanics of a Continuous Medium*. 1969.
93. Chang, T. and W. Guo, *A model for the through-thickness fatigue crack closure.* Engineering Fracture Mechanics, 1999. **64**(1): p. 59-65.
94. Louat, N., K. Sadananda, M. Duesbery, and A. Vasudevan, *A theoretical evaluation of crack closure.* Metallurgical Transactions A, 1993. **24**(10): p. 2225-2232.
95. Minakawa, K., G. Levan, and A. McEvily, *The influence of load ratio on fatigue crack growth in 7090-T6 and IN9021-T4 P/M aluminum alloys.* Metallurgical and Materials Transactions A, 1986. **17**(10): p. 1787-1795.
96. McClung, R., B. Thacker, and S. Roy, *Finite element visualization of fatigue crack closure in plane stress and plane strain.* International Journal of Fracture, 1991. **50**(1): p. 27-49.

97. Ewalds, H. and R. Furnee, *Crack closure measurement along the fatigue crack front of center cracked specimens.* International Journal of Fracture, 1978. **14**(2): p. R53-R55.
98. Fleck, N. and R. Smith, *Crack closure-is it just a surface phenomenon?* International Journal of Fatigue, 1982. **4**(3): p. 157-160.
99. Singh, K.D., K.H. Khor, and I. Sinclair, *Roughness- and plasticity-induced fatigue crack closure under single overloads: Finite element modelling.* Acta Materialia, 2006. **54**(17): p. 4393-4403.
100. Antunes, F., A. Chegini, R. Branco, and D. Camas, *A numerical study of plasticity induced crack closure under plane strain conditions.* International Journal of Fatigue, 2015. **71**: p. 75-86.
101. Solanki, K., S. Daniewicz, and J. Newman Jr, *Finite element modeling of plasticity-induced crack closure with emphasis on geometry and mesh refinement effects.* Engineering Fracture Mechanics, 2003. **70**(12): p. 1475-1489.
102. Chermahini, R., K. Shivakumar, and J. Newman Jr, *Three-dimensional finite-element simulation of fatigue crack growth and closure.* ASTM STP, 1988. **982**: p. 398-413.
103. Fleck, N.A., *Finite element analysis of plasticity-induced crack closure under plane strain conditions.* Engineering Fracture Mechanics, 1986. **25**(4): p. 441-449.
104. Fleck, N.A. and J.C. Newman Jr, *Analysis of crack closure under plane strain conditions.* ASTM STP, 1988. **982**: p. 319-341.
105. Solanki, K., S. Daniewicz, and J. Newman Jr, *Finite element analysis of plasticity-induced fatigue crack closure: an overview.* Engineering Fracture Mechanics, 2004. **71**(2): p. 149-171.
106. Williams, M., *Gn the stress distribution at the base of a stationary crack. I. appl*. 1957, Mech.
107. Roychowdhury, S. and R.H. Dodds Jr, *A numerical investigation of 3-D small-scale yielding fatigue crack growth.* Engineering Fracture Mechanics, 2003. **70**(17): p. 2363-2383.
108. Newman Jr, J.C., E.L. Anagnostou, and D. Rusk, *Fatigue and crack-growth analyses on 7075-T651 aluminum alloy coupons under constant- and*

variable-amplitude loading. International Journal of Fatigue, 2014. **62**(0): p. 133-143.

109. Borrego, L.P., F.V. Antunes, J.D. Costa, and J.M. Ferreira, *Numerical simulation of plasticity induced crack closure under overloads and high–low blocks.* Engineering Fracture Mechanics, 2012. **95**(0): p. 57-71.
110. Xu, Y., L. Wang, Y. Chen, and W. Tiu, *Load sequence effect on fatigue damage.* Key Engineering Materials, 2012. **488**: p. 545-548.
111. Paris, P. and L. Hermann, *Twenty years of reflection on questions involving fatigue crack growth, part II: some observations of crack closure.* Fatigue Thresholds, Fundamental and Engineering Applications, 1982. **1**: p. 11-33.
112. Von Euw, E., R. Hertzberg, and R. Roberts, *Delay effects in fatigue crack propagation.* ASTM STP, 1972. **513**: p. 230-259.
113. Fleck, N.A., I.F.C. Smith, and R.A. Smith, *Closure behaviour of surface cracks.* Fatigue & fracture of engineering materials & structures, 1983. **6**(3): p. 225-239.
114. Venkateswara Rao, K.T. and R.O. Ritchie, *Mechanisms for the retardation of fatigue cracks following single tensile overloads: behavior in aluminum-lithium alloys.* Acta Metallurgica, 1988. **36**(10): p. 2849-2862.
115. Shih, C., *Small-scale yielding analysis of mixed mode plane-strain crack problems.* ASTM STP, 1974. **560**(7): p. 187-210.
116. Fleck, N., *Influence of stress state on crack growth retardation.* Basic Questions in Fatigue., 1984. **1**: p. 157-183.
117. Lang, M. and G. Marci, *The influence of single and multiple overloads on fatigue crack propagation.* Fatigue & fracture of engineering materials & structures, 1999. **22**(4): p. 257-271.
118. Mcevily, A.J. and S. Ishihara, *On the retardation in fatigue crack growth rate due to an overload; a review*. 2001, SAE Technical Paper.
119. Robin, C., M. Busch, M. Chergui, H. Lieurade, and G. Pluvinage, *Influence of Series of Tensile and Compressive Overloads on 316 L Crack Growth.* Fatigue Crack Growth Under Variable Amplitude Loading, 1988: p. 87-97.
120. Robin, C., M.e. Louah, and G. Pluvinage, *Influence of an overload on the fatigue crack growth in steels.* Fatigue & fracture of engineering materials & structures, 1983. **6**(1): p. 1-13.

121. Donald, J.K., *Introducing the compliance ratio concept for determining effective stress intensity.* International Journal of Fatigue, 1997. **19**(93): p. 191-195.
122. Wu, J. and F. Ellyin, *A study of fatigue crack closure by elastic-plastic finite element analysis for constant-amplitude loading.* International Journal of Fracture, 1990. **82**(1): p. 43-65.
123. Song, J. and Y. Chung, *A review of crack closure measurement by compliance technique and the normalized-extended ASTM method as a currently most refined, practical and simple one.* Procedia Engineering, 2010. **2**(1): p. 777-786.
124. Lugo, M., S. Daniewicz, and J. Newman, *A mechanics based study of crack closure measurement techniques under constant amplitude loading.* International Journal of Fatigue, 2011. **33**(2): p. 186-193.
125. Zhang, W. and Y. Liu, *In situ SEM testing for crack closure investigation and virtual crack annealing model development.* International Journal of Fatigue, 2012. **43**: p. 188-196.
126. Lugo, M., S. Daniewicz, and J. Newman Jr, *A mechanics based study of crack closure measurement techniques under constant amplitude loading.* International Journal of Fatigue, 2011. **33**(2): p. 186-193.
127. Andersson, M., C. Persson, and S. Melin. *An in-situ SEM study of crack propagation*. in *ECF15, Stockolm 2004*. 2013.
128. Fellows, L. and D. Nowell, *Crack closure measurements using Moiré interferometry with photoresist gratings.* International journal of fatigue, 2004. **26**(10): p. 1075-1082.
129. Fellows, L. and D. Nowell, *Measurement of crack closure after the application of an overload cycle, using moiré interferometry.* International journal of fatigue, 2005. **27**(10): p. 1453-1462.
130. Christopher, C., M. James, E. Patterson, and K. Tee, *A quantitative evaluation of fatigue crack shielding forces using photoelasticity.* Engineering Fracture Mechanics, 2008. **75**(14): p. 4190-4199.
131. Wallhead, I., L. Edwards, and P. Poole, *A study of crack closure using the optical method of caustics and consequences for the use of ΔK eff as a fatigue crack driving force.* Engineering fracture mechanics, 1998. **60**(3): p. 291-302.

132. Marsavina, L., R. Tomlinson, E. Patterson, and J. Yates. *Investigation of crack closure by using thermoelastic stress analysis*. in *CD-ROM Proc. of the 16th European Conference of Fracture, Alexandroupolis*. 2006.
133. Xu, Y., P. Gregson, and I. Sinclair, *Systematic assessment and validation of compliance-based crack closure measurements in fatigue.* Materials Science and Engineering: A, 2000. **284**(1): p. 114-125.
134. Diaz, F., J. Yates, and E. Patterson, *Some improvements in the analysis of fatigue cracks using thermoelasticity.* International Journal of Fatigue, 2004. **26**(4): p. 365-376.
135. Khor, K., J.-Y. Buffiere, W. Ludwig, and I. Sinclair, *High resolution X-ray tomography of micromechanisms of fatigue crack closure.* Scripta materialia, 2006. **55**(1): p. 47-50.
136. Limodin, N., J. Rethore, J.-Y. Buffiere, F. Hild, S. Roux, W. Ludwig, J. Rannou, and A. Gravouil, *Influence of closure on the 3D propagation of fatigue cracks in a nodular cast iron investigated by X-ray tomography and 3D volume correlation.* Acta Materialia, 2010. **58**(8): p. 2957-2967.
137. Andersson, M., C. Persson, and S. Melin, *Experimental and numerical investigation of crack closure measurements with electrical potential drop technique.* International Journal of Fatigue, 2006. **28**(9): p. 1059-1068.
138. Spitas, V., C. Spitas, and P. Michelis, *A three-point electrical potential difference method for in situ monitoring of propagating mixed-mode cracks at high temperature.* Measurement, 2010. **43**(7): p. 950-959.
139. Nakagawa, N., V. Kogan, and G. Bozzolo, *Effect of crack closure on eddy current signals.* NDT and E International, 1997. **30**(3): p. 183-183.
140. Chen, Z., K. Aoto, and K. Miya, *Reconstruction of cracks with physical closure from signals of eddy current testing.* IEEE Transactions on Magnetics, 2000. **36**(4): p. 1018-1022.
141. Lee, C., Y. Rhyim, D. Kwon, and K. Ono, *Acoustic emission measurement of fatigue crack closure.* Scripta metallurgica et materialia, 1995. **32**(5): p. 701-706.
142. Chang, H., E. Han, J. Wang, and W. Ke, *Acoustic emission study of fatigue crack closure of physical short and long cracks for aluminum alloy LY12CZ.* International journal of fatigue, 2009. **31**(3): p. 403-407.

143. Singh, K.D., M.R. Parry, and I. Sinclair, *A short summary on finite element modelling of fatigue crack closure.* Journal of mechanical science and technology, 2011. **25**(12): p. 3015-3024.
144. Armero, F., *On the locking and stability of finite elements in finite deformation plane strain problems.* Computers & Structures, 2000. **75**(3): p. 261-290.
145. Hughes, T.J., *Generalization of selective integration procedures to anisotropic and nonlinear media.* International Journal for Numerical Methods in Engineering, 1980. **15**(9): p. 1413-1418.
146. Newman, J.C., *A finite-element analysis of fatigue crack closure*, in *Mechanics of Crack Growth*. 1976, ASTM International.
147. Rice, J., *Mechanics of crack tip deformation and extension by fatigue*, in *Fatigue crack propagation*. 1967, ASTM International.
148. McClung, R.C., *Fatigue crack closure and crack growth outside the small scale yielding regime*. 1988, University of Illinois at Urbana-Champaign.
149. Dougherty, J., J. Padovan, and T. Srivatsan, *Fatigue crack propagation and closure behavior of modified 1070 steel: finite element study.* Engineering Fracture Mechanics, 1997. **56**(2): p. 189-212.
150. Park, S.-J. and J.-H. Song, *Simulation of fatigue crack closure behavior under variable-amplitude loading by a 2D finite element analysis based on the most appropriate mesh size concept*, in *Advances in Fatigue Crack Closure Measurement and Analysis: Second Volume*. 1999, ASTM International.
151. Ward-Close, C. and R. Ritchie, *On the role of crack closure mechanisms in influencing fatigue crack growth following tensile overloads in a titanium alloy: near threshold versus higher ΔK behaviour.* Mechanics of Fatigue Crack Closure, 1988. **982**: p. 93-111.
152. Daniewicz, S. and J. Bloom, *An assessment of geometry effects on plane stress fatigue crack closure using a modified strip-yield model.* International Journal of Fatigue, 1996. **18**(7): p. 483-490.
153. Solanki, K., S. Daniewicz, and J. Newman, *A new methodology for computing crack opening values from finite element analyses.* Engineering Fracture Mechanics, 2004. **71**(7): p. 1165-1175.
154. McClung, R., *The influence of applied stress, crack length, and stress intensity factor on crack closure.* Metallurgical Transactions A, 1991. **22**(7): p. 1559-1571.

155. Dill, H. and C. Saff, *Spectrum crack growth prediction method based on crack surface displacement and contact analyses*, in *Fatigue crack growth under spectrum loads*. 1976, ASTM International.
156. Lankford, J., D.L. Davidson, and K.S. Chan, *The influence of crack tip plasticity in the growth of small fatigue cracks.* Metallurgical and Materials Transactions A, 1984. **15**(8): p. 1579-1588.
157. Antunes, F., L. Borrego, J. Costa, and J. Ferreira, *A numerical study of fatigue crack closure induced by plasticity.* Fatigue & fracture of engineering materials & structures, 2004. **27**(9): p. 825-835.
158. Newman, J., *Finite-element analysis of crack growth under monotonic and cyclic loading*, in *Cyclic stress-strain and plastic deformation aspects of fatigue crack growth*. 1977, ASTM International.
159. Palazotto, A. and E. Bednarz. *A Finite-Element Investigation of Viscoplastic-Induced Closure of Short Cracks at High Temperatures*. in *Fracture Mechanics: Perspectives and Directions (Twentieth Symposium)*. 1989. ASTM International.
160. Nguyen, O., E. Repetto, M. Ortiz, and R. Radovitzky, *A cohesive model of fatigue crack growth.* International Journal of Fracture, 2001. **110**(4): p. 351-369.
161. Kibey, S., H. Sehitoglu, and D. Pecknold, *Modeling of fatigue crack closure in inclined and deflected cracks.* International journal of fracture, 2004. **129**(3): p. 279-308.
162. Newman, J., J. Schneider, A. Daniel, and D. McKnight, *Compression pre-cracking to generate near threshold fatigue-crack-growth rates in two aluminum alloys.* International journal of fatigue, 2005. **27**(10): p. 1432-1440.
163. Newman Jr, J., J. Ruschau, and M. Hill, *Improved test method for very low fatigue-crack-growth-rate data.* Fatigue & Fracture of Engineering Materials & Structures, 2011. **34**(4): p. 270-279.
164. Klesnil, M. and P. Lukáš, *Influence of strength and stress history on growth and stabilisation of fatigue cracks.* Engineering Fracture Mechanics, 1972. **4**(1): p. 77-92.
165. Johnson, W., *Multi-parameter yield zone model for predicting spectrum crack growth*, in *Methods and Models for Predicting Fatigue Crack Growth Under Random Loading*. 1981, ASTM International.

166. Forman, R.G. and S.R. Mettu, *Behavior of surface and corner cracks subjected to tensile and bending loads in Ti-6Al-4V alloy.* 1990.
167. Newman Jr, J.C., *FASTRAN-2: A fatigue crack growth structural analysis program.* NASA STI/Recon Technical Report N, 1992. **92**: p. 30964.
168. Hu, W. and K. Walker. *Fatigue crack growth from a notch under severe overload and underload*. in *The International Conference on Structural Integrity and Failure*. 2006.
169. Castillo, E., A. Fernández-Canteli, and D. Siegele, *Obtaining S–N curves from crack growth curves: an alternative to self-similarity.* International Journal of Fracture, 2014. **187**(1): p. 159-172.
170. Suresh, S. and R.O. Ritchie, *Propagation of short fatigue cracks.* International Metals Reviews, 1984. **29**(1): p. 445-475.
171. Pearson, S., *Initiation of fatigue cracks in commercial aluminium alloys and the subsequent propagation of very short cracks.* Engineering Fracture Mechanics, 1975. **7**(2): p. 235-247.
172. ASTM International, *Standard Test Method for Measurement of Fatigue Crack Growth Rates*. 2011: ASTM International.
173. Hudak Jr, S., A. Saxena, R. Bucci, and R. Malcolm, *Development of standard methods of testing and analyzing fatigue crack growth rate data*. 1978, DTIC Document.
174. ISO, BS, *12108, 2002:'Metallic materials-Fatigue testing-Fatigue crack growth method'.* British Standards Institution, London.
175. Ruschau, J. and J. Newman. *Compression precracking to generate near threshold fatigue crack growth rates in an aluminum and titanium alloy*. in *Seventh International ASTM/ESIS Symposium on Fatigue and Fracture Mechanics (36th ASTM National Symposium on Fatigue and Fracture Mechanics)*. 2009. ASTM International.
176. Newman Jr, J.C. and Y. Yamada, *Compression precracking methods to generate near-threshold fatigue-crack-growth-rate data.* International Journal of Fatigue, 2010. **32**(6): p. 879-885.
177. Forth, S.C., J.C. Newman, and R.G. Forman, *On generating fatigue crack growth thresholds.* International Journal of Fatigue, 2003. **25**(1): p. 9-15.

178. Pippan, R., *Threshold and effective threshold of fatigue crack propagation in ARMCO iron I: The influence of grain size and cold working.* Materials Science and Engineering: A, 1991. **138**(1): p. 1-13.
179. Suresh, S., G. Zamiski, and D.R. Ritchie, *Oxide-induced crack closure: an explanation for near-threshold corrosion fatigue crack growth behavior.* Metallurgical Transactions A, 1981. **12**(8): p. 1435-1443.
180. Newman, J., *Fatigue and Crack-growth Analyses under Giga-cycle Loading on Aluminum Alloys.* Procedia Engineering, 2015. **101**: p. 339-346.
181. Li, B. and L. Rosa, *Prediction models of intrinsic fatigue threshold in metal alloys examined by experimental data.* International Journal of Fatigue, 2016. **82**: p. 616-623.
182. Chowdhury, P.B., H. Sehitoglu, and R.G. Rateick, *Predicting fatigue resistance of nano-twinned materials: Part II–Effective threshold stress intensity factor range.* International Journal of Fatigue, 2014. **68**: p. 292-301.
183. Wasen, J. and E. Heier, *Fatigue crack growth thresholds—the influence of Young's modulus and fracture surface roughness.* International journal of fatigue, 1998. **20**(10): p. 737-742.
184. Pippan, R. and P. Weinert, *The effective threshold of fatigue crack propagation in aluminium alloys. II. The influence of particle reinforcement.* Philosophical Magazine A, 1998. **77**(4): p. 875-886.
185. Varfolomeev, I., M. Luke, and M. Burdack, *Effect of specimen geometry on fatigue crack growth rates for the railway axle material EA4T.* Engineering Fracture Mechanics, 2011. **78**(5): p. 742-753.
186. Regazzi, D., I. Varfolomeev, S. Moroz, M. Luke, and S. Beretta, *Experimental and numerical investigations of fatigue crack closure in standard specimens.* DVM-AK Bruchvorgänge, DVM-Bericht, 2013. **245**: p. 157-166.
187. Hutař, P., L. Náhlík, M. Ševčík, S. Seitl, T. Kruml, and J. Polák. *Fatigue Crack Propagation Rate in EUROFER 97 Estimated Using Small Specimens*. in *Key Engineering Materials*. 2011. Trans Tech Publ.
188. Hookham, C.R., *Fatigue crack propagation rates and threshold stress intensity factor ranges for aluminium alloy sheet.*, in *ESDU Fatigue - Fracture Mechanics Series*. 2000-03. p. 1-32.

189. Boyce, B. and R. Ritchie, *Effect of load ratio and maximum stress intensity on the fatigue threshold in Ti–6Al–4V.* Engineering Fracture Mechanics, 2001. **68**(2): p. 129-147.
190. Kwofie, S., *Equivalent stress approach to predicting the effect of stress ratio on fatigue threshold stress intensity range.* International Journal of Fatigue, 2004. **26**(3): p. 299-303.
191. de Pannemaecker, A., S. Fouvry, and J.Y. Buffiere, *Reverse identification of short–long crack threshold fatigue stress intensity factors from plain fretting crack arrest analysis.* Engineering Fracture Mechanics, 2015. **134**: p. 267-285.
192. Nussbaumer, A., L. Borges, and L. Davaine, *Fatigue Design of Steel and Composite Structures : Eurocode 3: Design of Steel Structures, Part 1-9 Fatigue; Eurocode 4: Design of Composite Steel and Concrete Structures*. Vol. 1. 2012, Hoboken: Ernst & Sohn.
193. Suryanarayana, C., *Experimental techniques in materials and mechanics*. 2011: CRC Press.
194. Yu, J., H.C. Zhang, D. Deng, A. Iqbal, and S.Z. Hao, *Simulation and experiment for crack arrest in remanufacturing.* The International Journal of Advanced Manufacturing Technology, 2016. **87**(5-8): p. 1547-1556.
195. Nasr, N.Z., *Remanufacturing from Technology to Applications.* China Surface Engineering, 2007. **20**: p. 1-5.
196. Subramoniam, R., D. Huisingh, and R.B. Chinnam, *Remanufacturing for the automotive aftermarket-strategic factors: literature review and future research needs.* Journal of Cleaner Production, 2009. **17**(13): p. 1163-1174.
197. D'Adamo, I. and P. Rosa, *Remanufacturing in industry: advices from the field.* The International Journal of Advanced Manufacturing Technology, 2016. **86**(9-12): p. 2575-2584.
198. Yu, J., H.C. Zhang, D. Deng, A. Iqbal, and S.Z. Hao, *Simulation and experiment for crack arrest in remanufacturing.* The International Journal of Advanced Manufacturing Technology, 2013: p. 1-10.
199. Çelik, A., A.F. Yetim, A. Alsaran, and M. Karakan, *Effect of magnetic treatment on fatigue life of AISI 4140 steel.* Materials & design, 2005. **26**(8): p. 700-704.

200. Yan, X., D. Yang, and X. Liu, *Influence of heat treatment on the fatigue life of a laser-welded NiTi alloy wire.* Materials characterization, 2007. **58**(3): p. 262-266.
201. Conrad, H., J. White, W. Cao, X. Lu, and A. Sprecher, *Effect of electric current pulses on fatigue characteristics of polycrystalline copper.* Materials Science and Engineering: A, 1991. **145**(1): p. 1-12.
202. Stepanov, G. and A. Babutskii, *Effect of a high-density current pulse on the fatigue life of a steel specimen with a stress raiser.* Strength of materials, 1995. **27**(5-6): p. 300-303.
203. Bose, M., *Effect of saturated magnetic field on fatigue life of carbon steel.* physica status solidi (a), 1984. **86**(2): p. 649-654.
204. Kuphaldt, T.R., *Lessons In Electric Circuits, Volume I–DC.* Vol. Fifth Edition. Open Book Project, 2006.
205. Babutskyi, A., A. Chrysanthou, and C. Zhao, *Effect of pulsed magnetic field pre-treatment of AISI 52100 steel on the coefficient of sliding friction and wear in pin-on-disk tests.* Friction, 2014. **2**(4): p. 310-316.
206. Tang, G., Z. Xu, M. Tang, X. Chen, H. Zhou, and A. Lu, *Effect of a pulsed magnetic treatment on the dislocation substructure of a commercial high strength steel.* Materials Science and Engineering: A, 2005. **398**(1): p. 108-112.
207. Hosoi, A., T. Nagahama, and Y. Ju, *Fatigue crack healing by a controlled high density electric current field.* Materials Science and Engineering: A, 2012. **533**: p. 38-42.
208. Liu, L.H., L.J. Li, and Q.J. Zhai. *Microstructure Evolution and Grain Boundary Characteristics of Oriented Silicon Steel during Primary Recrystallization in a Pulsed Magnetic Field*. in *Advanced Materials Research*. 2013. Trans Tech Publ.
209. Lin, H., Y. Zhao, Z. Gao, and L. Han, *Effects of pulse current stimulation on the thermal fatigue crack propagation behavior of CHWD steel.* Materials Science and Engineering: A, 2008. **478**(1): p. 93-100.
210. Elliott-Bowman, B. and R. Qin, *The effects of electropulsing on metallic materials.* 2015.
211. Troitskii, O., *Electromechanical effect in metals.* JETP Lett.(English version), 1969. **10**: p. 11-14.

212. Karpenko, G., O. Kuzin, V. Tkachev, and V. Rudenko. *Influence of an electric current upon the low-cycle fatigue of steel*. in *Sov Phys Dokl*. 1976.
213. Sosnin, O., A. Gromova, Y.F. Ivanov, S. Konovalov, V. Gromov, and E. Kozlov, *Control of austenite steel fatigue strength.* International Journal of Fatigue, 2005. **27**(10): p. 1186-1191.
214. Zhao, Y., Y. Liang, W. Zhou, Q. Qin, and Q. Jiang, *Effect of a current pulse on the thermal fatigue behavior of cast hot work die steel.* ISIJ international, 2005. **45**(3): p. 410-412.
215. Hosoi, A., T. Yano, Y. Morita, and Y. Ju, *Quantitative evaluation of the displacement distribution and stress intensity factor of fatigue cracks healed by a controlled high-density electric current field.* Fatigue & Fracture of Engineering Materials & Structures, 2014. **37**(9): p. 1025-1033.
216. Levitin, V. and S. Loskutov, *The effect of a current pulse on the fatigue of titanium alloy.* Solid state communications, 2004. **131**(3): p. 181-183.
217. Konovalov, S., I. Komissarova, D. Kosinov, V. Gromov, and A. Semin. *Increase in Reliability of Metal Articles with Impulse Current Effect*. in *MATEC Web of Conferences*. 2016. EDP Sciences.
218. Jung, J., Y. Ju, Y. Morita, and Y. Toku, *Effect of pulsed electric current on the growth behavior of fatigue crack in Al alloy.* Procedia Structural Integrity, 2016. **2**: p. 2989-2993.
219. Garrison Jr, W., *Ultrahigh-strength steels for aerospace applications.* JOM, 1990. **42**(5): p. 20-24.
220. Nichipuruk, A., N. Noskova, E. Gorkunov, and E. Ponomareva, *The effect of the dislocation structure produced by plastic deformation on the magnetic and magneto-elastic properties of iron and low-carbon steel.* Physics of metals and metallography, 1992. **74**(6): p. 593-597.
221. Klamecki, B.E. *Effects of Pulsed Magnetic Treatment on Mechanical Characteristics of Manufactured Parts*. in *ASME 2006 International Manufacturing Science and Engineering Conference*. 2006. American Society of Mechanical Engineers.
222. Cai, Z., X. Duan, J. Lin, and H. Zhao, *Magnetostriction varieties and stress relief caused by pulsed magnetic field.* Frontiers of Mechanical Engineering, 2011. **6**(3): p. 354-358.

223. Konovalov, S., A. Atroshkina, Y.F. Ivanov, and V. Gromov, *Evolution of dislocation substructures in fatigue loaded and failed stainless steel with the intermediate electropulsing treatment.* Materials Science and Engineering: A, 2010. **527**(12): p. 3040-3043.
224. Yang, C., W. Xu, B. Guo, D. Shan, and J. Zhang, *Healing of fatigue crack in 1045 steel by using eddy current treatment.* Materials, 2016. **9**(8): p. 641.
225. Bhat, I., M. Muju, and P. Mazumdar, *Possible effects of magnetic fields in fatigue.* International journal of fatigue, 1993. **15**(3): p. 193-197.
226. Hosoi, A., T. Kishi, and Y. Ju. *Healing of fatigue crack treated with surface activated pre-coating method by controlling high density electric current*. in *ICF13*. 2013.
227. Tang, Y., A. Hosoi, Y. Iwase, and Y. Ju, *Effect of high-density electric current on the microstructure and fatigue crack initiation of stainless steel.* Materials Transactions, 2013. **54**(11): p. 2085-2092.
228. Sosnin, O., A. Gromova, E.Y. Suchkova, E. Kozlov, Y.F. Ivanov, and V. Gromov, *The structural-phase state changes under the pulse current influence on the fatigue loaded steel.* International Journal of Fatigue, 2005. **27**(10): p. 1221-1226.
229. Zhao-Long, L., H. Hai-Yun, F. Tian-You, and X. Xiu-San, *Fatigue life of metal treated by magnetic field.* Chinese Physics B, 2009. **18**(3): p. 1283.
230. Tanaka, K. and T. Mura, *A dislocation model for fatigue crack initiation.* Journal of Applied Mechanics(Transactions of the ASME), 1981. **48**(1): p. 97-103.
231. Alshits, V., E. Darinskaya, O. Kazakova, E.Y. Mikhina, and E. Petrzhik, *Magnetoplastic effect in non-magnetic crystals and internal friction.* Journal of alloys and compounds, 1994. **211**: p. 548-553.
232. Conrad, H., A.F. Sprecher, and F. Nabarro, *Dislocations in solids.* Elservier, Amsterdam, 1989: p. 499.
233. Babutskyi, A., A. Chrysanthou, M. Smelina, G. Stepanov, and M. Ziętara, *Effect of pulsed magnetic treatment on the corrosion of titanium.* Materials Science and Technology, 2017: p. 1-12.
234. Wu, S., H. Zhao, A. Lu, H. Fang, and F. Tang, *A micro-mechanism model of residual stress reduction by low frequency alternating magnetic field*

treatment. Journal of materials processing technology, 2003. **132**(1): p. 198-202.

235. Lu, A., F. Tang, X. Luo, J. Mei, and H. Fang, *Research on residual-stress reduction by strong pulsed magnetic treatment.* Journal of materials processing technology, 1998. **74**(1): p. 259-262.
236. Okazaki, K., M. Kagawa, and H. Conrad, *A study of the electroplastic effect in metals.* Scripta Metallurgica, 1978. **12**(11): p. 1063-1068.
237. Livesay, S., X. Duan, R. Priestner, and J. Colins, *An electroplastic effect in 3.25% silicon steel.* Scripta Metal, 2001. **44**: p. 5.
238. Klamecki, B.E., *Residual stress reduction by pulsed magnetic treatment.* Journal of Materials Processing Technology, 2003. **141**(3): p. 385-394.
239. Ludtka, G.M., *Method for residual stress relief and retained austenite destabilization*. 2004, Google Patents.
240. Cai, Z., J. Lin, L. Zhou, and H. Zhao, *Evaluation of effect of magnetostriction on residual stress relief by pulsed magnetic treatment.* Materials science and technology, 2004. **20**(12): p. 1563-1566.
241. Cai, z. and X. Huang, *Residual stress reduction by combined treatment of pulsed magnetic field and pulsed current.* Materials Science and Engineering: A, 2011. **528**(19–20): p. 6287-6292.
242. Ritchie, R., W. Yu, and R. Bucci, *Fatigue crack propagation in ARALL® LAMINATES: measurement of the effect of crack-tip shielding from crack bridging.* Engineering Fracture Mechanics, 1989. **32**(3): p. 361-377.
243. Lieberman, M.A. and A.J. Lichtenberg, *Principles of plasma discharges and materials processing*. 2005: John Wiley & Sons.
244. Zhao-Long, L., H. Hai-Yun, F. Tian-You, and X. Xiu-San, *Non-equilibrium statistical theory about microscopic fatigue cracks of metal in magnetic field.* Chinese Physics B, 2010. **19**(10): p. 108103.
245. Yu, J., H. Zhang, D. Deng, Q. Liu, and S. Hao, *Analysis of the relationship of crack arrest effects with fusion zone size by current detour and Joule heating.* The International Journal of Advanced Manufacturing Technology, 2014: p. 1-10.
246. Song, H. and Z.-J. Wang, *Microcrack healing and local recrystallization in pre-deformed sheet by high density electropulsing.* Materials Science and Engineering: A, 2008. **490**(1): p. 1-6.

247. Xiao, S., J. Guo, S. Wu, G. He, and S. Li, *Recrystallization in fatigued copper single crystals under electropulsing.* Scripta materialia, 2002. **46**(1): p. 1-6.
248. Cao, W.d. and H. Conrad, *On the effect of persistent slip band (PSB) parameters on fatigue life.* Fatigue & Fracture of Engineering Materials & Structures, 1992. **15**(6): p. 573-583.
249. Wheeler, H.A., *Formulas for the skin effect.* Proceedings of the IRE, 1942. **30**(9): p. 412-424.
250. Conrad, H., *Electroplasticity in metals and ceramics.* Materials Science and Engineering: A, 2000. **287**(2): p. 276-287.
251. Erber, T., S. Guralnick, R. Desai, and W. Kwok, *Piezomagnetism and fatigue.* Journal of Physics D: Applied Physics, 1997. **30**(20): p. 2818.
252. Benitez Velez, S., *The effect of residual magnetic field on the fatigue crack propagation of AerMet 100 alloy steel*. 1997, University of Puerto Rico, Mayaguez Campus.
253. Yetim, A., H. Kovacı, M. Aslan, and A. Çelik, *The effect of magnetic field on the wear properties of a ferromagnetic steel.* Wear, 2013. **301**(1): p. 636-640.
254. Zhipeng, C., L. Jian, Z. Haiyan, and L. Anli, *Orientation effects in pulsed magnetic field treatment.* Materials Science and Engineering: A, 2005. **398**(1): p. 344-348.
255. Aalco, *Aluminium Alloy - Commercial Alloy - 6082 - T6~T651 Plate*. 2017, Aalco.
256. Materials, A., *Aluminium Alloy 6082*. 2017, Aircraft Materials
257. NDT National Resource Centre, *Fracture Toughness*. 2017.
258. Zhan, W., N. Lu, and C. Zhang, *A new approximate model for the R-ratio effect on fatigue crack growth rate.* Engineering Fracture Mechanics, 2014. **119**: p. 85-96.
259. Huang, X. and T. Moan, *Improved modeling of the effect of R-ratio on crack growth rate.* International Journal of fatigue, 2007. **29**(4): p. 591-602.
260. Dubey, S., A. Soboyejo, and W. Soboyejo, *An investigation of the effects of stress ratio and crack closure on the micromechanisms of fatigue crack growth in Ti-6Al-4V.* Acta Materialia, 1997. **45**(7): p. 2777-2787.
261. Kujawski, D., *Enhanced model of partial crack closure for correlation of R-ratio effects in aluminum alloys.* International Journal of Fatigue, 2001. **23**(2): p. 95-102.

262. Correia, J.A., A.M. De Jesus, P.M. Moreira, and P.J. Tavares, *Crack closure effects on fatigue crack propagation rates: application of a proposed theoretical model.* Advances in Materials Science and Engineering, 2016. **2016**.
263. Hutchinson, J., *Analysis of closure in fatigue crack growth.* J. appl. Mech, 1978. **45**: p. 267-276.
264. Newman Jr, J. *Advances in finite-element modeling of fatigue-crack growth and fracture*. in *Fatigue*. 2002.
265. Xu, Y., J. Chen, J. Li, and Z. Zhu, *Improved fatigue and damage tolerant material design for aerospace industry.* Journal of Materials Science and Technology, 2005.
266. Newman Jr, J., *Analyses of fatigue crack growth and closure near threshold conditions for large-crack behavior.* 1999.
267. Wang, L., Y. Chen, W. Tiu, and Y. Xu, *Simulation of near-tip crack behaviour and its correlation to fatigue crack growth with a modified strip-yield model.* International Journal of Modelling, Identification and Control, 2008. **5**(1): p. 77-91.
268. Phillips, E.P., *Results of the Round Robin on opening-load measurement conducted by ASTM Task Group E24. 04.04 on Crack Closure Measurement and Analysis.* 1989.
269. Kujawski, D., *On assumptions associated with ΔK eff and their implications on FCG predictions.* International journal of fatigue, 2005. **27**(10): p. 1267-1276.
270. Carnahan, B., H.A. Luther, and J.O. Wilkes, *Applied numerical methods*. 1969: John Wiley & Sons, Inc.
271. Venkateswara Rao, K. and R. Ritchie, *Micromechanisms of transient fatigue crack growth behaviour in aluminium-lithium alloys following single tensile overloads.* Fatigue crack growth under variable amplitude loading. London: Elsevier Applied Science, 1988: p. 134-145.
272. Singh, K.D., K.H. Khor, and I. Sinclair, *Finite element and analytical modelling of crack closure due to repeated overloads.* Acta Materialia, 2008. **56**(4): p. 835-851.
273. Ritchie, R., *Mechanisms of fatigue crack propagation in metals, ceramics and composites: role of crack tip shielding.* Materials Science and Engineering: A, 1988. **103**(1): p. 15-28.

274. Ritchie, R., S. Suresh, and C. Moss, *Near-threshold fatigue crack growth in 2 1/4 Cr-1Mo pressure vessel steel in air and hydrogen.* Journal of Engineering Materials and Technology, 1980. **102**(3): p. 293-299.
275. Suresh, S. and R. Ritchie, *Mechanistic dissimilarities between environmentally influenced fatigue-crack propagation at near-threshold and higher growth rates in lower strength steels.* Metal Science, 1982. **16**(11): p. 529-538.
276. Newman, J.A. and R.S. Piascik, *Interactions of plasticity and oxide crack closure mechanisms near the fatigue crack growth threshold.* International Journal of Fatigue, 2004. **26**(9): p. 923-927.
277. Antunes, F., T. Sousa, R. Branco, and L. Correia, *Effect of crack closure on non-linear crack tip parameters.* International Journal of Fatigue, 2015. **71**: p. 53-63.
278. Phillips, E., *Results of the round robin on opening-load measurement.* NASA Technical Memorandum, 1989. **101601**.
279. Phillips, E., *Results of the second round robin on opening-load measurement.* NASA Technical Memorandum, 1993. **109032**.
280. Parry, M.R., *Finite element and analytical modelling of roughness induced fatigue crack closure*. 2000, University of Southampton.
281. McClung, R. and H. Sehitoglu, *On the finite element analysis of fatigue crack closure—1. Basic modeling issues.* Engineering Fracture Mechanics, 1989. **33**(2): p. 237-252.
282. Newman, J., *Analyses of fatigue crack growth and closure near threshold conditions for large-crack behavior.* ASTM SPECIAL TECHNICAL PUBLICATION, 2000. **1372**: p. 227-251.
283. De Iorio, A., M. Grasso, F. Penta, and G. Pucillo, *A three-parameter model for fatigue crack growth data analysis.* Frattura ed Integrità Strutturale, 2012(21): p. 21-29.
284. Ghonem, H. and S. Dore, *Experimental study of the constant-probability crack growth curves under constant amplitude loading.* Engineering Fracture Mechanics, 1987. **27**(1): p. 1-25.
285. Virkler, D., B. Hillberry, and P. Goel, *The statistical nature of fatigue crack propagation.* Journal of Engineering Materials and Technology, 1979. **101**(2): p. 148-153.

286. Wu, W. and C. Ni, *Statistical aspects of some fatigue crack growth data.* Engineering Fracture Mechanics, 2007. **74**(18): p. 2952-2963.
287. Frost, N.E. and D.S. Dugdale, *The propagation of fatigue cracks in sheet specimens.* Journal of the Mechanics and Physics of Solids, 1958. **6**(2): p. 92-110.
288. Mohanty, J.R., B.B. Verma, and P.K. Ray, *Determination of fatigue crack growth rate from experimental data: a new approach.* International Journal of Microstructure and Materials Properties, 2010. **5**(1): p. 79-87 %@ 1741-8410.
289. Barter, S., L. Molent, N. Goldsmith, and R. Jones, *An experimental evaluation of fatigue crack growth.* Engineering failure analysis, 2005. **12**(1): p. 99-128.
290. Mohanty, J., B. Verma, and P. Ray, *Determination of fatigue crack growth rate from experimental data: a new approach.* International Journal of Microstructure and Materials Properties, 2010. **5**(1): p. 79-87.
291. Grasso, M., F. Penta, P. Pinto, and G. Pucillo, *A four-parameters model for fatigue crack growth data analysis.* Frattura ed Integritá Strutturale, 2013(26): p. 69.
292. Aalco, *Alloy 2024 sheet and plate, excellent fatigue properties–consistent performance.* 2016, Alcoa mill products, Inc. p. 523-9596
293. MakeItFrom, *2024-T3 Aluminum vs. 2024-T351 Aluminum*. 2017.
294. Sasahara, H., *The effect on fatigue life of residual stress and surface hardness resulting from different cutting conditions of 0.45% C steel.* International Journal of Machine Tools and Manufacture, 2005. **45**(2): p. 131-136.
295. Carter, T.L., E.V. Zaretsky, and W.J. Anderson, *Effect of Hardness and Other Mechanical Properties on Rolling-Contact Fatigue Life of Four High-Temperature Bearing Steels*. 1960, National Aeronautics and Space Administration. Lewis Research Center, Cleveland.
296. Raveh, A., A. Bussiba, A. Bettelheim, and Y. Katz, *Plasma-nitrided α-β Ti alloy: layer characterization and mechanical properties modification.* Surface and Coatings Technology, 1993. **57**(1): p. 19-29.
297. Bussu, G. and P. Irving, *The role of residual stress and heat affected zone properties on fatigue crack propagation in friction stir welded 2024-T351 aluminium joints.* International Journal of Fatigue, 2003. **25**(1): p. 77-88.

298. Rubio-González, C., J. Ocana, G. Gomez-Rosas, C. Molpeceres, M. Paredes, A. Banderas, J. Porro, and M. Morales, *Effect of laser shock processing on fatigue crack growth and fracture toughness of 6061-T6 aluminum alloy.* Materials Science and Engineering: A, 2004. **386**(1): p. 291-295.
299. Kumar, T.A., G. Anne, N. Prasanna, and M. Muralidhara, *Effect of Electromagnetic Induction and Heat Treatment on the Mechanical and Wear Properties of LM25 Alloy.* Procedia Materials Science, 2014. **5**: p. 550-557.
300. Zhiqiang, C., J. Fei, Z. Xingguo, H. Hai, and J. Junze, *Microstructures and mechanical characteristics of electromagnetic casting and direct-chill casting 2024 aluminum alloys.* Materials Science and Engineering: A, 2002. **327**(2): p. 133-137.
301. Stoicănescu, M., M. Smeadă, V. Geamăn, and I. Radomir, *The influence of work parameters about the heat treatment applied to AlCu4Mg1, 5Mn-aluminum alloy.* Procedia-Social and Behavioral Sciences, 2012. **62**: p. 886-890.
302. Herbert, E.G., *The Hardening of Metals by Rotating Magnetic Fields.* Proceedings of the Royal Society of London. Series A, Containing Papers of a Mathematical and Physical Character, 1931. **130**(814): p. 514-523.
303. Zhan, L., W. Li, Q. Ma, and L. Liu, *The Influence of Different External Fields on Aging Kinetics of 2219 Aluminum Alloy.* Metals, 2016. **6**(9): p. 201.
304. Prabhu, T.R., *Effects of ageing time on the mechanical and conductivity properties for various round bar diameters of AA 2219 Al alloy.* Engineering Science and Technology, an International Journal, 2016.
305. Pakiela, Z., K. Ludwichowska, J. Ferenc, and M. Kulczyk. *Mechanical properties and electrical conductivity of Al 6101 and 6201 alloys processed by hydro-extrusion*. in *IOP Conference Series: Materials Science and Engineering*. 2014. IOP Publishing.
306. Salazar-Guapuriche, M.A., Y. Zhao, A. Pitman, and A. Greene. *Correlation of strength with hardness and electrical conductivity for aluminium alloy 7010*. in *Materials science forum*. 2006. Trans Tech Publ.
307. Tiryakioğlu, M., J. Campbell, and J.T. Staley. *Hardness-strength relationships in cast Al-Si-Mg alloys*. in *Materials science forum*. 2000. Trans Tech Publ.

308. Rosen, M., E. Horowitz, L. Swartzendruber, S. Fick, and R. Mehrabian, *The aging process in aluminum alloy 2024 studied by means of eddy currents.* Materials Science and Engineering, 1982. **53**(2): p. 191-198.
309. MatWeb, *Aluminum 2011-T6*. 2017, MatWeb.
310. TecQuipment Ltd., *SM1090 rotating fatigue machine user guide* 2004. 1-36.
311. WG4, C., *IACAS M53, Appendix IV, Guidance for elaluation for fatigue life*. 2009. p. 3-15.
312. YANG, D.-L., Y.-L. LIU, S.-B. LI, J.-H. YI, and J. TAO, *Investigation of uniaxial asymmetric high-cycle fatigue failure behavior of 7075-T651 aluminum alloy sheet.* 2015.
313. Ganvir, K.D. and V. Khangar. *Study on Fatigue Strength of A Dental Crown: A Review*. in *International Journal of Engineering Research and Technology*. 2014. ESRSA Publications.
314. Wilson, R., *Guide to the effect of shot peening on fatigue strength.* Engineering Sciences Data Unit, 1992.
315. Rao, C.R., *Factorial experiments derivable from combinatorial arrangements of arrays.* Supplement to the Journal of the Royal Statistical Society, 1947. **9**(1): p. 128-139.
316. Demirci, M., A. Samanchi, N. Tarakcioglu, and T. Asilturk. *optimization of fatigue life parameters with Taguchi Method*. in *6th International Advanced Technologies Symposium (IATS'11)*. 2011.
317. Chavan, H.V. and M.S. Yadav, *Investigate the effect of phosphate surface coating on the fatigue performance of the piston pin materials.* Technology, 2015. **6**(11): p. 244-250.
318. Macodiyo, D.O. and H. Soyama, *Optimization of cavitation peening parameters for fatigue performance of carburized steel using Taguchi methods.* Journal of Materials Processing Technology, 2006. **178**(1): p. 234-240.
319. Vidal, C., V. Infante, and P. Vilaça, *Assessment of improvement techniques effect on fatigue behaviour of friction stir welded aerospace aluminium alloys.* Procedia Engineering, 2010. **2**(1): p. 1605-1616.
320. Ugrasen, G., H. Ravindra, G.N. Prakash, and Y.T. Prasad, *Optimization of process parameters in pire EDM of HCHCr material using Taguchi's technique.* Materials Today: Proceedings, 2015. **2**(4): p. 2443-2452.

321. Dudrová, E. and M. Kabátová, *Fractography of sintered iron and steels.* Powder Metallurgy Progress, 2008. **8**(2): p. 59-75.
322. Moeser, M., *Fractography with the SEM (failure analysis)*. 2007.
323. Zhou, J., S. Xu, S. Huang, X. Meng, J. Sheng, H. Zhang, J. Li, Y. Sun, and E.A. Boateng, *Tensile Properties and Microstructures of a 2024-T351 Aluminum Alloy Subjected to Cryogenic Treatment.* Metals, 2016. **6**(11): p. 279.
324. Li, G.-R., J.-F. Cheng, H.-M. Wang, P.-S. Li, and C.-Q. Li, *Influence of a high pulsed magnetic field on the tensile properties and phase transition of 7055 aluminum alloy.* Materials Research Express, 2016. **3**(10): p. 106507.
325. Xie, C., S. Yang, H. Liu, Q. Zhang, Y. Wang, and Y. Zou, *Microstructure and mechanical properties of robot cold metal transfer Al5. 5Zn2. 5Mg2. 2Cu aluminium alloy joints.* Journal of Materials Processing Technology, 2018.
326. Zhang, G., J. Zhang, B. Li, and W. Cai, *Double-stage hardening behavior and fracture characteristics of a heavily alloyed Al–Si piston alloy during low-cycle fatigue loading.* Materials Science and Engineering: A, 2013. **561**: p. 26-33.
327. Lin, Y., Y.-Q. Jiang, Y.-C. Xia, X.-C. Zhang, H.-M. Zhou, and J. Deng, *Effects of creep-aging processing on the corrosion resistance and mechanical properties of an Al–Cu–Mg alloy.* Materials Science and Engineering: A, 2014. **605**: p. 192-202.
328. Roy, R.K., *Recrystallization behavior of commercial purity aluminium alloys*, in *Light Metal Alloys Applications*. 2014, InTech.
329. Rahnama, A. and R. Qin, *Effect of electric current pulses on the microstructure and niobium carbide precipitates in a ferritic-pearlitic steel at an elevated temperature.* Journal of Materials Research, 2015. **30**(20): p. 3049-3055.
330. Zhu, Y. and W. Lai, *Effects of electropulsing induced microstructural changes on THz-Reflection and electrical conductivity of Al-doped ZnO thin-films.* Journal of Surface Engineered Materials and Advanced Technology, 2016. **6**(03): p. 106.
331. Xu, X., Y. Zhao, B. Ma, and M. Zhang, *Rapid precipitation of T-phase in the 2024 aluminum alloy via cyclic electropulsing treatment.* Journal of Alloys and Compounds, 2014. **610**: p. 506-510.

332. Lu, Y., J. Wang, X. Li, W. Li, R. Li, and D. Zhou, *Effects of pre-deformation on the microstructures and corrosion behavior of 2219 aluminum alloys.* Materials Science and Engineering: A, 2018.
333. Li, G., L. Wang, Y. Liu, W. Zhang, X. Qiao, and Y. Wang, *Effects of high density electropulsing treatment on aging kinetics of GH4199 alloy.* Rare Metal Materials and Engineering, 2011. **40**(6): p. 961-966.
334. Li, C., H. Tan, W. Wu, S. Zhao, and H. Zhang, *Effect of electropulsing treatment on microstructure and tensile fracture behavior of nanocrystalline Ni foil.* Materials Science and Engineering: A, 2016. **657**: p. 347-352.
335. Zhu, Y., S. To, W. Lee, X. Liu, Y. Jiang, and G. Tang, *Effects of dynamic electropulsing on microstructure and elongation of a Zn–Al alloy.* Materials Science and Engineering: A, 2009. **501**(1-2): p. 125-132.
336. Sheng, Y., Y. Hua, X. Wang, X. Zhao, L. Chen, H. Zhou, J. Wang, C.C. Berndt, and W. Li, *Application of High-Density Electropulsing to Improve the Performance of Metallic Materials: Mechanisms, Microstructure and Properties.* Materials, 2018. **11**(2): p. 185.
337. Xie, D.Y., J. Yan, Y. Li, D. Qiu, G. Wu, X. Wang, B. Chen, Y. Shen, and G.-z. Zhu, *Ordered stacking faults within nanosized silicon precipitates in aluminum alloy.* Materials Letters, 2017. **190**: p. 225-228.
338. To, S., Z. YH, and L. WB, *Effects of current density on elongation of an electropulsing treated Zn-Al based alloy.* Materials transactions, 2009. **50**(12): p. 2772-2777.
339. Liu, Y., L. Zhan, Q. Ma, Z. Ma, and M. Huang, *Effects of alternating magnetic field aged on microstructure and mechanical properties of AA2219 aluminum alloy.* Journal of Alloys and Compounds, 2015. **647**: p. 644-647.

Appendices

Appendix A: Code for Strip Yield model

```
      PROGRAM CRACK_CLOSURE_MODELLING
      Implicit None
      Integer :: N, Loadcycle
      Double Precision :: S1
!     The dimension of smax and smin equals loadcycle
      Double Precision :: Smax(2000), Smin(2000)
!     Data Initialisations
      Loadcycle=2000
      Smax=5.0D1; Smin=0.0D1
      S1=5.0D1
      Smin(600)=0.0D1
      Smax(600)=7.0D1
      Open  (unit=10, file= "result1.out", status= "new")
      Write (unit=10, FMT=*) "Analytical Crack Closure Modelling"
      Print *, "Analytical Crack Closure Modelling"
100    Format (F10.4, 3(E12.5, 1x))
200    Format (1x, "X(I)", T12, "V(I)", T30, "S(I)", T45, "L(I)")
      Call Initialisation(S1)
      Print *, "Initialisation passed"
      DO N=1, 1000
!      Write (unit=10, FMT=*) "*****************************"
```

```
        Write (unit=10, FMT=*) "Results at N=", N
        Print *, "******************************"
        Print *, "Results at N=", N
        Call Crack_Extension(Smax(N))
        Print *, "Crack Extension passed"
        Call Smax_Data(Smax(N), N)
        Print *, "Smax_Data passed"
        Call Smin_Data(Smax(N),Smin(N),N)
        Print *, "Smin_Data passed"
        Call Crack_Opening(Smax(N),Smin(N),N)
        Print *, "Crack_Opening passed"
        End DO
        Write (unit=10, FMT=*) "End of the analysis"
        Close (unit=10)
        Print *, "End of the Analysis"
        END PROGRAM CRACK_CLOSURE_MODELLING


!       Define Module Global_Data
        Module Global_Data
        Implicit None
        Save
!       This module defines sample geometry, materials properties,
!       and some parameters.
        Integer :: N1
```

```
      Double Precision :: a0, af, rp0, rpmax, rpmax0, rpmax1
      Double Precision :: Pmax, Pmin, Pmax1, Pmin1
      Double Precision :: S(100), W(100), X(100), F(100), V(100)
      Double Precision :: L(100), Y(100), G(100, 100)
!     width is the whole width while a0 is the half length of
!     the intial physical crack.
      Double Precision, Parameter :: width=15.0D1, T=0.2D1,E=7.0D4
      Double Precision, Parameter :: Poisson=0.00D1, alpha=0.1D1
      Double Precision, Parameter :: epsilon=0.0005D1, pi=0.31415926D1
      Double Precision, Parameter :: SYS=37.2D1, UTS=48.3D1, R=0.00D1
      Double Precision, Parameter :: nm=0.01D1, nc=0.018D1
      End Module Global_Data


!     Define influence function F1(X1)
      Function F1(x1)
      Use Global_Data
      Implicit None
      Double Precision :: F1
      Double Precision, Intent(in) :: x1
      F1=2.0*(1.0-Poisson**2)*SQRT((af**2-X1**2)/cos(pi*af/width))/E
      End Function F1
```

```
!     Define Yield strength function Yield(x1)
      Function Yield(x1)
      Use Global_Data
      Implicit None
      Double Precision :: Yield
      Double Precision, Intent(in) :: x1
      Yield=(SYS+UTS)/2.0
      End Function Yield


!     Define Subroutine G1
      Subroutine G1
      USE Global_Data
      Implicit None
      Double Precision :: b1,b2,bb1,bb2,a1,a2,a3,a4,a5
      Double Precision :: c1,c2,c3,c4,c5,c6
      Double Precision :: c11,c22,c33,c44,a22,a33,t1,t2
      Integer :: I, J

      DO I=1, 100
      DO J=1, 100
      b1=X(J)-W(J)/2.0; b2=X(J)+W(J)/2.0
      bb1=sin(pi*b1/width)/sin(pi*af/width)
```

```
bb2=sin(pi*b2/width)/sin(pi*af/width)
If (bb2>(1.0-1.0D-25)) then
bb2=1.0-1.0D-25
End If
a1=2.0*(1.0-Poisson**2)*SQRT(1.0/cos(pi*af/width))/(pi*E)
c1=(af**2-b2*X(I))/(af*ABS(b2-X(I)))
If (c1<(1.0+1.0D-25)) then
c1=1.0+1.0D-25
End If
c2=log(c1+SQRT(c1**2-1.0))
c3=(af**2-b1*X(I))/(af*ABS(b1-X(I)))
If (c3<(1.0+1.0D-25)) then
c3=1.0+1.0D-25
End If
c4=log(c3+SQRT(c3**2-1.0))
a2=(b2-X(I))*c2
a3=(b1-X(I))*c4
c5=b1/af; c6=b2/af
If (c6>(1.0-1.0D-25)) then
c6=1.0-1.0D-25
End If
a4=SQRT(af**2-X(I)**2)*(asin(c6)-asin(c5))
a5=(asin(bb2)-asin(bb1))/(asin(c6)-asin(c5))
t1=a1*(a2-a3+a4)*a5
```

```
        c11=(af**2+b2*X(I))/(af*ABS(b2+X(I)))
        If (c11<(1.0+1.0D-25)) then
        c11=1.0+1.0D-25
        End If
        c22=log(c11+SQRT(c11**2-1.0))
        c33=(af**2+b1*X(I))/(af*ABS(b1+X(I)))
        If (c33<(1.0+1.0D-25)) then
        c33=1.0+1.0D-25
        End If
        c44=log(c33+SQRT(c33**2-1.0))
        a22=(b2+X(I))*c22
        a33=(b1+X(I))*c44
        t2=a1*(a22-a33+a4)*a5
        G(I,J)=t1+t2
        End DO
        End DO
        End Subroutine G1


!       Initialisation of the problem
        Subroutine Initialisation(S1)
        Use Global_Data
        Implicit None
!       Variable declarations
```

```
      Double Precision, Intent(in) :: S1
      Double Precision :: rp1,t1,t2,sum1,b11,b22,b33,b44
      Integer :: I, J
      Double Precision, External :: F1, Yield

      a0=2.0D1
      N1=0

100   Format (F10.4, 3(E12.5, 1x))
200   Format (1x, "X(I)", T12, "V(I)", T30, "S(I)", T45, "L(I)")
      t2=(SYS+UTS)/2.0
      Rp0=(pi/8.0)*(S1**2*pi*a0/(cos(pi*a0/width)*(alpha*t2)**2))
      DO I=1, 1000
      T1=a0-5.0*rp0; af=a0+rp0
!     Mesh, 40 in plastic zone and 60 in the wake
      DO J=1,10
      W(J)=0.11*rp0;    X(J)=t1+(real(J)-0.5)*0.11*rp0
      W(J+10)=0.11*rp0; X(J+10)=t1+1.1*rp0+(Real(J)-0.5)*0.11*rp0
      W(J+20)=0.11*rp0; X(J+20)=t1+2.2*rp0+(Real(J)-0.5)*0.11*rp0
      W(J+30)=0.11*rp0; X(J+30)=t1+3.3*rp0+(Real(J)-0.5)*0.11*rp0
      W(J+40)=0.05*rp0; X(J+40)=t1+4.4*rp0+(Real(J)-0.5)*0.05*rp0
      W(J+50)=0.01*rp0; X(J+50)=t1+4.9*rp0+(Real(J)-0.5)*0.01*rp0
      W(J+60)=0.01*rp0; X(J+60)=a0+(real(J)-0.5)*0.01*rp0
      W(J+70)=0.03*rp0; X(J+70)=a0+0.1*rp0+(Real(J)-0.5)*0.03*rp0
```

```
W(J+80)=0.05*rp0; X(J+80)=a0+0.4*rp0+(Real(J)-0.5)*0.05*rp0
W(J+90)=0.01*rp0; X(J+90)=a0+0.9*rp0+(Real(J)-0.5)*0.01*rp0
End DO

Y=(/((SYS+UTS)/2.0, J=1, 60), (yield(X(J)), J=61, 100)/)
S=(/(0.0D1, J=1, 60), (alpha*Y(J), J=61, 100)/)
Sum1=0.0D1
DO J=61, 100
b11=X(J)-W(J)/2.0; b22=X(J)+W(J)/2.0
b33=sin(pi*b11/width)/sin(pi*af/width)
b44=sin(pi*b22/width)/sin(pi*af/width)
If (b44>(1.0-1.0D-25)) then
b44=1.0-1.0D-25
End IF
sum1=sum1+alpha*Y(J)*(asin(b44)-asin(b33))
End DO
Rp1=sum1**2*4.0*(a0+rp0)/(pi*S1)**2-a0
If (ABS(rp1-rp0)<epsilon*rp0) then
Exit
End If
If (rp1>rp0) then
rp0=rp0*0.995
Else
rp0=rp0*1.005
```

```
        End If
        IF (rp0>(a0/4.5)) then
        rp0=a0/4.5
        End If
        End DO
!       Write total steps for intialisation to result file
        Write (unit=10,FMT=*) I-1, " iterations for initialisation"
!       print total steps for initialisation
        print *, I-1, " iterations for initialisation"
        Print *, "rp0=", rp0, "    rp1=", rp1
        Print *, "a0=", a0, "    af=", af

        rpmax=rp0
        rpmax1=rp0
        rpmax0=rp0

        F=(/(F1(X(J)), J=1, 100)/)
        Call G1
        DO I=1, 100
        Sum1=0.0D1
        DO J=61, 100
        Sum1=sum1+S(J)*G(I, J)
        End DO
        V(I)=S1*F(I)-sum1
```

```
      If (V(I)<1.0D-25) then
      V(I)=1.0D-25
      End IF
      End DO
      L=(/(0.0D1,I=1,60),(V(I)*(1.0-alpha*Y(I)/E),I=61,100)/)
!     write initialisation results to file
      Write (unit=10, FMT=*) "rp0=", rp0, "    rp1=", rp1
      Write (unit=10, FMT=*) "a0=", a0, "    af=", af
      write (unit=10, FMT=200)

      DO I=1, 100
      Write (unit=10, FMT=100) X(I), V(I), S(I), L(I)
      End DO

      End Subroutine Initialisation


      Subroutine Crack_Extension(Smax1)
      Use Global_Data
      Implicit None
!     Variable declarations
      Double Precision, Intent(inout) :: Smax1
      Double Precision rp, rp1, t1, t2, sum1, dmax
      Double Precision b11, b22, b33, b44
```

```
      Double Precision d1, d2, d3, d4, d5, d6
      Double Precision W2(100), X2(100), L2(100)
      Integer :: I, J, K
      Double Precision, External :: F1, Yield
100   Format (F10.4, 3(E12.5, 1x))
200   Format (1x, "X(I)", T12, "V(I)", T30, "S(I)", T45, "L(I)")
      W2=W; X2=X; L2=L
      N1=N1+1
      t2=(SYS+UTS)/2.0
      Pmax1=50.*SQRT(20.*cos(pi*a0/width)/(a0*cos(pi*20./width)))
      Pmin1=R*Pmax1
      Pmax=Pmax1*Smax1/50.0
      rp0=pi/8.0*Pmax**2*pi*a0/(cos(pi*a0/width)*(alpha*t2)**2)
      DO I=1, 1000
      T1=a0-5.0*rp0; af=a0+rp0
!     Mesh, 40 in plastic zone and 60 in the wake
      DO J=1,10
      W(J)=0.11*rp0;    X(J)=t1+(real(J)-0.5)*0.11*rp0
      W(J+10)=0.11*rp0; X(J+10)=t1+1.1*rp0+(Real(J)-0.5)*0.11*rp0
      W(J+20)=0.11*rp0; X(J+20)=t1+2.2*rp0+(Real(J)-0.5)*0.11*rp0
      W(J+30)=0.11*rp0; X(J+30)=t1+3.3*rp0+(Real(J)-0.5)*0.11*rp0
      W(J+40)=0.05*rp0; X(J+40)=t1+4.4*rp0+(Real(J)-0.5)*0.05*rp0
      W(J+50)=0.01*rp0; X(J+50)=t1+4.9*rp0+(Real(J)-0.5)*0.01*rp0
      W(J+60)=0.01*rp0; X(J+60)=a0+(real(J)-0.5)*0.01*rp0
```

```
W(J+70)=0.03*rp0; X(J+70)=a0+0.1*rp0+(Real(J)-0.5)*0.03*rp0
W(J+80)=0.05*rp0; X(J+80)=a0+0.4*rp0+(Real(J)-0.5)*0.05*rp0
W(J+90)=0.01*rp0; X(J+90)=a0+0.9*rp0+(Real(J)-0.5)*0.01*rp0
End DO

Y=(/((SYS+UTS)/2.0, J=1, 60), (yield(X(J)), J=61, 100)/)
S=(/(0.0D1, J=1,60), (alpha*Y(J), J=61,100)/)
Sum1=0.0D1
DO J=61, 100
b11=X(J)-W(J)/2.0; b22=X(J)+W(J)/2.0
b33=sin(pi*b11/width)/sin(pi*af/width)
b44=sin(pi*b22/width)/sin(pi*af/width)
If (b44>(1.0-1.0D-25)) Then
b44=1.0-1.0D-25
End IF
sum1=sum1+alpha*Y(J)*(asin(b44)-asin(b33))
End DO
Rp1=sum1**2*4.0*(a0+rp0)/(pi*Pmax)**2-a0
If (ABS(rp1-rp0)<epsilon*rp0) then
Exit
End If
If (rp1>rp0) then
rp0=0.995*rp0
Else
```

```
rp0=1.005*rp0
End If
IF (rp0>(a0/4.5)) then
rp0=a0/4.5
End If
End DO

!   Write total steps for Smax calculation at cycle N to result file
    Write (unit=10, FMT=*) I-1, " iterations for active rp at Smax"
!   print total steps for Smax calculation at cycle N
    print *, I-1, " iterations for active rp at Smax"

    If (rp0<rpmax*(1.0-epsilon)) Then
    W=W2; X=X2; L=L2
    af=a0+rpmax
    a0=a0+W(61)
    rp0=rpmax-W(61)
    rpmax=rpmax-W(61)
    t1=a0-5.0*rp0

    DO I=1, 60
    X(I)=X(I)+W(61)
    End DO
    DO I=6, 1, -1
```

```
DO J=10, 1, -1
K=J+(I-1)*10
L(K)=((W(K)-W(61))*L(K)+W(61)*L(K+1))/W(K)
End DO
End DO

DO J=1,10
W(J+60)=0.01*rp0; X(J+60)=a0+(real(J)-0.5)*0.01*rp0
W(J+70)=0.03*rp0; X(J+70)=a0+0.1*rp0+(Real(J)-0.5)*0.03*rp0
W(J+80)=0.05*rp0; X(J+80)=a0+0.4*rp0+(Real(J)-0.5)*0.05*rp0
W(J+90)=0.01*rp0; X(J+90)=a0+0.9*rp0+(Real(J)-0.5)*0.01*rp0
End DO

DO I=1, 10
L(I+60)=(0.0001*(I-1))*L(I+60)
L(I+60)=(L(I+60)+(0.0099-0.0001*(I-1))*L(I+61))/0.0099
End DO
DO I=1, 10
L(I+70)=(0.0297-0.009+0.0003*I)*L(I+70)
L(I+70)=(L(I+70)+(0.009-0.0003*I)*L(I+71))/0.0297
End DO
DO I=1, 10
L(I+80)=(0.0495-0.006+0.0005*I)*L(I+80)
L(I+80)=(L(I+80)+(0.006-0.0005*I)*L(I+81))/0.0495
```

```
End DO
DO I=1, 10
L(I+90)=(0.0099-0.001+0.0001*I)*L(I+90)
L(I+90)=(L(I+90)+(0.001-0.0001*I)*L(I+91))/0.0099
End DO

Else If (rp0>(1.0+epsilon)*rpmax1) Then
rpmax=rp0
rpmax1=rp0
a0=a0+W(61)
af=a0+rpmax

DO I=1, 60
d1=X(I)-W(I)/2.0
d2=X(I)+W(I)/2.0
DO J=60, 1, -1
d3=X2(J)-W2(J)/2.0
If (d1>=d3) Then
d5=L2(J)
Exit
End If
d5=0.0D1
End DO
DO J=60, 1, -1
```

```
d3=X2(J)-W2(J)/2.0
IF (d2>=d3) Then
d6=L2(J)
Exit
End IF
d6=0.0D1
End DO
L(I)=(d5+d6)/2.0
End DO
DO I=1, 100
X(I)=X(I)+W(61)
END DO
DO I=6, 1, -1
DO J=10, 1, -1
K=J+(I-1)*10
L(K)=((W(K)-W(61))*L(K)+W(61)*L(K+1))/W(K)
End DO
End DO

Else
DO I=1, 60
W(I)=W2(I); X(I)=X2(I); L(I)=L2(I)
End DO
DO I=1, 100
```

```
X(I)=X(I)+W(61)
End DO
DO I=6, 1, -1
DO J=10, 1, -1
K=J+(I-1)*10
L(K)=((W(K)-W(61))*L(K)+W(61)*L(K+1))/W(K)
End DO
End DO
a0=a0+W(61)
af=a0+rp0
rpmax=rp0
End If

DO I=59, 1, -1
If ((X(I)+W(I)/2.0-20.0)<(W(61)/2.0)) Then
DO J=1, I
L(J)=0.0D1
End DO
Exit
End IF
End DO

Write (unit=10, FMT=*) "rp0=",rp0,"  rp1=",rp1,"  rpmax=",rpmax
Write (unit=10, FMT=*) "a0=", a0, "    af=", af
```

```
      Print *, "rp0=",rp0,"    rp1=",rp1,"    rpmax=",rpmax
      Print *, "a0=", a0, "    af=", af

      F=(/(F1(X(I)), I=1, 100)/)
      Call G1
      END Subroutine Crack_Extension


      Subroutine Smax_Data(Smax1,N)
      Use Global_Data
      Implicit None
!     Variable declarations
      Double Precision, Intent(inout) :: Smax1
      Integer, Intent(inout) :: N
      Double Precision t1, sum1, dmax
      Integer :: I, J, K
      Double Precision, External :: F1, Yield
100   Format (F10.4, 3(E12.5, 1x))
200   Format (1x, "X(I)", T12, "V(I)", T30, "S(I)", T45, "L(I)")
      DO K=1, 400
      dmax=0.0D1
      DO I=1, 60
      t1=S(I)
      sum1=0.0D1
```

```
DO J=1, I-1
Sum1=sum1+S(J)*G(I, J)
End DO
DO J=I+1, 100
Sum1=sum1+S(J)*G(I, J)
End DO
S(I)=(Pmax*F(I)-L(I)-sum1)/G(I, I)
If (S(I)>0.0D1) Then
S(I)=0.0D1
Else If (S(I)<-Y(I)) Then
S(I)=-Y(I)
Else
End If
If (ABS(t1-S(I))>=SYS*epsilon) Then
dmax=ABS(t1-S(I))
End If
End DO
DO I=61, 100
t1=S(I)
sum1=0.0D1
DO J=1, I-1
Sum1=sum1+S(J)*G(I, J)
End DO
DO J=I+1, 100
```

```
        Sum1=sum1+S(J)*G(I, J)
        End DO
        S(I)=(Pmax*F(I)-L(I)-sum1)/G(I, I)
        If (S(I)>alpha*Y(I)) Then
        S(I)=alpha*Y(I)
        Else If (S(I)<-alpha*Y(I)) Then
        S(I)=-alpha*Y(I)
        Else
        End If
        If (ABS(t1-S(I))>=SYS*epsilon) Then
        dmax=ABS(t1-S(I))
        End If
        End Do
        If (dmax<=epsilon*SYS) Then
        Exit
        End If
        End DO

!       write iteration number at Smax
        write (unit=10,FMT=*) K-1," iterations at Smax"
!       print iteration number for Smax at cycle N at Smax
        print *, K-1, " iterations at Smax"

        DO I=1, 60
```

```
sum1=0.0D1
DO J=61, 100
sum1=sum1+S(J)*G(I, J)
End DO
V(I)=Pmax*F(I)-sum1
IF (V(I)<1.0D-25) Then
V(I)=1.0D-25
write (unit=10, FMT=*) "Crack surfaces are closed at Smax"
Else IF (V(I)<L(I)*(1.0-Y(I)/E)) Then
L(I)=V(I)*(1.0+Y(I)/E)
write (unit=10, FMT=*) "Crack surfaces are closed at Smax"
Else
End IF
End DO

DO I=61, 100
sum1=0.0D1
DO J=61, 100
sum1=sum1+S(J)*G(I, J)
End DO
V(I)=Pmax*F(I)-sum1
IF (V(I)<1.0D-25) Then
V(I)=1.0D-25
Else IF (V(I)<L(I)*(1.0-alpha*Y(I)/E)) Then
```

```
L(I)=V(I)*(1.0+alpha*Y(I)/E)
Else If (V(I)>L(I)*(1.0+alpha*Y(I)/E)) Then
L(I)=V(I)*(1.0-alpha*Y(I)/E)
Else
End IF
End DO

!   write Smax results at cycle N to file
IF (N1<2) Then
write (unit=10, FMT=200)
DO I=1, 100
Write (unit=10, FMT=100) X(I), V(I), S(I), L(I)
End DO
End IF
IF ((Real(N1/100.0)-Int(N1/100))<1.0D-10) Then
write (unit=10, FMT=200)
DO I=1, 100
Write (unit=10, FMT=100) X(I), V(I), S(I), L(I)
End DO
End If
IF (N1<100) Then
IF ((Real(N1/25.0)-Int(N1/25))<1.0D-10) Then
write (unit=10, FMT=200)
DO I=1, 100
```

```
      Write (unit=10, FMT=100) X(I), V(I), S(I), L(I)
      End DO
      End If
      End IF
      IF (N1>600) Then
      IF (N1<700) Then
      IF ((Real(N1/25.0)-Int(N1/25))<1.0D-10) Then
      write (unit=10, FMT=200)
      DO I=1, 100
      Write (unit=10, FMT=100) X(I), V(I), S(I), L(I)
      End DO
      End IF
      End IF
      End IF
      END Subroutine Smax_Data


      Subroutine Smin_Data(Smax1,Smin1,N)
      Use Global_Data
      Implicit None
!     Variable declarations
      Double Precision, Intent(inout) :: Smax1, Smin1
      Integer, Intent(inout) :: N
      Double Precision :: rp1, t1
```

```
      Double Precision :: b1, b2, b3, b4, sum1, dmax
      Integer :: I, J, K
      Double Precision, External :: F1, Yield
      Dmax=0.0D1
100   Format (F10.4, 3(E12.5, 1x))
200   Format ( 1x, "X(I)", T12, "V(I)", T30, "S(I)", T45, "L(I)")
      F=(/(F1(X(I)), I=1, 100)/)
      S=0.0D1
      Pmin=(Pmax1+Pmin1)/2-(Pmax1-Pmin1)*((25.0-Smin1)/25.0)/2

      DO K=1, 400
      dmax=0.0D1
      DO I=1, 60
      t1=S(I)
      sum1=0.0D1
      DO J=1, I-1
      Sum1=sum1+S(J)*G(I, J)
      End DO
      DO J=I+1, 100
      Sum1=sum1+S(J)*G(I, J)
      End DO
      S(I)=(Pmin*F(I)-L(I)-sum1)/G(I, I)
      If (S(I)>0.0D1) Then
      S(I)=0.0D1
```

```
Else If (S(I)<-Y(I)) Then
S(I)=-Y(I)
Else
End If
If (ABS(t1-S(I))>=SYS*epsilon) Then
dmax=ABS(t1-S(I))
End If
End DO
DO I=61, 100
t1=S(I)
sum1=0.0D1
DO J=1, I-1
Sum1=sum1+S(J)*G(I, J)
End DO
DO J=I+1, 100
Sum1=sum1+S(J)*G(I, J)
End DO
S(I)=(Pmin*F(I)-L(I)-sum1)/G(I, I)
If (S(I)>alpha*Y(I)) Then
S(I)=alpha*Y(I)
Else If (S(I)<-alpha*Y(I)) Then
S(I)=-alpha*Y(I)
Else
End If
```

```
If (ABS(t1-S(I))>=SYS*epsilon) Then
dmax=ABS(t1-S(I))
End If
End DO
If (dmax<=epsilon*SYS) Then
Exit
End If
End DO

DO I=1, 60
Sum1=0.0D1
DO J=1, 100
Sum1=sum1+S(J)*G(I, J)
End DO
V(I)=Pmin*F(I)-sum1
IF (V(I)<1.0D-25) Then
V(I)=1.0D-25
S(I)=-Y(I)
Else IF (V(I)<L(I)*(1.0-Y(I)/E)) Then
L(I)=V(I)*(1.0+Y(I)/E)
Else
End IF
End DO
```

```
DO I=61, 100
Sum1=0.0D1
DO J=1, 100
Sum1=sum1+S(J)*G(I, J)
End DO
V(I)=Pmin*F(I)-sum1
IF (V(I)<1.0D-25) Then
V(I)=1.0D-25
Else IF (V(I)<L(I)*(1.0-alpha*Y(I)/E)) Then
L(I)=V(I)*(1.0+alpha*Y(I)/E)
Else If (V(I)>L(I)*(1.0+alpha*Y(I)/E)) Then
L(I)=V(I)*(1.0-alpha*Y(I)/E)
Else
End IF
End DO

!     write Smin results at cycle N to file
      write (unit=10, FMT=*) K-1, " iterations at Smin"
      IF (N1<2) Then
      write (unit=10, FMT=200)
      DO I=1, 100
      Write (unit=10, FMT=100) X(I), V(I), S(I), L(I)
      End DO
      End IF
```

```
IF ((Real(N1/100.0)-Int(N1/100))<1.0D-10) Then
write (unit=10, FMT=200)
DO I=1, 100
Write (unit=10, FMT=100) X(I), V(I), S(I), L(I)
End DO
End If
IF (N1<100) Then
IF ((Real(N1/25.0)-Int(N1/25))<1.0D-10) Then
write (unit=10, FMT=200)
DO I=1, 100
Write (unit=10, FMT=100) X(I), V(I), S(I), L(I)
End DO
End If
End IF
IF (N1>600) Then
IF (N1<700) Then
IF ((Real(N1/25.0)-Int(N1/25))<1.0D-10) Then
write (unit=10, FMT=200)
DO I=1, 100
Write (unit=10, FMT=100) X(I), V(I), S(I), L(I)
End DO
End IF
End IF
End IF
```

```
!       Print iteration step number on screen
        print *, K-1, " iterations at Smin"
        END Subroutine Smin_Data




        Subroutine Crack_Opening(Smax1, Smin1, N)
        Use Global_Data
        Implicit None
        Double Precision, Intent(inout) :: Smax1, Smin1
        Integer, Intent(inout) :: N
        Integer :: I, J, K, M, I1, I2
        Double Precision :: dmax,dmax1, dmin1, sum1, t1, t2
        Double Precision :: Sopen, U1, U2
        Double Precision :: Kmax, Kop, b1, b2, b11, b22,b3
        Double Precision, External :: F1, Yield

100     Format (F10.4, 3(E12.5, 1x))
200     Format (1x, "X(I)", T12, "V(I)", T30, "S(I)", T45, "L(I)")
        Sopen=Pmin1

        Kmax=Pmax1*SQRT(pi*a0/cos(pi*a0/width))
        Kop=0.0D1
        DO I=1,60
```

```
b1=X(I)-W(I)/2
b2=X(I)+W(I)/2
b11=sin(pi*b1/width)/sin(pi*a0/width)
b22=sin(pi*b2/width)/sin(pi*a0/width)
If (b22>(1.0-1.0D-25)) Then
b22=1.0-1.0D-25
End IF
b3=asin(b22)-asin(b11)
Kop=Kop-2*S(I)*b3*SQRT(a0/(cos(pi*a0/width)*pi))
End DO
U1=Kop/Kmax
print *, "Crack opening level U1=", U1

DO K=1, 400
Dmax1=0.0D1
Dmin1=1.0D25
DO I=1, 60
T1=-S(I)
T2=V(I)-L(I)
If (t1>dmax1) then
Dmax1=t1
I1=I
End if
If (t2<dmin1) then
```

```
Dmin1=t2

I2=I

End if

End DO

If (dmax1>epsilon*SYS) then

Sopen=Sopen+dmax1*G(I1,I1)/F(I1)

Else if (dmin1>epsilon*L(60)) then

Sopen=Sopen-dmin1/F(I2)

Else

Exit

End If


S=0.0D1

DO M=1, 400

dmax=0.0D1

DO I=1, 60

t1=S(I)

sum1=0.0D1

DO J=1, I-1

Sum1=sum1+S(J)*G(I, J)

End DO

DO J=I+1, 100

Sum1=sum1+S(J)*G(I, J)

End DO
```

```
S(I)=(Sopen*F(I)-L(I)-sum1)/G(I, I)
If (S(I)>0.0D1) Then
S(I)=0.0D1
Else If (S(I)<-Y(I)) Then
S(I)=-Y(I)
Else
End If
If (ABS(t1-S(I))>=SYS*epsilon) Then
dmax=ABS(t1-S(I))
End If
End DO
DO I=61, 100
t1=S(I)
sum1=0.0D1
DO J=1, I-1
Sum1=sum1+S(J)*G(I, J)
End DO
DO J=I+1, 100
Sum1=sum1+S(J)*G(I, J)
End DO
S(I)=(Sopen*F(I)-L(I)-sum1)/G(I, I)
If (S(I)>alpha*Y(I)) Then
S(I)=alpha*Y(I)
Else If (S(I)<-alpha*Y(I)) Then
```

```
S(I)=-alpha*Y(I)
Else
End If
If (ABS(t1-S(I))>=SYS*epsilon) Then
dmax=ABS(t1-S(I))
End If
End DO
If (dmax<=epsilon*SYS) Then
Exit
End If
End DO

DO I=1, 100
Sum1=0.0D1
DO J=1, 100
Sum1=sum1+S(J)*G(I, J)
End DO
V(I)=Sopen*F(I)-sum1
If (V(I)<1.0D-25) then
V(I)=1.0D-25
End IF
End DO

End DO
```

```
      DO I=1, 60
      Sum1=0.0D1
      DO J=1, 100
      Sum1=sum1+S(J)*G(I, J)
      End DO
      V(I)=Sopen*F(I)-sum1
      IF (V(I)<1.0D-25) Then
      V(I)=1.0D-25
!     Else IF (V(I)<L(I)*(1.0-Y(I)/E)) Then
!     L(I)=V(I)*(1.0+Y(I)/E)
!     Else
      End IF
      End DO

      DO I=61, 100
      Sum1=0.0D1
      DO J=1, 100
      Sum1=sum1+S(J)*G(I, J)
      End DO
      V(I)=Sopen*F(I)-sum1
      IF (V(I)<1.0D-25) Then
      V(I)=1.0D-25
!     Else IF (V(I)<L(I)*(1.0-alpha*Y(I)/E)) Then
```

```
!     L(I)=V(I)*(1.0+alpha*Y(I)/E)
!     Else If (V(I)>L(I)*(1.0+alpha*Y(I)/E)) Then
!     L(I)=V(I)*(1.0-alpha*Y(I)/E)
!     Else
      End IF
      End DO

      U2=Sopen/Pmax1

!     write crack opening results at cycle N to file
      write (unit=10, FMT=*) K-1, " iterations for U calculation"
      write (unit=10, FMT=*) "U1=", U1, " U2=", U2
      IF (N1<2) Then
      write (unit=10, FMT=200)
      DO I=1, 100
      Write (unit=10, FMT=100) X(I), V(I), S(I), L(I)
      End DO
      End IF
      If ((Real(N1/100.0)-Int(N1/100))<1.0D-10) Then
      write (unit=10, FMT=200)
      DO I=1, 100
      Write (unit=10, FMT=100) X(I), V(I), S(I), L(I)
      End DO
      End If
```

```
      IF (N1<100) Then
      IF ((Real(N1/25.0)-Int(N1/25))<1.0D-10) Then
      write (unit=10, FMT=200)
      DO I=1, 100
      Write (unit=10, FMT=100) X(I), V(I), S(I), L(I)
      End DO
      End If
      End IF
      IF (N1>600) Then
      IF (N1<700) Then
      IF ((Real(N1/25.0)-Int(N1/25))<1.0D-10) Then
      write (unit=10, FMT=200)
      DO I=1, 100
      Write (unit=10, FMT=100) X(I), V(I), S(I), L(I)
      End DO
      End IF
      End IF
      End IF
!     write (unit=10, FMT=*) N1, "  ",a0, "  ", "  ",U1, "  ",U2
!     print crack opening results at cycle N on screen
      print *, K-1, " iterations for U2 calculation"
      print *, "Crack opening level U2=", U2
      END Subroutine Crack_Opening
```

Appendix B: Code for analytical model to identify threshold fatigue crack growth

```
%%%%%%%%%%%%%%%%%%%%%%%%%%%%%%%%%%%%%%%%%%
%%%%%%%%%%%%%%%
    %%%%%%%%%%%%%%%%%%%%%% Carica File
%%%%%%%%%%%%%%%%%%%%%%

%%%%%%%%%%%%%%%%%%%%%%%%%%%%%%%%%%%%%%%%%%
%%%%%%%%%%%%%%%

clear all
clc

[filename_r, pathname_r] = uigetfile({'*.dat','*.txt'},'Carica i dati','MultiSelect','on');
if isequal(filename_r,0)||isequal(pathname_r,0)
  disp('File non caricato.')
  clear filename_r pathname_r
else
  if iscell(filename_r)==1
    for l=1:size(filename_r,2)
      nome{l}=[pathname_r,filename_r{l}];
      disp(nome{l})
    end
  else
    nome0=[pathname_r,filename_r];
    disp(nome0)
    nome{1}=nome0;
    n=filename_r;
    clear filename_r
    filename_r{1}=n;
    clear n
```

```
    end
     %%%%%%%%%%%%%% ghonem %%%%%%%%%%%%%%%%%%%%
    R=0.6;
    Pmax=22.79;
    Pmin=13.68;
%       R= 0.5;
%       Pmax=22.25;
%       Pmin=11.13;
%       R=0.4;
%       Pmax=15.19;
%       Pmin=6.08;
    W=10.16;
    B=0.3175;
%%%%%%%%%%%%  virkler %%%%%%%%%%%%%%%%
%       R=0.2;
%       Pmax=23.35;
%       Pmin=4.67;
%       W=12.7;
%       B=0.254;
%%%%%%%%%%%%  Wu&Ni %%%%%%%%%%%%%%%%
%       R=0.2;
%       Pmax=4.5;
%       Pmin=0.9;
%       W=5;
%       B=1.2;
%%%%%%%%%%%%  MMateriale K %%%%%%%%%%%%%%%%
%       R=0.5;
%       DP1=5.678;
%       Pmax=DP1/(1-R);
%       Pmin=Pmax-DP1;
%       W=45;
%       B=20;

   for l=1:size(nome,2)
```

```
        Dati=importdata(nome{l});


%%%%%%%%%%%%%%%%%%%%%%%%%%%%%%%%%%%%%%%%%%
%%%%%%%%%%%%%%%
        %%%%%%%%%%%%%%%%%%% Interpolazione
%%%%%%%%%%%%%%%%%%%

%%%%%%%%%%%%%%%%%%%%%%%%%%%%%%%%%%%%%%%%%%
%%%%%%%%%%%%%%%
%       [m,n]=size(Dati);
        N=Dati(1:end,1); %t
        a=Dati(1:end,2); %w y(i)
        m=length(N);
        a1=a(1); %r Dati(1,2) y(1)
        am=a(m); %d Dati(m,2)
        Nm=N(m); %c x(m)

%       f1=fittype('((c-(((a0-(c*((N0/(N0+r))^esp)))/((-((N0/(N0+r))^esp)*exp(1/(beta-
1)))+(exp(((N0/(N0+r))^alfa)/(beta-((N0/(N0+r))^alfa))))))*(exp(1/(beta-
1)))))*(((x+N0)/(r+N0))^esp))+(((a0-(c*((N0/(N0+r))^esp)))/((-
((N0/(N0+r))^esp)*exp(1/(beta-1)))+(exp(((N0/(N0+r))^alfa)/(beta-
((N0/(N0+r))^alfa))))))*(exp((((x+N0)/(r+N0))^alfa)/(beta-
(((x+N0)/(r+N0))^alfa)))))','problem',{'c','r','a0'},'coefficients',{'alfa','beta','N0','esp'},'ind
ependent',{'x'});
%       s = fitoptions('Method','NonlinearLeastSquares','Lower',[1.1 1.8 0
1.25],'Upper',[50 50 30*Nm 3.7],'Robust','LAR','StartPoint',[1 1.5 2*Nm
1.5],'Algorithm','trust-region','MaxFunEvals',1e6,'MaxIter',1e6,'TolFun',1e-4,'TolX',1e-
4);
%       [f2,gof,fitness] = fit(N,a,f1,'problem',{am,Nm,a1},s);
        f1=fittype('(h*(((x+N0)/(r+N0))^esp))+(k*exp((((x+N0)/(r+N0))^alfa)/(beta-
(((x+N0)/(r+N0))^alfa))))','problem',{'r'},'coefficients',{'alfa','beta','N0','esp','h','k'},'indep
endent',{'x'});
```

```
        s = fitoptions('Method','NonlinearLeastSquares','Lower',[1.1 1.1 Nm 1.15 0.8
0.5],'Upper',[80 80 100*Nm 7 80 1],'Robust','LAR','StartPoint',[1.5 1.9 10*Nm 1.5 10
0.7],'Algorithm','trust-region','MaxFunEvals',1e6,'MaxIter',1e6,'TolFun',1e-6,'TolX',1e-
6);
        [f2,gof,fitness] = fit(N,a,f1,'problem',{Nm},s);
        coeff(l,:)=coeffvalues(f2);
        alpha(l,:)=coeff(l,1);
        beta(l,:)=coeff(l,2);
        N0(l,:)=coeff(l,3);
        p(l,:)=coeff(l,4);
        hmod(l,:)=coeff(l,5);
        kmod(l,:)=coeff(l,6);
%         kmod(l,:)=(a1-(am*((coeff(l,3)/(coeff(l,3)+Nm))^coeff(l,4))))/((-
((coeff(l,3)/(coeff(l,3)+Nm))^coeff(l,4))*exp(1/(coeff(l,2)-
1)))+(exp(((coeff(l,3)/(coeff(l,3)+Nm))^coeff(l,1))/(coeff(l,2)-
((coeff(l,3)/(coeff(l,3)+Nm))^coeff(l,1))))));
%         hmod(l,:)=am-(kmod(l,:)*exp(1/(coeff(l,2)-1)));
        Nfit(:,l)=linspace(-N0(l,:),Nm,1000);
        analitici(:,2*l)=f2(Nfit(:,l));
        analitici(:,(2*l)-1)=Nfit(:,l);
        grezzi{:,2*l}=Dati(:,2);
        grezzi{:,(2*l)-1}=Dati(:,1);
       for i=1:1000

afit(i,l)=(hmod(l)*(((Nfit(i,l)+N0(l))/(N0(l)+Nm))^p(l)))+(kmod(l)*exp((((Nfit(i,l)+N0(l))/(N
0(l)+Nm))^alpha(l))/(beta(l)-(((Nfit(i,l)+N0(l))/(N0(l)+Nm))^alpha(l)))));
        end
        a0(l,:)=kmod(l);
        Nt{l,:}=N;
        at{l,:}=a;
        Nmt(l,:)=N(m);
```

```
       %%%%% Virkler & Ghonem
%%%%%%%%%%%%%%%%%%%%%%%%%%%%%%%%%%%%%%%%%%%%
%%
        MM=(Pmax-Pmin)/B;
        MMmax=Pmax/B;
        t(l,:)=((2*(a0(l,:)/10))/W);
        FT(l,:)=(((pi*t(l,:))/(2*W))*(sec((pi*t(l,:))/2)))^0.5;
        DKth(l,:)=MM*FT(l,:);
        Kmax(l,:)=MMmax*FT(l,:);

        %%%%% Wu & Ni
%%%%%%%%%%%%%%%%%%%%%%%%%%%%%%%%%%%%%%%%%%%%
%%%%%%%%%%%
%       MM=(Pmax-Pmin)/(B*(W^0.5));
%       t(l,:)=((a0(l,:)/10)/W);
%       FT(l,:)=0.886+(4.64*t(l,:))-(13.32*(t(l,:)^2))+(14.72*(t(l,:)^3))-(5.6*(t(l,:)^4));
%       DKth(l,:)=MM*((2+t(l,:))/((1-t(l,:))^1.5))*FT(l,:);
%       MMmax = Pmax / (B*(W^0.5));
%       Kmax(l,:)=(MMmax*((2+t(l,:))/((1-t(l,:))^1.5))*FT(l,:));
        %%%%% Naples Dataset
%%%%%%%%%%%%%%%%%%%%%%%%%%%%%%%%%%%%%%%%%%%%
%%%%%%%
%       DP=Pmax-Pmin;
%       t(l,:)=a0(l,:)/W;
%       FT(l,:)=(DP/(B*(W^0.5)))*(10^1.5);
%       G(l,:)=((6*(t(l,:)^0.5))/((1+2*t(l,:))*((1-t(l,:))^1.5)))*((1.99-((t(l,:)*(1-t(l,:)))*(2.15-
(3.93*t(l,:))+(2.7*(t(l,:)^2))))));
%       DKth(l,:)=G(l,:)*FT(l,:);
%       Kmax(l,:)=G(l,:)*(Pmax/(B*(W^0.5)))*(10^1.5);




        data{:,l}=(fitness.residuals);
        R2(l,:)=(gof.rsquare);
```

```
%%%%%%%%%%%%%%%%%%%%%%%%%%%%%%%%%%%%%%%%%%%
%%%%%%%%%%%%%%%
    %%%%%%%%%%%%%%%%%%% test di Normalità
%%%%%%%%%%%%%%%%%%%

%%%%%%%%%%%%%%%%%%%%%%%%%%%%%%%%%%%%%%%%%%%
%%%%%%%%%%%%%%%

    %%%%%%%%%%%%%%%%% distribuzione Normale
%%%%%%%%%%%%%%%%%
%       [muhat,sigmahat,muci,sigmaci] = normfit(data{:,l});
%       [muhat,sigmahat] = normfit(data{:,l});
%       med_dev(l,:)=[muhat,sigmahat];
%       [hn(l,1),pn(l,1)] = chi2gof(data{:,l},'nbins',20,'cdf',{@normcdf,muhat
,sigmahat});
% %       optimization(:,l)=[coeff,med_dev,R2,hn,pn];



    Ncalc=N;
    acalc=a;

%       N=N(:,l);
%       a=a(:,l);
%%%%% ASTM method to estimate the Crack Growth Rate and the SIF
%%%%% Incremental Polynominal Method
%
    Numr = length(Ncalc);
    Camp= 7; % Numero di punti su cui campionare
for i=1:(Numr-Camp+1)
    NN=Ncalc(i:i+(Camp-1));
    aa=acalc(i:i+(Camp-1));
```

```
        C1=(0.5*(NN(1)+NN(Camp)));
        C2=(0.5*(NN(Camp)-NN(1)));
        N_centrale(i)=NN((Camp+1)/2); % definizione del punto centrale cui attribuire il
nuovo valore di cricca.
        fpar=fittype('(b2*((x-C1)/C2)^2)+(b1*((x-
C1)/C2))+b0','problem',{'C1','C2'},'coefficients',{'b0','b1','b2'},'independent',{'x'});
        spar = fitoptions('Method','NonlinearLeastSquares','Lower',[ -inf -inf -inf],'Upper',[
inf, inf, inf],'Robust','LAR','StartPoint',[20,0.2,0.2],'Algorithm','trust-
region','MaxFunEvals',1e6,'MaxIter',1e6,'TolFun',1e-6,'TolX',1e-6);
        [f2par,gofpar,fitnesspar] = fit(NN,aa,fpar,'problem',{C1,C2},spar);
        coeffpar=coeffvalues(f2par);
        b0=coeffpar(1);
        b1=coeffpar(2);
        b2=coeffpar(3);
        asec(i)=((b2*(((N_centrale(i)-C1)/C2)^2))+(b1*((N_centrale(i)-C1)/C2))+b0);
        dadNsec(i)=((b1/C2)+(2*b2*((N_centrale(i)-C1)/(C2^2))));
        Nsec(i)=N_centrale(i);

        %%%%% Virkler & Ghonem
%%%%%%%%%%%%%%%%%%%%%%%%%%%%%%%%%%%%%%%%%%%%%%%
%%
        MM=(Pmax-Pmin)/B;
        tsec(i)=((2*(asec(i)/10))/W);
        FTsec(i)=(((pi*tsec(i))/(2*W))*(sec((pi*tsec(i))/2)))^0.5;
        DKsec(i)=MM*FTsec(i);

        %%%%% Wu & Ni
%%%%%%%%%%%%%%%%%%%%%%%%%%%%%%%%%%%%%%%%%%%%%%%
%%%%%%%%%%%
%       MM=(Pmax-Pmin)/(B*(W^0.5));
%       tsec(i)=((asec(i)/10)/W);
%       FTsec(i)=0.886+(4.64*tsec(i))-(13.32*(tsec(i)^2))+(14.72*(tsec(i)^3))-
(5.6*(tsec(i)^4));
%       DKsec(i)=MM*((2+tsec(i))/((1-tsec(i))^1.5))*FTsec(i);
```

```
     %%%%% Materiale K
%%%%%%%%%%%%%%%%%%%%%%%%%%%%%%%%%%%%%%%%%%
%%%%%%%
%       DP=Pmax-Pmin;
%       tsec(i)=asec(i)/(10*W);
%       FTsec(i)=(DP/(B*(W^0.5)))*(10^1.5);
%       Gsec(i)=((6*(tsec(i)^0.5))/((1+2*tsec(i))*((1-tsec(i))^1.5)))*((1.99-((tsec(i)*(1-
tsec(i)))*(2.15-(3.93*tsec(i))+(2.7*(tsec(i)^2))))));
%       DKsec(i)=Gsec(i)*FTsec(i);



 end %for i=1:(Numr-Camp+1)
    Nsect(:,l)=Nsec;
    dadNsect(:,l)=dadNsec;
    DKsect(:,l)=DKsec;
    asect(:,l)=asec;
    fft=1000;
    Nr(:,l)=linspace(-N0(l,:),Nm,fft);
    for i=1:fft

ar(i,l)=(hmod(l)*(((Nr(i,l)+N0(l))/(N0(l)+Nmt(l)))^p(l)))+(kmod(l)*exp((((Nr(i,l)+N0(l))/(N
0(l)+Nmt(l)))^alpha(l))/(beta(l)-(((Nr(i,l)+N0(l))/(N0(l)+Nmt(l)))^alpha(l)))));
    end
    for i=1:fft
%      dadN(l,)=(am(l) + a1(l) / (exp(0.1e1 / (beta(l) - 1)) * (N0(l) / (N0(l) + Nm(l))) ^
p(l) - exp((N0(l) / (N0(l) + Nm(l))) ^ alfa(l) / (beta(l) - (N0(l) / (N0(l) + Nm(l))) ^ alfa(l))))
* exp(0.1e1 / (beta(l) - 1))) * ((N0(l) + Nr(l,i)) / (N0(l) + Nm(l))) ^ p(l) * p(l) / (N0(l) +
Nr(l,i)) - a1(l) / (exp(0.1e1 / (beta(l) - 1)) * (N0(l) / (N0(l) + Nm(l))) ^ p(l) - exp((N0(l) /
(N0(l) + Nm(l))) ^ alfa(l) / (beta(l) - (N0(l) / (N0(l) + Nm(l))) ^ alfa(l)))) * (((N0(l) +
Nr(l,i)) / (N0(l) + Nm(l))) ^ alfa(l) * alfa(l) / (N0(l) + Nr(l,i)) / (beta(l) - ((N0(l) + Nr(l,i)) /
(N0(l) + Nm(l))) ^ alfa(l)) + (((N0(l) + Nr(l,i)) / (N0(l) + Nm(l))) ^ alfa(l)) ^ 2 / (beta(l) -
```

```
((N0(l) + Nr(l,i)) / (N0(l) + Nm(l))) ^ alfa(l)) ^ 2 * alfa(l) / (N0(l) + Nr(l,i))) * exp(((N0(l) +
Nr(l,i)) / (N0(l) + Nm(l))) ^ alfa(l) / (beta(l) - ((N0(l) + Nr(l,i)) / (N0(l) + Nm(l))) ^ alfa(l)));
    dadN1(i,l) = hmod(l)*p(l)*((N0(l)+Nr(i,l))/(Nmt(l)+N0(l)))^(p(l) - 1);
    dadN2(i,l)=kmod(l)*exp(((((N0(l)+Nr(i,l))/(Nmt(l)+N0(l)))^alpha(l))/(beta(l) -
(((N0(l)+Nr(i,l))/(Nmt(l)+N0(l)))^alpha(l)))));
    dadN3(i,l)=((alpha(l)*((N0(l)+Nr(i,l))/(Nmt(l)+N0(l)))^(alpha(l) - 1))/(beta(l) -
((N0(l)+Nr(i,l))/(Nmt(l)+N0(l)))^alpha(l)) +
(alpha(l)*((N0(l)+Nr(i,l))/(Nmt(l)+N0(l)))^alpha(l)*((N0(l)+Nr(i,l))/(Nmt(l)+N0(l)))^(alpha
(l) - 1))/(beta(l) - ((N0(l)+Nr(i,l))/(Nmt(l)+N0(l)))^alpha(l))^2);
    dadN(i,l)=((dadN3(i,l)*dadN2(i,l))+dadN1(i,l))/(N0(l)+Nmt(l));

    %%%%% Virkler & Ghonem
%%%%%%%%%%%%%%%%%%%%%%%%%%%%%%%%%%%%%%%%%%%%%
%%
    MM=(Pmax-Pmin)/B;
    teq(i)=((2*(ar(i,l)/10))/W);
    FTeq(i)=(((pi*teq(i))/(2*W))*(sec((pi*teq(i))/2)))^0.5;
    DKeq(i)=MM*FTeq(i);
     %%%%% Wu & Ni
%%%%%%%%%%%%%%%%%%%%%%%%%%%%%%%%%%%%%%%%%%%%%
%%%%%%%%%%%%
%        MM=(Pmax-Pmin)/(B*(W^0.5));
%        teq(i)=((ar(i,l)/10)/W);
%        FTeq(i)=0.886+(4.64*teq(i))-(13.32*(teq(i)^2))+(14.72*(teq(i)^3))-
(5.6*(teq(i)^4));
%        DKeq(i)=MM*((2+teq(i))/((1-teq(i))^1.5))*FTeq(i);

      %%%%% Materiale K
%%%%%%%%%%%%%%%%%%%%%%%%%%%%%%%%%%%%%%%%%%%%%
%%%%%%%%
%        DP=Pmax-Pmin;
%        teq(i)=ar(i,l)/(10*W);
%        FTeq(i)=(DP/(B*(W^0.5)))*(10^1.5);
```

```
%       Geq(i)=((6*(teq(i)^0.5))/((1+2*teq(i))*((1-teq(i))^1.5)))*((1.99-((teq(i)*(1-
teq(i)))*(2.15-(3.93*teq(i))+(2.7*(teq(i)^2))))));
%       DKeq(i)=Geq(i)*FTeq(i);



    end
    DKeqt(:,l)=DKeq;
end

 figure(1)
 grid on
    hold on
    for k=1:size(Nt,1)
    plot(Nt{k,:},at{k,:},'*r')
    plot(Nfit(:,k),afit(:,k),'-b')
    end
    hold off

pers=[R2,coeff,hmod,kmod,a0,DKth,Kmax,Nmt];
% pers=[hn,R2,coeff,hmod,kmod,a0];
% [RHOP,PVALP] = corr(pers,'type','Pearson','rows','all');
% [RHOk,PVALk] = corr(pers,'type','Kendall','rows','all');
% [RHOs,PVALs] = corr(pers,'type','Spearman','rows','all');




 figure(2)
    hold on
    plot(Nr,dadN,'-r')
    plot(Nsect,dadNsect,'*b')
    hold off
 figure(3)
    hold on
```

```
    plot(ar,dadN,'-r')
    plot(asect,dadNsect,'*b')
    hold off
figure(4)
    hold on
    plot(Nr,ar,'-r')
    plot(N,a,'*b')
    hold off
figure(5)
    hold on
    plot(DKsect,dadNsect,'*r')
    plot(DKeqt,dadN,'--b')
    hold off
end
```

Appendix C: List of Published Papers

1. Mohin, M. A., Toofanny, H., Babutskyi, A., Lewis, A., & Xu, Y. G. (2016). Effect of Electromagnetic Treatment on Fatigue Resistance of 2011 Aluminum Alloy. Journal of Multiscale Modelling, 7(03), 1650004.
2. Lewis, A., Mohin, M., Chrysanthou, A., & Xu, Y. (2016). Effect of Plastic Deformation on Compliance Curve Based Crack Closure Measurement. Key Engineering Materials.
3. Grasso, M., De Iorio, A., Xu, Y., Haritos, G., Mohin, M., & Chen, Y. K. (2017). An analytical model for the identification of the threshold of stress intensity factor range for crack growth. Advances in Materials Science and Engineering, 2017.